Methods for Electrical Impedance Spectroscopy and Tomography Characterising Particles in Suspensions and Crystallisation Processes

Yanlin Zhao

Submitted in accordance with the requirements for the degree of

Doctor of Philosophy

The University of Leeds
Institute of Particle Science and Engineering
School of Process, Environmental and Materials Engineering

August 2012

The candidate confirms that the work submitted is her own, and that appropriate credit has been given where reference has been made to the work of others.

To my parents Ming Zhao & Xianfeng Zhu

My husband Dr. Jun Yao and my daughter Suyang Yao

Acknowledgements

I would like to thank my supervisors Professor Mi Wang and Dr. Robert. B. Hammond for their guidance, support and encouragement during the whole PhD study. Prof. Mi Wang has always been supportive in giving guidelines and invaluable suggestions for my study. He provided strong support and encouraged me to resist when I encountered difficulties in the research. I also want to thank Dr. Hammond for his good advice on the study of crystallisation processes.

I want to thank all my current and previous colleagues in the OLIL research group, Dr. Jiabin Jia, Dr. Qingchun Yuan, Dr. Inaki Schlaberg, Dr. Peng Guan, Dr. Jafar Khan, Dr. Jiamin Ye, Khalid Ismail and Yousef Faraj for their support and discussions. I would also like to thank the technician Mr. Robert Harris (Bob) for providing help during the construction of the experimental devices.

I would like to thank the Oversea Research Students Award Scheme and the Tetley & Lupton Scholarship provided by the University of Leeds for the financial support on my PhD study.

At last but not least, I would especially thank my family for their selfless support. My parents, Xianfeng Zhu and Ming Zhao help me to take care of my daughter on the last year of my PhD study. They give me all the love and help which they can give. My husband, Dr. Jun Yao provides strong moral encouragement and gives me all his love and understanding. I always remember my daughter, Suyang Yao, who was born during the third year of my PhD. Although I cannot always accompany her in her growth, she gives me the most precious memory in these unforgettable days.

Abstract

Electrical impedance spectroscopy (EIS) is a method used to study the frequency dependence of the dielectric properties of colloidal suspensions by applying an alternating electric field. When an alternating electric field is applied, a dipole moment can be induced on a charged-particle due to the relative motion between the particles and their electric double layer. The macroscopic display of induced dipole moment is usually represented by the impedance parameters, including the impedance real part, imaginary part, phase angle and the relaxation frequency. These quantities are related to the size, shape and surface of the dispersed particles, the nature of the dispersed medium, and also the concentration of the particles.

This thesis describes a fundamental study of the EIS method applied to colloidal particles. The relationship between the impedance parameters and the properties of particle suspensions is investigated. The study reveals the effects of particle size, particle concentration and ionic concentration dependence on the detected impedance parameters. Based on the study, new methods, including modelling, signal process, test set-up and data analysis, for characterisation of particles in suspensions are developed through the experimental approach and theoretical analysis. The methods are verified with silica suspensions and applied to crystallisation processes. The on-line measured electrical impedance spectra associated with L-glutamic acid nucleation-growth processes and a polymorphic transformation are analysed. It is demonstrated that the methods can be applied for on-line monitoring of the particle size and polymorphs in crystallisation processes. Electrical impedance tomography based on EIS measurement conducted with different materials, including non-conductive plastic bar, banana, and silica suspensions are studied. The responses of electric polarisation of colloidal particles on tomographic images can be observed. However, the difference in particle size cannot be observed in the tomographic images possibly due to the limits of the imaging resolution from an 8-electrode sensor and the signal quality affected by the limits of the common mode voltage rejection ratio of the instrument.

Table of Contents

Acknowledgements ..... **iv**

Abstract ..... **v**

Table of Contents ..... **vi**

List of Figures ..... **ix**

List of Tables ..... **xvi**

List of Symbols ..... **xvii**

List of Abbreviations ..... **xix**

Chapter 1 Introduction **1**

1.1 Background 1

1.2 Objective of My Research 2

1.3 Organization of the Thesis 3

Chapter 2 Electrokinetics of Colloids, Electrical Impedance Spectroscopy, Particle Sizing Methods and the Crystallisation Process **5**

2.1 Introduction 5

2.2 Electrokinetic Properties of Colloidal Particles 6

2.2.1 Colloidal Particle and Electrical Double Layer 6

2.2.2 Colloidal Particles under an Electric Field 10

2.2.3 Dielectric Dispersion 15

2.2.4 Dielectric Properties and Theoretical Modelling 20

2.2.5 Effect of Particle Size on Dielectric Properties 26

2.2.6 Effect of Particle Shape on Dielectric Properties 27

2.3 Electrical Impedance Spectroscopy 29

2.3.1 Introduction 29

2.3.2 Electrical impedance spectroscopy 29

2.3.3 Electrical Circuit Elements 31

2.3.4 Electrode System 35

2.3.5 Applications of Impedance Spectroscopy 37

2.4 Electrical Impedance Tomography 38

2.4.1 Introduction 38

2.4.2 Measurement Procedure 39

2.4.3 Common Mode Voltage 42

2.4.4 Imaging Reconstruction 44

2.5 Particle Sizing Methods 45

2.5.1 Microscopy 46

2.5.2 Sieving 48

2.5.3 Sedimentation 48
2.5.4 Counting technique 50
2.5.5 Light scattering/diffraction methods 52
2.5.6 Chromatography techniques 53
2.5.7 Electroacoustic Technique 54
2.5.8 Other techniques 55
2.6 On-line Particle Sizing Methods 56
2.6.1 Optical based methods 56
2.6.2 Non-optical based methods 59
2.7 Theory of the Crystallisation Process 66
2.7.1 Crystal Nucleation and Growth 66
2.7.2 Crystallisation of L-Glutamic Acid 70
2.7.3 On-line Monitoring of the Crystallisation Process 72
2.8 Summary 74
Chapter 3 Experimental Devices and Materials 76
3.1 Introduction 76
3.2 Materials 77
3.3 Devices for Colloidal Suspensions 78
3.4 Devices for Crystallisaion 80
3.4.1 Electrode sensor 80
3.4.2 Vessel and circulator 81
3.4.3 Temperature and turbidity sensor 82
3.4.4 Data acquisition system 84
3.4.4.1 SCC modules 84
3.4.4.2 Signal conditioning circuit (SCC) carrier 85
3.4.4.3 DAQ device 87
3.4.5 Focused Beam Reflectance Measurement 89
3.5 Devices for EIT Measurement 90
3.6 Methodology 91
3.7 Summary 93
Chapter 4 Development of the Electrical Impedance Spectroscopy Method for Characterising Particles in Silica Suspensions 95
4.1 Introduction 95
4.2 Physical properties of silica suspensions 96
4.2.1 Particle size distribution 96
4.2.2 Zeta potential and pH value 100
4.3 Calibration of cell constant 101
4.4 Particle size effect 102

4.4.1 Impedance spectra 103
4.4.2 Relative Changes of Phase angle 113
4.4.3 α dispersion and MWO dispersion 121
4.5 Particle concentration effect 131
4.6 Ionic concentration effects 136
4.7 Summary 142
Chapter 5 On-line Characterisation of Crystallisation Processes with Electrical Impedance Spectroscopy 143
5.1 Introduction 143
5.2 Methodology 144
5.3 Effect of Solid LGA Concentration 147
5.4 Effect of Solute Concentration 151
5.5 Effect of Temperature 154
5.6 On-line EIS during Crystallisation Processes 157
5.6.1 Electrical Impedance Spectra 157
5.6.2 Electrical Impedance Parameters Changing with Time 164
5.7 Polymorphism in Crystallisation Processes 170
5.7.1 Crystallisation with a Single α Form 170
5.7.2 Polymorphic Transformation 173
5.8 Summary 179
Chapter 6 Electrical Impedance Tomography Spectroscopy 180
6.1 Introduction 180
6.2 Methodology 181
6.3 EITS Measurement using an 8-electrode Sensor 183
6.3.1 Common Mode Voltage Rejection Ratio (CMMR) 183
6.3.2 Method for Reducing Common Mode Voltage Effect 186
6.3.3 Images at Low and High Frequency 189
6.3.4 Images of Banana in Tap Water 192
6.3.5 Images of Silica Suspensions 196
6.4 Summary 201
Chapter 7 Conclusions and Future Work 202
7.1 Conclusion 202
7.2 Future work 204
Reference 207
Appendix 217

List of Figures

Figure 2.1: Schematic diagram of the electric double layer and zeta potential 7

Figure 2.2: Forces on a charged particle (positively charged) under a static electrical 11

Figure 2.3: Electrophoresis patterns of polystyrene spheres 13

Figure 2.4: Schematic of the generation of the electrolyte concentration gradient responsible for α dispersion for a negatively charged particle 18

Figure 2.5: Cole-Cole plot of pure resistor 32

Figure 2.6: Cole-Cole plot of pure capacitor 32

Figure 2.7: Cole-Cole plot of pure inductor 33

Figure 2.8: Two-terminal electrochemical cell 36

Figure 2.9: Three-terminal electrochemical cell 36

Figure 2.10: Four-terminal electrochemical cell 37

Figure 2.11: The schematic of adjacent data sensing strategy 40

Figure 2.12: Measurement data for one frame image in an 8-electrode system 41

Figure 2.13: The typical profiles of measured voltages, reference voltages, and relative voltage changes, respectively in an 8-electrode system 42

Figure 2.14: A differential amplifier and its inputs and outputs 43

Figure 2.15: Reconstructed image (impedance real part) of a plastic rod in tap water using an 8-electrode system 45

Figure 2.16: Schematic diagram of the laser diffraction technique 57

Figure 2.17: Schematic diagram of the focused beam reflectance technique 58

Figure 2.18: Schematic diagram of the ultrasonic attenuation spectroscopy technique 60

Figure 2.19: The dependence of free energies of liquid and solid on temperature T ... 67

Figure 2.20: The free energy change associated with homogeneous nucleation of a sphere of radius r 68

Figure 2.21: The energy barrier/driving force for homogeneous and heterogeneous nucleation 68

Figure 2.22: Surface structure of growing crystal a) flat surfaces, b) steps, c) kinks 69

Figure 2.23: Development of a growth spiral starting from a screw dislocation 70

Figure 2.24: The chemical structure of LGA 70

Figure 2.25: Dissociation equations of L-glutamic acid 71

Figure 2.26: The two polymorphic forms of LGA: (a) α-form (prismatic); (b) β-form (needle-like platelets) 71

Figure 3.1: Photograph of the impedance analyzer (Solartron 1260 Impedance/Gain-Phase Analyzer) 79

Figure 3.2: Schematic of the four-electrode vessel 79

Figure 3.3: Photograph of the vessel with the four-electrode sensor 80

Figure 3.4: Photograph of the four-electrode sensor for crystallisation experiments.... 81

Figure 3.5: Glass jacketed vessel and magnetic stirrer 81

Figure 3.6: Julabo refrigerated and heating circulator (F32-HE) 82

Figure 3.7: Turbidity probe and transmittance box 83

Figure 3.8: Diagram of socket layouts on SC-2345 carrier. 86

Figure 3.9: SCC-RTD01 single channel wiring diagram (RTD input manual, NI) 86

Figure 3.10: Bottom view of the SCC module 87

Figure 3.11: PMD-1208LS screw terminal pin numbers 88

Figure 3.12: The pin numbers and associated signals on the PMD-1208LS 88

Figure 3.13: Diagram of the TracerDAQ software working window 89

Figure 3.14 Lasentec S400 FBRM probe and controller 89

Figure 3.15: Cylindrical vessel with an 8-electrode sensor 90

Figure 3.16: Perspex chamber as a housing for silica suspension 91

Figure 3.17: One and two chambers in the cylindrical vessel 91

Figure 3.18: Experimental setup for on-line measurement of EIS during crystallisation 92

Figure 3.19: The schematic of adjacent data sensing strategy for an 8-electrode sensor 93

Figure 4.1: Particle size distribution of 10.0 wt % silica suspensions 97

Figure 4.2: Particle size distribution of 5.0 wt % silica suspensions 97

Figure 4.3: Particle size distribution of 1.0 wt % silica suspensions 98

Figure 4.4: Particle size distribution of 0.5 wt % silica suspensions 98

Figure 4.5: Impedance spectra for silica suspensions (10.0 wt %) with different particle size (18.7^{12} nm, 190.1^{35} nm, 270.4^{70} nm, 220.2^{90} nm, 467.9^{220} nm); (a) cole-cole plot of impedance; (b) impedance real part vs. frequency; (c) impedance imaginary part vs. frequency; (d) phase angle vs. frequency plots. 107

Figure 4.6: Impedance spectra for silica suspensions (5.0 wt %) of different particle size (13.54^{12} nm, 91.28^{35} nm, 190.1^{70} nm, 199.7^{90} nm, 384.6^{220} nm); (a) Cole-Cole plot

of impedance; (b) impedance real part vs. frequency; (c) impedance imaginary part vs. frequency; (d) phase angle vs. frequency plots 109

Figure 4.7: Impedance spectra for silica suspensions (1.0 wt %) of different particle size (7.53^{12} nm, 58.77^{35} nm, 164.2^{70} nm, 180.9^{90} nm, 378.0^{220} nm); (a) Cole-Cole plot of impedance; (b) impedance real part vs. frequency; (c) impedance imaginary part vs. frequency; (d) phase angle vs. frequency plots 111

Figure 4.8: Impedance spectra for silica suspensions (0.5 wt %) of different particle size (7.53^{12} nm, 68.06^{35} nm, 148.1^{70} nm, 178.7^{90} nm, 425.8^{220} nm); (a) Cole-Cole plot of impedance; (b) impedance real part vs. frequency; (c) impedance imaginary part vs. frequency; (d) phase angle vs. frequency plots 113

Figure 4.9: Parallel RC equivalent circuit (R is resistance and C is capacitance) 114

Figure 4.10: The plots of relative changes in tan(θ) vs. particle size in the silica suspensions with different particle concentrations (a) 10.0 wt%, (b) 5.0 wt%, (c) 1.0 wt% and (d) 0.5 wt% 120

Figure 4.11: The imaginary part of complex permittivity spectra for silica suspensions (10.0 wt %) with different particle size (18.7^{12} nm, 190.1^{35} nm, 270.4^{70} nm, 220.2^{90} nm, 467.9^{220} nm) 123

Figure 4.12: The imaginary part of complex permittivity spectra for silica suspensions (5.0 wt %) with different particle size (13.54^{12} nm, 91.28^{35} nm, 190.1^{70} nm, 199.7^{90} nm, 384.6^{220} nm) 123

Figure 4.13: The imaginary part of complex permittivity spectra for silica suspensions (1.0 wt %) with different particle size (7.53^{12} nm, 58.77^{35} nm, 164.2^{70} nm, 180.9^{90} nm, 378.0^{220} nm) 124

Figure 4.14: The imaginary part of complex permittivity spectra for silica suspensions (0.5 wt %) with different particle size (7.53^{12} nm, 68.06^{35} nm, 148.1^{70} nm, 178.7^{90} nm, 425.8^{220} nm) 124

Figure 4.15: The relaxation frequency ω_α is plotted against particle size and is proportional to $1/(a+\kappa^{-1})^2$ for 10.0 wt% silica suspensions of different particle size (18.7^{12} nm, 190.1^{35} nm, 270.4^{70} nm, 220.2^{90} nm, 467.9^{220} nm) 126

Figure 4.16: The relaxation frequency ω_α is plotted against particle size and is proportional to $1/(a+\kappa^{-1})^2$ for 5.0 wt% silica suspensions of different particle size (13.54^{12} nm, 91.28^{35} nm, 190.1^{70} nm, 199.7^{90} nm, 384.6^{220} nm) 127

Figure 4.17: ω_{MWO} for silica suspensions (10.0 wt %) with different particle size (18.7^{12} nm, 190.1^{35} nm, 270.4^{70} nm, 220.2^{90} nm, 467.9^{220} nm) 129

Figure 4.18: ω_{MWO} for silica suspensions (5.0 wt %) with different particle size (13.54^{12} nm, 91.28^{35} nm, 190.1^{70} nm, 199.7^{90} nm, 384.6^{220} nm) 129

Figure 4.19: ω_{MWO} for silica suspensions (1.0 wt %) with different particle size (7.53^{12} nm, 58.77^{35} nm, 164.2^{70} nm, 180.9^{90} nm, 378.0^{220} nm) 130

Figure 4.20: ω_{MWO} for silica suspensions (0.5 wt %) with different particle size (7.53^{12} nm, 68.06^{35} nm, 148.1^{70} nm, 178.7^{90} nm, 425.8^{220} nm) 130

Figure 4.21: Impedance real part vs. frequency for silica suspensions (220 nm) with different particle concentrations (10.0 wt%, 5.0 wt%, 1.0 wt%, 0.5 wt%)..... 131

Figure 4.22: The dependence of ω_α on particle concentration for silica suspensions with different particle size (12 nm, 35 nm, 70 nm, 90 nm, 220 nm) 135

Figure 4.23: The relationship between the relative changes in tan(θ) and the particle concentration for silica suspensions..... 136

Figure 4.24: Impedance spectra for silica suspensions (12 nm, 5.0 wt %) without adding extra electrolyte and with 1.67 mM KCl electrolyte; (a) Cole-Cole plot of impedance; (b) impedance real part vs. frequency; (c) impedance imaginary part vs. frequency; (d) phase angle vs. frequency plots..... 138

Figure 4.25: The imaginary part of complex permittivity spectra for silica suspensions (12 nm, 5.0 wt %) without adding extra electrolyte and with 1.67 mM KCl electrolyte 139

Figure 4.26: The imaginary part of complex permittivity spectra for silica suspensions (5.0 wt%) with 1.67 mM KCl electrolyte and different particle size (12 nm, 35 nm, 70 nm, 90 nm, 220 nm) 141

Figure 4.27: The imaginary part of complex permittivity spectra for silica suspensions (10.0 wt%) with 1.67 mM KCl electrolyte and different particle size (12 nm, 70nm)... 141

Figure 5.1: Flow chart of the experimental procedure 146

Figure 5.2: (a) complex impedance plot; (b) impedance real part vs. frequency; (c) impedance imaginary part vs. frequency; (d) impedance phase angle vs. frequency plots in the saturated LGA solutions with different concentration of solid LGA phase 150

Figure 5.3: (a) complex impedance plot; (b) impedance real part vs. frequency; (c) impedance imaginary part vs. frequency; (d) impedance phase angle vs. frequency plots in the unsaturated LGA solutions with different LGA solute concentration 153

Figure 5.4: impedance imaginary part vs. frequency plot of LGA solution (a) during the crystallisation process; (b) without the crystallisation process at 50.0 °C, 40.5 °C, 32.7 °C, and 25.6 °C..... 155

Figure 5.5: Change of impedance (Z' and Z") at frequency 1259 kHz and turbidity with temperature during LGA crystallisation 156

Figure 5.6: Change of impedance (Z' and Z") at frequency 631 KHz and turbidity with temperature without the crystallisation process..... 156

Figure 5.7: Temperature and turbidity profiles..... 157

Figure 5.8: Linear fitting result for temperature profile..... 158

Figure 5.9: Crystal morphology at the early stage of crystallisation..... 158

Figure 5.10: Crystal morphology at the late stage of crystallisation (around 10 °C)... 159

Figure 5.11: (a) complex impedance plot; (b) impedance real part vs. frequency; (c) impedance imaginary part vs. frequency; (d) impedance phase angle vs. frequency plots of LGA solution during crystallisation process at 50.7 °C, 40.0 °C, 29.5 °C, and 19.5 °C 163

Figure 5.12: Relaxation frequencies change with temperature during LGA crystallisation processes 163

Figure 5.13: Temperature and turbidity profiles during crystallisation with a medium cooling rate 164

Figure 5.14: Linear fitting result for a temperature profile with a medium cooling rate165

Figure 5.15: crystal morphology at the early stage of crystallisation with a cooling rate of 0.40 °C/min 165

Figure 5.16: crystal morphology at the late stage of crystallisation with a cooling rate of 0.40 °C/min 166

Figure 5.17: Profiles of turbidity and the FBRM chord length distribution during LGA crystallisation with cooling rate of 0.40 ˚C/min 168

Figure 5.18: Chord length distributions at different stages of crystallisation (FBRM measurement) with a cooling rate of 0.40 ˚C/min 168

Figure 5.19: Change of impedance real part (Z'), imaginary part (Z"), and phase angle (θ) at frequency 1 MHz with time during LGA crystallisation with a cooling rate of 0.40 ˚C/min 169

Figure 5.20: Temperature and turbidity profiles for crystallisation at a constant temperature of 30 ˚C 171

Figure 5.21: crystal morphology at the early stage of crystallisation at a constant temperature of 30 °C 172

Figure 5.22: crystal morphology at the late stage of crystallisation at a constant temperature of 30 °C 172

Figure 5.23: Change of impedance real part (Z'), imaginary part (Z"), and phase angle (θ) at frequency 1 MHz with time during LGA crystallisation at a constant temperature of 30°C 173

Figure 5.24: Temperature and turbidity profiles for crystallisation at constant temperature of 60 ˚C 175

Figure 5.25: crystal morphology at different stage of polymorphic transformation 176

Figure 5.26: Change of impedance real part (Z'), imaginary part (Z") and phase angle (θ) at frequency 1 MHz with time during LGA crystallisation at 60 ˚C 177

Figure 5.27: Change of impedance real part (Z') at frequency 1 MHz with time in the crystallisation existing single α form and polymorphic transformation 177

Figure 5.28: Change of impedance imaginary part (Z") at frequency 1 MHz with time in the crystallisation existing single α form and polymorphic transformation 178

Figure 5.29: Change of phase angle (θ) at frequency 1 MHz with time in the crystallisation existing single α form and polymorphic transformation 178

Figure 6.1: Electrical impedance spectra of tap water measured at different electrode pairs (electrode pairs 1 and 2 are used for current exciting over 1Hz-32MHz 183

Figure 6.2: The schematic of eight resistors connected in a ring..... 184

Figure 6.3: Electrical impedance spectra measured on resistors 3, 4, 5, 6 and 7, respectively (1Hz-32MHz)..... 185

Figure 6.4 Electrical circuit of impedance measurement in the 8 resistors system 186

Figure 6.5: Electrical impedance spectra of tap water measured at different electrode pairs (electrode pair 1 and 2 is fixed for current exciting) using the RMM 188

Figure 6.6: Reconstructed impedance real part images of non-conductive plastic bar in tap water obtained at 79.4 kHz by (a) traditional method; (b) RMM..... 188

Figure 6.7: Tomographic image of non-conductive plastic bar in tap water obtained at 76.8 kHz using P2000 ERT system 189

Figure 6.8: Reconstructed images of non-conductive plastic bar in tap water obtained at 1000 Hz (a) real part image, (b) imaginary part image, (c) phase angle (tan (θ)) image, and (d) magnitude part image 190

Figure 6.9: Reconstructed images of non-conductive plastic bar in tap water obtained at 1 MHz (a) real part image, (b) imaginary part image, (c) phase angle (tan (θ)) image, and (d) magnitude part image..... 191

Figure 6.10 electrical impedance spectra of continuous phase (tap water) and mixing phase, measured at electrode pair of 5 and 6 (exciting current was applied to electrode pair of 1 and 2) 192

Figure 6.11: Reconstructed images of the banana in tap water obtained at 1000 Hz (a) real part image, (b) imaginary part image, (c) phase angle (tan (θ)) image, and (d) magnitude part image..... 194

Figure 6.12: Reconstructed images of banana in tap water obtained at 79.4 kHz (a) real part image, (b) imaginary part image, (c) phase angle (tan (θ)) image, and (d) magnitude part image..... 195

Figure 6.13: Tomographic image of banana in tap water obtained at (a) 1200 Hz and (b) 76.8 kHz using the P2000 ERT system..... 196

Figure 6.14: Reconstructed images of silica suspension (220 nm, 23.5 wt%) in water obtained at 1000 Hz (a) real part image, (b) imaginary part image, (c) phase angle (tan (θ)) image, and (d) magnitude part image..... 198

Figure 6.15: Reconstructed images of silica suspension (220 nm, 23.5 wt%) in water obtained at 79.4 kHz (a) real part image, (b) imaginary part image, (c) phase angle (tan (θ)) image, and (d) magnitude part image..... 199

Figure 6.16: Reconstructed images of two silica suspensions (220 nm and 35 nm, 19.5 wt%) in water obtained at 316 kHz (a) real part image, (b) imaginary part image, (c) phase angle (tan (θ)) image, and (d) magnitude part image..... 200

List of Tables

Table 2.1: Relations between the four basic immittance functions 31

Table 2.2: Summary of the typical on-line particle sizing techniques..... 62

Table 3.1: The pin numbers and associated signals on the socket of the SCC-2345 carrier 87

Table 4.1: Summary of the particle sizes for all silica samples..... 99

Table 4.2: Summary of zeta potentials for the silica samples at 25 ˚C 101

Table 4.3: The relative changes in tan(θ) in 10.0 wt% silica suspensions with different particle sizes..... 117

Table 4.4: The relative changes in tan(θ) in 5.0 wt% silica suspensions with different particle sizes..... 118

Table 4.5: The relative changes in tan(θ) in 1.0 wt% silica suspensions with different particle sizes..... 118

Table 4.6: The relative changes in tan(θ) in 0.5 wt% silica suspensions with different particle sizes..... 118

Table 4.7: The calculation results of conductivities (at 25 ˚C) of the silica suspensions (220 nm) with different particle concentrations using the MW equation..... 133

Table 5.1: the impedance data at 1 MHz in crystal suspensions with different solid phase concentration 150

Table 5.2 the impedance data at 1 MHz in unsaturated LGA solutions with different solute concentration..... 154

Table 5.3: The changing rates of impedance parameters at the different stages in crystallisation process..... 169

Table 6.1: The data of impedance real part for tap water at a sampled frequency (80 kHz)..... 181

List of Symbols

a	particle radius
A_c	common-mode gain
I	current
A_D	differential gain
C	actual concentration of solute
c	actual concentration of solute
C	capacitance
C^*	solute concentration in the saturated state
c^*	solute concentration in the saturated state
C_0	dipole coefficient of the particle
C_c or k	cell constant
C_d	double layer capacitance
χ_e	electric susceptibility
D	diffusion coefficient
e	elementary electric charge
E	electrical field strength
F	Faraday constant
F_d	drag force acting on the particle
K^*	complex conductivity
k_B	Bolzmann constant
K_e	conductivity of the electrolyte
K_L	conductivity of the medium solution
K_p	conductivity of the particle
K_s	surface conductivity
n_i	number of ions of type i per unit volume
n_i^0	bulk concentration of ions of type i
R	gas constant
R	resistance
R_0	resistance at 0 ˚C
R_T	resistance at temperature
s	supersaturation
σ'	real part of complex conductivity
σ''	imaginary part of complex conductivity
T	temperature
u	velocity of the dispersed particle
V	volume of suspension

V_c	common mode voltage
V_D	differential voltage
Y'	real part of admittance
Y or Y^* or G	complex admittance
Y''	imaginary part of admittance
Z'	real part of impedance
Z or Z^*	impedance
Z''	imaginary part of impedance
z_i	valency of ion *i*,
γ_{SL}	solid/liquid interfacial tension
ΔG	difference of Gibbs free energy
ε'	real part of permittivity
ε''	imaginary part of permittivity
ε^*	complex permittivity
ε_0	dielectric permittivity of a vacuum
ε_m	permittivity of the dispersed medium
ε_r	relative permittivity
η	dynamic viscosity
θ	phase angle
κ^{-1}	Debye length
λ	relative changes in tan(θ)
μ	electrophoretic mobility
ξ	zeta potential
ρ	volume density of the charge
ρ_m	density of the medium solution
σ_d	surface charge density in the diffuse layer
σ_s	surface charge
σ_ξ	surface charge density at the slipping plan
τ	relaxation time
Φ_0	potential at the particle surface
Φ_d	potential at the stern plane
ψ	electrostatic potential at a certain distance from the surface
ω	frequency
ω_{MWO}	relaxation frequency of MWO dispersion
ω_α	relaxation frequency of α dispersion
Φ	particle volume fraction
$\vec{P}_e$	electric polarisation density
$\vec{d}$	electric dipole moment
$\vec{D}$	electric displacement

List of Abbreviations

EIS	Electrical impedance spectroscopy
EIT	electrical impedance tomography
EITS	electrical impedance tomography spectroscopy
ERT	electrical resistance tomography
LGA	L-glutamic acid
VDM	volume diffusion model
SDM	surface diffusion model
MWO dispersion	Maxwell-Wagner-O'Konski dispersion
CMV	common mode voltage
CMRR	common-mode rejection ratio
CVP	colloidal vibration potential
ESA	electrosonic amplitude
FBRM	focused beam reflectance measurement
PSD	particle size distribution
PVM	particle vision and measurement
CSD	crystal size distribution
RTD	resistance temperature detector
DAQ	data acquisition system
SCC	signal conditioning circuit
SBP	sensitivity coefficient back projection method
RMM	reciprocal measurement method

Chapter 1

Introduction

1.1 Background

The particles in a colloidal suspension usually carry electrical charges. The layer of charges at the particle surface and the layer of the diffuse cloud of ions in the surrounding solution can be approximately modelled as an electrical double layer. At the presence of an electric field, some electrokinetic phenomena occur, such as electrophoresis, electro-osmosis, dielectric dispersion, colloid vibration potential, and electrokinetic sonic amplitude.

Electrical impedance spectroscopy (EIS) is a method used to study the frequency dependence of the dielectric permittivity and the electric impedance of colloidal suspensions by applying an alternating electric field. When an alternating electric field is applied, a dipole moment can be induced on a charged particle due to the relative motion between the particles and their electric double layer. The frequency dependence of the induced dipole moment is referred to as a law of dispersion (Dukhin and Shilov, 1980), which is usually described by the impedance real part, imaginary part, phase angle and characteristic relaxation frequency of the measurement. These quantities are related to the size, shape and surface area of the dispersed particles, the nature of the dispersed medium, and also the concentration of particles. By studying the relationship between the dispersion properties of colloidal suspensions and the characterisation of particles (including the particle size, concentration and ionic concentration), a new method may be developed for characterising the particles in suspensions and further be applied in the on-line monitoring of the crystallisation processes.

Crystals formed in crystallisation processes exhibit behaviour similar to charged

particles in colloids when subjected to an alternating electric field. Electrical impedance spectra observed during crystallisation processes manifest changes of impedance, phase angle and relaxation frequency. These characteristic changes may relate to the crystal size and/or polymorphic transformation during the crystallisation. However, the systemically study on this topic is lacking. Therefore, the study on the method of EIS for on-line monitoring crystallisation processes and other industrial processes are potentially very helpful.

Conventional process tomography (e.g. electrical resistance or impedance tomography) has demonstrated its capability for monitoring the particle concentration distribution and super-saturation distribution during temperature-controlled batch crystallisation. However, the current techniques based on signal attenuation in the time domain are seriously challenged in resolving the on-line spatial distribution of particle characteristics, e.g. the spatial distribution of the particle size distribution or the spatial distribution of polymorphic transformation in crystallisation processes. The method of electrical impedance tomography spectroscopy (EITS) may provide a capability for on-line analysis of particle characteristics.

1.2 Objective of My Research

The research studies the electrical impedance responses when applying an alternating electrical field to a colloidal particle suspension in both experimental and theoretical aspects. The electrical impedance spectra, including the impedance real part, imaginary part, phase angle and relaxation frequency are measured using the impedance analyzer, with development of a data analysis method. The effects of particle size, as well as the particle concentration and ionic concentration are investigated. In addition, the electrical impedance parameters, including the impedance real part, imaginary part, phase angle and relaxation frequency in the L-glutamic acid crystallisation processes are studied in order to probe the application of electrical impedance spectra for on-line monitoring of particle size. The overall aim of the project

is to provide physical chemistry fundamentals for developing electrical impedance spectroscopy, further, a new spectra-tomography (imaging) technique, for on-line measurement of particle characteristics and monitoring of particle size and polymorphic transformations in crystallisation processes. The objectives are listed below:

(1) To investigate the effects of particle size, particle concentration and ionic concentration on the electrical impedance spectra of silica suspensions.
(2) To develop a theoretical or empirical model to analyse the results obtained and establish relationships between particle size and electrical impedance parameters based on the “static” particle suspensions.
(3) To develop electrical impedance spectroscopy-based method for on-line measurement of crystals’ size and/or polymorphs in the crystallisation processes through an experimental approach and theoretical analysis.
(4) To investigate the feasibility of the electrical impedance tomography spectroscopy (EITS) technique for imaging the characteristics of particles in a two-dimensional domain.

1.3 Organization of the Thesis

The main chapters of this PhD thesis are structured as follows:

Chapter 1 A brief introduction to my research is given and the objectives of the PhD study are highlighted. The organization of the thesis is outlined.

Chapter 2 This chapter reviews the background of colloidal science as relevant to this study, the electrokinetics of colloids, electrical impedance spectroscopy and the electrical impedance tomography technique. The review also includes the existing particle sizing methods and the fundamentals of crystallisation processes.

Chapter 3 The experimental devices, materials and methodology are described in this chapter. The design and schematic of four-electrode sensors for EIS measurement in colloidal suspensions and crystallisation processes are described. The devices for crystallisation experiments and electrical impedance tomography spectroscopy

measurement are introduced.

Chapter 4 In this chapter, the EIS experimental results on colloidal particle suspensions are presented. The effects of particle size, particle concentration and ionic concentration are investigated through the electrical impedance spectra and permittivity spectra. The results are analysed and discussed based on the established theories. A new semi-empirical theory is established to explain the relationship between the particle size and the relative changes of phase angle.

Chapter 5 The on-line EIS experimental results on crystallisation processes are presented in this chapter. The changing of the impedance real part, imaginary part and phase angle as functions of crystal size, crystal concentration and ionic concentration are discussed. The polymorphs of L-glutamic acid during the crystallisation process are studied experimentally using the on-line EIS technique and off-line optical microscopic method. The changes of impedance parameters in the polymorphic transformation are discussed.

Chapter 6 In this chapter, electrical impedance tomography based on EIS measurement conducted in the phantom with different materials, including non-conductive plastic bar, banana and the silica suspensions are presented. The response of electric polarisation of colloidal particles on tomographic images and the observation of particle size effect from tomographic images are discussed.

Chapter 7 Conclusions and future work: the final chapter summaries the whole thesis, including the major findings and problems encountered. Finally, work which could be carried out in the future is recommended.

Chapter 2

Electrokinetics of Colloids, Electrical Impedance Spectroscopy, Particle Sizing Methods and the Crystallisation Process

Summary: This chapter reviews the physical foundations of the research, commences a review on electrokinetics of colloidal particles and continues by introducing electrical impedance spectroscopy and tomography techniques. The existing particle sizing methods for both off-line and on-line measurement are reviewed in the latter part. Finally, the background of the crystallisation process is introduced.

2.1 Introduction

This chapter covers a relevant, fundamental and essential literature review for electrokinetic phenomena of colloidal particles, electrical impedance spectroscopy, electrical impedance tomography, particle sizing methods and the theory of the crystallisation processes. The first part includes the foundations of colloidal science and the electrokinetics of colloidal particles in an external electric field. Existing research on the dielectric properties of colloidal particles in an oscillating electric field using electrical impedance spectra or permittivity spectra, for both theoretical and experimental aspects, is reviewed. In the second part, the basic principles of electrical impedance spectroscopy (EIS) and electrical impedance tomography (EIT) techniques are reviewed as potential techniques for particle characterisation. Later, the current status of particle sizing methods in both off-line and on-line techniques is reviewed, including the principles of measurement and their advantages and disadvantages for laboratory and industrial applications. Finally, the fundamentals of crystallisation are reviewed for the application of the EIS technique in crystallisation processes.

2.2 Electrokinetic Properties of Colloidal Particles

2.2.1 Colloidal Particle and Electrical Double Layer

A colloidal system is a two-phase system in which one phase is dispersed in a continuous phase. The particles of the dispersed phase may be of any shape and the size may vary from 1 nm to 10 μm (Cosgrove, 2005). A typical and important part of colloidal particles is their electrical double layer. Considering a colloidal particle in an electrolyte solution, the surface of the particle may become charged (for example, due to the dissociation of the surface groups). The charges created are balanced by the presence of ions of opposite sign absorbed on the particle surface and a layer of counter charges can be formed. Thus, an electric double layer exists around each particle. The double layer surrounding the particle exists as two parts: an inner region (Stern layer) where the ions are strongly bound and an outer region (diffuse layer) where they are less firmly associated. This diffuse layer (or the layer of counter charges carried by ions) has a notional boundary known as the slipping plane within which the particle acts as a single entity. The electrostatic potential difference between the Stern layer and the diffuse layer is known as the Zeta potential. Figure 2.1 shows a schematic diagram of the electric double layer and zeta potential.

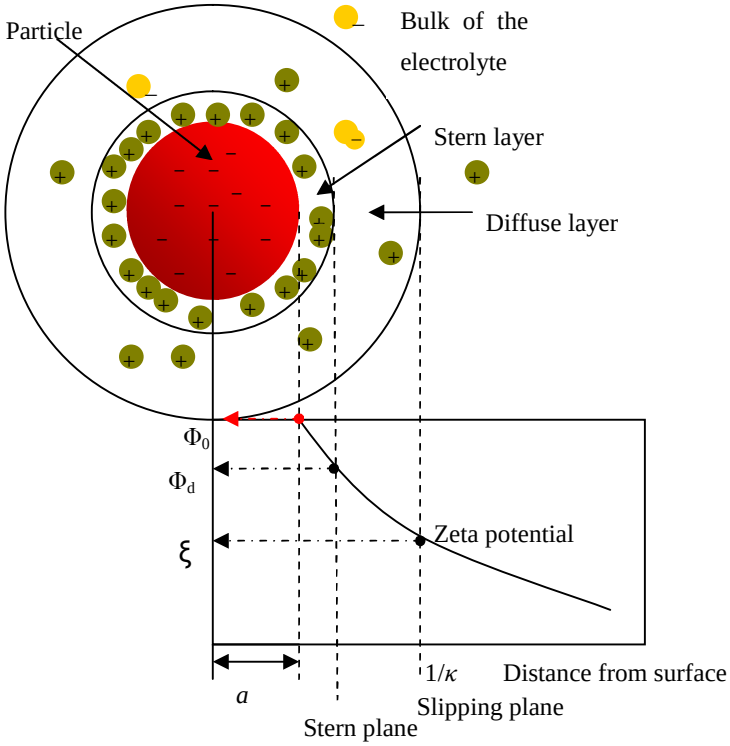

Figure 2.1: Schematic diagram of the electric double layer and zeta potential

where, Φ_0 is the potential at the particle surface, Φ_d is the potential at the stern plane, and ξ is the zeta potential at the slipping plane.

The theory for a diffuse double layer was first developed independently by Gouy (1910) and Chapman (1913), and the result is referred to as the Gouy-Chapman model (Hunter, 2001). In this model, the electric potential decreases exponentially away from the surface to the fluid bulk. Next, the electrical double layers at a flat surface and around a spherical particle are discussed.

(1) Double layer at a flat surface

For a flat surface immersed in a symmetrical electrolyte solution, an electrostatic potential, Ψ_0 exists on the surface. The relationship between the surface charge density and electrostatic potential can be expressed by Possion's equation (Hunter, 2001):

$$\mathrm{div}\,\mathbf{D} = \mathrm{div}(-\varepsilon\ \mathrm{grad}\psi) = \rho \qquad (2.1)$$

where ψ is the electrostatic potential at a certain distance from the flat surface, D is

the dielectric displacement, ε is the permittivity of the dispersed medium and ρ is the volume density of the charge.

Equation (2.1) can be rewritten as:

$$\operatorname{div}\operatorname{grad}\psi = \nabla^2\psi = -\frac{\rho}{\varepsilon} = -\frac{\rho}{\varepsilon_0\varepsilon_r} \tag{2.2}$$

where, ∇^2 is the Laplace operator, ε_0 is the dielectric permittivity of a vacuum $(\varepsilon_0 = 8.85\times10^{-12}\,\mathrm{F\,m^{-1}}\ \text{or}\ \mathrm{C\,V^{-1}\,m^{-1}})$ and ε_r is the relative permittivity of the dispersed medium.

The local concentration of each type of ion in the double layer region can be expressed by the Boltzmann equation:

$$n_i = n_i^0 \exp(-z_i e\psi / k_B T) \tag{2.3}$$

where, n_i is the number of ions of type *i* per unit volume, z_i is the valency of ion *i*, and n_i^0 is the bulk concentration of ions of type *i*.

The volume density of charge ρ is given by:

$$\rho = \sum_i n_i z_i e \tag{2.4}$$

From equations (2.2-2.4), the complete Poisson-Boltzmann equation can be obtained:

$$\nabla^2\psi = -\frac{1}{\varepsilon_0\varepsilon_r}\sum_i n_i^0 z_i e\ \exp(\frac{-z_i e\psi}{k_B T}) \tag{2.5}$$

The solution of Equation (2.5) is:

$$\tanh(ze\psi / 4k_B T) = \tanh(ze\psi_d / 4k_B T)\exp(-\kappa x) \tag{2.6}$$

where, ψ_d is the potential at the Stern plane, z_i is the valency of ion *i*, κ is called the Debye-Hückel parameter with dimensions of (length)$^{-1}$, and its inversion, κ^{-1} is called the Debye length, or double layer thickness:

$$\kappa = (\frac{e^2 \sum n_i^0 z_i^2}{\varepsilon_0 \varepsilon_r k_B T})^{1/2} \tag{2.7}$$

If we consider a symmetric electrolyte, $z_i = z_+ = -z_- = z$ and $n_i^0 = n^0$. The surface charge density in the diffuse layer σ_d relates to the stern potential ψ_d:

$$\sigma_d = -\frac{4n^0 ze}{\kappa} \sinh \frac{ze\psi_d}{2k_B T} \tag{2.8}$$

The differential capacitance of the diffuse layer, C_d, is given by (Dukhin and Goetz, 2002):

$$C_d = \frac{-d\sigma_d}{d\psi_d} = \varepsilon_0 \varepsilon_m \kappa \cosh(\frac{ze\psi_d}{2k_B T}) \tag{2.9}$$

(2) Double layer around a spherical particle

In the Gouy-Chapman model, a parameter, Debye length κ^{-1} is introduced which is usually used to characterize the thickness of the double layer. Concerning the double layer around a sphere particle, there is an additional geometric parameter involved, the radius of particle, *a*. The combination of the Debye length and the radius of the particle, *a*, produces a dimensionless parameter, κa, which plays an important role in the colloidal system. When $\kappa a >> 1$, which means the thickness of the double layer is much smaller than the radius of the particle, that is “thin double layer”. When $\kappa a << 1$, which means the thickness of the double layer is much larger than the radius of the particle, that is the “thick double layer”.

The Poisson-Boltzmann equation in the Gouy-Chapman model remains valid for the double layer around a spherical particle, but the Laplace operator for the case of spherical symmetry has a different form (Hunter, 2001):

$$\mathrm{div}\,\mathrm{grad}\,\psi = \frac{1}{r^2}\frac{\mathrm{d}}{\mathrm{d}r}(r^2 \frac{\psi}{\mathrm{d}r}) = -\frac{\rho(r)}{\varepsilon} \tag{2.10}$$

Using the Debye-Hückel approximation (assuming ψ to be very small), we get the

solution:

$$\psi = \psi_d (a/r) \exp[-\kappa(r-a)] \tag{2.11}$$

where *r* is the distance from the particle centre.

The relationship between diffuse charge and the stern potential is then:

$$\sigma_d = -\varepsilon_0 \varepsilon_m \kappa \psi_d (1 + \frac{1}{\kappa a}) \tag{2.12}$$

2.2.2 Colloidal Particles under an Electric Field

The electrokinetic phenomenon is one of the most common topics with regard to the behaviour of charged particle suspensions in an electric field, which has been studied extensively. An Electrokinetic phenomenon is the phenomena associated with the movement of charged particles through a continuous medium, or with the movement of a continuous medium over a charged surface (Hunter, 2001). The family of electrokinetic phenomena includes: electrophoresis, electro-osmosis, diffusiphoresis, capillary osmosis, sedimentation potential, streaming potential, colloid vibration current and electric sonic amplitude (Delgado et al., 2007).

Electrophoresis is the motion of charged colloidal particles, relative to a fluid under the influence of an external electric field. In contrast in the electro-osmosis process, the particles remain stationary but the ions in the adjoining fluid move under the external electric field. This phenomenon usually happens in a capillary or a porous medium (Delgado et al., 2007). In this research project, the focus is mainly on particles' moving under an electric field, therefore only the electrophoresis process is studied.

(1) Electrophoresis under a static electric field

Before considering the behaviour of particles in colloids in an alternating electric field, the discussion is started from the simple case: charged particles under static electric field. When a static electric field is applied to a colloidal suspension, both particles and counter-ions can move in opposite directions due to the difference in sign of the charge

carried. An analysis of the forces shows that the charged particles experience four different forces (Bier, 1967). Firstly, the static electric field exerts an electrostatic, Coulomb, force ($F_{electric}$) on the particles due to their surface charges. The second force, $F_{friction}$, is the Stokes friction, which affects all bodies moving in viscous fluids with low Reynolds number. The two remaining forces are caused by the presence of the counter-ions in the electrical double layer. The electric field exerts a force on the ions in the double layer. Since these ions are at some distance from the particle surface, they transfer part of the force to the particle through viscous stress. This force is called the electrophoretic retardation force, $F_{retardation}$. The last force is caused by the detachment of the particle from its surface ionic atmosphere. The particle moves away from the centre of its ionic atmosphere. The centre of the ionic atmosphere lags behind the centre of the particle. The Coulomb force between the particle and the ions tends to return them to the “proper” place, and is called the electrophoretic relaxation force, $F_{relaxation}$. Figure 2.2 is a schematic diagram which shows the forces on a charged particle (positive charged) under a static electrical field.

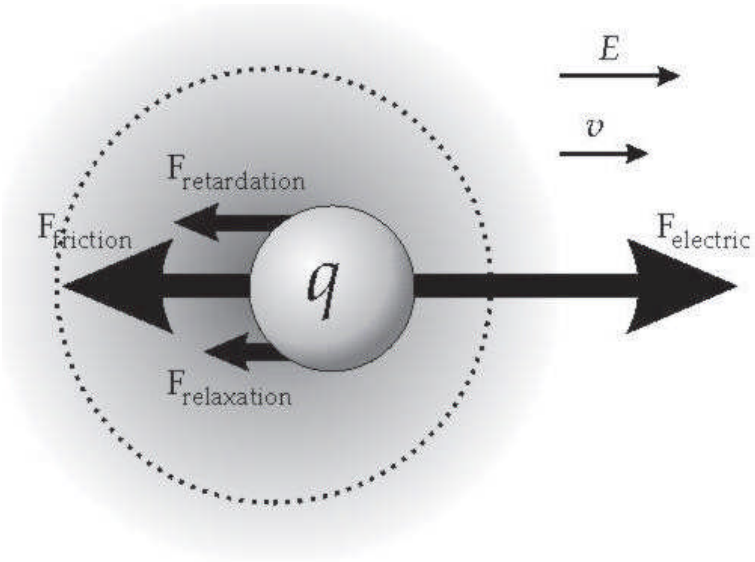

Figure 2.2: Forces on a charged particle (positively charged) under a static electrical field (http://lcp.elis.ugent.be/research/electrophoresis)

The electrophoretic velocity of particles in the presence of a static electrical field is linearly related to the strength of electric field with the form (Hunter, 2001):

$$u = \mu E \tag{2.13}$$

where, u is the velocity of the dispersed particle, μ is the electrophoretic mobility of the particle, and E is the strength of the applied field.

Electrophoretic mobility is an important parameter in colloid science, from which the zeta potential can be calculated. The earliest solution for μ was given by Smoluchowski (Wall, 2010) for the thin double layer case ($\kappa a >> 1$).

$$\mu = \frac{\varepsilon_r \varepsilon_0 \xi}{\eta} \tag{2.14}$$

where η is the dynamic viscosity of the dispersion medium, and ξ is the zeta potential. Smoluchowski's theory is very powerful because it is valid for dispersed particles of arbitrary shape and concentration (Hunter, 2001). However, it has limitations as it does not include the Debye length κ^{-1}, which is important for electrophoresis. Hückel (Wall, 2010) solved μ for the opposite extreme condition of a very thick double layer ($\kappa a << 1$). The mobility formula is:

$$\mu = \frac{2\varepsilon_r \varepsilon_0 \xi}{3\eta} \tag{2.15}$$

Approximate solutions have been obtained for the case where the double layer thickness is small or large compared with the particle radius. However, most of the colloidal systems in practice have κa values which lie outside the regimes where the approximate analytic formulas are valid. In order to obtain results of more practical significance, Henry calculated the mobility of a spherical particle with an arbitrary double layer thickness on the assumption that the charge density is unaffected by the applied field (Henry, 1931). The resulting formula for the electrophoretic mobility is:

$$\mu = \frac{2\varepsilon_r \varepsilon_0 \xi}{3\eta} f_1(\kappa a) \tag{2.16}$$

where $f_1(\kappa a)$ is a monotonically varying function which increases from 1.0 at $\kappa a = 0$ to 1.5 at $\kappa a = \infty$.

Later on, O'Brien (O'Brien and White, 1978) developed a computer program with the

governing differential equations to calculate the electrophoretic mobility for arbitrary *κa* values.

(2) Electrophoresis in an alternating electric field

Under a periodical alternating electric field, the charged particles in suspension display oscillatory movement. In the paper which was published in Science in 1965 (Sher and Schwan, 1965), the oscillatory migration of charged particles under a low frequency electric field was observed in photographs and the electrophoretic mobility was measured. The experiment was carried out with a frequency range of 1-10 Hz, electric field strength of 340 volt/cm and a particle size of 1 μm. A photograph of the particle's oscillatory migration is shown in Figure 2.3. At low frequencies, the electrophoretic mobility of colloidal particles is the same as the static mobility because the particle movement can follow the change of electric field. However, at high frequencies, the particle movement cannot follow the change of electric field and a relaxation process occurs.

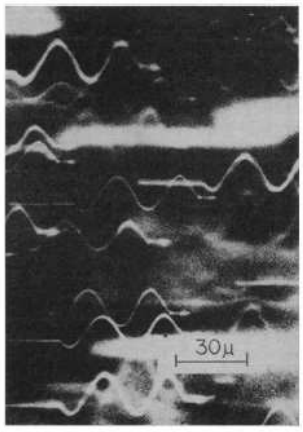

Figure 2.3: Electrophoresis patterns of polystyrene spheres (the oscillatory migration was recorded as a sine wave by moving the microscope) (Sher and Schwan, 1965)

The behaviour of charged colloidal particles in an alternating electric field has been studied theoretically over the past thirty years (Delacey and White, 1981, Babchin et al.,

1989, Sawatzky and Babchin, 1993, Fixman, 1983, Mangelsdorf and White, 1992, O'Brien, 1988). It becomes more attractive since the electroacoustic phenomenon was predicted by Debye in 1933 (Debye, 1933). DeLacey and White (Delacey and White, 1981) developed a numerical scheme by solving the governing equations which included Poisson's equation, charge density distribution, Navier-Stokes equations, force balance equation and the continuity equation.

These governing equations which are to describe the system at time t are shown below:

$$\nabla^2\psi = -\frac{4\pi}{\varepsilon_r}\rho \tag{2.17}$$

$$\rho(r,t) = \sum_{j=1}^{N} z_j e n_j(r,t) \tag{2.18}$$

$$\eta\nabla^2 u - \nabla p = \rho\nabla\psi \tag{2.19}$$

$$\nabla u = 0 \tag{2.20}$$

$$-\lambda_j(v_j - u) - z_j e\nabla\psi - kT\nabla\ln n_j = 0 \tag{2.21}$$

$$\nabla\cdot(n_j v_j) = -\frac{\partial n_j}{\partial t} \qquad j = 1, 2, \ldots\ldots, N \tag{2.22}$$

where, $\psi(r,t)$ is the electrical potential, $n_j(r,t)$ is the number density of the *j*th ionic species, $v_j(r,t)$ is the drift velocities of the ionic species, $u(r,t)$ is the velocity of liquid, λ_j is the drag coefficient, ε_r is the dielectric constant of electrolyte medium, *r* is the position vector from the centre of the particles and $p(r,t)$ is the pressure of the liquid at every position r in the system.

Equation (2.17) is Poisson's equation which gives the relationship between the electrostatic potential $\psi(r)$ and charge density. Equation (2.18) shows the charge density. Equations (2.19) and (2.20) are the Navier-Stokes equations for the fluid flow around the particles. Equation (2.21) represents the force balance on an ion. Equation

(2.22) is the continuity equation expressing the conservation of the number of each ion type in the system.

Under the applied field $E\,e^{-i\omega t}$, the particle velocity $U\,e^{-\omega t}$ is proportional to E:

$$U\,e^{-\omega t} = \mu E\,e^{-i\omega t} \tag{2.23}$$

The boundary conditions are:

$$u \xrightarrow[|r|\to\infty]{} -\mu \cdot E$$

$$u\,|_{\substack{\text{slipping}\\ \text{plane}}} = 0$$

Combining the above mobility equation with the governing equations and applying suitable boundary conditions, the electrophoretic mobility can finally be calculated using a perturbation scheme.

2.2.3 Dielectric Dispersion

In physics, dielectric dispersion is the dependence of the permittivity of a dielectric material on the frequency of an applied electric field. Considering the charged particles and their double layer under an alternating electric field, both particle and ions will be set in motion by the field, with the particle and counterions moving in opposite directions. As a result, the double layer distorts in an alternating fashion giving rise to an electric field which, at large distances from the particle, has the same form as that of an alternating electric dipole (O'Brien, 1982). The polarisation of the electric double layer reverses periodically but there is a phase lag between changes in polarisation and changes in electrical field. This phenomenon can be monitored by electrical impedance spectroscopy (sometimes called dielectric spectroscopy) and the complex conductivity, impedance, and permittivity is related to many quantities: particle size and shape, particle concentration, electrolyte properties (ionic concentration, ionic species), zeta potential, and so forth.

Two mechanisms are responsible to the dielectric dispersion of colloidal suspension.

The dispersion which occurs in MHz range is called the Maxwell-Wagner-O'Konski mechanism (MWO). It is caused by the different permittivities and conductivities of the particle and the surrounding medium (Dudley et al., 2003). At lower frequencies (Hz-MHz), the dispersion is caused by the polarisation of the counter ions in the diffuse double layer (DDL). This mechanism is called low frequency dielectric dispersion (LFDD) or α dispersion.

Some details of the α dispersion and MWO dispersion are discussed in the following paragraphs.

(1) α dispersion

There are two models used to explain α dispersion: the surface diffusion model (SDM) and the volume diffusion model (VDM). In the surface diffusion model (SDM), it is assumed that under the action of an external electric field, counter-ions in the double layer move only along the particle surface without exchanging with the bulk electrolyte ions (Schwarz, 1962, Schurr, 1964). Therefore, the relaxation time depends on the path length for movement of the counter-ions swarm (particle size, a) and the diffusion coefficient of counter-ions, D:

$$\tau_L = \frac{a^2}{2D} \tag{2.24}$$

where, *a* is the particle size, D is the diffusion coefficient and a thin double layer thickness is assumed.

The SDM model showed a coincidence between theory and the experimental results presented by Schwan (Schwan et al., 1962). However, since it uses a simple and restricted assumption, the SDM model is not likely to be met in practice. In real colloidal systems, the counter-ions in the diffuse double layer do not bind with the particles tightly, and thus the exchange of ions with the bulk electrolyte cannot be fully neglected. Based on this consideration, another mechanism, volume diffusion model (VDM) was proposed (Delgado et al., 1998, Lyklema et al., 1986). In VDM, the polarisation of the electric double layer is accompanied by a gradient of ionic concentration around the particle surface.

The formation of the ionic concentration gradient can be understood easily from the schematic in Figure 2.4, where a negatively charged spherical particle is under an electric field pointing in the direction from left to right. The counter-ions in the double layer move from the left to the right hand side of the particle (the outer boundary of the double layer) and this provokes a tangential electromigration flux of counterions J_{es}^{+}. The normal counterion flux, J_{en}^{+}, leaving the boundary towards the right is much weaker than the flux of J_{es}^{+} since there is no excess of counter-ions in the bulk electrolyte solution (Grosse and Delgado, 2010). Therefore, the concentration of counter-ions on the right hand side of the particle starts to increase. As for co-ions, they move from the neutral electrolyte to the right hand side of the particle (the outer boundary of the double layer) and provoke a normal electromigration flux of J_{en}^{-}, which is comparable to the normal electromigration flux of counterion, J_{en}^{+}. Since the concentration of co-ions in the electrical double layer is much lower than that in the bulk electrolyte solution, the co-ions concentration on the right hand side of particle also increases. Therefore, an accumulation of both counter-ions and co-ions is formed on the right hand side of the particle and a similar process produces a depletion of both counter-ions and co-ions on the left hand side of the particle. An increment of both the counter-ion and co-ion concentrations means the electrolyte concentration increases at the right hand side of the particle. This phenomenon is called “concentration polarisation”. The concentration gradient of the electrolyte, in turn, provokes a tangential diffusion flux J_{ds}^{+} along the particle surface and two normal diffusion fluxes, J_{dn}^{+}, J_{dn}^{-} enter into the bulk electrolyte solution. Such diffusion is a slow process and the diffusion currents need a finite time to be established, as a consequence, under the action of the external electric field, the suspension shows a dispersion which is called α relaxation.

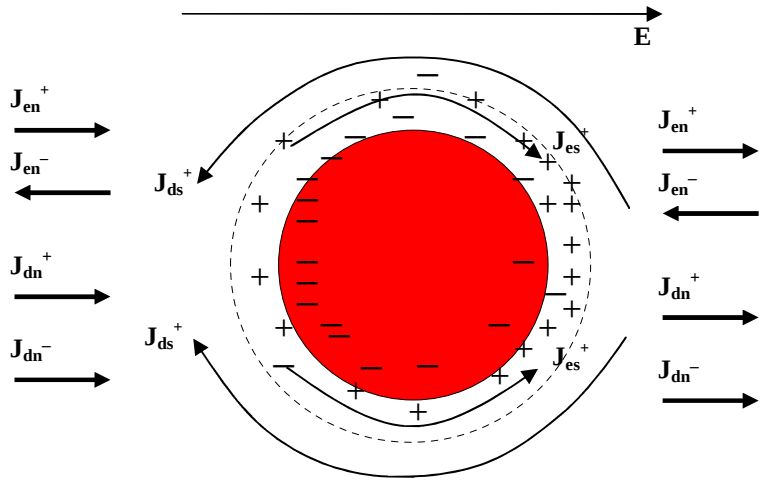

Figure 2.4: Schematic of the generation of the electrolyte concentration gradient responsible for α dispersion for a negatively charged particle

Compared with SDM, VDM is apparently closer to the real situation. The difference between these two mechanisms is that they use different theoretical hypotheses to describe the behaviour of the counter-ions in and outside of the electric double layer. VDM can be broadened to any value of double layer thickness, and Equation (2.24) can be revised to:

$$\tau_{\mathrm{L}} = \frac{(a+\kappa^{-1})^2}{2D_{\mathrm{eff}}} \tag{2.25}$$

$$D_{\mathrm{eff}} = \frac{D_{+}D_{-}(z_{+}+z_{-})}{D_{+}z_{+}+D_{-}z_{-}} \tag{2.26}$$

where, a is the particle radius, κ^{-1} is the Debye length, D_{eff} is the effective coefficient of diffusion, D_{+}, D_{-} are the diffusion coefficients of positive and negative ions, respectively, z_{+}, z_{-} are the valence of the ions, n_i^0 is the background electrolyte concentration, ε_r is the relative permittivity of electrolyte medium, k is the Boltzmann constant, and T is temperature .

Based on the derivation of the SDM model, relaxation frequency is independent of the particle concentration ϕ ; however, it has been proved incorrect through experiments by some researchers (He and Zhao, 2005, Barchini and Saville, 1995). The dependence

of relaxation frequency of α dispersion on the particle concentration is a complicated problem that is not yet fully understood. One of the possible explanations is the VDM mechanism, which can take the electrolyte concentration gradients of neighbouring particles into consideration. In concentrated suspensions, one particle is probably close to another particle and the double layer polarisation might be affected by changing the characteristic length of the volume diffusion mechanism (Delgado et al., 1998). For a dilute suspension, the characteristic length is the particle size. However, it becomes particle concentration dependent in concentrated suspensions (Delgado et al., 2007).

(2) MWO dispersion

The Maxwell-Wagner (MW) dispersion is due to the distribution of ionic charges near the interface between the particle and the electrolyte solution, which have different conductivities and electric permittivities. O'Konski (O'Konski, 1960) generalized the MW dispersion theory by including a surface conductivity in the particles, λ, which is assumed to be due to the excess concentration of ions very close to the surface of the charged particle. The resulting theory is called the Maxwell-Wagner-O'Konski (MWO) dispersion. The Maxwell-Wagner-O'Konski relaxation frequency is showed by Equation (2.27) (Delgado et al., 2007):

$$\omega_{MWO} = \frac{1}{\tau_{MWO}} = \frac{(1-\phi)K_p + (2+\phi)K_L}{\varepsilon_0[(1-\phi)\varepsilon_{rp} + (2+\phi)\varepsilon_{rs}]\varepsilon_{rs}} \tag{2.27}$$

where, K_p and ε_{rp} are the conductivity and relative permittivity of the particles, respectively. K_L and ε_{rs} are the conductivity and relative permittivity of the medium solution, respectively, ϕ is the particle volume fraction, and ε_0 is the permittivity of free space.

For low volume fractions and low permittivity of the particles, the relaxation time is given by Equation (2.28):

$$\tau_{MWO} \approx \frac{1}{2D\kappa^2} \tag{2.28}$$

τ_{MWO} is a measure of the time required for charges in the electrolyte solution to recover their equilibrium distribution after ceasing an external perturbation.

2.2.4 Dielectric Properties and Theoretical Modelling

Dielectric properties of colloidal suspensions, including impedance, complex conductivity, permittivity, relaxation frequency and phase angle, can be measured by electrical impedance spectroscopy. The changing of these dielectric properties with frequency of the applied electric field are all related to the characterisation of colloidal suspensions. Much related research has been done in studying the dielectric properties of colloidal particles by theoretical and experimental methods. However, the focus on particle size effect is quite limited. In this section, the theoretical analysis on dielectric properties of colloidal particle will be reviewed.

(1) Debye theory

The classical dielectric relaxation model is the Debye model and the complex permittivity can be given by the following equations (Cole and Cole, 1941):

$$\varepsilon^* - \varepsilon_H = (\varepsilon_L - \varepsilon_H)/(1 + i\omega\tau_0) \tag{2.29}$$

$$\varepsilon' = \varepsilon_H + (\varepsilon_L - \varepsilon_H)/[1 + (\omega\tau_0)^2] \tag{2.30}$$

$$\varepsilon'' = (\varepsilon_L - \varepsilon_H)\omega\tau_0/[1 + (\omega\tau_0)^2] \tag{2.31}$$

where, ε_H, ε_L, and ε^* are the high and low frequency limiting permittivity, and complex permittivity respectively, ω is the frequency, τ_0 is the single relaxation time, and ε' and ε'' are the real and imaginary permittivities.

Although the simplest way of fitting the dielectric properties is use of the Debye model, it is not suitable for many systems, particularly colloidal suspensions since they do not follow the pattern predicted by this simple model (Asami, 2002).

(2) Cole-Cole model

The Cole-Cole model is an empirical generalization of the Debye theory. It seems to agree reasonably well with the experimental data (Carrique et al., 1995). The complex permittivity for the Cole-Cole model is given by the following equations (Sauer et al., 1990):

$$\varepsilon^* - \varepsilon_H = (\varepsilon_L - \varepsilon_H)/[1 + (i\omega\tau_0)^{1-\alpha}] \tag{2.32}$$

$$\varepsilon' = \varepsilon_H + \frac{(\varepsilon_L - \varepsilon_H)[1 + (\omega\tau_0)^{1-\alpha}\sin(\pi\alpha/2]}{1 + (\omega\tau_0)^{2(1-\alpha)} + 2(\omega\tau_0)^{1-\alpha}\sin(\pi\alpha/2)} \tag{2.33}$$

$$\varepsilon'' = \frac{(\varepsilon_L - \varepsilon_H)(\omega\tau_0)^{1-\alpha}\cos(\pi\alpha/2)}{1 + (\omega\tau_0)^{2(1-\alpha)} + 2(\omega\tau_0)^{1-\alpha}\sin(\pi\alpha/2)} \tag{2.34}$$

where, ε_H, ε_L, and ε^* are the high and low frequency limiting permittivity and complex permittivity respectively, ω is the frequency, τ_0 is the relaxation time, α is an constant ($0< \alpha <1$).

The Cole-Cole model cannot directly relate the permittivity or relaxation frequency to the particle size. However, the experimental data can be fitted using the Cole-Cole model and the values of permittivity and relaxation frequency can be calculated. Several authors (Grosse and Foster, 1987, Lim and Franses, 1986) have studied the size dependence of relaxation frequency ω_c, using this method. The results showed that ω_c is inversely proportional to the square of the particle radius, which is consistent with Equation (2.24) for α dispersion. Although the Cole-Cole model is a relatively simple model, it does not show any effects of double layer thickness and zeta potential on dielectric properties. Therefore, a more integrated model is necessary to reproduce the theoretical prediction of dielectric response.

(3) Classic electrokinetic model

The first numerical calculation for the dielectric response using the classic electrokinetic model has been given by Delacey and White (Delacey and White, 1981). In this model, the response of the particle and the surrounding electrolyte to an alternating electric field is obtained by solving the governing equations, which are

already shown in Section 2.2.2, part (2). By applying suitable boundary conditions and solving the governing equations, the electrophoretic mobility of spherical particles can be obtained. However, Delacey and White just indicated the calculation method but did not provide the numerical results for the mobility. In their work, a numerical scheme for getting the complex conductivity and permittivity response based on the governing equations is developed.

For an imposed electrical field, $< \bar{E} >= \bar{E}_0 e^{i\omega t}$, and the current passing through the suspension, $< \bar{I} >= \bar{I}_0 e^{i\omega t}$, the complex conductivity of the suspension can be defined by a linear relation: $K^* = \frac{\bar{I}_0}{\bar{E}_0}$.

Formally, K^* can be written as:

$$K^*(\omega) = K(\omega) + \frac{\omega\varepsilon''(\omega)}{4\pi} - \frac{i\omega\varepsilon'(\omega)}{4\pi} \tag{2.35}$$

The increments of conductivity and permittivity by adding particles in a medium solution are given by:

$$K(\omega) = K^{\infty} + \phi\Delta K(\omega) + \vartheta(\phi^2) \tag{2.36}$$

$$\varepsilon'(\omega) = \varepsilon_{rs} + \phi\Delta\varepsilon'(\omega) + \vartheta(\phi^2) \tag{2.37}$$

$$\varepsilon''(\omega) = \phi\Delta\varepsilon''(\omega) + \vartheta(\phi^2) \tag{2.38}$$

where, K^{∞} is the conductivity of the electrolyte medium, ε_{rs} is the permittivity of the electrolyte medium, ϕ is the particle volume fraction. The tiny contribution from the second and higher order of ϕ can be ignored, and only the lowest order term is considered.

Substituting Equations (2.36) – (2.38) into Equation (2.35), we obtain:

$$\begin{aligned} K^*(\omega) &= K^{\infty} + \phi\Delta K(\omega) + \frac{\omega\phi\Delta\varepsilon''(\omega)}{4\pi} - \frac{i\omega[\varepsilon_{rs} + \phi\Delta\varepsilon'(\omega)]}{4\pi} \\ &= (K^{\infty} - \frac{i\omega\varepsilon_{rs}}{4\pi}) + \phi[\Delta K(\omega) + \frac{\omega\Delta\varepsilon''(\omega)}{4\pi} - \frac{i\omega\Delta\varepsilon'(\omega)}{4\pi}] \end{aligned} \tag{2.39}$$

Therefore, the increment of conductivity can be expressed by:

$$\Delta K^*(\omega) = \Delta K(\omega) + \frac{\omega \Delta\varepsilon''(\omega)}{4\pi} - \frac{i\omega\Delta\varepsilon'(\omega)}{4\pi} \tag{2.40}$$

The derivation of $\Delta K^*(\omega)$ has to involve the perturbation scheme for the governing equations. The solving procedure will not be given in detail here, but a final expression is given:

$$\Delta K^*(\omega) = \frac{3}{a^3}(K^\infty - \frac{i\omega\varepsilon_{rs}}{4\pi})C_0(\omega) \tag{2.41}$$

$$C_0(\omega) = C_0^R(\omega) + iC_0^I(\omega) \tag{2.42}$$

$$\Delta\varepsilon'(\omega) = \frac{3\varepsilon_{rs}}{a^3}[C_0^R(\omega) - \frac{4\pi K^\infty}{\omega\varepsilon_0}C_0^I(\omega)] \tag{2.43}$$

$$\Delta\varepsilon''(\omega) = \frac{3\varepsilon_{rs}}{a^3}C_0^I(\omega) \tag{2.44}$$

where, *a* is the particle radius, C_0 is the dipole coefficient of the particle, $C_0^R(\omega)$ is the real part of the dipole coefficient, $C_0^I(\omega)$ is the imaginary part of dipole coefficient.

In their paper, DeLacey and White showed the numerical results of dielectric increments changing with frequency. The dependences of conductivity and permittivity increments on zeta potential, double layer thickness and ionic species are described.

DeLacey's theory is applicable for all values of zeta potential, double layer thickness and for general values of ionic valences. However, the authors omitted the acceleration term $\rho_m \frac{\partial u}{\partial t}$ in the Navier-Stokes equation and approximated the sum of the forces on the colloidal particle to zero. This approximation was made because the acceleration term is very small compared with the viscous term at frequencies below 10^4 Hz, and therefore can be neglected. However, this approximation is not suitable for the cases with high frequency ω >> 10^4 Hz, and should be modified by adding the acceleration term in the Navier-Stokes equation (Delacey and White, 1981).

In Mangelsdorf and White's paper (Mangelsdorf and White, 1997), they modified the theory developed by DeLacey and White by adding the acceleration term in both the

Navier-Stocks equation and the force balance equation. This calculation was called the "full" calculation (F), which extended DeLacey's theory to a high frequency range. Mangelsdorf and White compared the real and imaginary parts of the dipole coefficient C_0 obtained from different calculations, which included the De Lacey and White's theory (D), the "full" calculation (F), the Hinch's theory (H) (Hinch et al., 1984), and the O'Brien' theory (O) (O'Brien, 1986).

The O'Brien' theory was derived for a dilute suspension of spherical particles with thin double layer (κa >> 1) at high frequency range (f >> D/a^2) where D is the ion diffusion coefficient and a is the particle radius. It was derived using the approximate procedure of Delacey's theory, and an analytical expression for C_0 is given:

$$C_0(\omega) = \frac{(2\lambda - \frac{i\omega\varepsilon_{rp}}{4\pi K^{\infty}}) - (1 - \frac{i\omega\varepsilon_{rs}}{4\pi K^{\infty}})}{2(1 - \frac{i\omega\varepsilon_{rs}}{4\pi K^{\infty}}) + (2\lambda - \frac{i\omega\varepsilon_{rp}}{4\pi K^{\infty}})} \tag{2.45}$$

$$\lambda = \frac{n_i^{\infty} z_i^2 \sqrt{2}}{\kappa_i a \lambda_i} (\sum_{j=1}^{N} \frac{z_j^2 n_j^{\infty}}{\lambda j})^{-1} (1 + \frac{3\lambda_i \overline{\mu}}{z_i^2 e}) \exp(-e z_i \xi / 2k_B T) \tag{2.46}$$

Here, $\exp(-e z_i \xi / 2k_B T)$ >>1

$$\kappa_i = (\frac{e^2 n_i^{\infty} z_i^2}{\varepsilon_{rs} k_B T})^{1/2} \tag{2.47}$$

$$\overline{\mu} = \frac{\varepsilon_{rs} k_B T}{6\pi \eta_s e} \tag{2.48}$$

where, the subscript i refers to the counter-ion of highest charge, ε_{rp} is the relative permittivity of the particles, ε_{rs} is the relative permittivity of the medium solution, z is the valence of ions, n^{∞} is the number density of ions in bulk electrolyte concentration, η_s is the viscosity of medium solution, λ_i is the drag coefficient, κ_i is the Debye-Hückel parameter, a is the particle radius, ξ is the zeta potential, and k_B is the Boltzmann constant.

Hinch *et al.* (Hinch et al., 1984) derived the dipole coefficient of the spherical particles

in dilute suspension with κa >>1 at low frequencies ($\omega << \kappa^2 D$).

From the above equations, we find that the dipole coefficients C_0 are functions of ξ and κa if the physical properties of the electrolyte and ion species are constant. Some researchers (O'Brien, 1982, Mangelsdorf and White, 1997, Rosen and Saville, 1991, Saville, 1994, Grosse and Tirado, 2001) have studied the variations of complex conductivity, permittivity and dipole coefficient with ξ and κa from both numerical solution and experiments. The results can be explained qualitatively by the charges in the double layer. From basic double layer theory, the parameters ξ and κa are related to the surface charge density of a spherical particle by a semi-empirical equation (Hunter, 2001):

$$\sigma_\xi = \varepsilon_r \varepsilon_0 \frac{kT}{ze} \kappa [2\sinh(z\tilde{\xi}/2) + \frac{4}{\kappa a}\tanh(z\tilde{\xi}/4)] \tag{2.49}$$

$$\tilde{\xi} = e\xi / kT \tag{2.50}$$

where, σ_ξ is the surface charge density at slipping plane, ξ is zeta potential, k is Boltzmann constant, κ is Debye-Hückel parameter, T is temperature, and a is the particle radius.

Therefore, the dipole coefficient and complex conductivity are also closely connected with surface charge density of particles. If we keep ξ and κ constant, the surface charge density will increase with decreasing particle radius a, and the dipole coefficient (real part and imaginary part) will also change with a. Although the approximate analytical solution of dipole coefficient provides an easy way to calculate the complex conductivity and impedance, it cannot be applied over a wide range since some assumptions are involved in the derivation (Mangelsdorf and White, 1997, O'Brien, 1986).

The comparison of the dipole coefficient C_0 obtained from different calculations, which include the De Lacey's theory (D) (Delacey and White, 1981), the "full" calculation (F) (Mangelsdorf and White, 1997), Hinch's theory (H) (Hinch et al., 1984), and O'Brien' theory (O) (O'Brien, 1986), shows that the inertial term in the Navier-Stokes equation

has almost no significant effect on the dipole coefficient up to 10^6 Hz. Under the conditions of κa =1 and κa =10, O'Brien's theory and Hinch's theory show a big discrepancy with De Lacey's theory and "full" calculation. However, they perform much better in the case of κa =50 through the frequency range 1Hz to 10^7 Hz (Mangelsdorf and White, 1997).

2.2.5 Effect of Particle Size on Dielectric Properties

The effect of particle size on dielectric properties has been studied experimentally by some researchers (Arroyo et al., 1999, Kijlstra et al., 1993, Lim and Franses, 1986, Sauer et al., 1990). Arroyo *et al.* compared the dielectric properties of two polystyrene suspensions with small (23 nm) and large (530 nm) particles. The small particles showed a large relaxation frequency, which is consistent with the relationship between the relaxation frequency and particle size for α relaxation. Kijlstra *et al.* discussed the low-frequency dielectric response of dilute aqueous hematite and silica sols. The results show that for silica sols, the dielectric increments (permittivity and conductivity) were hardly affected by the value of κa. In contrast with silica, the dielectric increments of hematite sols increase with κa. Furthermore, for both sols, the dielectric increments increase with increasing surface charge density. The relaxation frequency, is roughly, inversely proportional to the square of particle radius, as the α dispersion theory predicts. However, the study on particle size effect did not concern the κa values in different suspensions, or propose a mathematical treatment in the data analysis. In Lim and Franses's study, the complex permittivity and conductivity were studied in polymer particle dispersions with four different particle sizes. The experimental results show that the relaxation frequency is proportional to $(a+\kappa^{-1})^n$, where n ≈ 1.5, which is slightly different from the α dispersion theory. The main issue concerning the outcome of this experiment is that the authors used different particle materials, particle concentrations, and κa values, which might have caused inconsistent fitting of the results. A similar problem occurs in Sauer's study; the values of particle concentration and κa values were not fixed or included in data treatment when they studied the size effect on

relaxation frequency.

The theoretical studies on particle size effect are also very limited. A numerical study which discussed the effect of size polydispersity of colloidal suspensions on their dielectric properties was published by Carrique *et al.*, (Carrique et al., 1998). They provided a theoretical prediction on the relationship between particle size distribution and dielectric properties. The simulation results show that there is no difference in the dielectric increments obtained from a monodisperse suspension and a polydisperse suspension which have the same volume-averaged mean radius. Carrique *et al.*, (Carrique et al., 2008) studied the dielectric response of a concentrated colloidal suspension in a salt-free medium by simulation. The results show that both α and MWO relaxation frequencies move to the high frequency side with decreasing particle size under the conditions of fixed volume fraction and particle charge density.

Based on the literature review, the studies of particle size effect on dielectric properties mainly focus on the permittivity and conductivity, obtained from the permittivity spectra. Relevant studies based on electrical impedance spectroscopy are very limited. The particle size range which was studied is narrow (usually 3-4 different sizes). The effects of other parameters (for example, particle concentration, double layer thickness, ionic concentration) were not fully considered or treated in experiments or data analysis. Therefore, in our project, a more careful and thorough experimental study which particularly focuses on the particle size effect was carried out.

2.2.6 Effect of Particle Shape on Dielectric Properties

In the previous discussion, the dielectric properties of colloidal suspensions are all based on the assumption of ideal spherical particles. However, the shapes of particles in practice may include long cylinder, ellipsoid, oblate spheroid, rod, and so on. The electrical potential outside of the particles and the induced dipole moment are affected by the particle shape or the surface geometry of particles. Asami (Asami, 2002) studied

and reviewed the complex dielectric constant of colloidal suspensions with different shapes (ellipsoid, sphere, cylinder, and lamellar) in an AC field. Some of the results are listed below:

For spheres ($L_x = L_y = L_z = 1/3$):

$$\varepsilon^* = \varepsilon_a^*[1 + 3\phi \frac{\varepsilon_p^* - \varepsilon_a^*}{2\varepsilon_a^* + \varepsilon_p^*}], \text{ when } \phi << 1 \quad (2.51)$$

For cylinders ($L_x = L_y = 1/2$), whose longitudinal direction is perpendicular to the direction of the electric field, E:

$$\varepsilon^* = \varepsilon_a^*[1 + 2\phi \frac{\varepsilon_p^* - \varepsilon_a^*}{\varepsilon_a^* + \varepsilon_p^*}], \text{ when } \phi << 1 \quad (2.52)$$

For ellipsoids whose surface is expressed as:

$$\frac{x^2}{R_x^2} + \frac{y^2}{R_y^2} + \frac{z^2}{R_z^2} = 1 \quad (2.53)$$

where, R_x, R_y, R_z are the semi-axes along the x-, y-, z-axes, respectively.

The complex dielectric constant of ellipsoid orientation at random is:

$$\varepsilon^* = \varepsilon_a^*[1 + \frac{1}{3}\phi \sum_{k=x,y,z} \frac{\varepsilon_p^* - \varepsilon_a^*}{\varepsilon_a^* + (\varepsilon_p^* - \varepsilon_a^*)L_k}], \text{ when } \phi << 1 \quad (2.54)$$

When the *k*-axis of ellipsoids are parallel to the electric field, E:

$$\varepsilon^* = \varepsilon_a^*[1 + \phi \frac{\varepsilon_p^* - \varepsilon_a^*}{\varepsilon_a^* + (\varepsilon_p^* - \varepsilon_a^*)L_k}], \text{ when } \phi << 1 \quad (2.55)$$

where, L_k is the depolarisation factor along the *k*-axis, which is determined by the semi-axes along the x-, y-, z- directions, ε_a^* is the complex permittivity of the disperse medium, ε_p^* is the complex permittivity of the particles, and ϕ is the particle volume fraction.

The particle shape effect on dielectric polarisation was studied by Sihvola (Sihvola, 2007). The polarisation of particles with different shapes (sphere, spheroids, ellipsoids,

regular polyhedra, circular cylinder, semisphere, and double sphere) was studied theoretically. Although some theoretical analyses of the particle shape effects have been done, evidence of experimental research has not been found. Therefore, it is important to study the particle shape effects on dielectric properties in colloidal system, and furthermore, to study the shape of crystals in the crystallisation process.

2.3 Electrical Impedance Spectroscopy

2.3.1 Introduction

Spectroscopic techniques are favourable methods used for microscopic measurement of many chemical systems. The different types of spectroscopy can be classified according to the type of energy, including:

- Electromagnetic radiation: microwave, infrared, visible, ultraviolet, x-ray, and gamma spectroscopy.
- Electrons and neutrons (de Broglie wavelength)
- Ultrasonic wave
- Alternating electrical field

Various spectroscopic techniques have been applied to study the colloidal interface, and crystallisation of colloids such as Fourier transformation infra-red (FTIR) spectroscopy, Raman spectroscopy, nuclear magnetic resonance (NMR) spectroscopy, ultra-violet (UV) spectroscopy, impedance spectroscopy and ultrasonic spectroscopy. In this section, the discussion will focus on electrical impedance spectroscopy and its applications.

2.3.2 Electrical impedance spectroscopy

Electrical impedance spectroscopy is sometimes called “Dielectric Spectroscopy” when the polarisation effect, as a result of an electric field, is expressed in terms of

frequency-dependent complex permittivity and conductivity rather than impedance. Electrical impedance spectroscopy (EIS) is a powerful technique to investigate the electrokinetic properties of materials and their interfaces (Macdonald, 1987). The Experimental impedance spectroscopy data can be analysed using a suitable physical model (for example, the equivalent circuit model) to explain the physical or chemical processes in the material/interface. The EIS measurement can be achieved by applying an alternating voltage to the system and measuring the AC current response. If a sinusoidal potential $V(t) = V_m \sin(\omega t)$ excitation, involving a single frequency $f = \omega / 2\pi$, is applied to a material, the response to this potential is an AC current signal $I(t) = I_m \sin(\omega t + \theta)$. Here, θ is the phase difference between the voltage and the current, which is zero for purely resistive behaviour. The conventional impedance is defined as $Z(\omega) = V(t) / I(t)$. The magnitude or modulus of the impedance is $|Z(\omega)| = V_m / I_m(\omega)$, and the phase angle is θ. Usually, the complex impedance can be written by its real part and imaginary part:

$$Z = Z' + jZ'' \tag{2.56}$$

Where, $j = \sqrt{-1}$, Z' is the impedance real part and Z" is the impedance imaginary part, showing as equations:

$$\mathrm{Re}(Z) = Z' = |Z| \cos(\theta) \tag{2.57}$$

$$\mathrm{Im}(Z) = Z'' = |Z| \sin(\theta) \tag{2.58}$$

$$\theta = \tan^{-1}(Z'' / Z') \tag{2.59}$$

$$|Z| = [(Z')^2 + (Z'')^2]^{1/2}. \tag{2.60}$$

Impedance Z can also be expressed in terms of resistance (R) and reactance (X) components as $Z = R + jX$.

There are four closely related functions in impedance spectroscopy. These are most

conveniently expressed as (Hodge et al., 1976):

Complex impedance: $Z = (Y)^{-1} = Z' + jZ''$ (2.61)

Complex admittance: $Y = (Z)^{-1} = Y' + jY''$ (2.62)

Complex permittivity: $\varepsilon = (M)^{-1} = \varepsilon' - j\varepsilon''$ (2.63)

Complex modulus: $M = (\varepsilon)^{-1} = M' + jM''$ (2.64)

Table 2.1 shows the relationship between the four basic functions (Macdonald, 1987).

Table 2.1: Relations between the four basic immittance functions

	M	**Z**	**Y**	**ε**
M	M	$\mu_c Z$	$\mu_c Y^{-1}$	ε^{-1}
Z	$\mu_c^{-1} M$	Z	Y^{-1}	$\mu_c^{-1}\,\varepsilon^{-1}$
Y	$\mu_c M^{-1}$	Z^{-1}	Y	$\mu_c\,\varepsilon$
ε	M^{-1}	$\mu_c^{-1} Z^{-1}$	$\mu_c^{-1} Y$	ε

Here, $\mu_c \equiv j\omega C_c$, and $C_c = \varepsilon_0 A_c / l$.

2.3.3 Electrical Circuit Elements

Electrical impedance spectroscopy (EIS) data is commonly analysed by fitting it to an equivalent electrical circuit model. Most of the circuit elements in the model are common electrical elements such as resistors, capacitors, and inductors. To be meaningful, the elements in the model should have a basis in the physical electrochemistry of the system. As an example, most models contain a resistor that models the resistance of a cell's solution. Knowledge of the impedance of the standard circuit components is therefore very useful. We will start to look at the electrical impedance of the simplest circuit elements: pure resistor, capacitor and inductor.

(1) Pure resistor

For a pure resistor of magnitude R, the electrical impedance response shows a real

part $Z_R^{'} = R$, an imaginary part $Z_R^{''} = 0$ and the phase angle $\theta_R = 0$ for all frequencies. This is shown on a plot of the real and imaginary part as a point on the real axis (Figure 2.5), which is sometimes called the Cole-Cole plot (Cole and Cole, 1941).

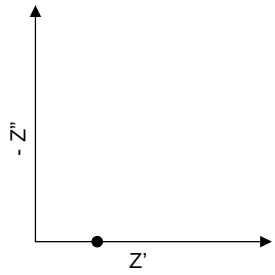

Figure 2.5: Cole-Cole plot of pure resistor

(2) Pure capacitor

For a pure capacitor of magnitude C, the electrical impedance response shows a real part $Z_C^{'} = 0$, an imaginary part $Z_C^{''} = -\frac{1}{\omega C}$, and the phase angle $\theta_C = 90°$. As the frequency increases the magnitude of the impedance decreases (shown in Figure 2.6).

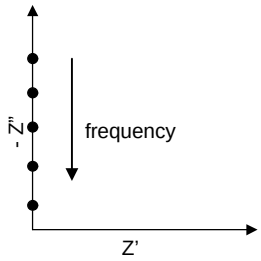

Figure 2.6: Cole-Cole plot of pure capacitor

(3) Pure inductor

For a pure inductor of magnitude L, the electrical impedance response shows a real part $Z_L^{'} = 0$, an imaginary part $Z_L^{''} = \omega L$, and the phase angle $\theta_L = -90°$. As the frequency increases the magnitude of the impedance increases (shown in Figure 2.7).

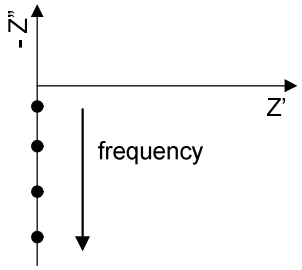

Figure 2.7: Cole-Cole plot of pure inductor

One of the most attractive aspects of electrical impedance spectroscopy as a tool for investigating the electrical properties of materials and systems is the direct connection between the behaviour of a real system and that of the idealised circuit model. Next, we will define and discuss the analogies between equivalent circuit elements and the physical electrochemistry of systems.

(1) Electrolyte resistance

Solution resistance is often a significant factor in the impedance of an electrochemical cell. The resistance of an ionic solution depends on the ionic concentration, type of ions, temperature and the geometry of the area in which the current is carried. The conductivity of the solution, *k*, is more commonly used in electrolyte resistance calculations. Its relationship with solution resistance is:

$$R = k\frac{l}{A} \Rightarrow k = \frac{l}{RA} \tag{2.65}$$

The major problem in calculating solution resistance concerns the determination of current flow path (*l*) and the geometry of electrolyte that carries the current (*A*). In the study of electrical impedance spectroscopy, the electrolyte resistance is usually obtained by fitting a model to experimental EIS data.

(2) Double layer capacitance

As an electrode in a colloidal suspension system, the electric double layer exists at two interfaces. One is the interface between charged particles and the surrounding ion solution and another is the interface between the electrode and its surrounding

electrolyte. The electrical double layer at the interface can be treated as a capacitor in the equivalent circuit model (Wang, 2005).

(3) Charge transfer resistance at the electrode-electrolyte interface

If an electrochemical reaction occurs at the electrode surface, there should be a current passing through the electrode-electrolyte interface. We call this the Faradic current. The charge transfer reaction:

$$O + ne = R \tag{2.66}$$

The charge transfer resistance is (Canagaratna, 1980):

$$R_{ct} = \frac{RT}{nFi_0} \tag{2.67}$$

where, R is the gas constant, T is the temperature, n is the number of electrons involved in the reaction, F is the Faraday's constant, and i_0 is the exchange current density.

(4) Diffusion and Warburg impedance

For a case that an electrochemical reaction occurs at the electrode surface, the concentration of reactant or product on the surface of the electrode is different from the one in the bulk solution. Therefore, the diffusion process must be considered in the analysis of electrical impedance spectra. Diffusion can create impedance known as Warburg impedance. Warburg impedance can be used to model semi-infinite linear diffusion that is unrestricted diffusion to a large planar electrode. The equation for the Warburg impedance, Z_w, of an infinite diffusion path along the electrode is (Doi, 1990):

$$Z_w = \sigma_w(\omega)^{-1/2}(1 - j) \tag{2.68}$$

σ_w is the Warburg coefficient defined as:

$$\sigma_w = \frac{RT}{n^2F^2A\sqrt{2}}\left(\frac{1}{C_O^*\sqrt{D_O}} + \frac{1}{C_R^*\sqrt{D_R}}\right) \tag{2.69}$$

where, ω is the frequency, D_O is the diffusion coefficient of the oxidant, D_R is the diffusion coefficient of the reductant, C^* is the bulk concentration of the diffusing species, A is the surface area of the electrode, F is the Faraday constant and n is the number of electrons transferred.

(5) Constant phase element

For an ideally polarised electrode, the impedance Z consists of a capacitance (C_d) in series with the solution resistance. The corresponding complex plane plot should exhibit a straight vertical line intersecting the Z'-axis at Z′ = R_Ω. However, on a real electrode/electrolyte interface with contamination and surface roughness, the complex impedance plot shows a straight line intersecting the Z′-axis at (R_Ω, 0) at an angle smaller than 90°. It means that the electrode impedance consists of resistance R_Ω in series with a complex impedance Z_c with the special property that its phase angle is independent of frequency. This phenomenon is called the "constant phase angle". The impedance of a constant phase element has the form (Zoltowski, 1998):

$$Z_{\mathrm{CPE}} = A(j\omega)^{-\alpha} \tag{2.70}$$

When this equation describes a capacitor, the constant A = 1/C (the inverse of the capacitance) and the exponent α = 1. For a constant phase element, the exponent α is less than 1. For α = 0, it is a reciprocal of resistance, and for α = -1, it is an inductance. The "double layer capacitor" on real cells often behaves like a CPE instead of a capacitor.

2.3.4 Electrode System

The electrode system which is used in electrical impedance spectroscopy measurement usually includes three different forms: 2-electrode, 3-electrode and 4-electrode systems.

(1) Two electrode system

The most basic form of cell comprises two electrodes immersed in an electrolyte

(Figure 2.8). Application of a potential across the electrodes causes a current to flow through the cell. These two electrodes are known as the working electrode (WE) and secondary (or counter) electrode (SE). In electrochemical impedance measurements, a exciting potential is applied between the electrodes, and a current response to this potential is also measured from the two electrodes to obtain the impedance response. This type of arrangement is used for the investigation of electrolyte properties, such as conductivity, when the dominant parameter is the electrolyte resistance. The two electrode cell is common and easy to use; however the problem of the electrode polarisation (electrode-electrolyte interface effects) usually significantly influences the measurements.

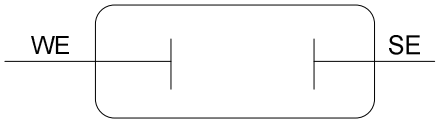

Figure 2.8: Two-terminal electrochemical cell

(2) Three electrode system

If there is a reaction at the working electrode, we may need to determine the relationship between the current on the one hand and the voltage that is required to drive this reaction on the other hand. For this case a third electrode, we call it the reference electrode, is required. The current can flow between the working electrode and counter electrode, while the potential of the working electrode is measured against the reference electrode. This set-up can be used in basic research to investigate the kinetics and mechanism of the electrode reaction occurring on the working electrode surface. Figure 2.9 shows the schematic diagram of the three electrode system.

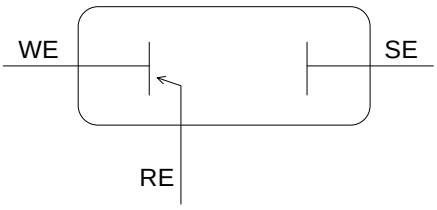

Figure 2.9: Three-terminal electrochemical cell

(3) Four electrode system

Finally, a four-terminal cell can be used to provide an analysis of processes occurring within the electrolyte (Figure 2.10). The purpose of the working and counter electrodes is only to enable the current flow. Two sensor electrodes are used to measure the voltage drop in the solution. The four electrode system can decrease the electrode polarisation effect because the electrode functions are separated, and no current passes through the two sensor electrodes (Mazzeo and Flewitt, 2007). The effect of electrode polarisation results from the formation of an electrical double layer on electrode surfaces due to the accumulation of charges (Feldman et al., 2001). The associated capacitance and complex impedance created due to the electrode polarisation influence the measurement of electrical impedance. Therefore, it is necessary to decrease the effect using a four electrode system.

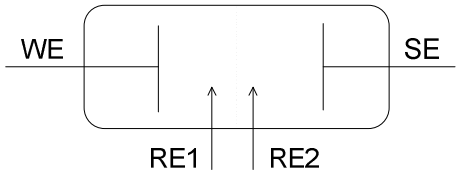

Figure 2.10: Four-terminal electrochemical cell

2.3.5 Applications of Impedance Spectroscopy

Impedance spectroscopy has a wide range of applications. It can be used to characterize the micro-structure of materials, to study solid state devices, the electrochemical reactions and the corrosion process of materials. In colloidal science, impedance spectroscopy is usually used to study the dielectric properties and the kinetic aspects of electrochemistry. The research on the dielectric properties of colloidal suspensions has been reviewed in detail in section 2.2.

In biological science, electrical impedance spectroscopy shows a valuable application for in-situ biomass characterisation in cell-culture manufacturing processes and fermentation (Hauttmann and Muller, 2001). A suspension of cells usually can be

regarded as being composed of three separate parts: the conducting cytoplasm, the outer plasma membrane and the aqueous and ionic suspension medium. When an electric field is applied to the cell suspension, the positive and negative ions move in opposite directions and accumulate at the plasma membranes. This results in the development of a charge separation or polarisation at the poles of the cells, which can be treated as a spherical capacitor. By measuring the capacitance of the suspension using electrical impedance spectroscopy, the biomass or cell concentration can be estimated (Carvell and Dowd, 2006).

Impedance spectroscopy can also be used in the study of crystallisation and solidification processes. The solidification of a ceramic-suspension was studied using complex impedance spectroscopy (Novak et al., 2001). A sharp increase in the high-frequency resistance of the ceramic suspension was observed for the time interval where the solidification of the suspension occurred. The high-frequency resistance is a function of temperature and the ceramic concentration. It was proved that impedance spectroscopy is a useful tool for monitoring the solidification process. The in-situ impedance measurement was carried out on the melting and crystallisation of solid-state polymer electrolytes (Marzantowicz et al., 2006). The ionic conductivity, dielectric constant, and the electric polarisation of both the pure PEO and PEO-LiTFSI polymer electrolyte were studied during the crystallisation process. The changes of the electrical properties, which depend on the semicrystalline structure of the polymer, were studied in the heating and cooling process.

2.4 Electrical Impedance Tomography

2.4.1 Introduction

Electrical impedance tomography (EIT) is one of the process tomography techniques to provide an on-line non-invasive imaging measurement. EIT has shown promise in both biomedical (Brown and Seagar, 1987) and industrial applications, including brain

imaging (Holder, 1992, Boone et al., 1994), pulmonary investigation (Metherall et al., 1996, Brown et al., 1994, Harris et al., 1987), breast cancer screening (Zou and Guo, 2003, Kim et al., 2007), and flow measurement (Wang et al., 2002). The impedance values, which include the real part, imaginary part, amplitude and phase angle components can be used for imaging respectively to provide more information about the test system than the imaging based on the impedance real part, viz. the resistance (Gersing and Osypka, 1994, Glickman et al., 2002). The application of phase angle imaging on three objects, including non-conductive plastic rod, metallic rod and banana, has been demonstrated by researchers at the University of Leeds (Schlaberg et al., 2008). The phase angle images for non-conductive plastic rod and metallic rod are invisible with only a noise feature; however, in the test with a banana, the object appears in phase image.

The imaging based on the resistance is called electrical resistance tomography (ERT), which is often used to provide the conductivity distribution (Xu et al., 2007). With EIT measurements, the images of impedance real part, impedance imaginary part, phase angle, and magnitude can be obtained. However, in the process industries, it is not common to use the imaginary part or phase angle due to the dominant change in conductivity in most applications or complication in the use of other impedance information. Most of the applications of EIT in the process industries rely on the conductivity difference between two phases in fluids to obtain the concentration profiles and characterisation of the fluid dynamics (Holden et al., 1998, Wang et al., 2000).

2.4.2 Measurement Procedure

The measurement strategy of EIS is basically similar to that of EIT, based on a four-electrode system, except the data acquisition and image reconstruction process is required in EIT. A typical EIT sensor consists of a set of electrodes (could be 8, 16, 32, or 64) evenly mounted around the circular vessel which contains the samples being measured. In EIT, the adjacent electrode pair strategy (Seagar et al., 1987) is commonly used in data sensing strategy. The exciting currents (alternating current) are

applied to one pair of electrodes and the resulting voltages are measured sequentially or synchronously on other adjacent electrode pairs. Figure 2.11 shows the schematic of this adjacent data sensing strategy for a 16-electrode system. Current is applied to a pair of electrodes, e.g. electrode 1 and 2, meanwhile the voltages are measured on another adjacent electrode pair, e.g. between 3 and 4, 4 and 5, up to 15 and 16. Then the excitation current is moved on to electrodes 2 and 3, and the same set of voltage is measured on the rest of the electrodes. After all the electrodes are excited and voltages are measured, one frame of cross-sectional image can be reconstructed to represent the electrical impedance distribution. The mutual impedance which includes the impedance real part, imaginary part, phase angle and amplitude can be calculated from the voltages divided by the currents.

Apart from the adjacent strategy, there are another two strategies, called the opposite strategy (Dickin and Wang, 1996) and the adaptive strategy (Cook et al., 1994), based on the positions of current injection and voltage measurement. Comparing these strategies, the adjacent strategy requires minimal hardware to implement and image reconstruction can be performed relatively quickly with minimal computer resources (Dickin and Wang, 1996).

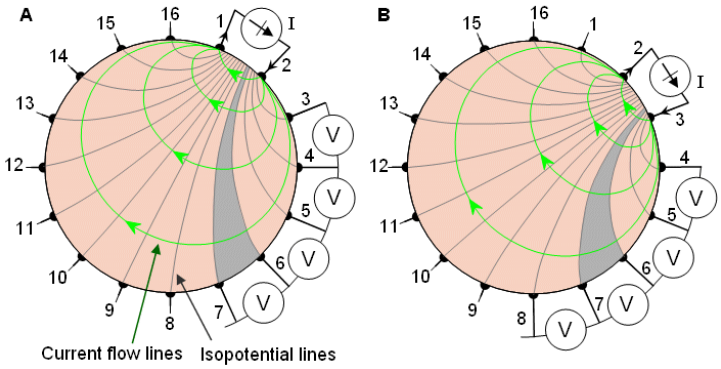

Figure 2.11: The schematic of adjacent data sensing strategy (http://www.bem.fi/book/26/26.htm)

For the adjacent strategy, based on the reciprocity theorem, the total number of unique measurements is N(N-1)/2 for a N electrodes system (Wang et al., 1995, Szczepanik

and Rucki, 2007). Ignoring those measurements involved with the working electrodes in the adjacent strategy, the number of unique measurements becomes N(N-3)/2 Therefore, for an 8-electrode system, the total number of unique measurements is 20, and for a 16-electrode system, the total number of unique measurement is 104. Figure 2.12 shows an example of the measurement data for one frame image in an 8-electrode system.

Adjacent protocol, 8 sensors, 1 planes, 20 data per plane, frame 213

Plane 1: Min 303.223, Max 1088.87, Mean 616.187 (mV)

Voltage Measurement Pairs

Current Injection Pairs	02 - 03	03 - 04	04 - 05	05 - 06	06 - 07	07 - 08	Measurement Set
08 - 01	1.060e+003	4.507e+002	3.408e+002	4.282e+002	1.089e+003		1
01 - 02		9.766e+002	4.282e+002	3.423e+002	4.463e+002	9.277e+002	2
02 - 03			9.424e+002	4.058e+002	3.447e+002	4.331e+002	3
03 - 04				8.936e+002	3.657e+002	3.032e+002	4
04 - 05					8.545e+002	3.589e+002	5
05 - 06						9.326e+002	6

Figure 2.12: Measurement data for one frame image in an 8-electrode system

EIT measurement in most process applications is based on the relative changes of the samples, which means a reference should be taken at the beginning. For example, a vessel is filled with a homogeneous solution (for example, tap water or distilled water), which is called the reference. The voltage values (V_r) measured from different electrode pairs for the reference solution are recorded and saved. Next, a second phase or material is added into the reference solution, and the measured voltage values (V_m) taken from different electrode pairs are recorded as well. The relative voltage change is determined by Equation (2.71):

$$\text{voltage relative change} = \frac{V_m - V_r}{V_r} \tag{2.71}$$

Figure 2.13 shows the typical profiles of measured voltages, reference voltages, and relative voltage changes, respectively in an 8-electrode system. The number on the x-axis means the number of the series of measurement. It can be found that the large relative voltage differences are observed mainly on the bottom parts of U-shaped V_m

and V_r curves, which are the voltages measured between the two electrodes opposite to the position of the exciting electrodes (for example, the voltages between 5 and 6 electrodes when the exciting current is applied to 1 and 2 electrodes in an 8-electrode system). The large-relative changes mean the small V_m and V_r, play more important roles in precise image reconstruction although technically, measuring small voltages accurately is much more difficult than measuring large voltages.

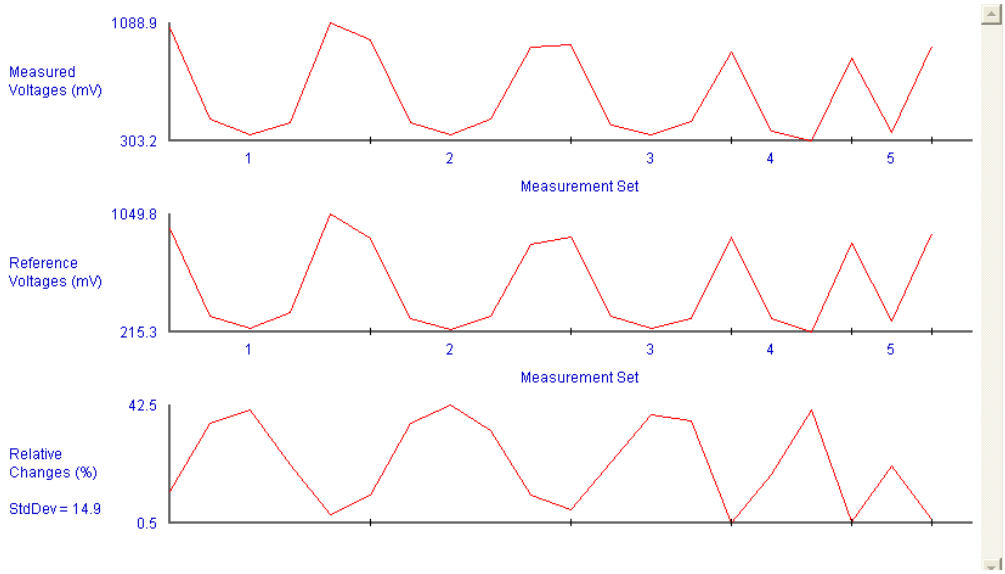

Figure 2.13: The typical profiles of measured voltages, reference voltages, and relative voltage changes, respectively in an 8-electrode system

2.4.3 Common Mode Voltage

In EIT measurements, the common mode voltage effect and stray capacitance are the major sources of instrumentation error. The voltage measurement in an EIT system usually uses differential voltage measurement, which could result in a reduction in voltage signals compared with the single-ended voltages. However, in practice, the precision of differential voltage measurement is affected by the measurement error due to non-zero common mode amplifier gain (Murphy and Rolfe, 1988, McEwan et al., 2007).

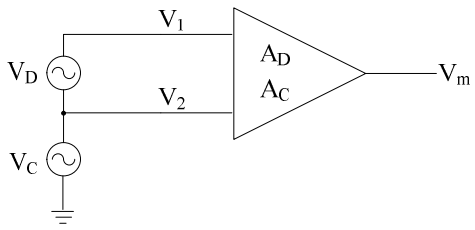

Figure 2.14: A differential amplifier and its inputs and outputs

As shown in Figure 2.14, the differential amplifier has differential gain A_D and common-mode gain A_c. If the instrumentation amplifier is ideal, A_c is zero and the out-put voltage V_m is only related to the differential voltage V_D and differential gain A_D. The output voltage, V_m, can be calculated using Equation (2.72):

$$V_{\mathrm{m}} = A_{\mathrm{D}} V_{\mathrm{D}} \tag{2.72}$$

However, a real amplifier has non-zero A_c, and could respond to both V_D and V_C, therefore, V_m is given by:

$$V_{\mathrm{m}} = A_{\mathrm{D}} V_{\mathrm{D}} + A_{\mathrm{C}} V_{\mathrm{C}} = A_{\mathrm{D}} (V_1 - V_2) + A_{\mathrm{C}} (\frac{V_1 + V_2}{2}) \tag{2.73}$$

where, V_c is common mode voltage (CMV), V_1 and V_2 are voltages between individual electrodes and the ground, respectively.

The common-mode rejection ratio (CMRR) is given by:

$$\mathrm{CMRR} = 20 \log_{10} | \frac{A_{\mathrm{D}}}{A_{\mathrm{C}}} | \tag{2.74}$$

In order to minimize the effect of common mode voltage, it is preferable that CMRR is as large as possible. For a real instrumentation amplifier, CMRR is usually large under DC conditions, and drops with increasing frequency. Typical CMRR values are in the range of 100 -120 dB under DC and decreased to 60 dB at 1MHz (Holder, 2005).

Since it is difficult to reject the effect of common mode voltage, particularly at higher frequencies, a voltage feedback system is usually used in EIT measurement to decrease CMV (Rosell and Riu, 1992). The common mode feedback (CMFB) can be applied to an extra electrode, or the current source (Rosell and Riu, 1992). Although

CMFB can decrease the common mode voltage, it also brings a limitation, which comes from the phase delay of the feedback circuit. The phase delay will cause a phase error in the demodulation and possible feedback oscillation at high frequencies (Wang et al., 1993).

2.4.4 Imaging Reconstruction

EIT imaging, which reflects the electrical impedance distribution in a phantom, is achieved by a process of image reconstruction. There are two types of algorithms for data reconstruction, qualitative algorithms and quantitative algorithms. The qualitative algorithm depicts a change in voltage relative to initially acquired reference data, and the image reconstruction is fast for providing on-line measurement. The qualitative algorithm utilizes a back projection algorithm, as a typical example, which can be performed by multiplying a pre-calculated sensitivity map (matrix) to a relative voltage change (vector) to reconstruct images (Dickin and Wang, 1996). This algorithm is simple and fast but not accurate enough.

For accurately reconstructing images, a quantitative algorithm, an iterative Newton-Raphson-based algorithm, was developed which is accurate but relatively slow (Yorkey et al., 1987). The reconstruction process starts from an estimation of a set of initial voltage values (in practice, it is usually the reference data) to solve the forward problem. The forward problem can be solved using a finite-element-method-based solver and the initial conductivity distribution values to obtain a set of calculated voltages. Then the calculated voltages are compared with the measured voltages from the data acquisition system. The least-squares error between the two sets of voltages is calculated and compared to a pre-defined error. If it is larger than the pre-defined error criterion, the initial voltage values are modified according to the optimization rules, and then fed into the forward solver for the next iteration, until the error criterion is met.

Figure 2.15 shows a reconstructed image of a plastic rod in tap water using an 8-electrode system and a back-projection algorithm. The coloured bar denotes the value

of conductivity, which changes from low to high with a colour change from blue to red. The blue area in Figure 2.17 presents the existence of a non-conductive material in the tap water.

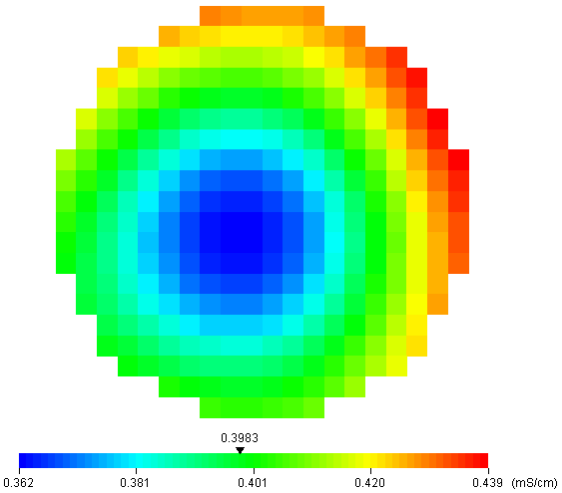

Figure 2.15: Reconstructed image (impedance real part) of a plastic rod in tap water using an 8-electrode system

2.5 Particle Sizing Methods

Many different techniques have been used for determining particle size/particle size distribution over a wide range of applications both in research and industrial fields. The major classes of particle sizing methods have been reviewed and are shown in the list given below:

(1) Microscopy

(2) Sieving

(3) Sedimentation analyses

(4) Counting techniques

(5) Light scattering/diffraction methods

(6) Chromatography techniques

(7) Other techniques

Each of these is based on a different principle of measurement and is applicable only to a specific range of particle sizes. The details of each technique in the above list are discussed, including several sub-classes given in the subsequent paragraph. The advantages and disadvantages of different particle sizing methods are also reviewed.

2.5.1 Microscopy

Microscopy is often used to measure the particle size and shape as an absolute method because the individual particles can be observed and measured directly. As an off-line measurement, the sample preparation before microscopy measurement should be considered carefully in order to get good results. The most popular microscopy methods include optical microscopy, scanning electron microscopy (SEM) and transmission electron microscopy (TEM).

1) Optical microscopy

Optical microscopy can measure particles with a size range from about 0.8 μm to 150 μm (Allen, 1990). Satisfactory sampling in optical microscopy can be achieved by preparing a slide containing a uniformly dispersed sample. The imaging produced may be viewed directly by eye or by normal light-sensitive/digital cameras to generate an image. The captured images are usually suitable for counting and sizing to obtain the particle size distribution.

2) Scanning electron microscopy (SEM)

A scanning electron microscope is a type of electron microscope that scans a sample with a high-energy beam (5-50 keV) (Allen, 1990) of electrons in a series of parallel tracks. The electrons interact with atoms at or near the surface of the sample to produce secondary electrons, back-scattered electrons, light and transmitted electrons. These signals can be detected and then a 2-dimensional image can be displayed on a screen. The signals which are commonly used for imaging include secondary electrons and backscattered electrons. The secondary electrons are most valuable for showing the surface topography and backscattered electrons can be used to obtain the material

contrast (Klang et al., 2012). For conventional measurement using SEM, the samples need to be electrically conductive. Therefore, for non-conductive samples, a layer of metal (usually gold) must be coated on the surface of the sample. The applicable size range of SEM is wide, from the order of nanometre to millimetre (Abbireddy and Clayton, 2009).

3) Transmission electron microscopy (TEM)

The operating principle of TEM is that a beam of electrons is transmitted through an ultra-thin sample and interacts with the sample as it passes through. Imaging can be obtained by utilizing the information contained in the electron waves coming from the sample (Liu, 2005). TEM can provide a significantly higher resolution than an optical microscope since the imaging relies on the electron beam. The applicable range of size for TEM measurement is usually from 1 nm to 5 μm (Abbireddy and Clayton, 2009), which is very useful for nano-particle sizing in scientific fields.

Advantages:

- Suitable for a relatively broad range of sizes (optical microscopy is suitable for relatively large particle sizes and TEM is suitable for nano-particles)
- Images are high quality and detailed.
- TEM can provide information on element and compound structure.
- SEM can provide the topographical imaging.

Disadvantages:

- SEM and TEM are expensive methods.
- Samples must be prepared before the measurement, and the potential effect from sample preparation might be involved.
- SEM and TEM are not suitable for an on-line measurement due to their current form of sample preparation and hardware involving the electron beam and vacuum chamber.

2.5.2 Sieving

As one of the most simple and inexpensive methods, sieving is usually used for particle sizing in powder materials. The particle size is effectively defined by the size of the hole through which a particle can just pass (Abbireddy and Clayton, 2009). A variety of sieve apertures are currently in use and they can be classified as coarse (4-100 mm), medium (0.2-4 mm) and fine (less than 0.2 mm) (Allen, 1990). In the practical applications, a sieve is usually used for coarse materials (for example sand), and not suitable for nano-particles. Although the sieving method is simple and cheap, it is time consuming and influenced easily by the particle shape, humidity and the human operation (Nathierdufour et al., 1993).

Advantages:

- simple and inexpensive

Disadvantages:

- Time consuming
- Only suitable for relatively large particles
- Influenced easily by the particle shape, humidity and human operation
- Not suitable for developing on-line measurement.

2.5.3 Sedimentation

As a traditional technique, sedimentation determines the particle size distribution by measuring the time required for the particles to settle a known distance in a fluid. The principle is based on Stokes' law, which assumes the particle shape to be spherical and flow to be laminar (Allen, 1990). When a terminal velocity is reached, it is assumed that the drag force and the buoyancy force on the particle are exactly balanced by the gravitational force. Therefore, the drag force at the time that particles reach the terminal velocity can be presented as:

$$F_{\mathrm{d}} = \frac{4}{3}\pi a^3(\rho_{\mathrm{p}} - \rho_{\mathrm{f}})g \tag{2.75}$$

where, F_d is the drag force acting on the particle, *a* is the particle radius, g is the gravitational acceleration, ρ_p is the density of the particle, and ρ_f is the density of the fluid.

It is also known that the drag force of particles in a size range of micrometres can be approximated as being proportional to the particle's velocity, which is expressed by (Allen, 1990):

$$F_{\mathrm{d}} = 6\pi\eta a\upsilon_{\mathrm{s}} \tag{2.76}$$

where, η is the viscosity of the liquid and υ_s is the particle terminal velocity.

Combining Equations (2.75) and (2.76), the relationship between particle radius and terminal velocity can be obtained:

$$\upsilon_{\mathrm{s}} = \frac{2}{9}\frac{a_s^2}{\mu}(\rho_{\mathrm{p}} - \rho_{\mathrm{f}})g \tag{2.77}$$

The particle size a_s shown in Equation (2.77) is called the Stokes radius. The principle of using the sedimentation method is reliant on the relationship between particle terminal velocity and particle size. By measuring the particle velocity in sedimentation, particle size can be obtained. In practise, the particle velocity is usually determined by measuring the change of concentration with time at a known depth, and the plot of particle concentration against Stokes radius gives the particle size distribution (Allen, 1992). The sedimentation techniques can be classified into incremental and cumulative methods according to the measurement principle, the homogeneous and line start methods according to the suspension type, and the gravitational and centrifugal types according to the force field involved. More details about the sedimentation methods have been reviewed by Allen (Allen, 1992).

Due to the assumption used for derivation of Stokes' law, the sedimentation method is only suitable for spherical particles, for fluids with low Reynolds number (< 0.2), and low particle concentration (volume concentration is lower than 2%) (Allen, 1990). The reliable measurement range of the gravitational sedimentation method is believed to be between 2 μm and 60 μm (Abbireddy and Clayton, 2009), although the suitable range is variable with the material types of particle and fluid. For very small particles (< 2 μm), the particle movement due to Brownian motion is comparable with, or even exceeds, the movement caused by gravitation, therefore it is unsuitable to calculate the particle size using Stokes' equation in this situation. For very large particles (> 60 μm), turbulence is involved in the sedimentation and the assumption of laminar flow in Stokes law is no longer valid. The measurement range of the centrifugal sedimentation method is broader than the gravitational method (0.01-100 μm), since the effects of convection, diffusion, and Brownian motion can be reduced by speeding up the settling process by centrifugal force (Provder, 1997).

Advantages:

- Inexpensive and easy operation
- Relatively good repeatability
- Relatively broad test range

Disadvantages:

- Relatively long test time
- Not accurate for high particle concentration and non-spherical particles
- Not suitable under turbulent conditions
- Not suitable for developing on-line measurement

2.5.4 Counting technique

In the counting technique, the interaction of one particle and an external field is utilised

for size measurement. Based on the different external fields, there are two categories: the Coulter counter and Optical counter (Allen, 1997).

1) Coulter counter

The Coulter counter is also called the electrical sensing zone method. For this method, the particles are suspended in an electrolyte and forced to pass through a small orifice, which is located between two electrodes by applying an electrical field. The changes in electrical resistivity when particles pass through the orifice can produce a pulse, which is approximately proportional to the volume of the particle. After measuring a large number of particles which have passed through the orifice, the particle size distribution can be obtained. The size range of this method is about 0.4-1200 μm (Abbireddy and Clayton, 2009).

2) Optical particle counter

The principle of the optical counter method is similar with the Coulter counter, except the external field is changed to the optical beam. The amplitude of light scattered or blocked by a single particle is a function of particle size, therefore, particle size distribution can be determined by measuring the light intensity after being scattered or blocked (Barth and Sun, 1985). The measurement range of the optical counter method is broad but could be varied due to different ways of detection. Generally, the size range is from 0.5 μm to > 300 μm.

Advantages:

- Simple in concept and easy to calibrate with known size standard sample.
- Relatively broad test range.
- The optical particle counter method can be developed to an on-line method easily.

Disadvantages:

- For the Coulter counter method, the particles must be dispersed in an electrolyte and must be of a non-conductive material.
- For the Optical counter method, the accuracy of measurement is affected by the

particle shape significantly.

- Not suitable for nano-particles (<1 μm)

2.5.5 Light scattering/diffraction methods

Light scattering/diffraction methods are very popular particle sizing methods and include several categories based on the principle of measurement. The major categories have dynamic light scattering, laser diffraction, focused beam reflectance measurement (FBRM), and time of flight (Marshall et al., 1991). The laser diffraction method is based on the proportional relationship between the intensity and angle of forward diffraction of a laser beam and the particle size. As the particle size decreases, the scattering angle of the laser beam increases logarithmically, and the scattering intensity decreases. By measuring the angular distribution of the intensity of the scattered laser beam using a detector, the particle size distribution can be obtained (Ma et al., 2000).

The dynamic light scattering method measures the time dependent fluctuations of scattering light intensity, which is caused by the Brownian motion of the particles in the suspension. Based on the Stokes-Einstein theory of Brownian motion, the particle size can be related to the diffusion coefficient by Equation (Brar and Verma):

$$D = \frac{k_B T}{6\pi\eta a} \tag{2.78}$$

where, D is the diffusion coefficient, k_B is Boltzmann's constant, T is temperature, η is viscosity, and *a* is particle radius.

The analysis of the intensity fluctuations can provide the diffusion coefficient of particles and therefore give the particle radius based on Equation (2.78).

The focused beam reflectance measurement and time of flight technique are usually used as an on-line sizing method and will be discussed in the next section (2.6) in detail.

Advantages:

- Fast and precise analysis.
- Simple, no sample preparation need
- Small volume of samples are required
- Size range could extend to 1 nm as the smallest size for the dynamic light scattering method (Zetasizer Nano user manual, Malvern)

Disadvantages (Eshel et al., 2004):

- Relatively expensive instrumentation
- The accuracy of measurement is affected by the particle shape (non-spherical particle)
- Not suitable for high concentration samples (< 5% weight concentration for 10 nm-100 nm particles, <1% weight concentration for > 100 nm particles) (Zetasizer Nano User Manual, Malvern)

2.5.6 Chromatography techniques

Chromatography techniques include two main categories: hydrodynamic chromatography (HDC) and field flow fractionation (FFF). The hydrodynamic chromatography method is based on the separation of particles in suspensions by passing through packed columns or a capillary column. The measurement range of hydrodynamic chromatography is 20 nm to <1μm for packed column and 0.7-50 μm for capillary (HDC) (Barth and Sun, 1985). Field flow fractionation is a kind of one phase chromatography. The basic principle is the separation of particles with a solvent stream which enters a thin channel (Provder, 1997) under the effect of the field.

Advantages:

- Relatively wide measurement size range (variable in different methods).
- Results are independent of particle density for chromatography techniques

Disadvantages:

- Particle deposition in packed columns
- Complex mathematics is involved to derive the absolute particle size distribution.
- Not suitable for developing on-line measurement.
- Not suitable for high concentration samples (< 5% weight concentration for 10 nm-100 nm particles, <1% weight concentration for > 100 nm particles) (Zetasizer Nano User Manual, Malvern)

2.5.7 Electroacoustic Technique

The electroacoustic phenomenon, which was first predicted by Debye in 1933, results from coupling between acoustic and electric fields (Dukhin and Goetz, 2002). The electroacoustic effect is the generation of electric fields by acoustic wave or the generation of acoustic waves by the application of an alternating electric field (O'Brien et al., 1990). The former is known as the colloidal vibration potential (CVP) and the latter is known as the electrosonic amplitude (ESA). The technique of electroacoustics can produce information about the electrical properties of colloids. In principle, it can be used for particle sizing (Dukhin and Goetz, 2002).

In the case of an electric field as the driving force, the generated electrosonic amplitude (ESA) can be expressed by:

$$ESA(\omega) = -\frac{\phi \Delta\rho \mu_E}{\rho_m} F(Z_T, Z_s) A(\omega) \tag{2.79}$$

where, μ_E is the dynamic electrophoretic mobility of colloidal particle, ρ_m is the density of medium, Φ is the volume fraction of particles, $\Delta\rho$ is the density difference between the particle and the medium, $F(Z_T,Z_s)$ is a function of the acoustic impedances of the transducer and the suspension, $A(\omega)$ is an instrument constant found by calibration.

For the case of the acoustic wave being the driving force, the generated colloid vibration potential (CVP) can be described by:

$$E_{CVP} = -\frac{\phi \Delta \rho \mu_E}{\rho_m K^*} \nabla P \tag{2.80}$$

where, $\Delta\rho$ is the density difference between the particle and the medium, μ_E is the dynamic electrophoretic mobility of charged particle, Φ is the volume fraction of particles, ρ_m is the density of medium, K^* is the complex conductivity of suspension, P is the pressure caused by the acoustic wave and ∇P denotes the gradient of pressure.

The dynamic mobility μ_E can be determined by Equations (2.79) and (2.80) from electroacoustic measurement and from the dynamic mobility, the particle size and zeta potential can be determined (O'Brien et al., 1995).

Advantages:

- Can work for samples with high particle concentration (1-40 volume percent) (www.colloidal-dynamics.com/docs/CD_products_for_emulsions.pdf)
- Can measure particle size distribution and zeta potential simultaneously from a single set of data

Disadvantages:

- Only suitable for charged particles
- The desired particle size distribution can only be deduced from measured electroacoustic spectrum for a limited range of conductivity and some restrictive assumptions about the nature of the double layer.
- The uncertainties in the model and theory make it impossible to obtain any more detailed information than a simple lognormal approximation to the actual PSD.

2.5.8 Other techniques

There are some other kinds of particle sizing methods which are not included in the above categories, for example, ultrasonic attenuation spectroscopy, small-angle X-ray scattering, and differential electrical mobility. Ultrasonic attenuation spectroscopy has

received increasing attention due to its wide application range of particle size (10 nm-1 mm), high concentration (up to 50% vol) and development of the on-line sizing technique (Mougin et al., 2003). As one of the common on-line sizing techniques, ultrasonic attenuation spectroscopy will be further reviewed in section 2.6.2. The small-angle X-ray scattering (SAXS) method is essentially based on the same physical principle of laser diffraction, but using a shorter radiation wavelength. SAXS can provide precise size measurement for nano-particles (McKenzie et al., 2010). However, the instrumentation is relatively expensive compared with other techniques and the operation must be carried out more carefully as a high radiation source is involved. The differential electrical mobility method can separate the charged particles according to their electrical mobility which is related to their particle size. The instrumentation measures the number concentration of particles in several size channels (Peters et al., 1993). This method is usually used for on-line size measurement for aerosols.

2.6 On-line Particle Sizing Methods

With increasing requirements for on-line controlling of particle size during industrial processing, the study and development of on-line particle sizing methods has become more valuable. The current on-line particle sizing methods are not sufficient and are limited to specific conditions based on their principles. In this section, the state of the art of the typical on-line particle sizing methods is reviewed.

2.6.1 Optical based methods

Optical sensing is still the most widely used on-line particle sizing method. The common optical methods based on-line sizing methods include laser diffraction (Abbas et al., 2002), focused beam reflectance measurement (FBRM) (Scholl et al., 2006, Abbas et al., 2002), optical counter (light blockage or scattering) (Allen, 1990), time of flight (Weiss et al., 1997) and the digital imaging method (De Anda et al., 2005). The

basic principle of the optical methods is based on the interactions between individual particles and laser/light beams. The measuring system usually consists of a light emitting source and a light detection assembly. The principles of these on-line measurement techniques are summarised as follows:

(1) Laser diffraction

The laser beam scattered by the particles is collected and measured over a range of solid angles in the forward direction of the incident beam. The scattering angle and intensity are functions of the particle size. The schematic diagram of the laser diffraction technique is showed in Figure 2.16.

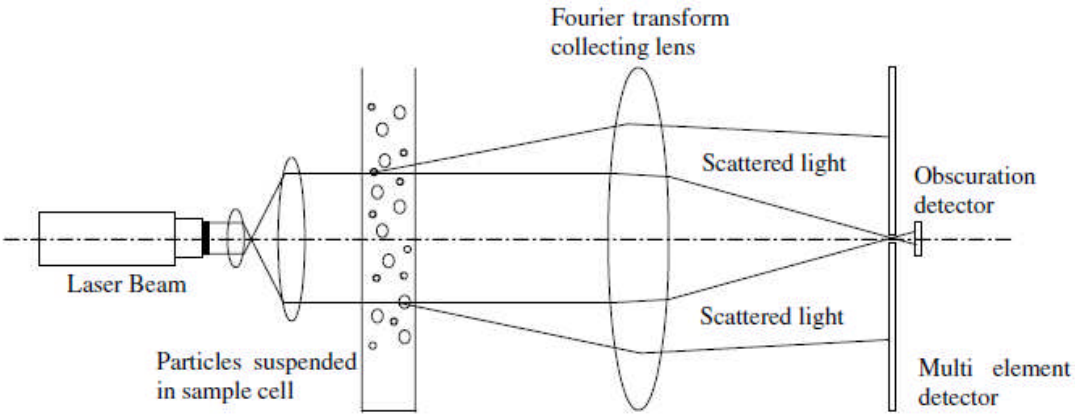

Figure 2.16: Schematic diagram of the laser diffraction technique (Abbas et al., 2002)

(2) Focused beam reflectance measurement (FBRM)

The focused laser beam rapidly scans across particles and the time period of back-scattering is recorded. The back-scattering time is multiplied by the scan speed of the laser beam to produce a distance from one edge of the particle to the other, which is called a chord length. As the distance measured by FBRM is the chord length, which is easily affected by the particle shape and the position of the particle passing through the laser beam, the accuracy of the FBRM technique is limited, especially for non-spherical particles (Dowding et al., 2001). The measurement does not give a true particle size distribution as the laser beam is unlikely to cut right across the centre of particle, but a

distribution of the chord lengths. The method also tends to give an oversized result when used in measuring transparent particles (for example, emulsion droplets). However, as one of the major advantages, the FBRM technique can operate with very high concentrations of particles (40 % by volume) (Allen, 1997). It is a real on-line technique since there is no need for dilution or sampling and therefore the errors caused by dilution or sampling can be avoided. A schematic diagram of the focused beam reflectance technique is shown in Figure 2.17.

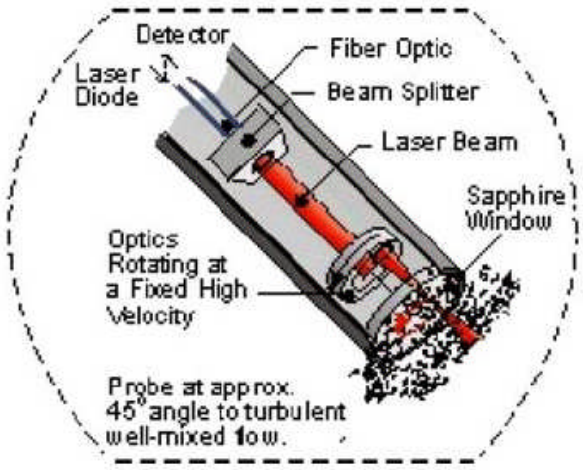

Figure 2.17: Schematic diagram of the focused beam reflectance technique (Abbas et al., 2002)

(3) Optical counter

The measurement methods of the optical counter can be based on light scattering, light obscuration and direct imaging. When the particles pass through the beam, the amount of light which is cut off, or scattered by particles can be measured and produce pulses on the photodiode. The height of the pulse is proportional to the projected area of particles which is related to particle size.

(4) Time of flight

This technique is usually used for aerosols. The particle size can be measured as follows: particles in an air stream enter into a sensing zone through a fine nozzle via an accelerating flow field. Particles can be accelerated in the air flow field according to the

particle size, with smaller particles being accelerated more rapidly than larger particles. Two parallel laser beams are used to detect the position of particles in the sensing zone as the laser beams are scattered when particles pass through the beams. The two laser beams are fixed and therefore, the time of particles passing through can be measured and recorded. The aerodynamic time of flight is a function of particle size, density and shape (Cheng et al., 1993).

(5) Digital imaging method

With developments in computer and digital techniques, the digital imaging method has become increasingly popular used for on-line particle size measurement. A typical system includes a light source, a CCD (charge coupled device) camera, and a PC with video digitizer and software. The particle size and shape can be measured from the digital image obtained by the instrument (Barrett and Glennon, 2002). The digital imaging method provides the ability to see particles as they naturally exist in a crystallizer, vessel or pipeline, but the visualisation is easily affected by the particle concentration and the condition of stir or flow rate.

2.6.2 Non-optical based methods

The commercialised non-optical based on-line particle sizing methods are fewer than the optical based methods. Two popular methods are reviewed here, ultrasonic attenuation spectroscopy and the differential electrical mobility method.

(1) Ultrasonic attenuation spectroscopy

Ultrasonic attenuation spectroscopy is one of the few commercialised non-optical methods. The principle of the technique is based on the attenuation of an ultrasonic wave passing through a particle suspension. The mechanisms of attenuation include intrinsic absorption, thermal coupling of phases, visco-inertial coupling of phase, and elastic scattering, which are all related to the particle size, concentration, the spacing of the transmitter and receiver, and other physical parameters (viscosity, the velocity of

sound in water, particle density etc.) (Shukla et al., 2010). By using a range of frequencies, a series of relationships between particle size and attenuation can be obtained to generate the particle size distribution. Figure 2.21 shows a schematic diagram of the ultrasonic attenuation spectroscopy technique used in the crystallisation process.

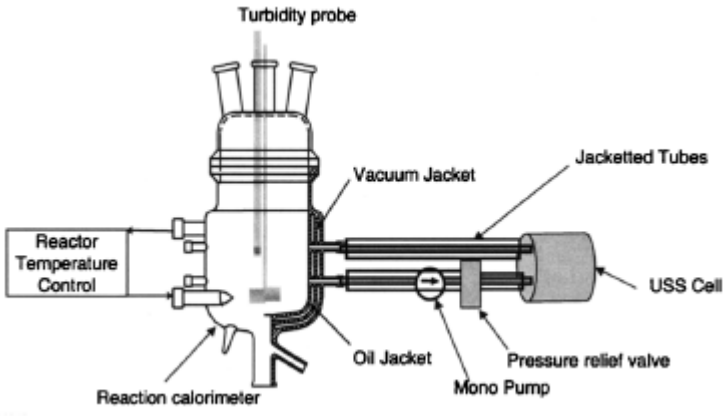

Figure 2.18: Schematic diagram of the ultrasonic attenuation spectroscopy technique (Mougin et al., 2003)

(2) Differential electrical mobility method

As mentioned in section 2.5.7, the principle of the differential electrical mobility method is based on the electrical mobility which is related to the particle size when the particles pass through an electrical field. The electrical mobility can be related to particle size by:

$$\mu_p = \frac{neC}{3\pi\eta a} \tag{2.81}$$

where, μ_p is electrical mobility, n is the number of charges on the particle, e is the elementary charge, C is a correction parameter, η is gas velocity, *a* is particle size.

Size calibration is necessary for this method and the particle size can be calculated from the electrical mobility distribution (Ehara et al., 2000).

Table 2.2 summarises the typical on-line particle sizing techniques, including the applied size range, principle, the main advantages and disadvantages, and the manufacturer/developer.

From the Table 2.2, it can be seen that the current commercial on-line particle sizing methods have their particular application field and suitable size range. Most of the optical based techniques are inherently unsuitable for examining the dense crystal/solution slurries (for example, in the batch crystallisation process). As these optical particle sizing methods cannot work at representatively high solid concentration levels, a difficult and time-consuming sampling step is therefore needed for the dilution of the solid/liquid suspension, a process which can, in turn, lead to significant modification of the particle size distribution. The non-optical based methods, except ultrasonic attenuation spectroscopy, are usually suitable for aerosols not liquid solutions. The ultrasonic attenuation spectroscopy method can be used in the dense liquid suspensions, however, the measurement is easily affected by the bubbles and the calculation of size distribution needs some parameters whose on-line values are difficult to obtain.

Table 2.2: Summary of the typical on-line particle sizing techniques

Model	**Principle**	**Size range**	**Manufacture/Developer**	**Advantages**	**Disadvantages**
Insitec	Laser diffraction	0.1-2500 μm	Malvern (http://www.malvern.com/)	■ First principle based technique ■ Wide measuring range ■ Fast, reproducible, and high resolution	■ Not suitable for high particle concentration suspensions ■ Sampling or dilution from the main stream or batch solution causes error
Mytos & Twister	Laser diffraction with twister sampler	0.25-3500 μm	Sympatec (http://www.sympatec.com/EN/LaserDiffraction/HELOS.html）		
Safir	Laser diffraction with a sample reservoir	0.1- 875 μm	Sympatec http://www.sympatec.com/EN/LaserDiffraction_Process/SAFIR.html		
Lasentec	Focused beam reflectance measurement (FBRM)	0.5 -2000 μm	Mettler Toledo (http://uk.mt.com/gb/en/home/products/L1_AutochemProducts/L2_ParticleSystemCharacterization/FBRM.html)	■ Without the need for sampling or dilution ■ Suitable for high particle concentration (40 % by volume)	■ Not accurate for the non-spherical particles ■ Only get the distribution of chord length, not the true particle size ■ Not suitable for transparent particles (emulsion droplets)
Hiac PM4000 liquid particle counter	Optical particle counter	4, 6, 14, and 21 μm size channels	Pacific Scientific (http://www.particle.com/hiac-liquid-particle-	■ Simple affordable and easy for maintenance ■ High temperature and	■ Only provide 4 size channels ■ Only suitable for the liquid

			counters/hiac-pm4000)	pressure capabilities for harsh environments	system
MET ONE series air particle counter	Optical particle counter	0.5 to 10.0 μm Or 4 size channels	Pacific Scientific (http://www.particle.com/met-one-air-particle-counters/remote/met-one-6000p)	■ Offers accurate and reliable continuous particle monitoring	■ Only suitable for the gas/solid system ■ Unable to detect nano-particles (< 0.5μm)
Condensation particle counter	Optical particle counter	10 nm -5 μm	TSI Inc. (http://www.tsi.com/Condensation-Particle-Counters/)	■ Can measure nano-particles down to 10 nm	■ Only suitable for aerosols ■ Do not provide direct information on the original size (small particles are condensed for optical detection)
Aerodynamic particle sizer Spectrometer	Time of flight	0.5 -20 μm	TSI Inc. (http://www.tsi.com/)	■ Double-crest optics produce high-quality measurement	■ Maximum particle concentration: 1000 particles/cm^3 ■ Need diluter for high concentration samples ■ Only suitable for airborne solids and nonvolatile liquids
Particle vision and measurement (PVM)	Digital image analysis	2μm to 1mm	Mettler Toledo (http://us.mt.com/us/en/home/products/L1_AutochemProducts/L2_ParticleSystemCharacteriz	■ Provide real time imaging without sampling process ■ Operate at full process concentration	■ Probe based tool, the clogging of probe may occur and cause error

			ation/PVM.html)	■ Can observe not only the particle size but also particle shape	
Digital video microscopy	Digital imaging analysis	140 µm to 16mm (dependent on the lens employed)	GlaxoSmithKline	■ Can measure particle size and shape at the same time ■ No sampling process involved	■ CCD camera detects via a small window at the wall of the reactor, therefore only small portion of the sample can be measured ■ Suitable for big particles
Ultrasonic extinction (OPUS)	Ultrasonic attenuation spectroscopy	10 nm – 3mm	Sympatec (http://www.sympatec.com/EN/UltrasonicExtinction/UltrasonicExtinction.html)	■ Suitable for high concentration particles (up to 70% vol)	■ Non-absolute technique and requires an extended set of parameters for the exact evaluation of size distribution. ■ The presence of small gas bubbles can cause strong scatter ultrasound and bring errors for the measurement
Scanning mobility particle sizer spectrometer	Electrical mobility technique and optical particle counter	10 nm to 1,000 nm (up to 167 size channels)	TSI Inc. (http://www.tsi.com/Scanning-Mobility-Particle-Sizer-Spectrometer-3034/)	■ Can measure nano-particles down to 10 nm	■ Only suitable for aerosols
Differential mobility	Electrical mobility technique	10 to 1000 nm or 2 to	TSI Inc. (http://www.tsi.com/Diff	■ Can measure nano-particles	■ Only suitable for aerosols

analyzer		150 nm (depends on the model)	erential-Mobility-Analyzers/)		

2.7 Theory of the Crystallisation Process

2.7.1 Crystal Nucleation and Growth

Crystallisation is the process of formation of solid crystals from a homogeneous solution. It is also a chemical solid-liquid separation technique in industry and can be thought to include precipitation or reactive crystallisation. Crystallisation is one of the most important industrial processes in the pharmaceuticals, biotechnology, mineral processing and other chemical engineering industries.

The crystallisation process consists of two major events, nucleation and crystal growth (Muller, 2004). Nucleation is the step where the solute molecules dispersed in the solvent start to gather into clusters, on the nanometer scale, that need to reach a critical size in order to become stable nuclei. Such critical size is dictated by the operating conditions, such as temperature and supersaturation. Supersaturation is a prerequisite for all crystallisation processes to occur. The definition of supersaturation is given by the concentration difference (Myerson, 2001):

$$s = c - c^* \tag{2.82}$$

or a ratio of concentrations:

$$s = \frac{c}{c^*} \tag{2.83}$$

where, s is the supersaturation, c is the actual concentration of solute and c^* is the solute concentration in the saturated state.

Supersaturation is an important parameter in crystallisation. The nucleation and growth is driven by the existing supersaturation in the solution. When the solubility of a solution is exceeded and it is supersaturated, the molecules start to associate and form aggregates.

The crystal nucleation mechanism can be classified into two types: homogeneous nucleation and heterogeneous nucleation. Homogeneous nucleation generally occurs with much more difficulty in the interior of a uniform substance. From the viewpoint of thermodynamics, the driving force for nucleation is from the difference of the Gibbs free energy between the liquid and solid at a certain temperature T. Gibbs free energy is the maximum amount of non-expansion work which can be extracted from a closed system.

The dependence of Gibbs free energies of the liquid and solid on temperature T is shown in Figure 2.19 (Porter and Easterling, 1992).

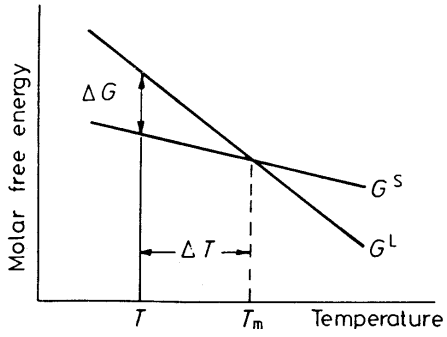

Figure 2.19: The dependence of free energies of liquid and solid on temperature T (T_m is the melting point, G^S is free energy of solid, and G^L is free energy of liquid)

From Figure 2.19 we can see that when $T < T_m$, the free energy of the solid is smaller than that of the liquid, which means the solid state should be more stable than the liquid state. Therefore, materials prefer to stay in solid state during decreasing of the temperature. The difference in free energy between solid and liquid states at temperature T is the driving force for nucleation. For a spherical solid with radius *a*, the driving force for nucleation is (Myerson, 2001):

$$\Delta G = -\frac{4\pi a^3}{3}\Delta G_v + 4\pi a^2 \gamma_{SL} \tag{2.84}$$

where, $\Delta G_V = G_L - G_S$, γ_{SL} is the solid/liquid interfacial tension and *a* is the particle radius. The first term in the equation shows the negative contribution to free energy and the driving force for nucleation, but the second term shows the positive contribution to free energy due to the formation of new solid/liquid interface. Figure 2.20 shows the free energy change associated with homogeneous nucleation of a sphere of radius *a*.

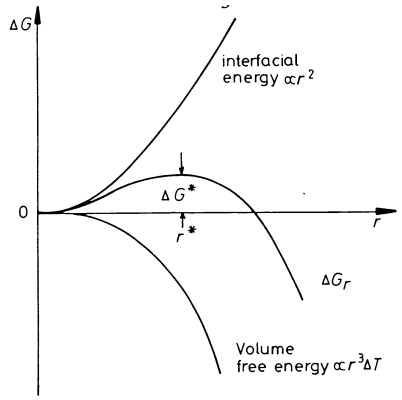

Figure 2.20: The free energy change associated with homogeneous nucleation of a sphere of radius r (Porter and Easterling, 1992).

In the case of heterogeneous nucleation, the nuclei can form at preferential sites such as mould wall, impurities, and catalysts. By so doing, the energy barrier/driving force to nucleation can be substantially reduced. Compared with homogeneous nucleation, heterogeneous nucleation quite frequently and easily occurs in the practical crystallisation process due to its low energy barrier. Figure 2.21 shows the energy barrier/driving force for homogeneous and heterogeneous nucleation.

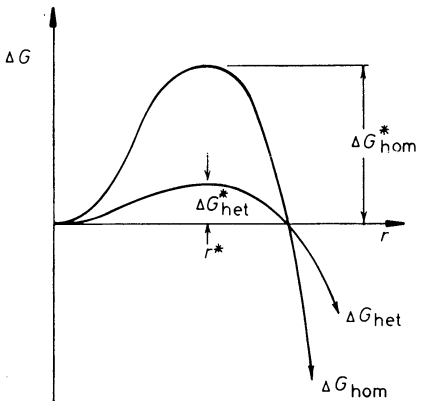

Figure 2.21: The energy barrier/driving force for homogeneous and heterogeneous nucleation (Porter and Easterling, 1992).

The crystal growth is the subsequent growth of the nuclei that succeed in achieving the critical cluster size. After crystal nucleation, the second stage, growth, rapidly ensues. Crystal growth spreads outwards from the nucleating site. In this faster process, the elements which form the motif add to the growing crystal in a prearranged system, the crystal lattice. For crystal growth, the liquid/solid interface plays an important role. The

crystal growth mechanism based on the existence of an adsorbed layer of solute atoms or molecules on a crystal face was first suggested by Volmer (Muller, 2004). This is depicted in Figure 2.22. The growing crystal surface is not simply a flat layer but also made up of steps, kinks, surface-adsorbed growth units, edge vacancies and surface vacancies. The general mechanism of molecule integration on the crystal face is adsorption on the surface followed by its diffusion along the surface to a step or kink for incorporation (Myerson, 2001). This growth model is called two-dimensional theory, which describes a layer-by-layer fashion of crystal growth. The two-dimensional theory provides a manner of crystal growth; however, it is unreasonable for growth at moderate to low supersaturation (Muller, 2004). The spiral growth proposed by Frank provides a way for crystal growth under moderate to low supersaturation. If a screw dislocation has been formed on the crystal surface, the face can grow perpetually up a spiral staircase and develop a growth spiral (Figure 2.23). Here, we will not discuss the crystal growth mechanisms in depth as it is not the main focus of this project.

After the initial period of growth, the volume fraction of the solid phase approaches the equilibrium one, and the particle coarsening starts to occur. The larger particles grow at the expense of the smaller ones in an effort to reduce the surface energy of the system. This process is called Ostwald ripening (Myerson, 2001). Consequently, the volume fraction of the solid phase remains essentially constant but the crystal size becomes non-uniform. Both large crystals and small crystals exist in the solution and form a broad particle size distribution.

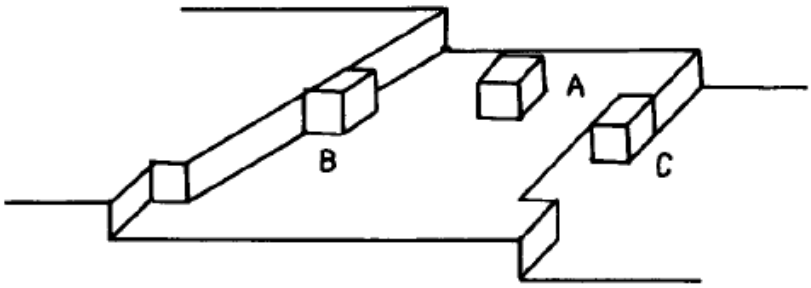

Figure 2.22: Surface structure of growing crystal a) flat surfaces, b) steps, c) kinks (Myerson, 2001)

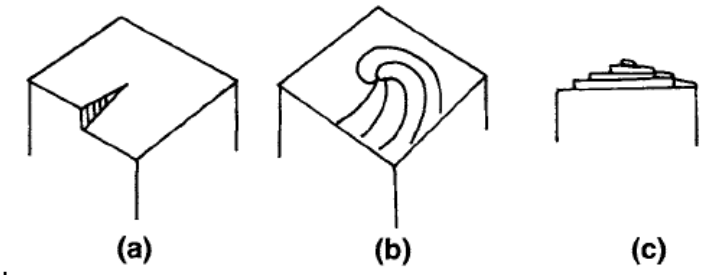

Figure 2.23: Development of a growth spiral starting from a screw dislocation (Muller, 2004).

2.7.2 Crystallisation of L-Glutamic Acid

L-Glutamic acid (LGA) is widely used in the pharmaceutical industry; hence it is a good, representative material in developing an understanding of crystallisation processes and polymorphic transitions. L-Glutamic acid has the formula $C_5H_9NO_4$. The molecule has two carboxylic groups (-COOH) and an amino acid group (-NH_2), which is shown in Figure 2.24.

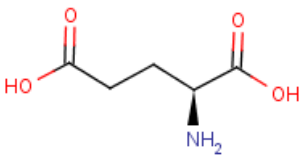

Figure 2.24: The chemical structure of LGA
(http://en.wikipedia.org/wiki/L-Glutamic_Acid)

As amino acids have both the active groups of an amine and a carboxylic acid they can be considered as both acid and base. At a certain pH known as the isoelectric point, the amine group has a positive charge (is protonated) and the acid group has a negative charge (is deprotonated). The whole molecule carries no net electric charge, which is known as a zwitterion. The isoelectric point of LGA is 3.22. As LGA contains two carboxylic groups and one amino acid group, the amino group can be protonated and one or both of the carboxylic groups can be ionized at certain pH values. The dissociation of LGA is determined by its pK_a value, which is known as the acidity constant or the acid-ionization constant. The three pK_a values of LGA and the equilibrium reaction are shown below:

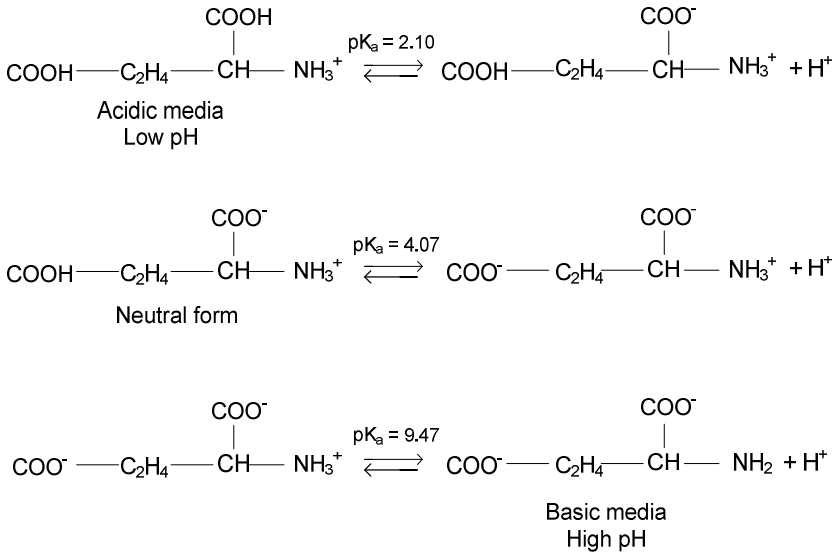

Figure 2.25: Dissociation equations of L-glutamic acid (Neuberger, 1936)

L-glutamic acid (LGA) has two known polymorphs of a metastable α form (prismatic) and a stable β form (needle-like shape) (Figure 2.26). In this work, L-glutamic acid was chosen for study because it is a relatively well-studied compound that has two polymorphs with contrasting morphologies, the rather compact prismatic shape and the elongated needle-like crystals. Generally the α-form is preferred for industrial purposes because its crystal habit is advantageous for handling (Kitamura, 1989). However, it is difficult to obtain pure α-form LGA in the crystallisation process because the α-form is a metastable form which can easily transform to stable β-form.

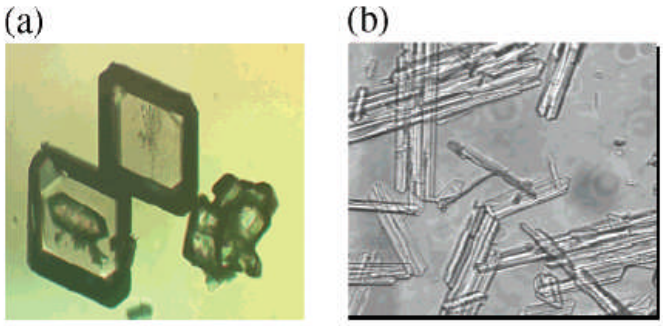

Figure 2.26: The two polymorphic forms of LGA: (a) α-form (prismatic); (b) β-form (needle-like platelets) (Hammond et al., 2004).

Many researchers have studied the crystallisation of L-glutamic acid and its polymorphism. When cooling crystallisation is carried out in a stirred vessel, generally

first the metastable α form is produced and subsequently transformed to the stable β form, according to Ostwald's rule of stages (Kitamura, 1989, Garti and Zour, 1997, Ferrari and Davey, 2004, Ono et al., 2004). Without agitation and for low supersaturation the stable β form can be observed to form directly (Kitamura, 1989). Some researchers also found that the transformation rate of α form to β form increased with crystallisation temperature (Kitamura, 1989, Ono et al., 2004).

Kitamura (Kitamura, 2002) studied the controlling factor of polymorphism in the L-glutamic acid crystallisation process. He found that the supersatuation effect was hardly observed, and the supersaturation ratio hardly had any effect on the crystallisation ratio of LGA polymorphs at each temperature. However, on the other hand, the intensive effect of temperature was observed, i.e. the nucleation rate of α form relatively decreases with an increase in temperature at constant supersaturation ratio.

2.7.3 On-line Monitoring of the Crystallisation Process

High value-added speciality chemicals, such as pharmaceuticals are often manufactured in batch crystallisation processes. The non-linearity of process variables during batch crystallisation requires on-line techniques to measure these variables. The control of crystal-size distribution (CSD) and polymorphs of products in particular are important because these two properties have significant effects on downstream operations such as filtration, drying, transport, and storage. Various types of on-line monitoring techniques for CSD and polymorphs measurement are reviewed.

(1) On-line measurement of crystal size

The current commercially available methods mainly rely on optical techniques, such as laser diffraction, focused beam reflectance measurement (FBRM), multiple light scattering, and digital video microscope. These techniques were already reviewed in section 2.2. Except for the FBRM technique, other optical techniques are inherently unsuitable for examining the dense crystal/solution slurries produced in the batch crystallisation process. The FBRM technique, as reviewed in section 2.2, is not accurate for the non-spherical particles and can only get the distribution of chord length, not the true particle size due to its measurement principle.

There are some other on-line sizing methods for batch crystallisation of L-glutamic acid.

Ultrasonic spectroscopy for particle-size measurement was investigated during the batch crystallisation of L-glutamic acid (Mougin et al., 2002). It can be used for high particle concentration, but the accuracy is limited due to a pump assisted ultrasonic spectrometer cell and the requirement of an extended set of physical properties of LGA crystals and aqueous solution. Jacques *et al*. (Jacques et al., 2005) developed a new tomographic technique, based on synchrotron X-ray diffraction, to study the crystallite size/shape characteristics in a stirred reactor. This technique is expensive and requires levels of high safety to be followed. The current state of on-line sizing methods in the crystallisation process shows an attractive prospect for development of new techniques and encourages further development in both experimental and theoretical aspects.

(2) In-situ monitoring of polymorphs

Different offline analytical techniques have been used to characterize the polymorphs obtained during crystallisation, such as x-ray diffraction (XRD), scanning electron micrographs (SEM), solid-state NMR and thermal analysis (Threlfall, 1995). Up to now, three techniques have been applied for in-situ monitoring of polymorphs during crystallisation: X-ray diffraction (Dharmayat et al., 2008), Raman spectroscopy (Scholl et al., 2006), and particle vision and measurement (PVM) (De Anda et al., 2005). An in-situ X-ray diffraction technique combines a powder X-ray diffraction and a flow-through cell to provide analysis of the polymorphic phase during the crystallisation process. The requirement for instrumentation is a little high, and the measurement might be easily affected due to the sample pumping process. In the LGA crystallisation process, the in-situ Raman spectroscopy technique can be used to detect the α phase and β phase utilizing their characteristic peaks at 1004 $cm^{-1}$and 941 cm^{-1} respectively. The PVM technique can detect the polymorphs of crystals by observing the crystal shapes directly. This method is straightforward, but not suitable for dense suspensions.

All of the current on-line techniques for particle sizing or polymorphs monitoring can only give 2-D images or the measurement of uniform suspension. The 3-D imaging based on tomography techniques for detection of spatial distribution of size or polymorphs might be promising in the future work. In addition, the limitation of optical techniques due to the opaque nature of suspensions in the crystallisation process requires development of a new non-optical based particle characteristic technique.

2.8 Summary

The important and basic foundations concerning colloids, electric double layers and electrokinetics of colloidal particles in an electric field have been reviewed in this chapter. The motivation to review the background is to provide the physical foundations of the behaviour of charged particles in an external electric field. These underpin study of the relationship between the characterisation of particles and their inherent electrokinetic properties as utilized in this research. Electrical impedance spectroscopy (EIS) is a well-known method for characterizing electrokinetic properties of materials and their interfaces. Characterisation of charged particles in colloids (including particle size and concentration) using EIS is a new technique which relies on the presence of an electrical double layer associated with the charged particles and their surface areas. In the presence of a periodic, alternating electric-field, the charged particles in a suspension can show an oscillatory movement or vibration due to the polarisation of the electrical double layer. The measured impedance parameters (the real part, imaginary part, phase angle and relaxation frequency) are related to the particle size, polymorph, particle concentration and the electrochemical and hydrodynamic properties of the dispersed medium. Tomography imaging by utilizing the impedance phase angle has been demonstrated by researchers at the University of Leeds. However, the theoretical analysis was not provided to explain the phase angle image which appears in a banana phantom. The latter part of this chapter reviewed current particle sizing methods including both off-line and on-line methods.

Based on the literature review, the current on-line particle sizing methods are limited and cannot fully satisfy the requirements for industrial processes. Therefore, seeking a new on-line particle sizing method is desirable from both an academic and industrial perspective. It is realized that EIS and EIT techniques share the same basic measurement principles. Therefore, the study of particles in suspensions using electrical impedance spectroscopy could provide the foundation for developing an EIS-based on-line sizing method and it could be further developed into an electrical impedance tomography spectroscopy (EITS) technique and then measure and image particle assemblies with different particle size or other particle characteristics in two or even three spatial dimensions. From the literature review, up to now, the characterisation of particle distributions (particle size and concentration) in colloids by tomography imaging method, utilizing the imaginary impedance or phase angle, has not been studied either in experimental or theoretical aspects. No research has been carried out studying the crystallisation processes using the on-line electrical impedance

spectroscopy method. Therefore, it is valuable to study the relationship between crystal size or morphology and electrical impedance spectra. The study can provide important knowledge for the application of EIS and EIT techniques for particle characterisation in crystallisation processes.

Chapter 3
Experimental Devices and Materials

Summary: This chapter describes the experimental devices and materials used for electrical impedance spectroscopy (EIS) and electrical impedance tomography spectroscopy (EITS) measurements in colloidal suspensions and crystallisation processes. The methodologies for designing of experimental set-up, including vessel, electrode sensor, data acquisition system, cooling and heating system and methodology are provided in detail.

3.1 Introduction

This chapter introduces all devices and materials involved in the experimental work. The methodologies for designing of devices and choosing materials are described in detail. The first part of the experiments is EIS measurement of colloidal particle suspensions. The objective is to understand the relationship between the particle size and electrical dispersion properties (e.g. impedance, complex permittivity and relaxation frequency), as well as the effects of particle concentration and ionic concentration under off-line and static conditions for developing an EIS based particle characterisation method. The major devices in this part include an impedance analyzer, a vessel with a four-electrode sensor and co-axial cables. The materials used in this part are aqueous silica suspensions of different particle sizes and concentrations.

The second part of the experiments is on-line EIS measurement in crystallisation processes. The purpose of the experiments is to apply the electrical impedance spectroscopy method into on-line particle characterisation in crystallisation processes and study the relationship between impedance parameters (impedance real part, imaginary part, phase angle, and relaxation frequency) and the time evolution of crystal size distribution and concentration. The major devices in this part include an impedance analyzer, a 4-electrode sensor, jacket-vessel, cooling and heating circulator, magnetic stirrer, turbidity and temperature sensors, a data acquisition system and focused beam reflectance measurement (FBRM) sensor and device. The material studied in the crystallisation processes is L-glutamic acid.

The third part of experiments is EIT measurement of different materials to investigate the feasibility of obtaining tomography imaging based on data from electrical impedance spectra. The major devices include an impedance analyzer, an 8-electrode sensor, a cylinder shaped vessel, and a Perspex chamber, which served as a housing for colloidal particles and water. The materials used in the experiments include non-conductive polymer, banana and silica suspensions.

3.2 Materials

From the literature review, it is understood that the particle size measurement using EIS basically relies on the electric double layer on the surface of charged particles. Therefore, colloidal particle suspensions with different particle sizes were chosen for these experiments. The commercial silica colloidal suspensions with different particle sizes (at least 5 different sizes) were selected for the experiment since they can be obtained easily. The aqueous silica suspensions of different particle sizes, which were supplied by Fuso Chemical Co., Ltd. Japan, were used in the experiments. However, there is a problem in using commercial samples as supplied because of the presence of unknown ionic species and lack of a precise particle concentration in suspensions. Therefore, the commercial samples need to be pre-treated to remove the unknown ionic species before carrying out experiments. A convenient method for the pre-treatment is described below:

The original samples were firstly de-ionized using mixed bed ion exchange resin (Bio-red), and then diluted to different weight concentrations (10.0 wt%, 5.0 wt%, 1.0 wt%, 0.5 wt%) using de-ionized water without adding additional electrolyte. In order to study the effect of ionic concentration, different amounts of KCl solution were added to the suspensions. The particle size, zeta potential, pH value and conductivity value of pre-treated samples were characterised using the ZetaSizer (nano series, Malvern) instrument, a pH meter (Eutech Instruments pH 300) and conductivity meter (Jenway 470).

The material used to investigate a typical crystallisation process is L-glutamic acid (LGA). From the literature review, it is known that L-glutamic acid has been extensively studied for its crystallisation behaviour and the two polymorphic forms (α form and β form) can be obtained easily by cooling crystallisation. Hence, L-glutamic acid should be ideal for EIS measurement in crystallisation processes.

The materials used in EIT measurement include a non-conductive polymer rod (the handle of a screwdriver), banana and silica suspensions. As a type of biological material, banana may show more significant capacitance properties than the non-conductive polymer rod, which might be reflected in EIT imaging. The silica suspensions used in EIT measurements are from the same batch as those suspensions used in EIS measurement.

3.3 Devices for Colloidal Suspensions

The devices which are used to measure electrical impedance spectroscopy in silica suspensions include an impedance analyzer (Figure 3.1) and a vessel with a four-electrode sensor (Figures 3.2 and 3.3). The purpose of using a four-electrode sensor is to decrease the effects of electrode polarisation at the electrode-electrolyte interface on the measurements. The four-electrode sensor designed includes two plate electrodes and two needle electrodes, which are all made of stainless steel. The two plate electrodes are designed in a square shape with dimensions of 40 mm * 40 mm, and the distance between two electrodes is 30 mm. Two needle electrodes are put in the middle of the two plate electrodes. The diameter of the needle is 0.337 mm and the distance between the two needle electrodes is 10 mm. Comparing the size of the two needle electrodes, the two plate electrodes are much bigger in surface area, therefore it can be assumed that the electric field is parallel and uniform between the two plates and the interference of the two needle electrodes to the field can be ignored.

In EIS measurement, two plate electrodes are used to apply the excitation voltage and two needle electrodes are used to measure the impedance via the voltage drop between the two electrodes and the current through the sample. The whole vessel is made of Perspex (Poly methyl methacrylate) and has an internal dimension of 40 mm (length) * 30 mm (width) * 40 mm (height) in order to fit the 4-electrode sensor. A base was designed to fix the vessel and four BNC male connectors were mounted on the base, which can be used to connect the sensor to the impedance analyzer with coaxial cables. The schematic drawing and photograph of the vessel and four-electrode sensor are shown in Figures 3.2 and 3.3.

Figure 3.1: Photograph of the impedance analyzer (Solartron 1260 Impedance/Gain-Phase Analyzer)

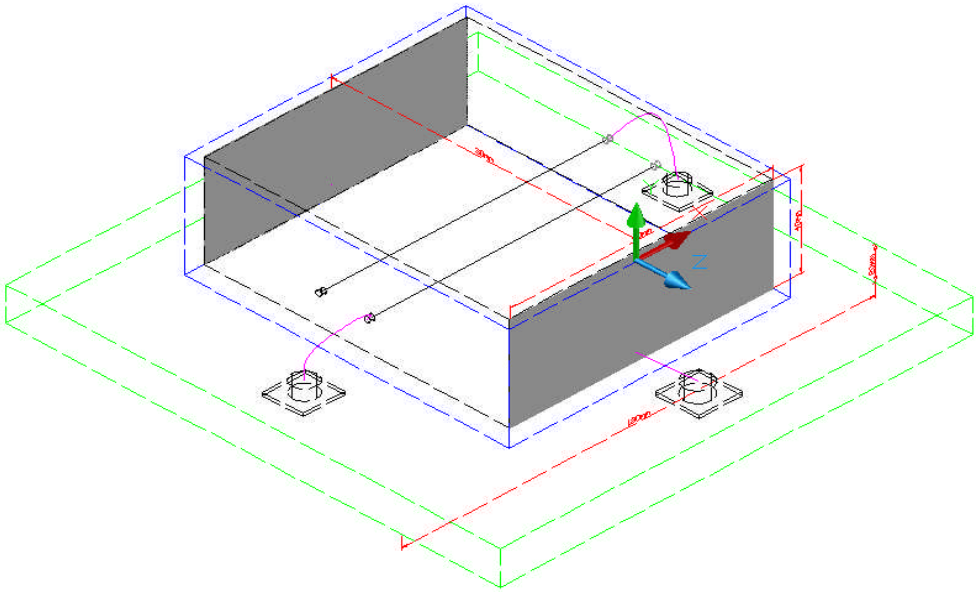

Figure 3.2: Schematic of the four-electrode vessel

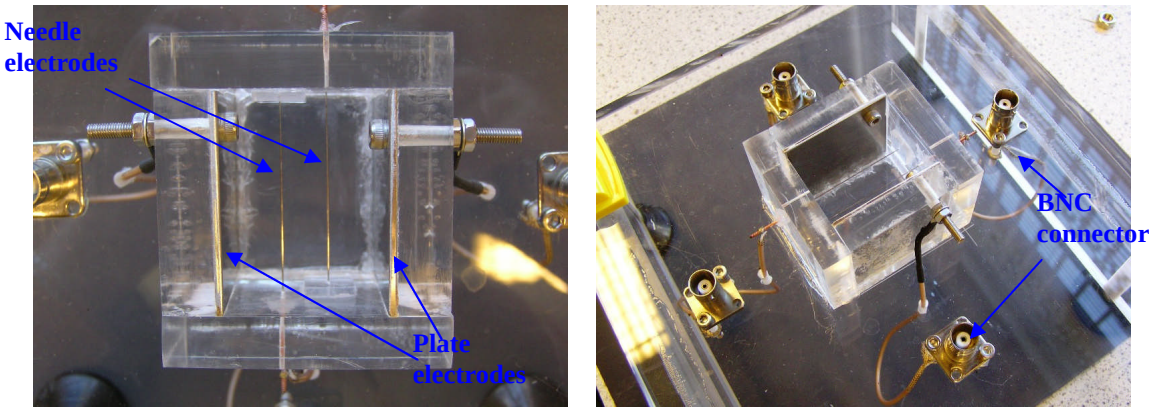

Figure 3.3: Photograph of the vessel with the four-electrode sensor

3.4 Devices for Crystallisaion

The experimental set-up is designed for on-line measurement of electrical impedance spectra during cyrstallisation processes. The devices employed in our experimental set-up include:

(1) Electrical impedance analyzer (Solartron 1260 Impedance/Gain-Phase Analyzer)

(2) Four-electrode sensor

(3) Glass jacketed vessel

(4) Refrigerated and heating circulator

(5) Magnetic stirrer and a magnetic Teflon covered stir bar

(6) Temperature and turbidity sensors

(7) Data acquisition system

(8) Focused beam reflectance measurement (FBRM) device

3.4.1 Electrode sensor

The proposed electrode system in crystallisation experiments is also a four-electrode sensor, but is different from the one used in the experiments for colloidal suspensions. Because the vessel employed in crystallisation is a cylinder with a 3 litre capacity, the electrode sensor was designed to have two big hemispherically shaped electrodes and two needle electrodes, which have to fit into the vessel (Ma.T, 2007). Figure 3.4 shows

a photograph of the electrode sensor employed in the crystallisation experiments.

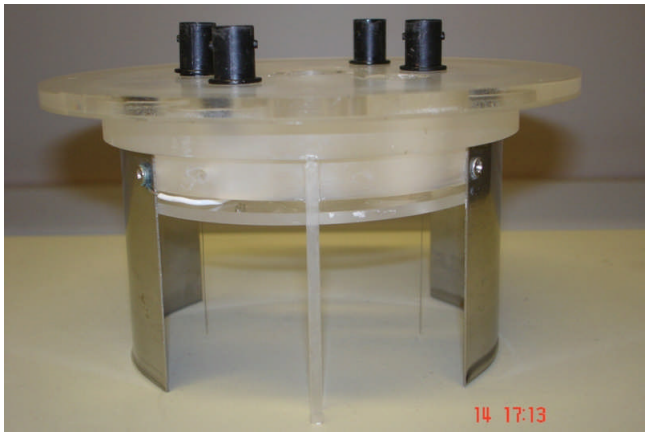

Figure 3.4: Photograph of the four-electrode sensor for crystallisation experiments.

3.4.2 Vessel and circulator

The glass jacketed vessel used in the crystallisation experiments has a cylindrical in shape and has a 3 litre capacity. The mixing of solution in the vessel can be controlled using a magnetic stirrer and the temperature inside the vessel can be controlled by use of a Julabo refrigerated and heating circulator (F32-HE). Figures 3.5 and 3.6 show the photographs of the jacketed vessel, magnetic stirrer and refrigerated and heating circulator, respectively.

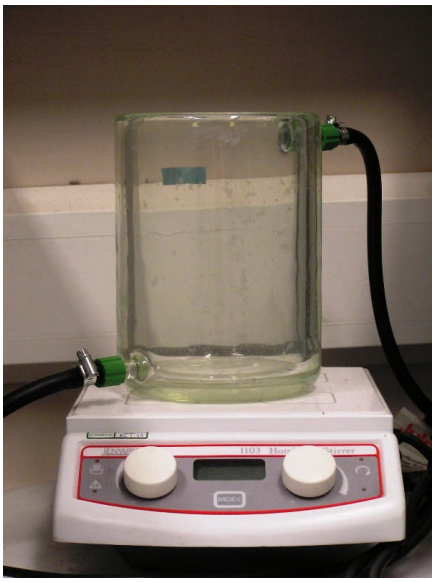

Figure 3.5: Glass jacketed vessel and magnetic stirrer

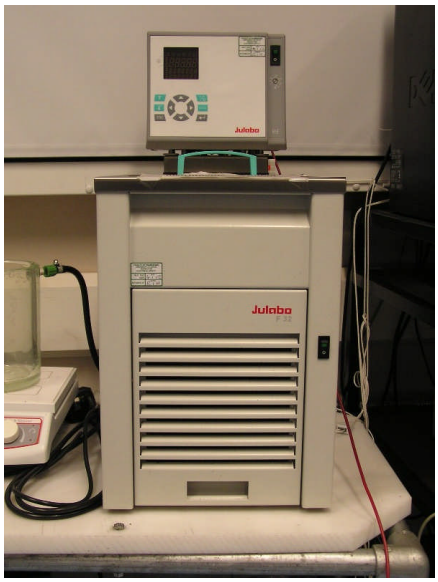

Figure 3.6: Julabo refrigerated and heating circulator (F32-HE)

3.4.3 Temperature and turbidity sensor

1) Temperature sensor

A resistance temperature detector (RTD) is usually used during the crystallisation process due to its excellent stability over long periods of time and accurate readings. The principle of operation is to correlate the resistance of a metal with temperature by a positive temperature coefficient. The hotter the metal becomes, the larger the value of the electrical resistance. A PT100 temperature probe (also called a platinum resistance thermometer) was chosen in the experiments. The PT100 type has a resistance of 100 ohms at 0 ˚C and 138.5 ohms at 100 ˚C. The relationship between temperature and resistance is approximately linear and follows the equation (3.1):

$$R_T = R_0 \times [1 + A \times T + B \times \mathrm{T}^2 + C \times (T - 100) \times T^3] \quad (3.1)$$

where R_T is the resistance at temperature T, R_0 is the resistance at 0 ˚C, and

A = 3.9083e-3

B = -5.775e-7

C = -4.183e-12 (below 0 ˚C), or C = 0 (above 0 ˚C)

Since the crystallisation experiments were always carried out above 0 ˚C, and the

coefficient B is much smaller than A, Equation (3.1) can be reduced to:

$$R_T = 100 + 0.3908T \tag{3.2}$$

2) Turbidity sensor

A turbidity sensor measures suspended solids in water, typically by measuring the amount of light transmitted through the water. The probe used in our experiments was manufactured “in-house”. The components of the turbidity sensor include the probe and transmittance box. The probe is made of two optical fibres, a screw mirror, and a stainless steel shaft. As the working principles, a red laser light is sent along one of the optical fibres via a transmittance box. The light is reflected by the screw mirror, and sent back to the transmittance box by another optical fibre. The transmittance box can be used to convert the light intensity to a voltage recorded by a data acquisition system. Under an ideal situation, in clear water, 100% of the laser light can be sent back to the transmittance box via the screw mirror. In the solution containing solid particles, some of the red light is scattered by the particles, hence the light intensity sent back to the transmittance box is less than 100%. Figure 3.7 shows a photograph of the turbidity probe and transmittance box.

Figure 3.7: Turbidity probe and transmittance box

3.4.4 Data acquisition system

The data acquisition (DAQ) system plays an important role in collecting temperature and turbidity data on-line during the experiment. Usually the DAQ system can collect all of the signals that measure the real physical conditions and convert them into digital numeric signals which can be recorded by the PC. The DAQ system which was used in the experiments consisted of three parts:

(1) Signal conditioning circuit (SCC) models, which can accept the sensors' input signals and transfer the signals to the DAQ device.

(2) A signal conditioning circuit (SCC) carrier usually uses together with SCC models to transfer signals to data acquisition (DAQ) devices.

(3) Data acquisition (DAQ) device, which converts analogue signals to digital signals.

In this research, the SCC system (from National instruments) included a portable, shielded SC-2345 carrier and two SCC modules, which were SCC-RTD01 resistance temperature detector (RTD) and SCC-FT01 feedthrough module.

3.4.4.1 SCC modules

(1) SCC-RTD01 Module

The SCC-RTD01 is a dual-channel module that accepted 2, 3, or 4-wire platinum RTDs. The temperature sensor used in this project was a PT-100 temperature probe, which is suitable for the SCC-RTD01 module. Because the measured data from the DAQ system are voltages, they have to be converted to temperature data by performing the following steps to use the standard equations for the PT100 temperature sensor. Based on Ohm's law, the resistance at temperature T can be calculated from the excitation current and measured voltage. The exciting current of the SCC-RTD01 module is 1 mA, therefore, the temperature reading can be obtained by Equation (3.3):

$$T = \frac{1}{0.3908}(R_T - 100) = \frac{1}{0.3908}(\frac{V}{0.001mA} - 100) \quad (3.3)$$

Since SCC-RTD01 has a fixed gain of 25 for amplifying the signal, the RTD voltage can be calculated by Equation (3.4):

$$V_{RTD} = \frac{V_{ESERIES}}{25} \tag{3.4}$$

where,

V_{RTD} is the SCC-RTD01 model input voltage.

$V_{ESERIES}$ is the reading voltage from DAQ device.

25 is the Gain of the SCC-RTD01 module.

Equation (3.3) can be rearranged as:

$$\mathrm{T} = \frac{1}{0.3908} \times \left(\frac{\frac{V_{ESERIES}}{25}}{0.001mA} - 100\right) \tag{3.5}$$

According to the equation (3.5), the temperature of the solution during the crystallisation process can be calculated from the measured voltage data $V_{ESERIES}$.

(2) SCC-FT01 Feedthrough Module

SCC-FT01 is a feedthrough module can be plugged into a single-stage analogue input SCC socket on the SCC carrier. Since the turbidity data obtained from transmittance are voltages already, they can be transferred to the DAQ device directly, and no conversion should be involved here.

3.4.4.2 Signal conditioning circuit (SCC) carrier

The SCC carrier used in our DAQ system is the SC-2345 carrier from National Instruments. The SC-2345 carrier included 20 SCC sockets, labelled J1 to J20. Sockets J1 to J8 can be used for the single-stage analogue input conditioning. Sockets J9 to J16 were used for either digital I/O modules or dual-stage analogue input conditioning. The power supply for the SC-2345 carrier was SCC-PWR01, 5 VDC from the DAQ device. Figure 3.8 shows the socket layouts on the SC-2345 carrier. At the bottom-right hand side, there is a screw terminal block, which could be used to connect the SC-2345 carrier to the analogue-to-digital converter by wiring.

The SCC-RTD01 is plugged into the J2 socket (an AI socket, ACH 1/9) on the SC-2345 carrier for single-stage input conditioning. The connection between the PT100 probe

and the SCC-RTD01 module is a 4-wire connection, which is shown in the diagram (Figure 3.9).

The SCC-FT01 was plugged into socket J4 (an AI socket, ACH 3/11) on the SC-2345 carrier for single-stage input conditioning. The connection between the turbidity probe and the SCC-FT01 module was a 2-wire connection, with the green wire connecting to pin 6, and the white wire connecting to pin 4.

The bottom view of the SCC modules is the same for both SCC-RTD01 and SCC-FT01 (Figure 3.10). For our DAQ device, only two pins were used and the pin numbers, with associated signals, are listed in Table 3.1.

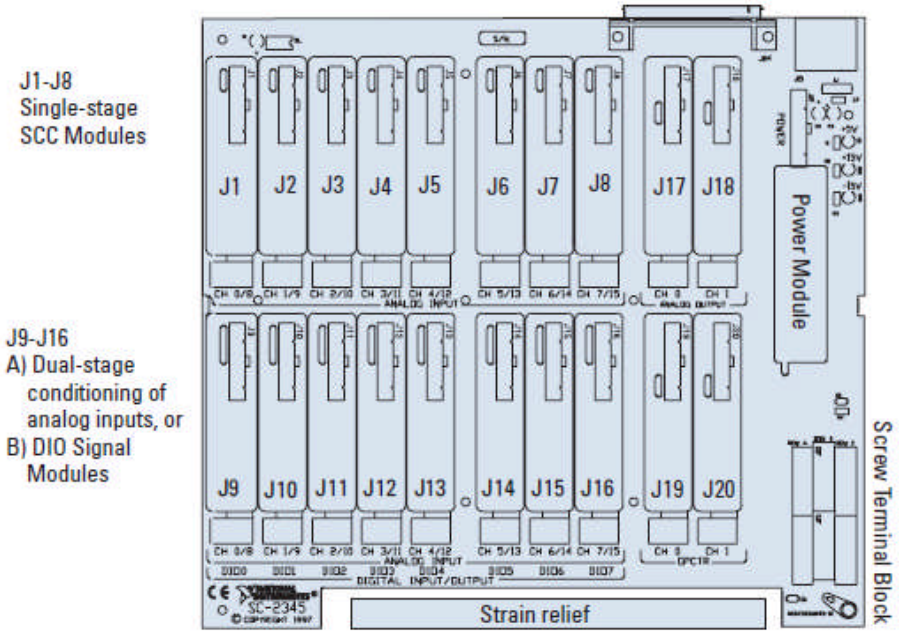

Figure 3.8: Diagram of socket layouts on SC-2345 carrier.

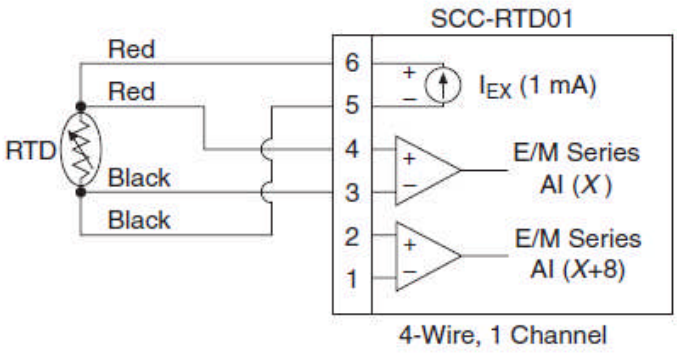

Figure 3.9: SCC-RTD01 single channel wiring diagram (RTD input manual, NI)

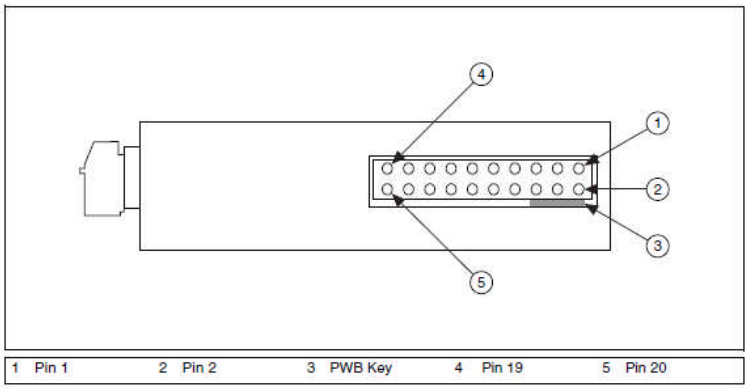

Figure 3.10: Bottom view of the SCC module

Table 3.1: The pin numbers and associated signals on the socket of the SCC-2345 carrier

Pin Number on SCC module	J1-J8: single analog input
1	AI (x) to DAQ device
6	AI GND

3.4.4.3 DAQ device

1. Analogue-to-digital converter

The analogue-to-digital converter selected for the experiments is a PMD-1208LS personal measurement device from Measurement Computing. Figures 3.11 and 3.12 show the pin numbers and associated signals on the PMD-1208LS. The pin numbers 1 and 3 on the PMD-1208LS were connected to pin numbers 1 and 6 on the J2 socket of SC-2345 carrier separately via the screw terminal block to provide the data acquisition for the PT100 temperature sensor. Similarly, the pin numbers 4 and 6 on the PMD-1208LS were connected to pin numbers 1 and 6 on the J4 socket of the SC-2345 carrier separately via the screw terminal block to provide the data acquisition for the turbidity sensor. Pin numbers 9 and 30 on the PMD-1208LS were connected to the GND and + 5V on the power module of the SC-2345 carrier to provide the power supply for the SC-2345 carrier.

Figure 3.11: PMD-1208LS screw terminal pin numbers

Pin	Signal Name	Pin	Signal Name
1	CH0 IN HI	21	Port A0
2	CH0 IN LO	22	Port A1
3	GND	23	Port A2
4	CH1 IN HI	24	Port A3
5	CH1 IN LO	25	Port A4
6	GND	26	Port A5
7	CH2 IN HI	27	Port A6
8	CH2 IN LO	28	Port A7
9	GND	29	GND
10	CH3 IN HI	30	PC+5V
11	CH3 IN LO	31	GND
12	GND	32	Port B0
13	D/A OUT 0	33	Port B1
14	D/A OUT 1	34	Port B2
15	GND	35	Port B3
16	CAL	36	Port B4
17	GND	37	Port B5
18	TRIG_IN	38	Port B6
19	GND	39	Port B7
20	CTR	40	GND

Figure 3.12: The pin numbers and associated signals on the PMD-1208LS

2. Software

The TracerDAQ software is used to record data from the temperature and turbidity sensors. The working window is shown in Figure 3.13. It can be seen that two lanes are included to record the temperature and turbidity data at the same time. The recorded data are shown as voltages and they could be analysed directly for the turbidity results, but have to be converted to temperature data using Equation (3.5) for the temperature results.

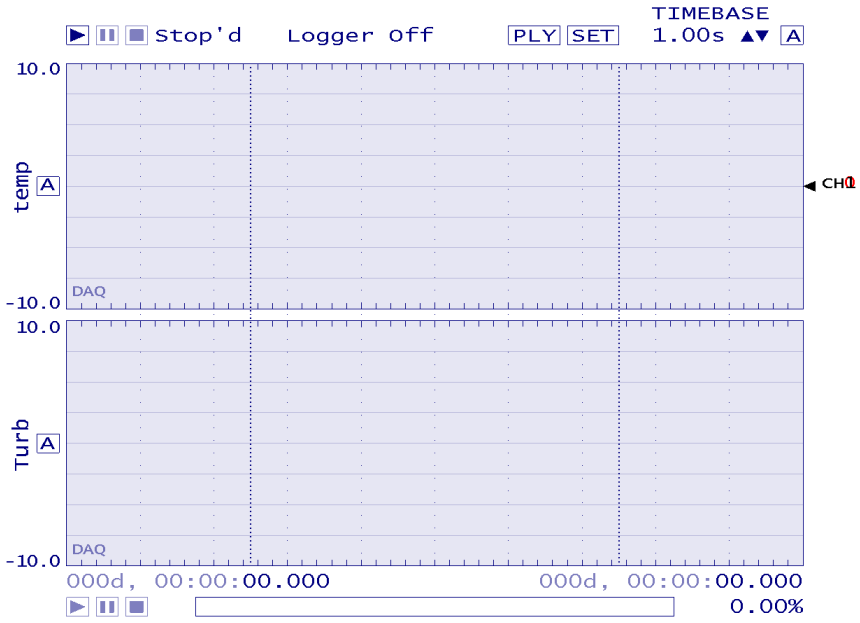

Figure 3.13: Diagram of the TracerDAQ software working window

3.4.5 Focused Beam Reflectance Measurement

A focused beam reflectance measurement (FBRM) device was used to detect changes in both particle size and particle counts on-line by measuring the chord length distribution during crystallisation processes. The advantages and disadvantages of this technique have been reviewed in Chapter 2. Although FBRM is not accurate for non-spherical particles, it provides a reference for on-line changing of particle size in our experiments. Figure 3.14 shows pictures of a Lasentec S400 FBRM probe and controller (Mettler Toledo).

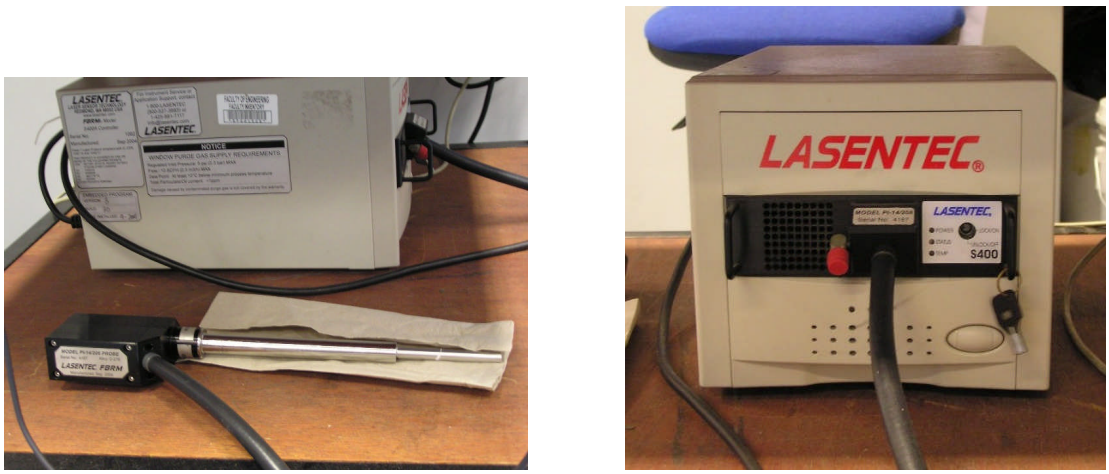

Figure 3.14 Lasentec S400 FBRM probe and controller

3.5 Devices for EIT Measurement

The devices for EIT measurement based on electrical impedance spectroscopy include an impedance analyzer (Figure 3.1), a cylinder shaped vessel with an 8-electrode sensor (Figure 3.15), and Perspex chamber (Figure 3.16). The vessel shown in Figure 3.15 actually has a 16-electrode sensor; however, only 8 electrodes were used in experiments. Because the EIT measurement based on electrical impedance spectroscopy is very time consuming, due to the manual operation, using an 8-electrode sensor can decrease the number of measurements (20 times for an 8-electrode sensor but 104 times for a16-electrode sensor). Therefore, the strategy for the 8-electrode sensor is to use electrode 1, leave its adjacent electrode 2 unused and then use electrode 3, leave electrode 4 unused, and so on (as shown in Figure 3.15). The Perspex chamber is a hollow square with a hole on top for adding the testing silica suspension. The dimensions of the Perspex chamber are a height of 125 mm, length of 20 mm, width of 62 mm and the aperture on top is 10 mm in diameter. Cling film is glued on both sides of the chamber to hold the silica suspension to prevent leakage. In order to measure tomography imaging of silica suspensions (water as reference), one or two chambers were put into the cylindrical vessel and fixed by clamps. Figure 3.17 shows pictures of the experimental set-up of chambers in the cylindrical vessel.

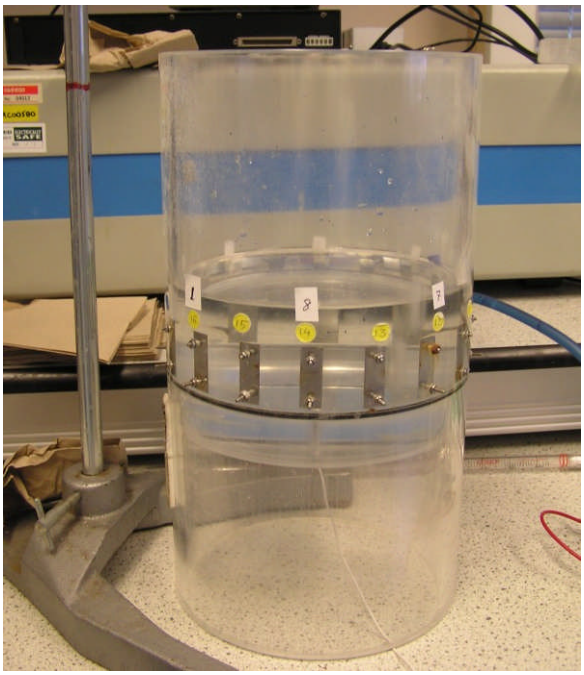

Figure 3.15: Cylindrical vessel with an 8-electrode sensor

Figure 3.16: Perspex chamber as a housing for silica suspension

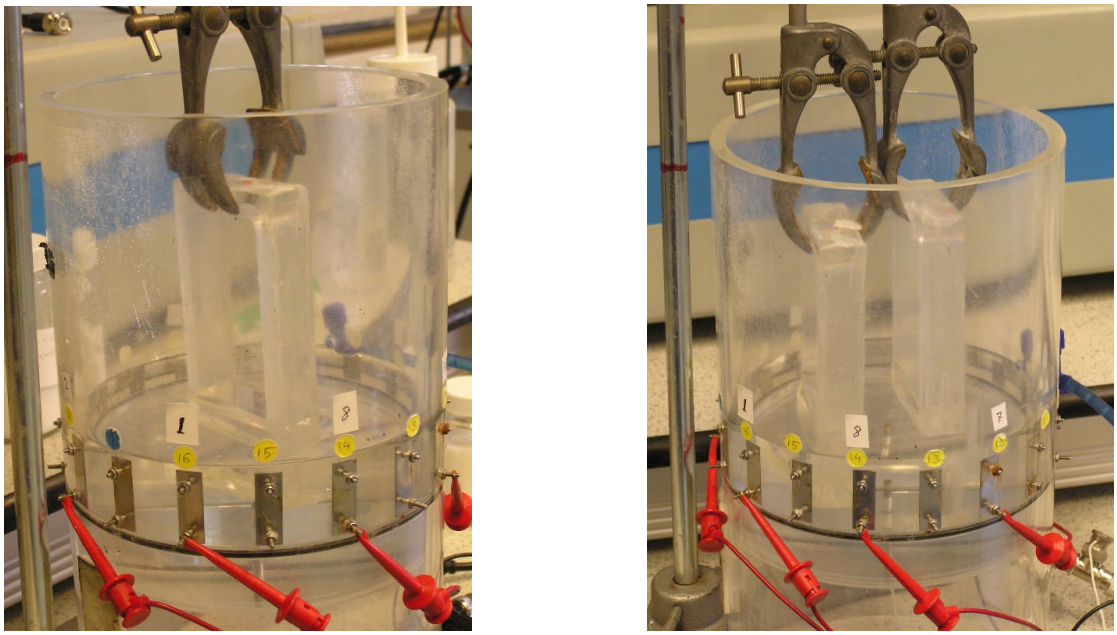

Figure 3.17: One and two chambers in the cylindrical vessel

3.6 Methodology

The EIS measurement in colloidal suspensions was carried out by applying an alternating excitation current (20 mA), which can be achieved by setting the voltage generator to 1 volt (since 50 ohm resistance involved in the circuit of generator output), with a frequency spectrum from 1 Hz to 32 MHz to the two plate-electrodes and taking the EIS response from the two needle electrodes. The electrical impedance spectra were obtained using a Solartron 1260 Impedance/Gain-Phase Analyzer, with “smart”

software.

The EIS measurement in crystallisation processes was carried out by applying an alternating excitation current (20 mA) with a frequency spectrum from 1 Hz to 20 MHz to the two hemispherically shaped electrodes and taking the EIS response from the two needle electrodes. The electrical impedance spectra were recorded using the same software and impedance analyzer as those used for measuring the silica suspension. The crystallisation processes were achieved using a simple cooling method without involving any chemical reaction. The experiments were carried out using a glass jacketed-vessel, Julabo thermostated bath, data acquisition system, impedance analyzer (Solartron 1260), four-electrode sensor and data processing software. The electrical impedance spectra were recorded automatically by PC during the nucleation and growth processes. The time required for testing EIS from 1Hz to 20 MHz is about 2.5 minutes and there was no pause between the 2 loops. The solution temperature was recorded at the start point of every loop. Vessel stirring was provided using a magnetic stirrer rotating at a constant speed of 400 rpm. The temperature and turbidity were measured by using a PT100 temperature sensor and turbidity sensor, respectively. Signals were logged onto a computer via the data acquisition system. FBRM measurement was started at the same time as the EIS measurement and the data were recorded by FBRM control interface software. The whole experimental set-up is depicted in Figure 3.18.

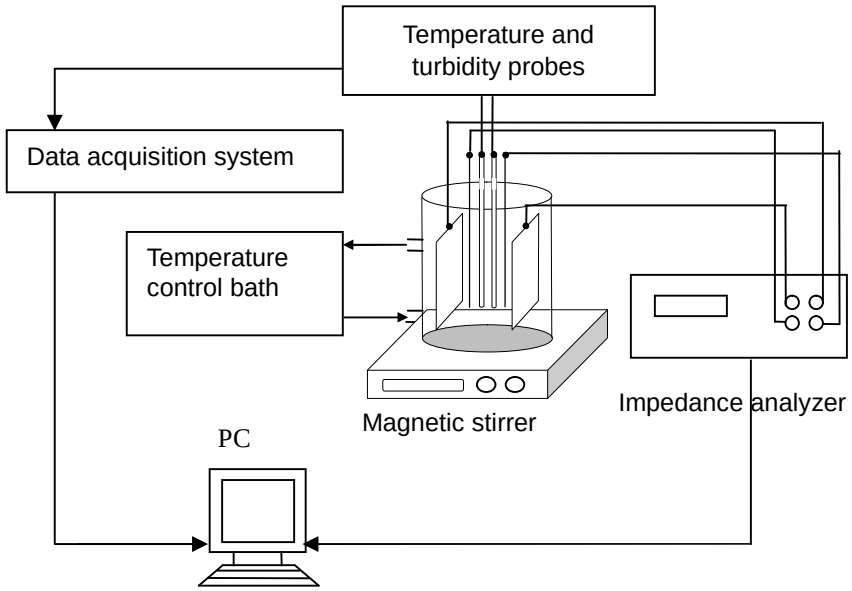

Figure 3.18: Experimental setup for on-line measurement of EIS during crystallisation

The general methodology of electrical impedance tomography (EIT) based on spectroscopic measurement is realised through applying an exciting current onto one pair of electrodes within an 8-electrode sensor and measuring the resulting voltages sequentially on other adjacent electrode pairs. Figure 3.19 shows a schematic of this adjacent data sensing strategy for an 8-electrode system. Current is applied to a pair of electrodes, e.g. electrode 1 and 2 through the impedance analyzer, meanwhile the voltages are measured on other adjacent electrode pairs, e.g. between 3 and 4, 4 and 5, up to 7 and 8. Then the excitation current is moved on to electrodes 2 and 3, and the same sets of voltages are acquired on the rest of the electrodes. The EIS measurement is exactly the same as the measurement in colloidal suspensions (20 mA excitation current with a frequency spectrum from 1 Hz to 32 MHz). After all the electrodes were excited and voltages measured, the total number of electrical impedance spectra, 20, can be completed. Then 20 electrical impedance data at a fixed frequency can be used for imaging reconstruction based on the back projection algorithm. The reconstructed cross-sectional image represents the electrical impedance distribution in a phantom.

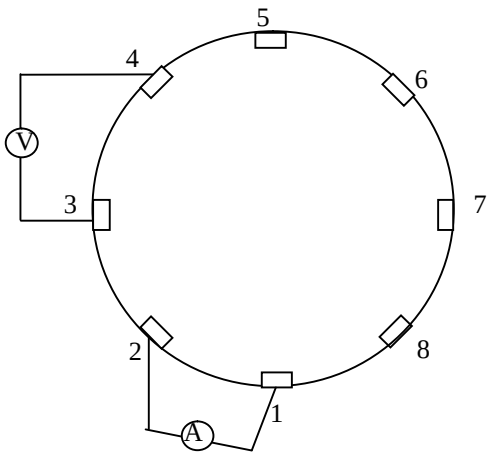

Figure 3.19: The schematic of adjacent data sensing strategy for an 8-electrode sensor

3.7 Summary

All devices and materials used in the experiments are described in this chapter. The four-electrode sensor plays a very important part in electrical impedance spectroscopy measurement, therefore the two four-electrode sensors used in the colloidal suspensions and crystallisation experiments are described individually. The instruments

for on-line monitoring of the crystallisation process are introduced, and the data acquisition system for on-line measurement of temperature and turbidity data is described in detail. Finally, the experimental devices and methodology of electrical impedance tomography spectroscopy (EITS) measurement method is briefly described.

Chapter 4
Development of the Electrical Impedance Spectroscopy Method for Characterising Particles in Silica Suspensions

Summary: The experimental approach and data analysis for developing an electrical impedance spectroscopy method for particle characterisation are reported in this chapter. The physical properties of the silica suspensions, including particle size distribution (PSD), zeta potential and pH values are reported at the beginning of the chapter. The relationship between particle size and dielectric properties (including impedance, phase angle and relaxation frequency) are investigated and analysed. In addition, the effects of particle concentration and ionic concentration on electrical impedance spectra are analysed.

4.1 Introduction

This chapter reports the experimental results from electrical impedance spectroscopy measurements on silica suspensions. The main aim is to develop a method of EIS and verify its capability for characterising colloidal particles in suspensions. Due to the lack of a valid theoretical model for the complex relationship between particle properties and electrical impedance spectroscopy, it was proposed to study the matter using an experimental approach by measuring the electrical impedance spectra of the silica suspensions under an alternating electrical field and analysing the effects of the particle size, particle concentration and ionic concentration, in relation to the electrical impedance spectra and permittivity spectra. The relationship between particle size and dielectric properties, including impedance, phase angle and relaxation frequency, are established based on the experimental results and the theoretical model. The outcome of the study provides a fundamental understanding of the capability of EIS for process application, typically, the crystallisation processes to be specifically addressed in the next chapter.

4.2 Physical properties of silica suspensions

4.2.1 Particle size distribution

Since the original silica samples underwent a pre-treatment process before EIS measurement, the specifications provided by the vender were not reliable. Therefore, the particle size distributions (PSD) of all pre-treated samples were measured for the use in the following analysis. The ZetaSizer Nano Series (Nano-ZS) from Malvern Instruments was used for PSD measurement. The concept of measurement is based on dynamic light scattering, which was introduced in Chapter 2, section 2.5.5. In PSD curves, the x-axis shows the distribution of particle size, while the y-axis shows the relative intensity of the scattered light. The PSD curves typically show up as a large peak at one particular size indicating the primary particle size. In the case of polydispersity, a secondary or third peak may be observed, indicating that the sample contained two or three dominating particle sizes.

The recorded PSD curves are shown below in Figures 4.1-4.4 for the four particle concentrations (10.0 wt%, 5.0 wt%, 1.0 wt%, and 0.5 wt%) and five suspensions with different particle sizes (12, 35, 70, 90, 220 nm), respectively. The sizes shown in brackets were provided by the manufacturer. It can be seen that for the silica suspensions with high concentrations (10.0 wt% and 5.0 wt%), the samples with particles in 12, 35 and 70 nm sizes show more than one peak in PSD profiles, which indicates that aggregation has occurred in these samples. The aggregation might be caused by the dilution and de-ionization treatments in the sample preparation. For the silica suspension with a 70 nm size, only one peak is observed in the size distribution for low concentration samples (1.0 wt% and 0.5 wt%), which may indicate that the effect of aggregation decreases with decreasing the particle concentration. However, for silica suspensions with 12 and 35 nm particle sizes, two peaks are observed in the distribution even at low concentrations (1.0 wt% and 0.5 wt%). The particle sizes measured using the ZetaSizer instrument are different from the sizes of the original samples specified by the manufacturer, which may be due to the pre-treatment process to all of the silica samples. Therefore, a summary of the particle sizes for all of the silica samples studied in this research is shown in Table 4.1. In order to make clear sense of the particle size measured by the ZetaSizer and the size provided by the manufacturer, a notation of X^a is used to show the measured particle size. Here, X shows the particle size measured using the ZetaSizer, and superscript, *a*, shows the particle size provided by the manufacturer.

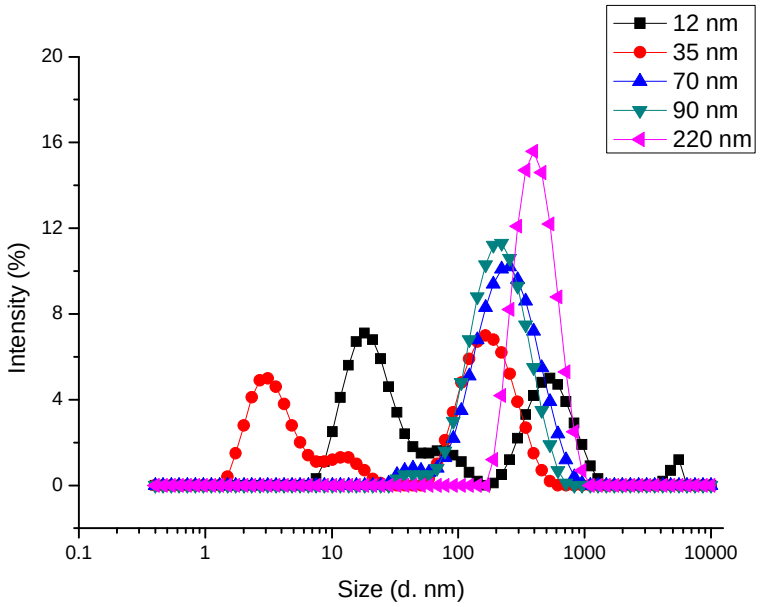

Figure 4.1: Particle size distribution of 10.0 wt % silica suspensions

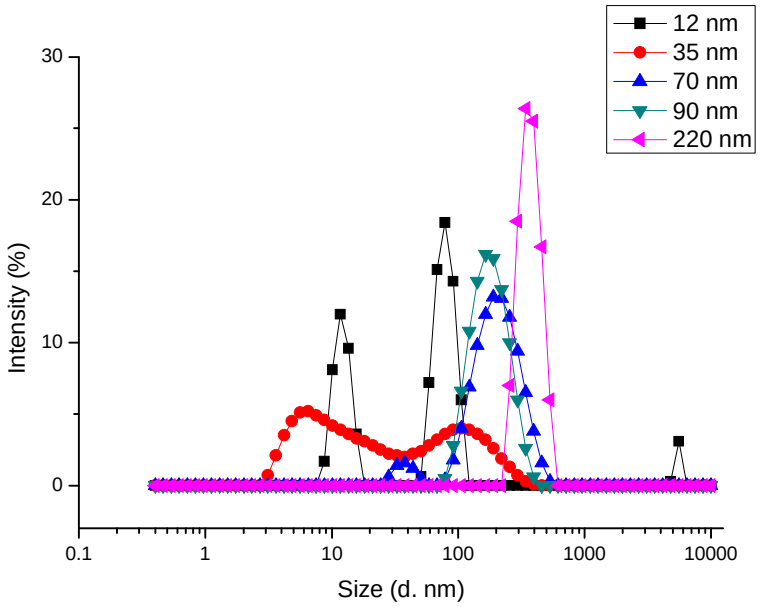

Figure 4.2: Particle size distribution of 5.0 wt % silica suspensions

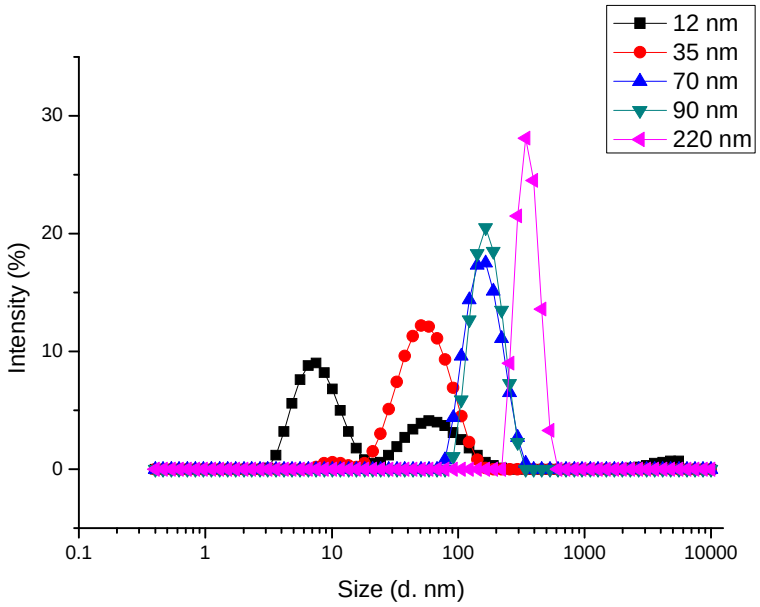

Figure 4.3: Particle size distribution of 1.0 wt % silica suspensions

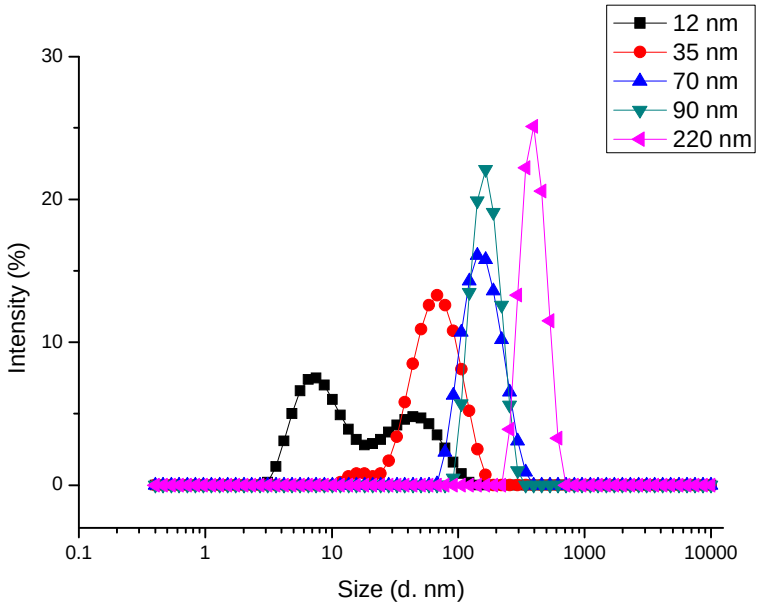

Figure 4.4: Particle size distribution of 0.5 wt % silica suspensions

Table 4.1: Summary of the particle sizes for all silica samples

Concentration (wt %)	Primary particle size from vender (nm)	Primary size measured by ZetaSizer (nm)	Secondary size measured by ZetaSizer (nm)
10.0	12	18.17	458.7
5.0	12	13.54	78.82
1.0	12	7.53	58.77
0.5	12	7.53	43.82
10.0	35	190.1	3.615
5.0	35	91.28	6.50
1.0	35	58.77	10.1
0.5	35	68.06	15.69
10.0	70	270.4	44.48
5.0	70	190.1	37.84
1.0	70	164.2	N.A.
0.5	70	148.1	N.A.
10.0	90	220.2	N.A.
5.0	90	199.7	N.A.
1.0	90	180.9	N.A.
0.5	90	178.7	N.A.
10.0	220	467.9	N.A.
5.0	220	384.6	N.A.
1.0	220	378.0	N.A.
0.5	220	425.8	N.A.

4.2.2 Zeta potential and pH value

Table 4.2 gives a summary of zeta potentials, ξ, at different values of pH for all of the silica suspensions. It can be seen that the zeta potentials show negative values for all of the samples indicating negative charge sited on the silica particles. The main trend of zeta potentials shows that ξ increases with increasing pH value. This result is similar to the one shown in the literature (Gun'ko et al., 2001, Metin et al., 2011). In the literature, it is observed that the iso-electric point of silica suspensions is around pH 2.5 and the absolute value of zeta potential is smaller than 40 mV for solutions with pH < 7. As the silica suspensions were de-ionized before measurement, the pH values of the samples are all smaller than 7 and the absolute values of zeta potential for most of the samples are smaller than 30 mV ($|\xi| < 30$ mV). As mentioned in the operating manual of the ZetaSizer instrument, colloidal suspensions with zeta potentials less positive than 30 mV or less negative than 30 mV are unstable because the zeta potential is not strong enough to repel the particles from each other if there is no other form of stabilization, such as stabilization through the addition of surfactant. Aggregation and sedimentation usually occur in unstable colloidal suspensions. This phenomenon has been demonstrated by the PSD measurement. A very popular method, which is used to increase the absolute of zeta potential, is to adjust the pH value of suspensions to alkaline range by adding alkali (for example, NaOH). However, this might have two undesirable effects for EIS measurement. The first is a possible shifting of the relaxation frequency to the high frequency range, even exceeding the measurement range of the instrumentation due to the increase in ionic concentration. The second is that the particle size effect on EIS might become insignificant in the suspensions with a high background ionic concentration, which is unfavourable for studying the particle size effect. The details about the ionic concentration effect will be discussed in section 4.5. Hence, considering the disadvantages, the pH values of silica samples were not adjusted in the experiments.

Table 4.2: Summary of zeta potentials for the silica samples at 25 ˚C

Concentration (wt %)	Particle size (nm) (from vender)	Zeta potential (mV)	pH value
10.0	12	-5.0	4.58
10.0	35	-17.2	5.75
10.0	70	-16.6	6.61
10.0	90	-24.1	6.84
10.0	220	-1.1	6.60
5.0	12	-10.1	4.73
5.0	35	-22.1	5.96
5.0	70	-30.0	6.43
5.0	90	-29.9	6.65
5.0	220	-38.4	6.72
1.0	12	-18.0	5.03
1.0	35	-20.0	6.14
1.0	70	-29.1	6.34
1.0	90	-25.6	6.32
1.0	220	-35.4	6.30
0.5	12	-21.8	5.59
0.5	35	-24.6	6.01
0.5	70	-19.4	6.15
0.5	90	-46.6	6.25
0.5	220	-32.7	6.45

4.3 Calibration of cell constant

The impedance-related functions include admittance Y, modulus M, and dielectric permittivity ε. The relations between the four impedance-related functions have been shown in Chapter 2, Table 2.1. The calculation of modulus and dielectric permittivity needs a constant C_c, which is called the cell constant. The expression of the cell constant is shown in Equation (4.1):

$$C_c = \frac{l}{A} \tag{4.1}$$

where, *l* is the separation distance between the two needle electrodes, and A is the area of the parallel plate electrodes.

Although the shape and size of the measurement vessel was known, the accurate value of the cell constant should be calculated via a calibration process. The calibration process is usually carried out using a standard electrolyte solution (KCl), which has a known conductivity value. In the experiment, a standard electrolyte solution (KCl), with conductivity of 82 μs/cm at 25 ˚C, was used to calibrate the four-electrode system and obtain the cell constant. The calculation is described as follows:

The expressions of Impedance Z^* and admittance Y^* have been shown in the Chapter 2, Equations (2.56) and (2.62).

The complex conductivity is related to admittance and impedance by:

$$K^* = C_c \cdot Y^* = C_c \cdot \frac{1}{Z^*} \tag{4.2}$$

where, C_c is the cell constant, the unit of Z^* is ohm, the unit of Y^* is S (ohm^{-1}), and the unit of K^* is S/m.

The cell constant can be calculated by measuring the impedance of the standard KCl solution (here, the standard KCl has conductivity of 82 μs/cm):

$$C_c = \frac{K^*(\omega)}{\mathrm{Y}^*(\omega)} = Z^*(\omega) * 0.0082 S/m \tag{4.3}$$

For the calibration, the conductivity should be measured under a static state, therefore, the calibration was carried out within the low frequency range (<10 Hz). The cell constant obtained by the calibration process is 8.66 m^{-1}.

4.4 Particle size effect

In this section, the particle-size effect on the electrical impedance spectra and permittivity spectra is investigated in the silica suspensions with different particle sizes and particle concentrations. The particle concentrations which were studied include 10.0 wt%, 5.0 wt%, 1.0 wt%, and 0.5 wt% and five different particle sizes: 12 nm, 35

nm, 70 nm, 90 nm, 220 nm (size from the manufacturer), were used in the experiments. In order to minimize the influence from ionic species, all of the samples were pre-treated to remove the ions in the solution before the measurement.

4.4.1 Impedance spectra

The electrical impedance spectra for the silica suspensions with different concentrations (10.0 wt%, 5.0 wt%, 1.0 wt%, 0.5 wt%) and various values of particle size (12 nm, 35 nm, 70 nm, 90 nm, 220 nm) are shown in Figures 4.5-4.8. Five arcs can be observed in Figures 4.5 (a) - 4.8(a), which shows the dielectric response of the suspensions under the external electric field. If the arc is assumed to be a regular semicircle, then a parallel RC equivalent circuit (R is resistance and C is capacitance) can be used as a static model to simulate the EIS results. The analysis is qualitative since the assumption of a semicircle is idealised.

The impedance of parallel RC circuit can be expressed by:

$$Z = \frac{1}{Y} = \frac{R}{1 + j\omega RC} = \frac{R}{1 + (\omega RC)^2} - j\frac{\omega R^2 C}{1 + (\omega RC)^2} \tag{4.4}$$

The impedance real part (Z'), imaginary part (Z") and phase angle (θ) can be expressed by:

$$Z'(\omega) = \frac{R}{1 + (\omega RC)^2} \tag{4.5}$$

$$Z''(\omega) = -\frac{\omega R^2 C}{1 + (\omega RC)^2} \tag{4.6}$$

$$\tan\theta = \frac{Z''(\omega)}{Z'(\omega)} = -\omega RC \tag{4.7}$$

where, R is the resistance, C is the capacitance, ω is the frequency, Z' is the impedance real part, Z'' is the impedance imaginary part, and θ is the phase angle.

The impedance imaginary part is a function of frequency. If the derivative of Z'' is equal to zero, a minimum of Z'' at a certain frequency can be obtained:

$$\frac{dZ''}{d\omega} = \frac{R^2C[1-(\omega RC)^2]}{[1+(\omega RC)^2]^2} = 0 \tag{4.8}$$

The frequency where $Z''(\omega)$ reaches a minimum is called the relaxation frequency and has the expression:

$$\omega_{\text{relaxation}} = \frac{1}{RC} \tag{4.9}$$

The peak position on the plot of impedance imaginary part shows the relaxation frequency.

Figures 4.5 (b) - 4.8 (b) show that the impedance real parts at frequencies lower than 10 kHz increase with increasing particle size. However, at the higher frequency (for example, 1 MHz), the impedance real parts do not show a significant difference from the samples with different particle size.

From Figures 4.5 (c)-4.8 (c), it can be seen that the relaxation begins at the frequency range of 10 kHz-1MHz since several peaks can be observed in the plot of impedance imaginary parts, which is the characteristic of relaxation as explained by Equation (4.9). The relaxation frequencies of silica suspensions with different particle size, obtained from the peak positions, shift to lower frequency range with increasing particle size. By comparing the impedance imaginary-part plots in Figures 4.5 (c)-4.8 (c), it can be seen that in the low concentration silica suspensions (1.0 wt% and 0.5 wt%), the change of relaxation frequency becomes insignificant and irregular with increasing particle size. The possible reason is that with decreasing particle concentration, the electrical signal caused by the polarisation of the double layer under the external excitation is getting weak. Therefore, it becomes more difficult to distinguish the change in signal caused by changing of the particle size from the combination of exciting electrical signal and the detecting signal. As an important parameter, the relaxation frequency will be studied further in the permittivity curves in section 4.3.2.

Figures 4.5 (d)-4.8 (d) show the phase angles for a fixed particle concentration (for example, 10.0 wt%), but with different particle size as a function of frequency. The particle size effect on the phase angle can be observed clearly in the suspensions with high particle concentration (10.0 wt% and 5.0 wt%). However, in the silica suspensions with low particle concentrations (1.0 wt% and 0.5 wt%), the change in phase angle as a function of particle size becomes insignificant, e.g. the variation is much smaller than in

the silica suspensions with high concentrations. Because the measured impedance signal is the total signal from all of the particles, adding the exciting electrical signal, the lower the particle concentration the smaller the electrical signal caused by the polarisation of double layers around the particles in the suspensions. It is not clear whether the origin of the small variation in phase angle is from the properties of charged particles or the intrinsic precision of the measurement as it is difficult to detect and separate the small signal using the hardware currently available. Since the physical meaning of phase angle cannot be directly related to the particle size, the tangent function of the phase angle tan(θ), is used. The detailed analysis based on the relative changes in tan(θ) is shown in the next section 4.3.2.

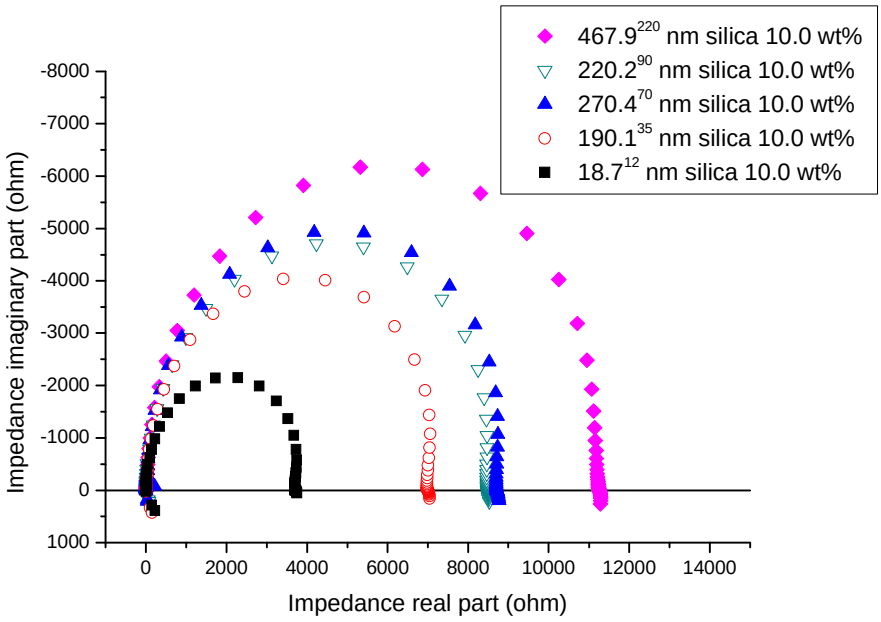

(a)

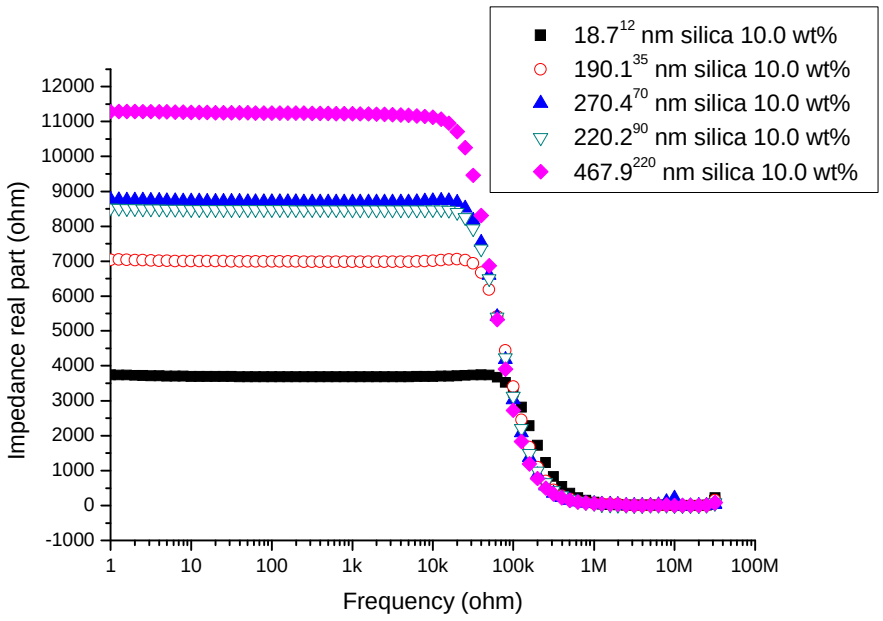
18.7[12] nm silica 10.0 wt%
190.1[35] nm silica 10.0 wt%
270.4[70] nm silica 10.0 wt%
220.2[90] nm silica 10.0 wt%
467.9[220] nm silica 10.0 wt%
Impedance real part (ohm)
12000
11000
10000
9000
8000
7000
6000
5000
4000
3000
2000
1000
0
-1000
1
10
100
1k
10k
100k
1M
10M
100M
Frequency (ohm)

(b)

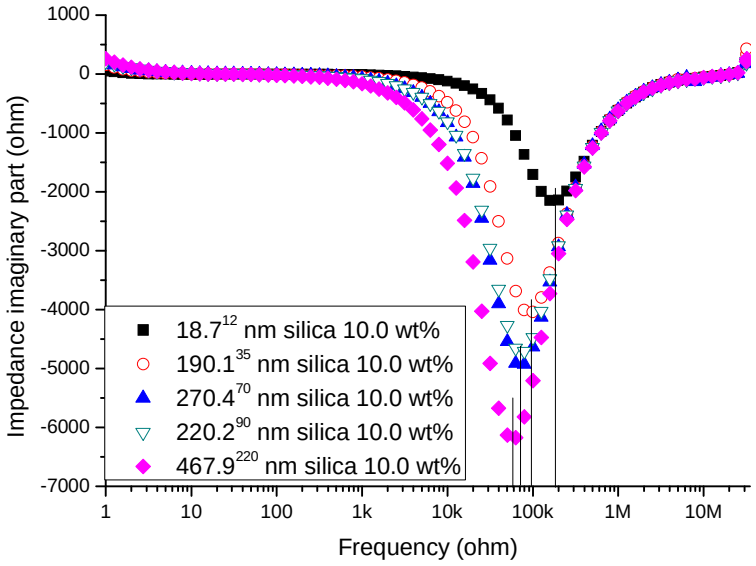
Impedance imaginary part (ohm)
1000
0
-1000
-2000
-3000
-4000
-5000
-6000
-7000
18.7[12] nm silica 10.0 wt%
190.1[35] nm silica 10.0 wt%
270.4[70] nm silica 10.0 wt%
220.2[90] nm silica 10.0 wt%
467.9[220] nm silica 10.0 wt%
1
10
100
1k
10k
100k
1M
10M
Frequency (ohm)

(c)

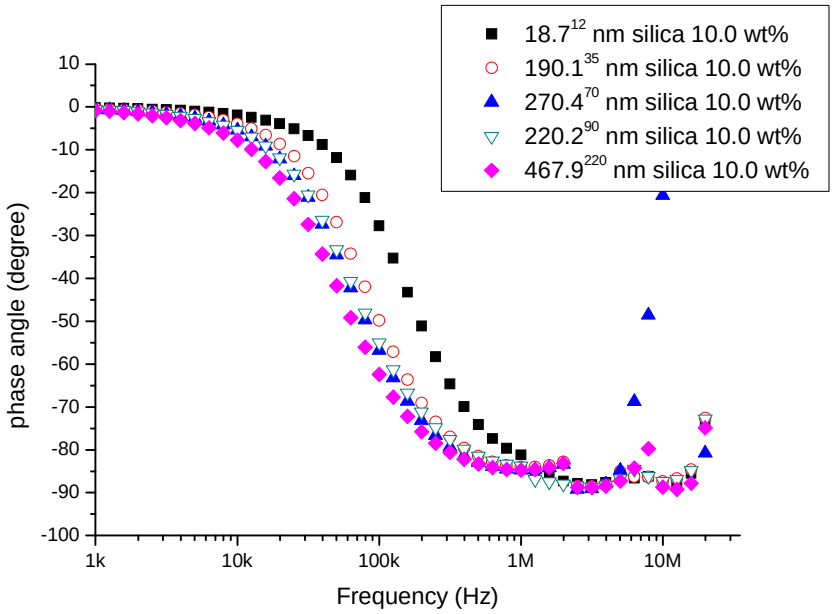

(d)

Figure 4.5: Impedance spectra for silica suspensions (10.0 wt %) with different particle size (18.7[12] nm, 190.1[35] nm, 270.4[70] nm, 220.2[90] nm, 467.9[220] nm); (a) cole-cole plot of impedance; (b) impedance real part vs. frequency; (c) impedance imaginary part vs. frequency; (d) phase angle vs. frequency plots.

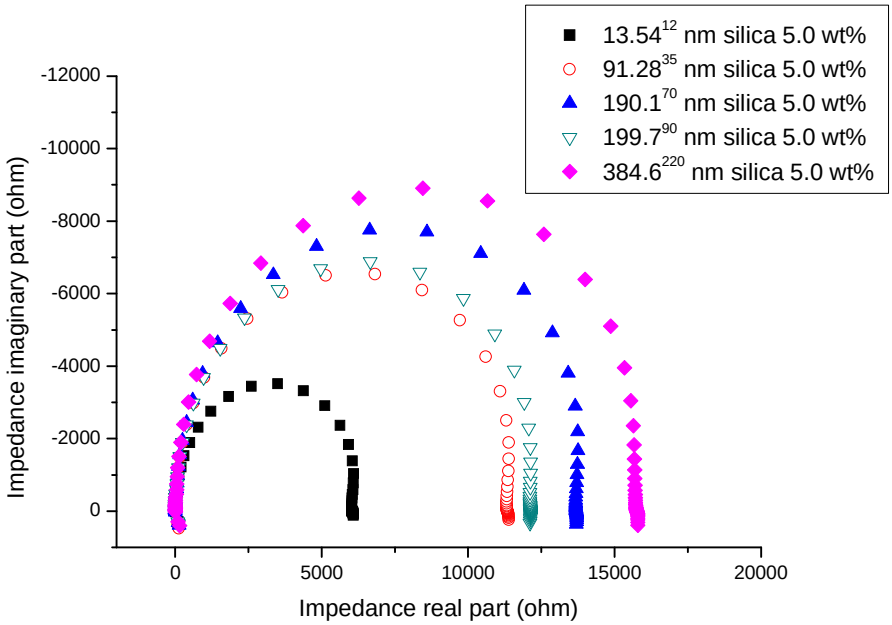

(a)

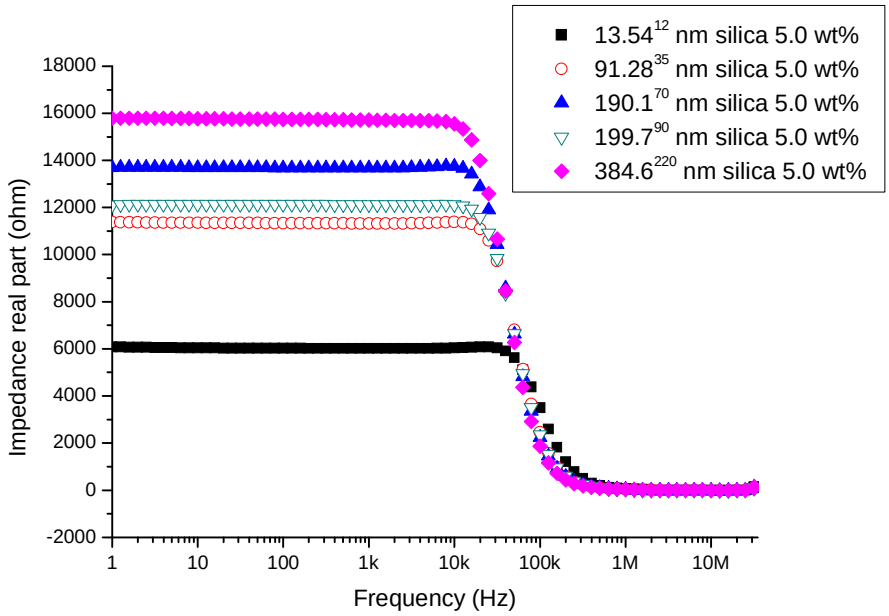
13.54[12] nm silica 5.0 wt%
91.28[35] nm silica 5.0 wt%
190.1[70] nm silica 5.0 wt%
199.7[90] nm silica 5.0 wt%
384.6[220] nm silica 5.0 wt%
Impedance real part (ohm)
18000
16000
14000
12000
10000
8000
6000
4000
2000
0
-2000
1
10
100
1k
10k
100k
1M
10M
Frequency (Hz)

(b)

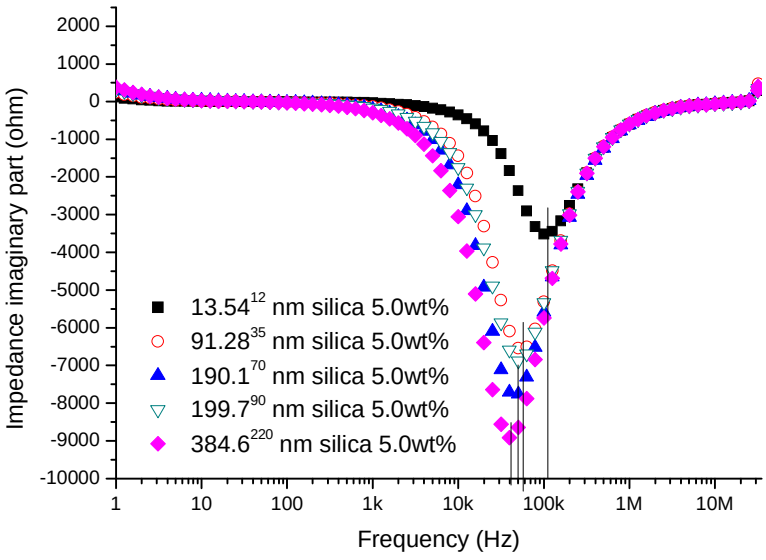
Impedance imaginary part (ohm)
2000
1000
0
-1000
-2000
-3000
-4000
-5000
-6000
-7000
-8000
-9000
-10000
13.54[12] nm silica 5.0wt%
91.28[35] nm silica 5.0wt%
190.1[70] nm silica 5.0wt%
199.7[90] nm silica 5.0wt%
384.6[220] nm silica 5.0wt%
1
10
100
1k
10k
100k
1M
10M
Frequency (Hz)

(c)

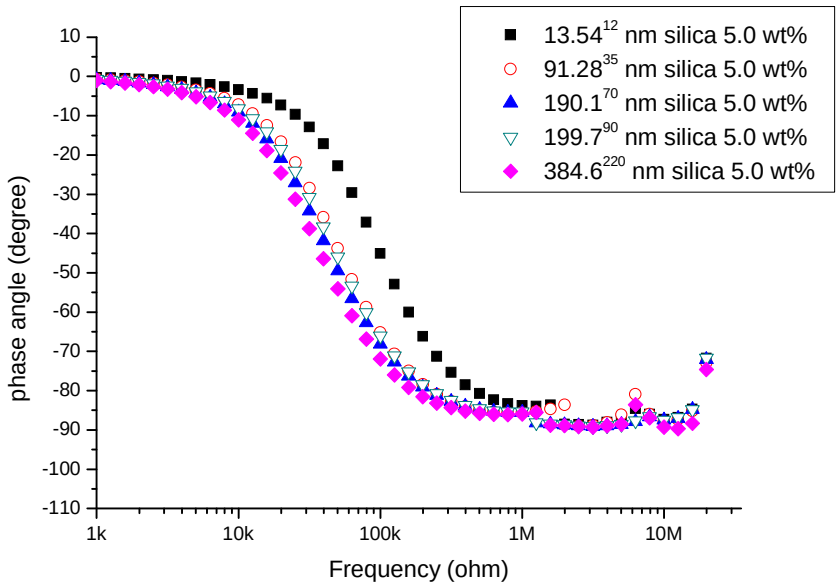

(d)

Figure 4.6: Impedance spectra for silica suspensions (5.0 wt %) of different particle size (13.54[12] nm, 91.28[35] nm, 190.1[70] nm, 199.7[90] nm, 384.6[220] nm); (a) Cole-Cole plot of impedance; (b) impedance real part vs. frequency; (c) impedance imaginary part vs. frequency; (d) phase angle vs. frequency plots

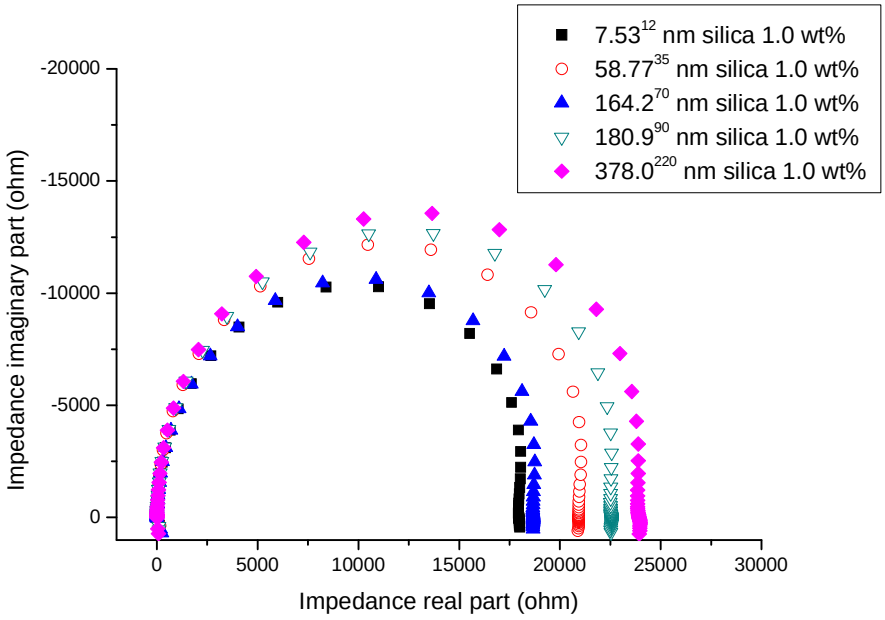

(a)

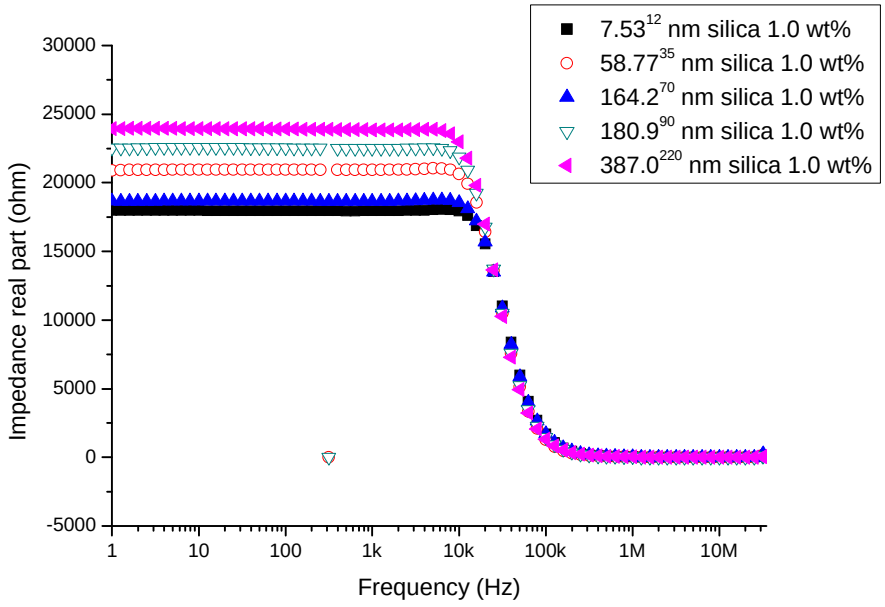
7.53[12] nm silica 1.0 wt%
58.77[35] nm silica 1.0 wt%
164.2[70] nm silica 1.0 wt%
180.9[90] nm silica 1.0 wt%
387.0[220] nm silica 1.0 wt%
Impedance real part (ohm)
30000
25000
20000
15000
10000
5000
0
-5000
1
10
100
1k
10k
100k
1M
10M
Frequency (Hz)

(b)

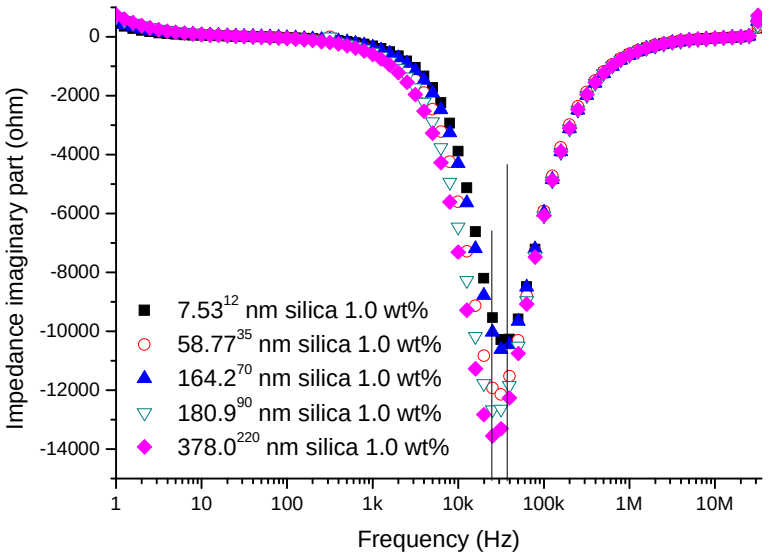
Impedance imaginary part (ohm)
0
-2000
-4000
-6000
-8000
-10000
-12000
-14000
7.53[12] nm silica 1.0 wt%
58.77[35] nm silica 1.0 wt%
164.2[70] nm silica 1.0 wt%
180.9[90] nm silica 1.0 wt%
378.0[220] nm silica 1.0 wt%
1
10
100
1k
10k
100k
1M
10M
Frequency (Hz)

(c)

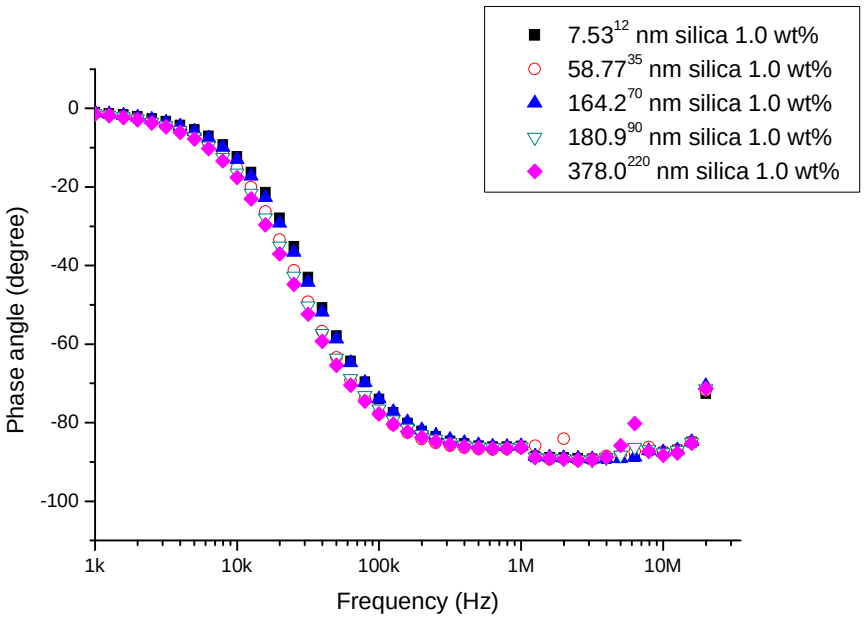

(d)

Figure 4.7: Impedance spectra for silica suspensions (1.0 wt %) of different particle size (7.53[12] nm, 58.77[35] nm, 164.2[70] nm, 180.9[90] nm, 378.0[220] nm); (a) Cole-Cole plot of impedance; (b) impedance real part vs. frequency; (c) impedance imaginary part vs. frequency; (d) phase angle vs. frequency plots

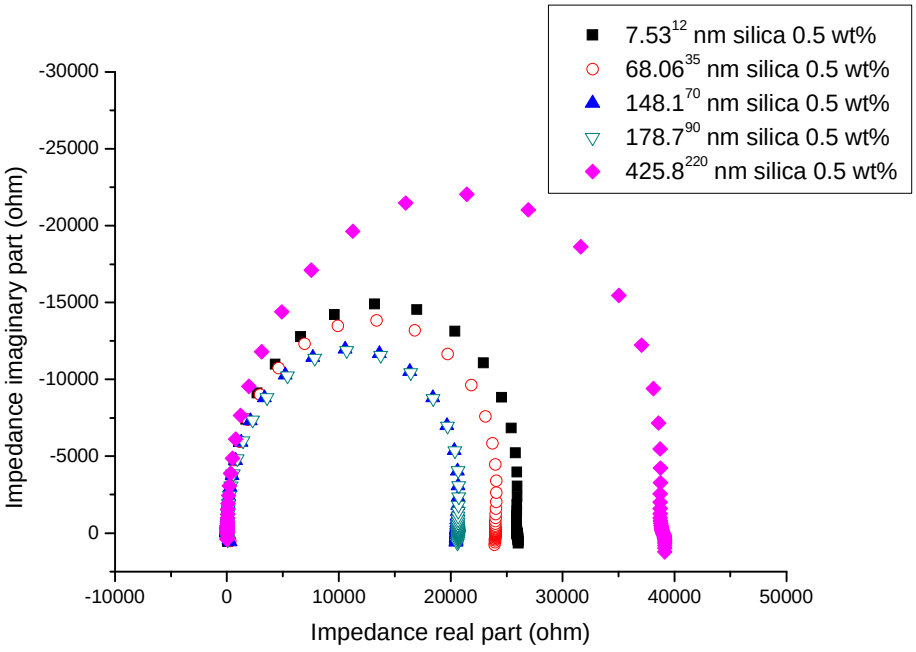

(a)

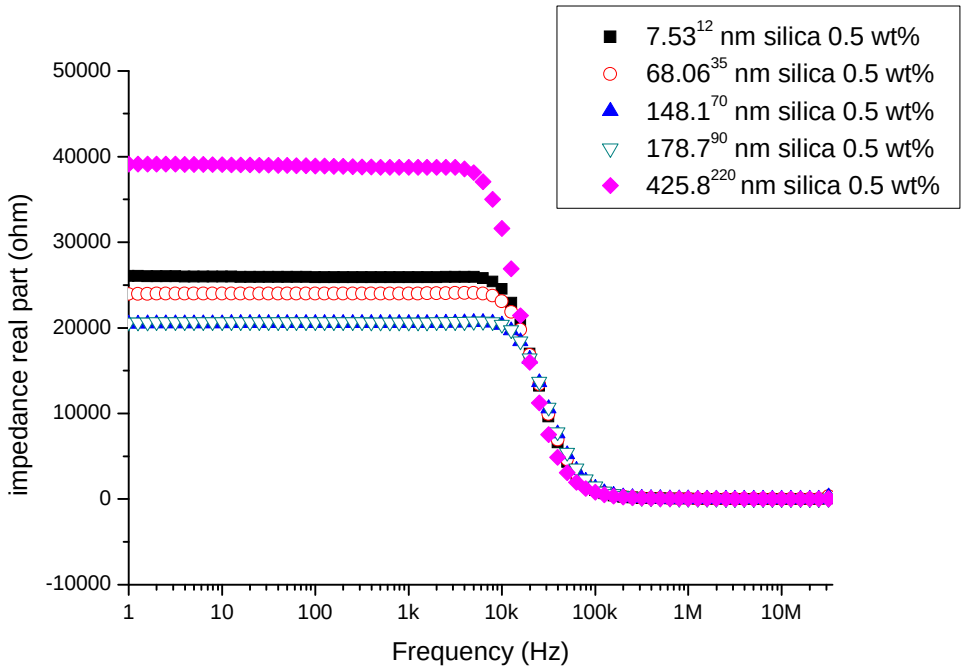
7.53[12] nm silica 0.5 wt%
68.06[35] nm silica 0.5 wt%
148.1[70] nm silica 0.5 wt%
178.7[90] nm silica 0.5 wt%
425.8[220] nm silica 0.5 wt%
impedance real part (ohm)
50000
40000
30000
20000
10000
0
-10000
1
10
100
1k
10k
100k
1M
10M
Frequency (Hz)

(b)

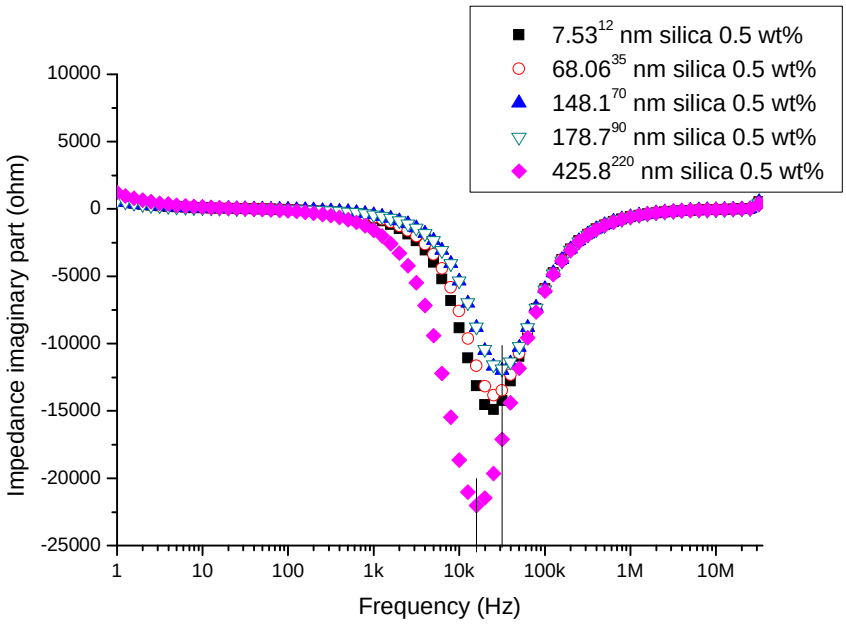
7.53[12] nm silica 0.5 wt%
68.06[35] nm silica 0.5 wt%
148.1[70] nm silica 0.5 wt%
178.7[90] nm silica 0.5 wt%
425.8[220] nm silica 0.5 wt%
Impedance imaginary part (ohm)
10000
5000
0
-5000
-10000
-15000
-20000
-25000
1
10
100
1k
10k
100k
1M
10M
Frequency (Hz)

(c)

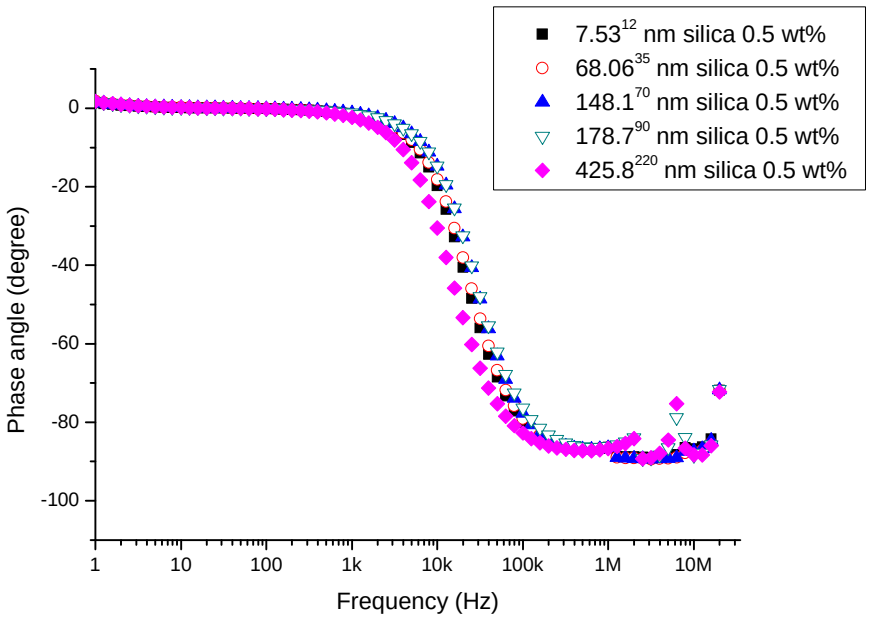

(d)

Figure 4.8: Impedance spectra for silica suspensions (0.5 wt %) of different particle size (7.53[12] nm, 68.06[35] nm, 148.1[70] nm, 178.7[90] nm, 425.8[220] nm); (a) Cole-Cole plot of impedance; (b) impedance real part vs. frequency; (c) impedance imaginary part vs. frequency; (d) phase angle vs. frequency plots

4.4.2 Relative Changes of Phase angle

The study of relative changes in tan(θ) uses the same principle as for electrical impedance tomography (EIT) measurement, which has been introduced in Chapter 2, section 2.4.2. To calculate the relative changes in tan(θ), a reference should be appointed. In this study, the de-ionized water was chosen as the reference, because the ionic concentrations in the silica suspensions were very low (after pre-treatment using ion exchange resin). The effect from ionic concentration could be decreased if both the reference and measurement samples have low ionic concentrations.

As discussed in section 4.3.1, the impedance spectra can be simulated by an equivalent circuit shown in Figure 4.9.

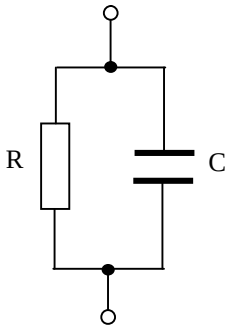

Figure 4.9: Parallel RC equivalent circuit (R is resistance and C is capacitance)

Here, C and R can be calculated by fitting the experimental results into Equations (4.5) and (4.6).

The relative changes in tan(θ) can be expressed by:

$$\frac{\Delta \tan\theta_{j,j+1}}{\tan\theta_j} = \frac{\tan\theta_{j+1} - \tan\theta_j}{\tan\theta_j} = \frac{-\omega R_{j+1} C_{j+1} + \omega R_j C_j}{\omega R_j C_j} = \frac{R_j C_j - R_{j+1} C_{j+1}}{R_j C_j} \tag{4.10}$$

where, de-ionized water is treated as reference j, particle suspensions are treated as measured system j+1.

Let λ denote the relative changes in tan(θ),

$$\lambda = \frac{\Delta \tan\theta_{j,j+1}}{\tan\theta_j} \tag{4.11}$$

From Equation (4.10), it can be found that the relative changes in tan(θ) are frequency independent, which could simplify the calculation in the following analysis. However, this case only occurs when the parallel RC equivalent circuit model is used. In some other cases, for example, the EIT phantom, the parallel RC equivalent circuit model might not be suitable and therefore, λ is a function of frequency. The relative changes in tan(θ) in EIT measurements will be discussed further in Chapter 6.

The next step is to find out the relationship between λ and the particle size. In a colloidal suspension, the presence of an electric field $\vec{E}$ causes the charges in the double layer to be slightly polarised, inducing a local electric dipole moment, which can be expressed by the electrical polarisation density:

$$\vec{P}_e = \frac{\sum \vec{d}}{V} = \frac{N\vec{d}}{V} = \frac{\frac{\phi V}{\frac{4}{3}\pi a^3}\vec{d}}{V} = \frac{\phi}{\frac{4}{3}\pi a^3}\vec{d} \tag{4.12}$$

where, $\vec{P}_e$ is the electric polarisation density, $\vec{d}$ is the electric dipole moment, V is the volume of suspension, Φ is the particle volume fraction and *a* is the particle radius.

The electric displacement for a field-dependent polarisation phenomena is defined by:

$$\vec{D} = \varepsilon\vec{E} = \varepsilon_0\varepsilon_r\vec{E} = \varepsilon_0(1+\chi_e)\vec{E} = \varepsilon_0\vec{E} + \varepsilon_0\chi_e\vec{E} = \varepsilon_0\vec{E} + \vec{P}_e \tag{4.13}$$

where, $\vec{D}$ is the electric displacement, $\vec{E}$ is the electric field, ε is the permittivity of the material, ε_0 is the permittivity of free space, χ_e is the electric susceptibility, $\varepsilon_r = 1 + \chi_e$ is the relative permittivity, $\vec{P}_e$ is the electrical polarisation density due to the presence of $\vec{E}$, and defined as:

$$\vec{P}_e = \varepsilon_0\chi_e\vec{E} \tag{4.14}$$

The electrical dipole moment of a spherical particle in a colloid under an external electric field has been derived by Dukhin *et al.* (Dukhin and Shilov, 1980):

$$\vec{d} = \vec{d}_0 + \vec{d}_p = \varepsilon_e a^3\vec{E}\left(-\frac{1}{2} + \frac{3}{2}\frac{\mathrm{Rel}}{1+\mathrm{Rel}}\right) \tag{4.15}$$

$$\mathrm{Rel} = \frac{K_s}{K_e a} \tag{4.16}$$

where, $\vec{d}$ is the electric dipole moment, K_s is the surface conductivity, K_e is the conductivity of the electrolyte, a is the radius of the particle, E is the applied electric field, ε_e is the permittivity of electrolyte, $\vec{d}_o$ is the dipole moment which is independent of K_s and caused by the distinction between the dielectric constants of the materials of the particle and medium, and $\vec{d}_p$ is the charge component of the dipole moment.

Therefore, the electrical polarisation density can be expressed by:

$$\vec{P}_{\mathrm{e}} = \frac{\phi}{\frac{4}{3}\pi a^3}\varepsilon_{\mathrm{e}} a^3 \vec{E}(-\frac{1}{2} + \frac{3}{2}\frac{\mathrm{Rel}}{1+\mathrm{Rel}}) = \frac{3\phi\varepsilon_{\mathrm{e}}}{4\pi}\vec{E}(-\frac{1}{2} + \frac{3}{2}\frac{\mathrm{Rel}}{1+\mathrm{Rel}}) \tag{4.17}$$

Combining Equations (4.17) and (4.14), gives:

$$\varepsilon_0 \chi_e = \frac{3\phi\varepsilon_{\mathrm{e}}}{4\pi}(-\frac{1}{2} + \frac{3}{2}\frac{\mathrm{Rel}}{1+\mathrm{Rel}}) = \frac{3\phi\varepsilon_{\mathrm{e}}}{4\pi}\frac{2K_s - K_e a}{2(K_e a - K_s)} \tag{4.18}$$

The surface conductivity K_s is a function of surface charge σ_s (Jimenez et al., 2007):

$$\mathrm{K_s} = \frac{\mathrm{e}D}{k_{\mathrm{B}}T}\sigma_s = A\sigma_s \tag{4.19}$$

where, e is the charge of an electron, k_{B} is the Boltzmann constant, T is temperature, and D is the diffusion coefficient of ions. A is a constant since the above parameters are all constant.

For a parallel RC equivalent circuit, tan(θ) can be expressed by:

$$\tan(\theta) = -\omega RC = -\frac{\omega C}{G} \tag{4.20}$$

where, G is the admittance.

Based on the definition of capacitance and admittance, we have:

$$C = \varepsilon_0 \varepsilon_r \frac{A}{d} = \varepsilon_0 (1 + \chi_e) k \tag{4.21}$$

$$G = k\sigma \tag{4.22}$$

where, k is the cell constant and σ is the conductivity of suspension.

Therefore, tan(θ) can be related to the value of $\varepsilon_0 \chi_e$ by:

$$\tan\theta = -\frac{\omega C}{G} = -\frac{k\omega\varepsilon_0(1+\chi_e)}{k\sigma} = -\frac{\omega\varepsilon_0}{\sigma} - \frac{\omega\varepsilon_0\chi_e}{\sigma} \tag{4.23}$$

As shown in the Equations (4.18) and (4.19), $\varepsilon_0 \chi_e$ is related to the particle size and surface charge in the case that the particle volume fraction remains constant. The surface charge is a function of particle size as well, because the surface areas of the

particles increase with decreasing particle size if the volume fraction remains constant. Therefore, from Equation (4.23) it can be deduced that tan(θ) is a function of particle size. However, it is difficult to obtain the exact expression for tan(θ) and particle size, because the surface conductivity in Equation (4.18) is difficult to measure experimentally and the exact relationship between the surface charge and particle size is not available. Therefore, a qualitative analysis is carried out based on the experimental results. A semi-empirical relationship between the relative changes in tan(θ) and the particle size is developed based on the discussion.

Tables 4.3-4.6 show the values of λ changing with the particle size in the silica suspensions of different concentrations. In these tables, the particle diameters are the measured results using the ZetaSizer. The relationships between λ and the particle size in the silica suspensions with different particle concentrations are shown in Figure 4.10. Based on the results, a linear, proportional relationship between λ and the particle diameter is proposed and the linear fitting results are shown in Figure 4.10 as well.

It can be found that in the silica suspensions with relatively high particle concentrations (10.0 wt% and 5.0 wt%), λ is approximately proportional to the particle size by showing good linear fitting results. However, in the silica suspensions with relatively low particle concentrations (1.0 wt% and 0.5 wt%), the linear fitting results are not as good as those in the suspensions with high concentrations. One of the possible reasons is the small variations in phase angles as shown in Figures 4.7 (d) and 4.8 (d), because the calculation of λ relies on the values of phase angles. The possible reasons for the small variations in phase angles which occur in the low concentration suspensions have been analysed in section 4.3.1. Another possible reason is that the assumption of parallel RC equivalent circuit model is not accurate for describing the real situation of the silica particles under an external electric field. A more suitable and accurate model needs to be considered in order to get a better fitting result.

Table 4.3: The relative changes in tan(θ) in 10.0 wt% silica suspensions with different particle sizes

Particle diameter (nm)	**Particle concentration**	**λ**
$467.9^{(220)}$	10.0 wt%	0.806
$220.2^{(90)}$	10.0 wt%	0.853
$270.4^{(70)}$	10.0 wt%	0.848
$190.1^{(35)}$	10.0 wt%	0.881
$18.17^{(12)}$	10.0 wt%	0.939

Table 4.4: The relative changes in tan(θ) in 5.0 wt% silica suspensions with different particle sizes

Particle diameter (nm)	Particle concentration	λ
$384.6^{(220)}$	5.0 wt%	0.725
$199.7^{(90)}$	5.0 wt%	0.785
$190.1^{(70)}$	5.0 wt%	0.761
$91.28^{(35)}$	5.0 wt%	0.802
$13.54^{(12)}$	5.0 wt%	0.897

Table 4.5: The relative changes in tan(θ) in 1.0 wt% silica suspensions with different particle sizes

Particle diameter (nm)	Particle concentration	λ
$378.0^{(220)}$	1.0 wt%	0.587
$180.9^{(90)}$	1.0 wt%	0.612
$164.2^{(70)}$	1.0 wt%	0.5495
$58.77^{(35)}$	1.0 wt%	0.5187
$7.53^{(12)}$	1.0 wt%	0.694

Table 4.6: The relative changes in tan(θ) in 0.5 wt% silica suspensions with different particle sizes

Particle diameter (nm)	Particle concentration	λ
$425.8^{(220)}$	0.5 wt%	0.324
$178.7^{(90)}$	0.5 wt%	0.641
$148.1^{(70)}$	0.5 wt%	0.641
$69.06^{(35)}$	0.5 wt%	0.420
$7.53^{(12)}$	0.5 wt%	0.544

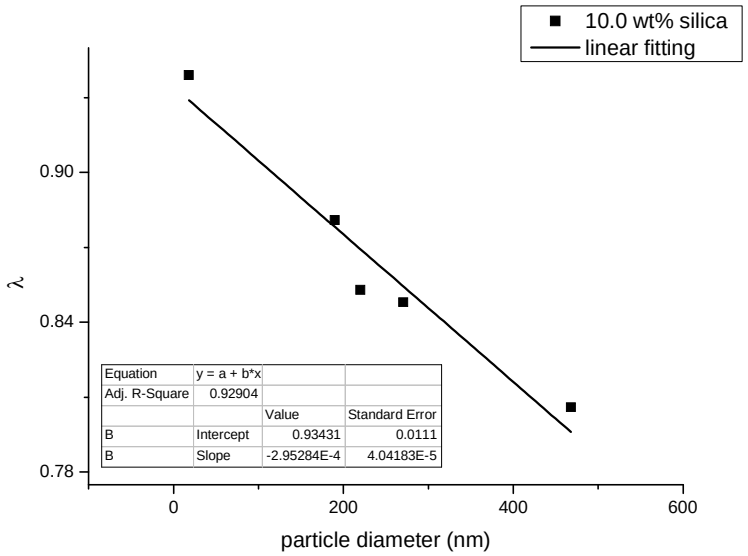

Equation	y = a + b*x		
Adj. R-Square	0.92904		
		Value	Standard Error
B	Intercept	0.93431	0.0111
B	Slope	-2.95284E-4	4.04183E-5

(a)

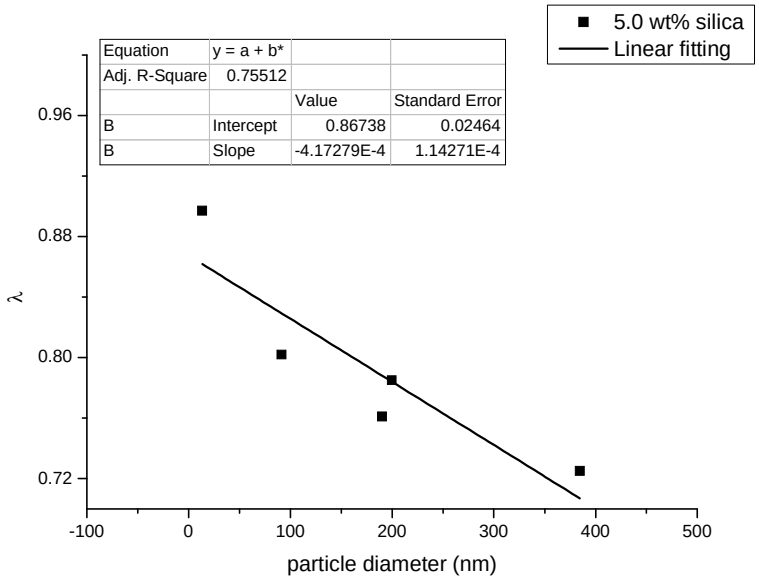

Equation	y = a + b*		
Adj. R-Square	0.75512		
		Value	Standard Error
B	Intercept	0.86738	0.02464
B	Slope	-4.17279E-4	1.14271E-4

(b)

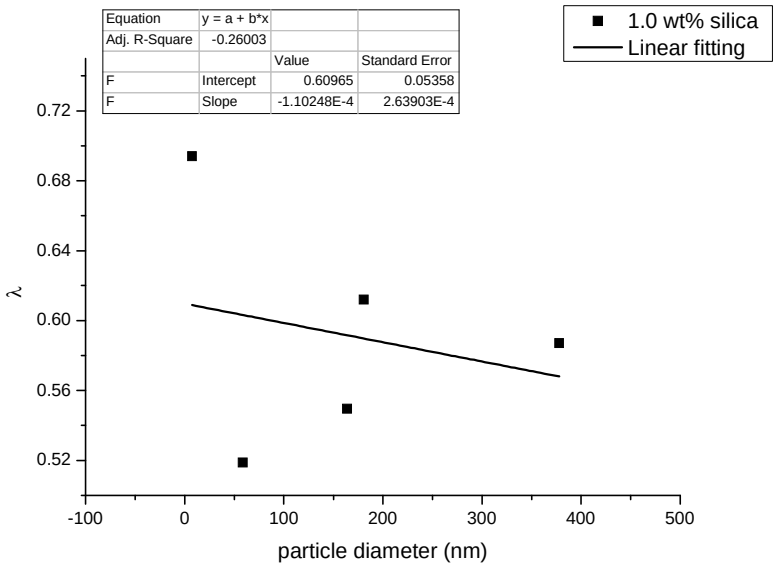

(c)

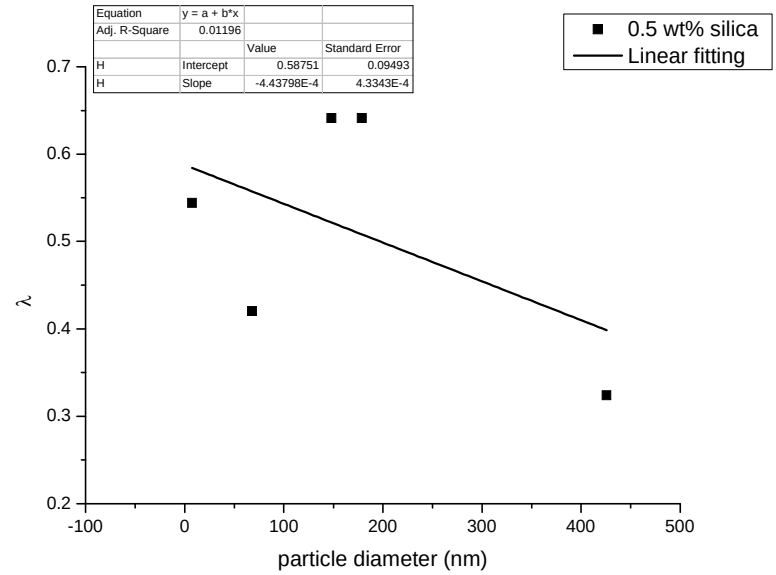

(d)

Figure 4.10: The plots of relative changes in tan(θ) vs. particle size in the silica suspensions with different particle concentrations (a) 10.0 wt%, (b) 5.0 wt%, (c) 1.0 wt% and (d) 0.5 wt%

4.4.3 α dispersion and MWO dispersion

As reviewed in Chapter 2, section 2.2.3, the two relaxation mechanisms, α dispersion and MWO dispersion might be observed at the frequency range in our experiments. From the plot of the impedance imaginary part in Figures 4.11 (c) – 4.14 (c), these two relaxation mechanisms cannot be distinguished since only one peak can be observed across the whole measured frequency range (shown in section 4.3.1). The possible reason is that the two peaks showing α and MWO dispersions are merged together and cannot be separated in the plot of impedance imaginary part. Since the different dielectric functions (impedance, permittivity, and admittance) could show the relaxation peaks at different frequencies (Gerhardt, 1994), some relaxation peaks which couldn't be observed in the impedance curves might be observed in the permittivity curves. Therefore, in order to get the information about the two dispersions, the permittivity curves were plotted. The complex conductivity and permittivity can be converted from the impedance data by the relationships which are shown below:

The impedance Z^* and complex conductivity K^* can be expressed as below:

$$Z^*(\omega) = Z'(\omega) + iZ''(\omega) \tag{2.61}$$

$$K^*(\omega) = \sigma'(\omega) + i\sigma''(\omega) \tag{4.24}$$

where, Z' and Z'' are the real and imaginary parts of the impedance, σ' and σ'' are the real and imaginary parts of the complex conductivity.

The relationship between the impedance and complex conductivity is given by:

$$K^*(\omega) = \frac{C_C}{Z^*(\omega)} \tag{4.25}$$

Here, C_c is called the cell constant. The cell constant can be calculated via calibration using a standard electrolyte solution. The value of the cell constant is 8.66 for the vessel used in our experiments.

The general presentation of the complex conductivity is given by:

$$K^*(\omega) = \sigma(\omega = 0) - i\omega\varepsilon^*(\omega) \tag{4.26}$$

Considering charged particles in motion, the complex permittivity can be expressed as:

$$\varepsilon^*(\omega) = \varepsilon_0 \varepsilon_r^* = \varepsilon_0 \left[\varepsilon_r'(\omega) + i\varepsilon_r''(\omega) \right] \tag{4.27}$$

$$K^*(\omega) = \sigma(\omega = 0) + \omega\varepsilon_0 \varepsilon_r''(\omega) - i\omega\varepsilon_0 \varepsilon_r'(\omega) \tag{4.28}$$

Comparing Equations (4.24) and (4.28), we can immediately get,

$$\varepsilon_r'(\omega) = \frac{-\sigma''(\omega)}{\omega\varepsilon_0} \tag{4.29}$$

$$\varepsilon_r''(\omega) = \frac{\sigma'(\omega) - \sigma'(\omega = 0)}{\omega\varepsilon_0} \tag{4.30}$$

where, ε_0 is the absolute permittivity of the vacuum.

According to Equation (4.30), the imaginary part of permittivity can be calculated from the measured impedance data. Figure 4.11–Figure 4.14 show the imaginary part of the complex permittivity for the silica suspensions with different concentrations (10.0 wt%, 5.0 wt%, 1.0 wt%, 0.5 wt%) and various values of particle size. In order to clearly observe the α dispersion and MWO dispersion, which usually occur in the kHz to MHz range, permittivity curves show the data from 1 kHz to 32 MHz. It is easy to identify two different groups of relaxation peaks from these figures. The peaks between 10 kHz to 100 kHz are due to the α dispersion, which is associated with the polarisation of the double layer and presents the time taken for the transport of ions at the diffuse double layer over distances of the order of the particle radius. It can be found that all of the silica suspensions exhibit negative values of ε" at the α relaxation peaks. This phenomenon is contrary to many simulations and experimental results shown in the literature (Kijlstra et al., 1993, Lim and Franses, 1986, Sauer et al., 1990). However, a recent journal paper (Bradshaw-Hajek et al., 2010) presented a similar result by using simulation. It showed that for the systems where κa > 1 and |ξ| > 25.7 mV, negative ε" values can be observed at the α relaxation frequency range. The reason for this phenomenon was explained as the colloidal suspensions are treated as a conductive (or part conductive) medium in the simulation therefore the constraint of positive ε" for a dielectric medium no longer holds (Bradshaw-Hajek et al., 2010). In our experiments, the conditions of κa > 1 and |ξ| > 25.7 mV are satisfied for some of the samples, but the negative values of ε" exist in all of the samples. The possible reasons include not only

the one mentioned by Bradshaw-Hajek but also the possible systematic error in the calculation, because in the calculation of ε'' using the equation (4.30), the conductivity values at the lowest frequency (ω = 1 Hz) were used as the DC conductivity (ω=0).

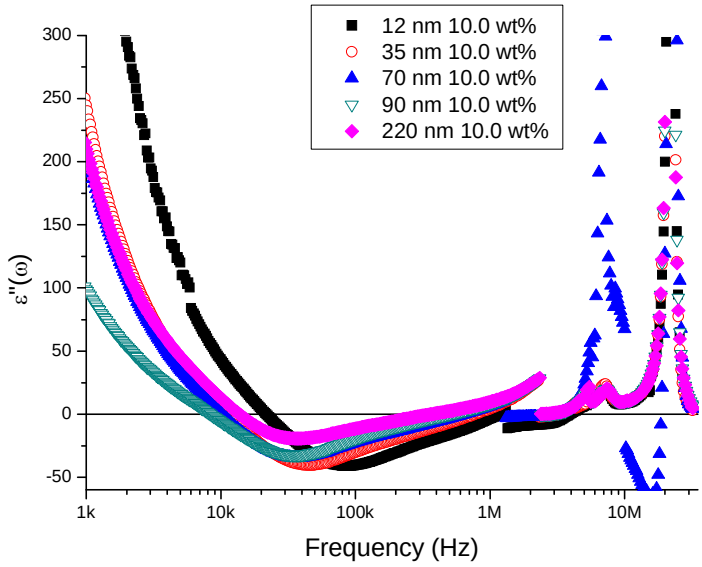

Figure 4.11: The imaginary part of complex permittivity spectra for silica suspensions (10.0 wt %) with different particle size (18.7^{12} nm, 190.1^{35} nm, 270.4^{70} nm, 220.2^{90} nm, 467.9^{220} nm)

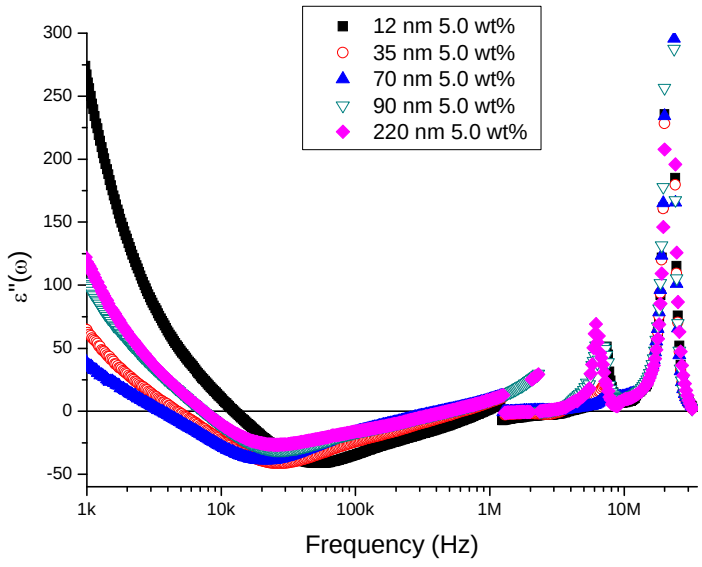

Figure 4.12: The imaginary part of complex permittivity spectra for silica suspensions (5.0 wt %) with different particle size (13.54^{12} nm, 91.28^{35} nm, 190.1^{70} nm, 199.7^{90} nm, 384.6^{220} nm)

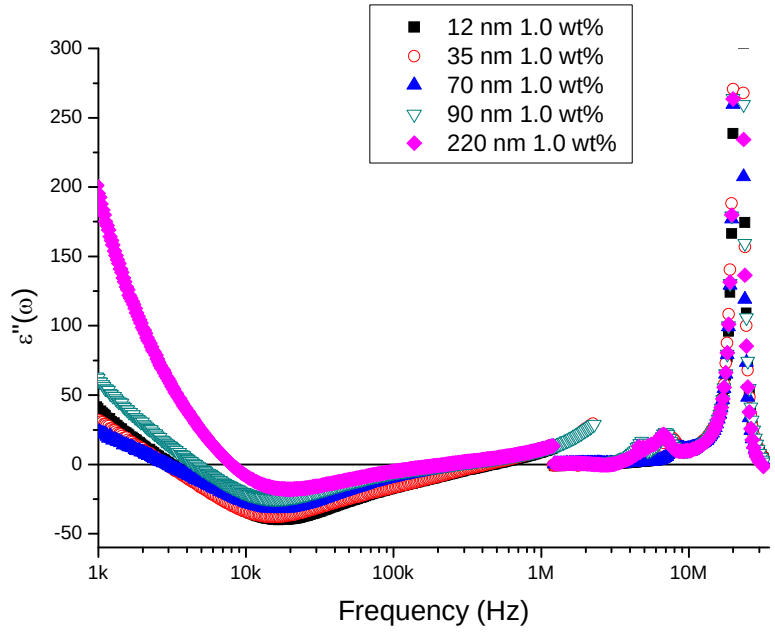

Figure 4.13: The imaginary part of complex permittivity spectra for silica suspensions (1.0 wt %) with different particle size (7.53^{12} nm, 58.77^{35} nm, 164.2^{70} nm, 180.9^{90} nm, 378.0^{220} nm)

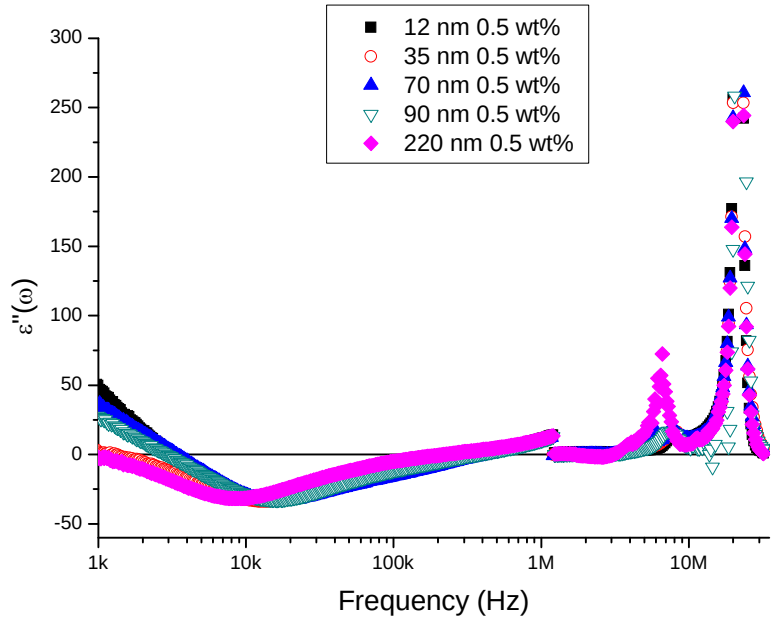

Figure 4.14: The imaginary part of complex permittivity spectra for silica suspensions (0.5 wt %) with different particle size (7.53^{12} nm, 68.06^{35} nm, 148.1^{70} nm, 178.7^{90} nm, 425.8^{220} nm)

For dilute suspensions, the frequency at which α relaxation occurs can be estimated via an equation derived from the model established by Delacey and White (Delacey and White, 1981):

$$\omega_\alpha \approx \frac{2D}{(a+\kappa^{-1})^2} \tag{4.31}$$

where, *a* is the particle radius, κ^{-1} is the double layer thickness and D is the diffusion coefficient of ions.

Here, the definition of a dilute suspension is not explicit in the literature. However, in a review paper (Grosse and Delgado, 2010), the authors state that a volume fraction of 1% should be treated as a concentrated suspension since the particle concentration dependence of α relaxation frequency loses linearity when the particle volume fraction is larger than 1%. The relationship between the particle concentration and α relaxation frequency will be discussed in section 4.4.

The value of κ^{-1} can be calculated from the ionic concentration by Equation (4.32) (Hunter, 2001):

$$\kappa^{-1} = \sqrt{\frac{\varepsilon_0 \varepsilon_r k_B T}{2 N_A e^2 I}} \tag{4.32}$$

where *I* is the ionic strength of the electrolyte (mole/m^3), ε_0 is the permittivity of free space, ε_r is the dielectric constant of solvent (78.5 for water), k_B is the Boltzmann constant, *T* is the absolute temperature, N_A is the Avogadro number, and *e* is the elementary charge.

For a symmetric monovalent electrolyte,

$$\kappa^{-1} = \sqrt{\frac{\varepsilon_0 \varepsilon_r RT}{2F^2 C_0}} \tag{4.33}$$

where, R is the gas constant, F is the Faraday constant, and C_0 is the molar concentration of the electrolyte (mole/litre).

At room temperature (25 ˚C), the Debye length can be expressed by:

$$\kappa^{-1} = \frac{0.304}{\sqrt{C_0}} \text{ (nm)} \qquad (4.34)$$

In the experiment, it is difficult to measure the exact values of the ionic concentration in silica suspensions. However, the approximate values of ionic concentration could be estimated from the concentration of H^+ and OH^- ions, which could be calculated from pH values, although the neglect of other kinds of ions may make the calculation not accurate enough. The relationship between relaxation frequency ω_α and particle size in 10.0 wt% and 5.0 wt% silica suspensions is shown in two figures (Figures 4.15 and 4.16), respectively. For both of the figures, the particle radii, *a*, are all obtained from the particle sizes measured using the ZetaSizer, which have been shown in section 4.2.1, Table 4.1. The linear fitting results are shown in Figures 4.15 and 4.16 by the red line. It can be seen that the relaxation frequency ω_α is proportional to the particle size as in the relationship shown in Equation (4.31). The experimental results are coincident with the results shown by other researchers (Schwan et al., 1962, Carrique et al., 1998, Kijlstra et al., 1993, Sauer et al., 1990). For silica suspensions with low concentrations (1.0 wt% and 0.5 wt%), the particle size effect on the relaxation frequency ω_α is not prominent (shown in Figures 4.13 and 4.14) and hence it will not be discussed further using Equation (4.31).

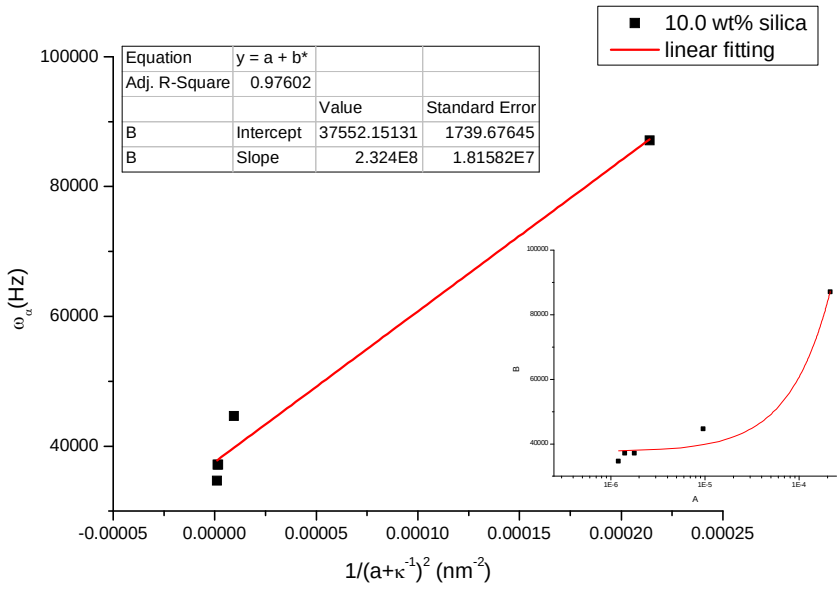

Figure 4.15: The relaxation frequency ω_α is plotted against particle size and is proportional to $1/(a+\kappa^{-1})^2$ for 10.0 wt% silica suspensions of different particle size (18.7^{12} nm, 190.1^{35} nm, 270.4^{70} nm, 220.2^{90} nm, 467.9^{220} nm)

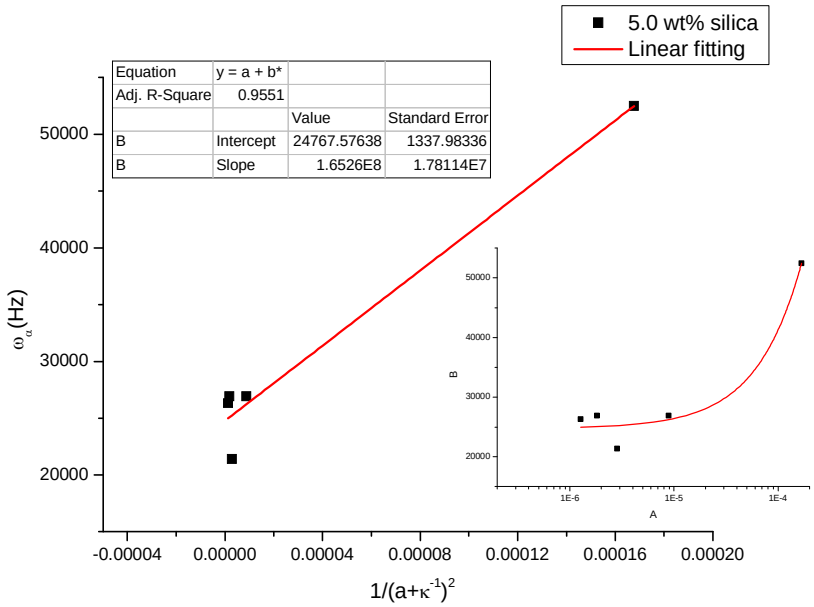

Figure 4.16: The relaxation frequency ω_α is plotted against particle size and is proportional to $1/(a+\kappa^{-1})^2$ for 5.0 wt% silica suspensions of different particle size (13.54^{12} nm, 91.28^{35} nm, 190.1^{70} nm, 199.7^{90} nm, 384.6^{220} nm)

The MWO dispersion occurs at higher frequency. There are two groups of peaks which can be found in the MHz range. One is around 8 MHz and another one around 20 MHz. It is believed that the groups of peaks around 8 MHz represent the Maxwell-Wagner relaxation because it has been proved experimentally by some researchers that MWO relaxation occurs at around several MHz (Zhao and He, 2006, Blum et al., 1995, Ballario et al., 1976). The group of peaks around 20 MHz are probably caused by the effect of parasitic inductance which can be seen from the small arcs with Z”>0 at the high frequency range (around 20 MHz) in Figure 4.5 (a). The high frequency inductive behaviour is usually caused by the physical inductance of the cables, wires, and instrumentation (He et al., 2011). This phenomenon causes a deviation in EIS measurement, and the EIS data obtained above 20 MHz will not be used in the discussion. The Maxwell-Wagner-O’Konski relaxation occurs when the two contacting phases, the particle and medium solution, have different conductivities and electric permittivities. The expression for the relaxation frequency of the MWO dispersion is shown in Equation (4.35) (Delgado et al., 2007) :

$$\omega_{MWO} = \frac{2k_m + k_p + \phi(k_m - k_p)}{\varepsilon_0[(2\varepsilon_m + \varepsilon_p) + \phi(\varepsilon_m - \varepsilon_p)]} \tag{4.35}$$

where, k_p is the conductivity of the particle, k_m is the conductivity of the medium, ε_p is the permittivity of the particle, ε_m is the permittivity of the medium, and ϕ is the particle volume fraction.

Here, the particle conductivity k_p should be modified to include the contribution of surface conduction (O'Konski, 1960), k^σ, and given to a expression for k_p:

$$k_p = k_{pb} + \frac{2k^\sigma}{a} \tag{4.36}$$

As the above relaxation frequency ω_{MWO} is derived based on the assumption of a thin double layer, Equations (4.35) and (4.36) are accurate for thin double layer suspensions. For thick double layer suspensions, the surface conduction is not well defined. In the experiments conducted in the study, the ionic concentration of silica suspensions is low, which causes a thick double layer (comparable with the particle size). Therefore, it is difficult to calculate the relaxation frequency of WMO dispersion accurately, but quantitatively, ω_{MWO} should be related to the particle concentration and particle size. The experimental results for the relaxation frequency of MWO dispersion are shown in Figure 4.17 – Figure 4.20. It can be seen that for the samples with highest concentration, 10.0 wt%, ω_{MWO} does not change with changing particle size. With decreasing particle concentration, ω_{MWO} becomes particle size dependent and moves to a lower frequency range with increasing particle size.

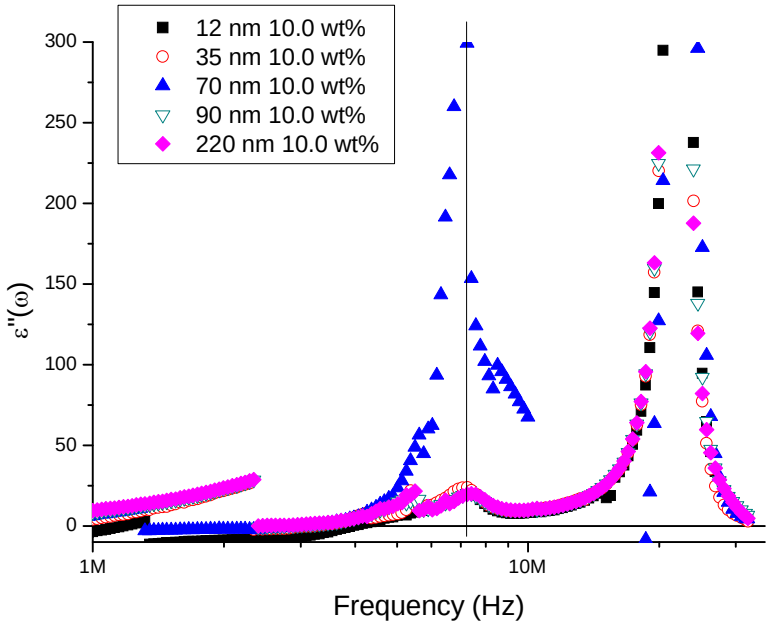

Figure 4.17: ω_{MWO} for silica suspensions (10.0 wt %) with different particle size (18.7[12] nm, 190.1[35] nm, 270.4[70] nm, 220.2[90] nm, 467.9[220] nm)

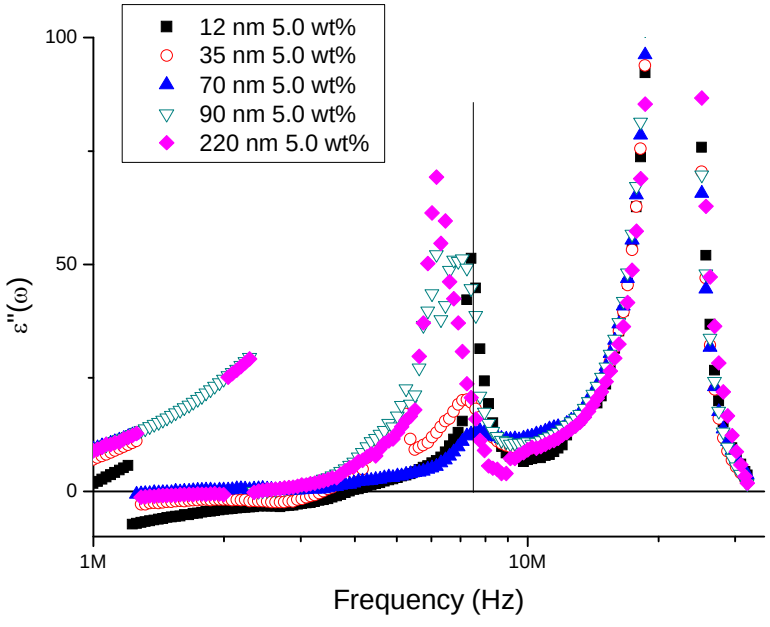

Figure 4.18: ω_{MWO} for silica suspensions (5.0 wt %) with different particle size (13.54[12] nm, 91.28[35] nm, 190.1[70] nm, 199.7[90] nm, 384.6[220] nm)

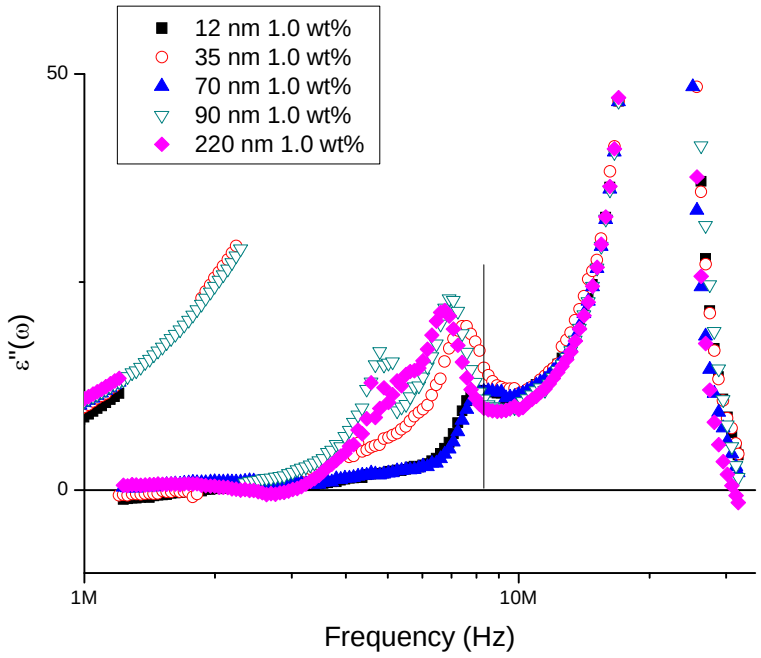

Figure 4.19: ω_{MWO} for silica suspensions (1.0 wt %) with different particle size (7.53[12] nm, 58.77[35] nm, 164.2[70] nm, 180.9[90] nm, 378.0[220] nm)

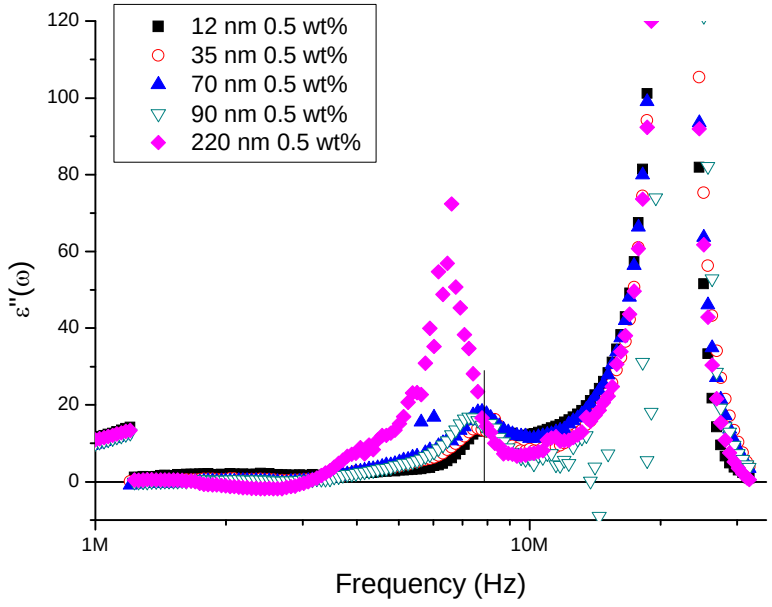

Figure 4.20: ω_{MWO} for silica suspensions (0.5 wt %) with different particle size (7.53[12] nm, 68.06[35] nm, 148.1[70] nm, 178.7[90] nm, 425.8[220] nm)

4.5 Particle concentration effect

In this section, the particle concentration effects on electrical impedance spectra and permittivity spectra are studied. The effects could be mainly represented by the impedance real-part, the phase angle, and the relaxation frequency of the α dispersion. Figure 4.21 shows the impedance real part as a function of frequency in silica suspensions with fixed particle size (220 nm) but different concentrations (10.0 wt%, 5.0 wt%, 1.0 wt%, 0.5 wt%). Here, the particle size of 220 nm is the size of original sample and provided by the specification from the vendor. The silica suspensions (220 nm) with different concentrations were prepared, using the same original samples, by dilution. The particle sizes measured using the ZetaSizer for suspensions with different concentrations are not exactly same as shown in Table 4.1. In the discussion of particle concentration effect, the difference in the particle size is neglected. Figure 4.21 indicates that the impedance real parts decrease with increasing particle concentration. This result is contrary to the usual understanding which is indicated by the decrease of conduction (or increase of impedance real part) after adding non-conducting particles to the suspensions. However, the result does not only show the pure particle concentration effect, because it might be affected by the ionic concentrations in the background solutions. In order to analyse the effect from the ionic concentrations, the silica suspensions were filtered using a syringe filter and the particles were removed from the suspensions.

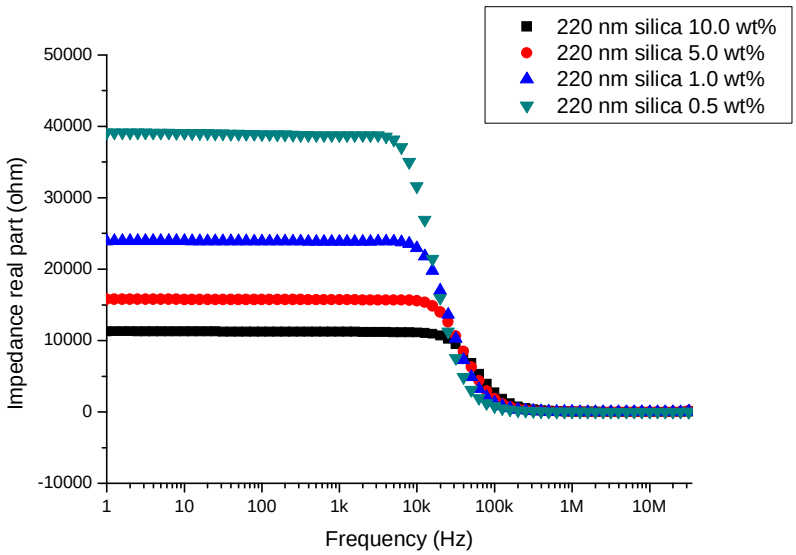

Figure 4.21: Impedance real part vs. frequency for silica suspensions (220 nm) with different particle concentrations (10.0 wt%, 5.0 wt%, 1.0 wt%, 0.5 wt%)

Both the conductivities of silica suspensions and the background solutions without particles inside were measured using a conductivity meter. Then the result was put into the Maxwell-Wagner equation (MW) to inversely calculate the conductivity of suspensions in order to compare the calculated results with the measured results. The MW equation can be used to calculate the conductivity of a mixed phase and expressed by (McLachlan and Sauti, 2007):

$$\sigma_m = \sigma_1 \frac{2\sigma_1 + \sigma_2 - 2\phi(\sigma_1 - \sigma_2)}{2\sigma_1 + \sigma_2 + \phi(\sigma_1 - \sigma_2)} \tag{4.37}$$

where, the subscripts *1*, *2* and *m* denote the continuous phase, the disperse phase and the mixed phase respectively; ϕ is the volume fraction of the dispersed phase.

For the silica suspensions, the continuous phase is the background solution; the dispersed phase is the SiO_2 particles. The conductivity of particles (non-conductive material) is assumed to be 0. The conductivity of the continuous phase, σ_1, can be measured by a conductivity meter. Therefore, σ_m can be calculated using the MW equation. The calculated values of conductivity for a mixed phase (suspensions), $\sigma_{m\text{-}calculate}$, are shown in the table 4.7, and compared with the values ($\sigma_{m\text{-}measure}$) measured by a conductivity meter.

From Table 4.7, it can be seen that for the suspensions with different particle concentrations, $\sigma_{m\text{-}measure}$ are all smaller than those calculated using the MW equation. The possible reasons arise from the parameters used in the calculation, σ_2 and ϕ. Firstly, σ_2 is assumed to be zero in this case, which is an extreme assumption. In the real situation, σ_2 should be larger than 0, although it is still very small. Secondly, the particle volume fraction had to be calculated using an estimated particle density since the particle density was not provided by the manufacturer and the measurement is difficult. Therefore, a particle density of 2.0 g/cm^3 from the literature (Rosen and Saville, 1991) is used in the calculation. This value might be an over-estimate or under-estimate and thus cause the particle volume fraction to be higher or lower than the real values.

Based on the above discussion, the analysis of particle concentration effect on the impedance real part must take into consideration the conductivities of background solutions. σ_1 can be measured experimentally or calculated using the MW equation if the separation of particles and background solution is difficult for the case of small particles (<100 nm).

Table 4.7: The calculation results of conductivities (at 25 ˚C) of the silica suspensions (220 nm) with different particle concentrations using the MW equation

Particle concentration	**Particle volume fraction Φ**	**σ_1 (μs/cm)**	**$\sigma_{m\text{-}measure}$ (μs/cm)**	**$\sigma_{m\text{-}calculate}$ (μs/cm)**
10.0 wt%	4.76 %	20.70	13.01	19.26
5.0 wt%	2.38 %	13.22	10.65	12.75
1.0 wt%	0.476 %	7.457	7.061	7.40
0.5 wt%	0.238 %	5.375	4.30	5.356

The particle concentration not only influences the impedance real part but also affects the relaxation frequency of the α dispersion. The literature review article reveals claims of proof by both simulations and experiments that the α relaxation frequencies increase with increasing particle concentrations (or particle volume fraction) (Delgado et al., 1998, Carrique et al., 2003). For non-dilute suspensions, with increasing particle concentration, the distance between two particles becomes smaller, and the electrical double layers may partially overlap, especially in the case of low ionic concentration (the case in our experiments). The increase of relaxation frequency ω_α with increasing particle concentration (or volume fraction) can be explained by the decrease in the diffusion length due to the presence of neighbouring particles. The theoretical approach for this phenomenon is based on a so-called cell model, in which a single particle (spherical, with radius a), is immersed in a concentric shell of electrolyte solution with external radius b, such that the particle volume fraction can be obtained from:

$$\phi = (\frac{a}{b})^3 \tag{4.38}$$

The diffusion length, L_D, is defined as the length scale over which ionic diffusion takes place around the particle. For the two extreme cases, very dilute suspension and very concentrated suspension, the L_D is equal to *a* and *b*-*a*, respectively (*b* is half the average distance between the centres of neighbouring particles).

From the discussion in section 4.3.3, the relaxation frequency ω_α is proportional to diffusion length, therefore, for a very dilute suspension with thin double layer:

$$\omega_\alpha \propto \frac{D}{a^2} \tag{4.39}$$

For a very concentrated suspension with thin double layer:

$$\omega_\alpha \propto \frac{D}{(b-a)^2} \tag{4.40}$$

For the common case, the diffusion length can be expressed by (Delgado et al., 2007):

$$L_D = (\frac{1}{a^2} + \frac{1}{(b-a)^2})^{-1/2} = a(1+\frac{1}{(\phi^{-1/3}-1)^2})^{-1/2} \tag{4.41}$$

Therefore, the relaxation frequency ω_α for non-diluted suspension is:

$$\omega_{\alpha,c} = \omega_{a,d}(1+\frac{1}{(\phi^{-1/3}-1)^2}) \tag{4.42}$$

where, $\omega_{\alpha,d}$ is the relaxation frequency for very dilute suspensions, and $\omega_{\alpha,c}$ denotes the relaxation frequency for non-dilute suspensions.

The experimental result of the dependence of $\omega_{\alpha,c}$ on particle concentration for silica suspensions with fixed particle size is shown in Figure 4.22. The line in the figure is just for the connection between two points without any other meaning. It can be seen that ω_α increases with increasing particle weight concentrations in the five series of samples with varying particle size, which follow the trend indicated by Equation (4.42). The increment of $\omega_{\alpha,c}$ is much larger in the samples with the smallest particle size (12 nm), which means the particle concentration effect on the relaxation frequency might be stronger for the smaller particles.

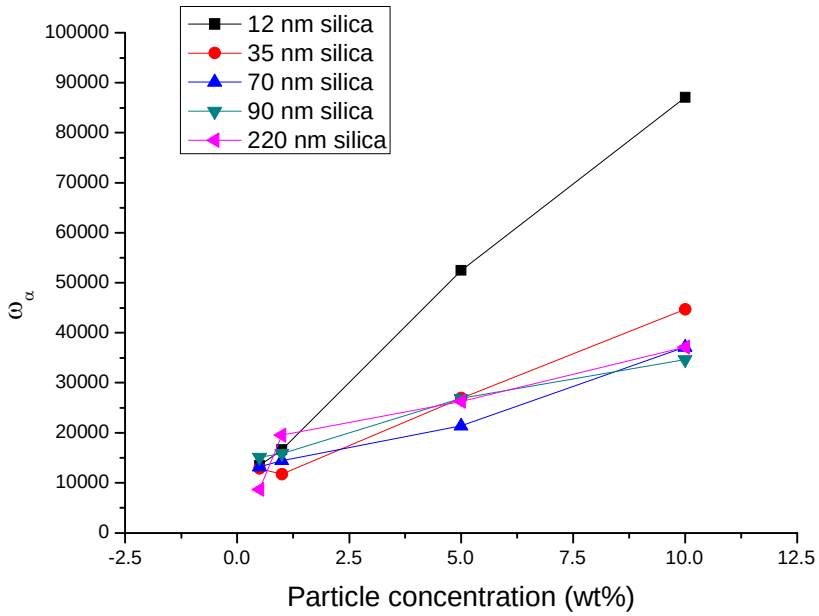

Figure 4.22: The dependence of ω_α on particle concentration for silica suspensions with different particle size (12 nm, 35 nm, 70 nm, 90 nm, 220 nm)

The effect of particle concentration on the impedance phase angle is analysed by the relative changes in tan(θ) as discussed in section 4.3.2 and the result is shown in Figure 4.23. The line in the figure is just for the connection between two points without any other meaning and the particle sizes shown in the figure are from the vender. For all the samples, with increasing particle concentration, an increment in λ can be observed. As discussed in section 4.3.2, λ reflects the electrical polarisation density caused by the polarisation of the double layer. With increasing particle concentration, the electrical polarisation density increases as shown in Equation (4.18). Therefore, the values of λ increase with increasing particle concentrations.

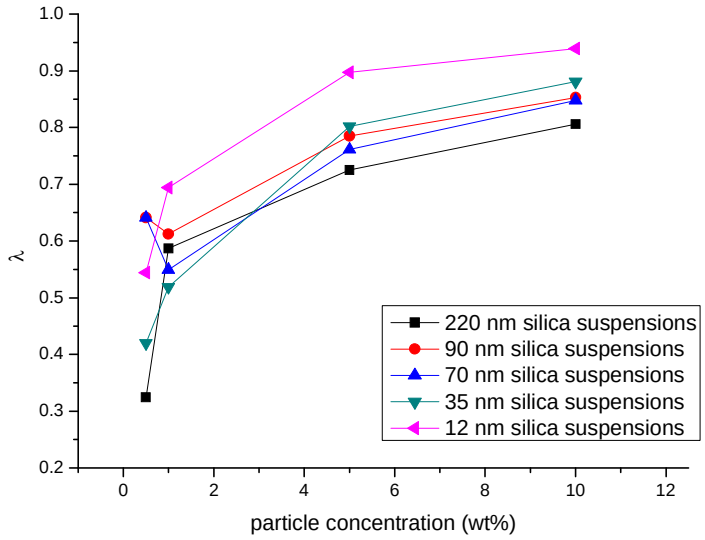

Figure 4.23: The relationship between the relative changes in tan(θ) and the particle concentration for silica suspensions.

4.6 Ionic concentration effects

In this section, the ionic concentration effects on electrical impedance spectra and permittivity spectra are analysed. The analysis is achieved by comparing the electrical impedance spectra and permittivity spectra of the silica suspensions with and without an electrolyte addition of 1.67 mM KCl. Figure 4.24 shows the electrical impedance spectra in 12 nm, 5.0 wt% silica suspensions without adding extra electrolyte and with 1.67 mM KCl electrolyte. It can be seen that the impedance real part decreases significantly with increasing ionic concentration, which can be understood very straight forwardly, since the suspension becomes more conductive after adding electrolyte. Figure 4.24 (c) shows that the relaxation frequency increases significantly with increasing the ionic concentration, which will be discussed further in the later part of this section on permittivity spectra. The phase angle results show a significant shift to a higher frequency range for the silica suspension with 1.67 mM KCl, compared with the silica suspension without added electrolyte.

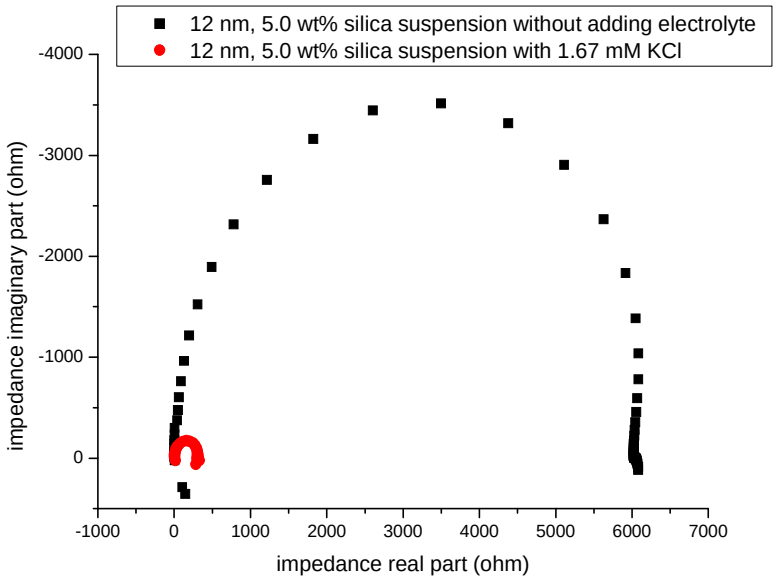
12 nm, 5.0 wt% silica suspension without adding electrolyte
12 nm, 5.0 wt% silica suspension with 1.67 mM KCl
impedance imaginary part (ohm)
-4000
-3000
-2000
-1000
0
-1000
0
1000
2000
3000
4000
5000
6000
7000
impedance real part (ohm)

(a)

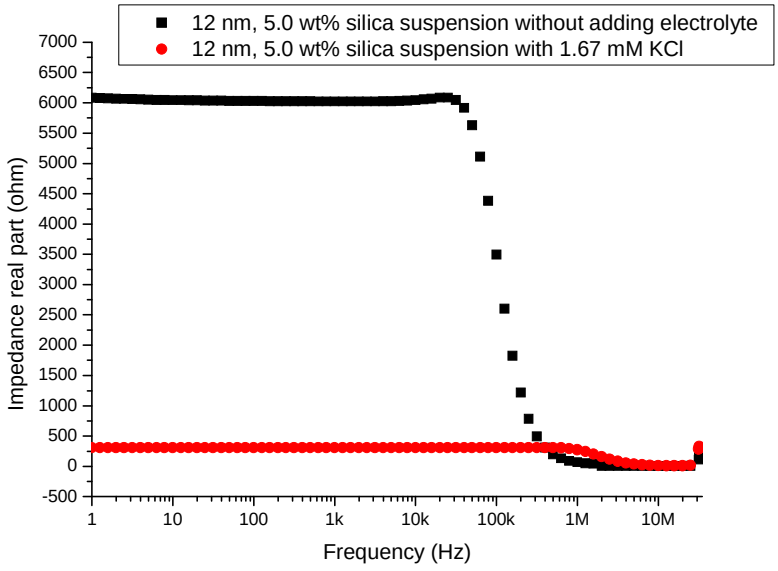
12 nm, 5.0 wt% silica suspension without adding electrolyte
12 nm, 5.0 wt% silica suspension with 1.67 mM KCl
Impedance real part (ohm)
7000
6500
6000
5500
5000
4500
4000
3500
3000
2500
2000
1500
1000
500
0
-500
1
10
100
1k
10k
100k
1M
10M
Frequency (Hz)

(b)

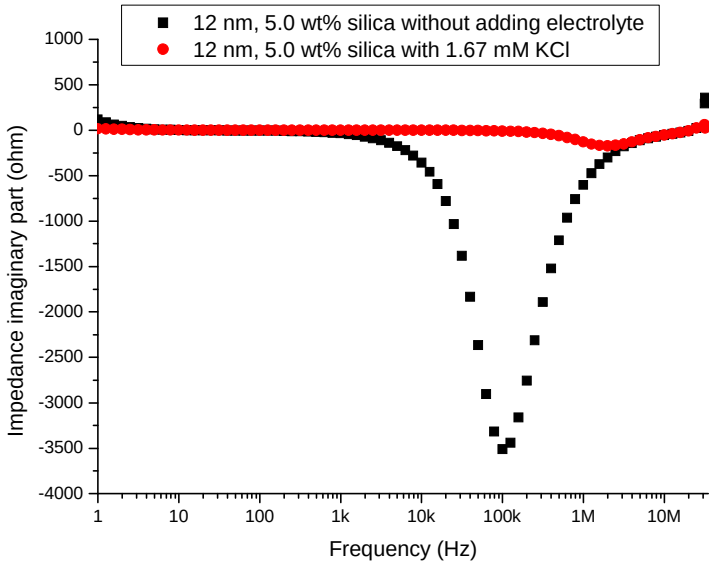

(c)

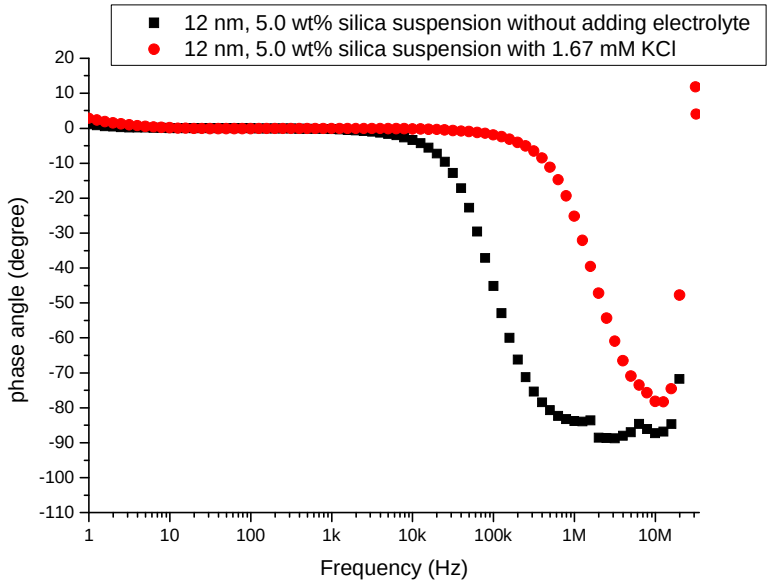

(d)

Figure 4.24: Impedance spectra for silica suspensions (12 nm, 5.0 wt %) without adding extra electrolyte and with 1.67 mM KCl electrolyte; (a) Cole-Cole plot of impedance; (b) impedance real part vs. frequency; (c) impedance imaginary part vs. frequency; (d) phase angle vs. frequency plots

Figure 4.25 shows the imaginary part of permittivity spectra of 12 nm, 5.0 wt% silica suspensions without addition of extra electrolyte and with 1.67 mM KCl electrolyte. It can be found that the relaxation frequencies, ω_α of silica suspensions increase after addition of electrolyte (KCl). This phenomenon could be explained by Equations (4.31) and (4.33). From Equation (4.33), the electrical double layer thickness κ^{-1} is related to the ionic concentration and decreases with increasing ionic concentration. By adding the electrolyte in the suspension, the double layer thickness decreases significantly and causes a high relaxation frequency of the α dispersion as shown in Equation (4.31).

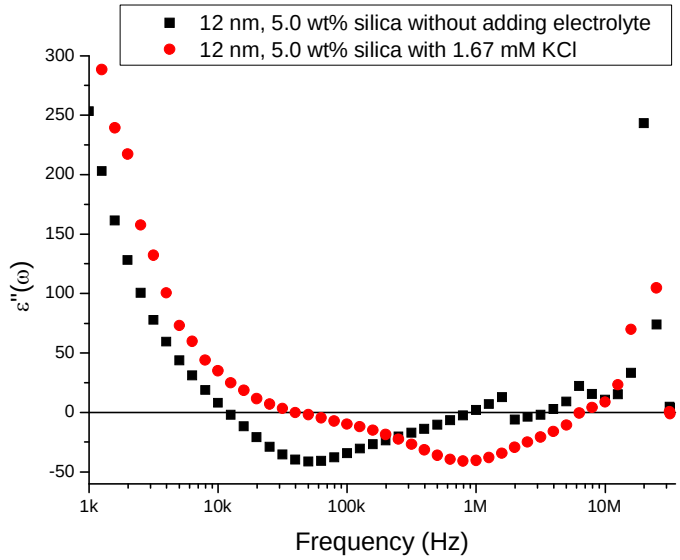

Figure 4.25: The imaginary part of complex permittivity spectra for silica suspensions (12 nm, 5.0 wt %) without adding extra electrolyte and with 1.67 mM KCl electrolyte

In addition, the ionic concentration effect is studied in a series of suspensions which have the same particle concentration (5.0 wt% or 10.0 wt%) but different particle size. The results are shown in Figure 4.26 and Figure 4.27. It can be seen that after adding electrolyte (KCl) to the suspensions, the relaxation frequencies, ω_α remain almost constant for samples with different particle size, which means that the particle size effect becomes insignificant. This result has not been reported by any other researchers. To understand the possible reasons, the influence of ionic concentration on the zeta potential might be considered. From the literature, it is known that in colloidal systems increasing ionic concentration tends to reduce the absolute values of zeta potential at a constant pH value (Hunter, 1981, Delgado et al., 1986, Saka and Guler, 2006). The lower |ξ| means that relative to the bulk electrolyte concentration there are fewer ions in the double layer in high electrolyte concentration solutions.

Therefore, the electrical dipole moment caused by the electrical double layer becomes small. This relationship between the dipole strength C_0 and zeta potential ξ has been proved by simulation (Mangelsdorf and White, 1997). For a symmetrical electrolyte, the dipole strength can be expressed by Equations (4.43) and (4.44):

$$C_0(\omega) = \frac{(2\lambda - \frac{i\omega\varepsilon_r}{4\pi K^\infty}) - (1 - \frac{i\omega\varepsilon_0}{4\pi K^\infty})}{2(1 - \frac{i\omega\varepsilon_0}{4\pi K^\infty}) + (2\lambda - \frac{i\omega\varepsilon_r}{4\pi K^\infty})} \tag{4.43}$$

where, K^∞ is the static bulk electrolyte conductivity, ε_r is the permittivity of the particle, λ is the non-dimensional double layer conductivity parameter, which can be given by:

$$\lambda = \frac{2}{\kappa a}(1 + \frac{3m}{z^2})[\cosh(\frac{ez\xi}{2K_B T}) - 1] \tag{4.44}$$

$$m = \frac{z_i D_i \overline{\mu}}{e} = \frac{z_i D_i}{e} \frac{\varepsilon_0 k_B T}{6\pi\eta_0 e} \tag{4.45}$$

where, z is the charge of type *i* ion, D_i is the drag coefficient of ion, η_0 is the viscosity of the medium, T is the temperature.

Since the dipole strength is weak, the polarisation of a electrical double layer becomes weak, and hence, it might cause the particle size effect on the relaxation frequency to become tiny. The results on ionic-concentration effect suggest that it is better to study the particle size effect under high absolute values of zeta potential (Iξl). However, in order to get a high Iξl, acid or alkali must be added into the suspension, which causes the ionic concentration to be increased at the same time. As discussed above, with the higher ionic concentration, the relaxation frequency moves to higher frequency range, which brings difficulties to the measurement using the current hardware (the frequency limit is 32 MHz for the Solartron 1260 impedance analyser). Besides, to adjust the pH values in the suspensions with different particle size, it is difficult to keep the ionic concentration constant at the same time in the experimental operation. Considering these aspects, the suspensions with very low ionic concentration were studied in these experiments.

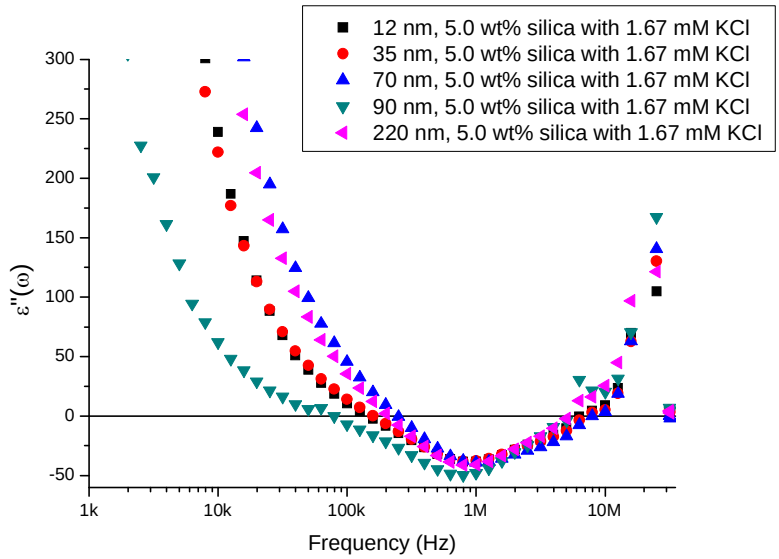

Figure 4.26: The imaginary part of complex permittivity spectra for silica suspensions (5.0 wt%) with 1.67 mM KCl electrolyte and different particle size (12 nm, 35 nm, 70 nm, 90 nm, 220 nm)

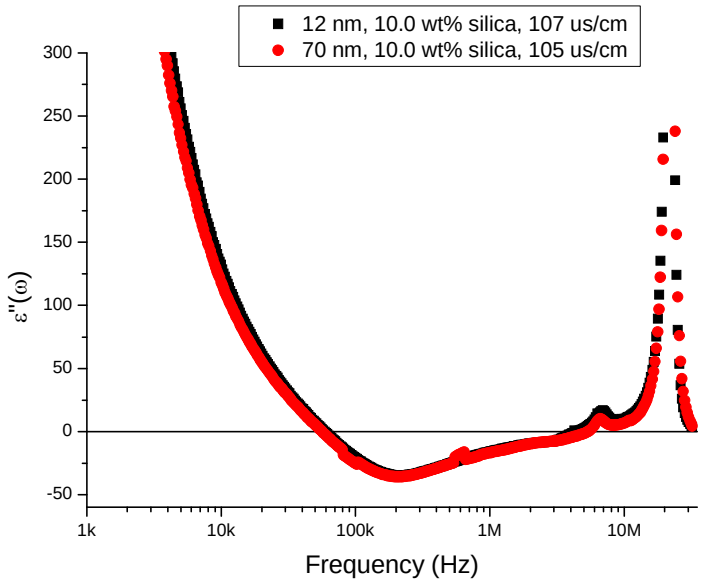

Figure 4.27: The imaginary part of complex permittivity spectra for silica suspensions (10.0 wt%) with 1.67 mM KCl electrolyte and different particle size (12 nm, 70nm)

4.7 Summary

In summary, this chapter presents the experimental results on the electrical impedance spectra and permittivity spectra of the silica suspensions. The effects of particle size, particle concentration and ionic concentration on the impedance, relaxation frequency, and phase angles are analysed and discussed in detail. The α relaxation frequencies shown in the permittivity spectra are a function of particle size changing inversely with the square of particle size and double layer thickness for the silica suspensions with relatively high concentrations (10.0 wt% and 5.0 wt%). However, the size effect becomes indistinct for the samples with low concentrations (1.0 wt% and 0.5 wt%). Another important parameter which could reflect the particle size effect is the impedance phase angle, θ. The relative changes in tan(θ) show a linear proportional relationship with the particle size. This linear proportional relationship works well for experimental results in the silica suspensions with relatively high concentrations (10.0 wt% and 5.0 wt%), but not so well for the silica suspensions with relatively low concentrations (1.0 wt% and 0.5 wt%) .

The particle concentration effect can be reflected by the impedance real part by considering the conductivities of background solutions. Besides, with increasing particle concentration, the α relaxation occurs at a higher frequency range, which can be explained by the decrease of the diffusion length in the presence of neighbouring particles. The relative changes in tan(θ) reflect the electrical polarisation density caused by the polarisation of the double layers, and increase with increasing particle concentrations.

Finally, the ionic concentration effect studied in KCl solution shows that a high ionic concentration is unfavourable for detecting the particle size effect within the suspensions with low absolute value of zeta potential. A good method to overcome the problem is to get a high |ξ| by adjusting the pH value and measuring the electrical impedance spectra at a high frequency range (> 10 MHz) using a suitable impedance analyzer.

Chapter 5
On-line Characterisation of Crystallisation Processes with Electrical Impedance Spectroscopy

Summary: The method of on-line characterisation of colloids with electrical impedance spectroscopy for the crystallisation process is demonstrated in this chapter. On-line measured electrical impedance spectra associated with L-glutamic acid (LGA) nucleation-growth processes are presented and analysed. The information content of the electrical impedance, phase angle and relaxation frequencies of the crystal suspensions during the crystallisation process are assessed. Polymorphism of LGA in crystallisation is studied by the on-line impedance measurement and the off-line optical microscopic method.

5.1 Introduction

Crystallisation processes are common unit operations in the pharmaceutical and special fine-chemicals industries. On-line monitoring or even controlling of the crystal size and shape during crystallisation process is important because the size and shape of crystals have significant effects on downstream operations such as filtration, drying, transport and storage. The on-line analytical techniques for crystal sizing have been reviewed in Chapter 2. As a comparatively new technique, the electrical impedance spectroscopy (EIS) method is proposed to on-line measure the particle size relying on the presence of an electrical double layer associated with the charged particle surface. One of the advantages of the EIS method is that it can be applied in high concentration suspensions since the electrical signal is stronger from high concentration suspensions comparing optical methods. Another valuable advantage is that the EIS method has a potential to be developed to an electrical impedance tomography spectroscopy (EITS) technique and hence to measure the particle size distribution in two or even three spatial dimensions with a high temporal resolution, so called dynamic imaging of particle size distribution.

However, challenges in the study of the crystallisation process exist because crystallisation is a dynamic process, in which several factors (including the

concentration of the solid LGA phase, the concentration of solute, temperature and crystal size) change simultaneously with time. The first challenge is that it is difficult to extract the information of crystal size from the measured impedance data since it always accompanies with the effects from other factors. Therefore, a series of experiments was designed to study the effects of relevant factors on the impedance spectra by changing one factor and fixing other factors constant. The experimental details are described in section 5.2. The second challenge is that the solid LGA concentration and solute concentration cannot be measured on-line due to the limitation of the instruments in the study. Therefore, only the qualitative analysis was targeted in the study. The third challenge is that the EIS measurement over a wide range of frequencies (1Hz to 32MHz) takes about 2.5 minutes using the available EIS facility. Within that time, the properties of crystal suspension change very quickly. Thus, some errors are expected in the EIS measurement. In order to decrease the time consumed by scanning the process with a wide range of frequencies, an impedance measurement using a fixed frequency was chosen to study the changing of impedance parameters (real part, imaginary part and phase angle) with time in the crystallisation process. Unfortunately, the impedance measurement at a fixed frequency cannot provide the information of the relaxation frequency. This difficulty might be solved by the improvement of hardware in the future, which will be further discussed in Chapter 7.

This chapter reports the results of on-line electrical impedance spectroscopy measurement during L-glutamic acid crystallisation processes. The aim is to study the feasibility, applicability and challenges in the use of the proposed method on characterising the crystal size and morphology, as well as to analyse the effects of different factors, including temperature, solid concentration and ionic concentration, on electrical impedance spectra.

5.2 Methodology

The basic strategy of the crystallisation experiments has been described in Chapter 3, section 3.5. In this section, the details of crystallisation experiments are presented according to different purposes.

Since the growth of crystal size during the crystallisation process is not the only factor which may cause the change of electrical impedance spectra, it is necessary to study

the effects from other factors separately (including the temperature, solid LGA concentration and solute concentration) by changing one factor and keeping other factors constant. Firstly, in order to study the contribution of solid LGA phase to the change in impedance parameters (real part, imaginary part, phase angle and relaxation frequency), experiments with a series of known LGA solid concentrations were carried out. A saturated LGA solution made with a concentration of 7.2 g/L at room temperature (20 °C) was prepared. By adding different amounts of solid LGA, solutions with different concentrations of solid LGA (0 g/L, 2.94 g/L, 5.88 g/L, 8.82 g/L, 11.76 g/L, 14.7 g/L) were obtained and then the electrical impedance spectra of these solutions at a constant temperature (20 °C) were measured. Secondly, in order to study the solute concentration effect on impedance parameters, the under-saturated LGA solutions with different concentrations (1.916 g/L, 3.833 g/L, 5.749 g/L, 7.664 g/L, 9.580 g/L) were prepared and the electrical impedance spectra of these solutions at a constant temperature (20°C) were studied. Thirdly, the effect of temperature was studied in two different processes: crystallisation and non-crystallisation. The study on the non-crystallisation process was carried out using an LGA solution with a concentration of 5.0 g/L. By cooling the LGA solution from 60 °C to 10 °C at the rate of 0.68 °C/min, the effect of temperature on EIS was investigated in the absence of phase separation since in that temperature range, the solution remains under-saturated and no crystallisation occurs. The study of the crystallisation process was carried out using a saturated LGA solution with a concentration of 21.9 g/L at 60 °C. Similarly, by cooling the LGA solution from 60 °C to 10 °C at the same rate (0.68 °C/min), the effect of temperature on EIS can be studied.

After finishing the study on the different factors, the crystallisation process was monitored on-line using EIS and the changes of electrical impedance parameters with the crystal size were studied. The experiment was carried out using 21.9 g/L LGA solution (Sigma-Aldrich Chemicals). The crystallisation was firstly achieved by cooling the LGA solution from 60 °C to 10 °C at a rate of 0.68 °C/min and the impedance spectra at different temperatures were measured. Then the experiment was carried out by cooling the LGA solution from 60 °C to 10 °C at a rate of 0.40 °C/min and the changing of impedance parameters at a fixed frequency (1 MHz) were recorded. The crystal morphologies at the early stage and late stage of crystallisation were observed off-line by the optical microscope. The crystal sizes were measured on-line by using focused beam reflectance measurement (FBRM). Temperature and turbidity profiles were recorded on-line using temperature and turbidity sensors.

The above crystallisation processes produce single α form of L-glutamic acid. In order to study the polymorphism of LGA and minimise the temperature effect, two experiments were designed. In the first experiment, a crystallisation process, which can produce a single α form with prismatic shape, was carried out by heating the LGA solution with a initial concentration of 21.9 g/L to 70 °C and then cooled down to 30 °C by a rate of 0.97 °C/min. Then the temperature was kept at 30 °C and crystallisation occurred after an induction time. In the second experiment, a crystallisation process, which can form two crystal morphologies (α form and β form) and involve a polymorphic transformation process, was carried out by heating the LGA solution with an initial concentration of 48 g/L to 80 °C and then cooled down to 60 °C by a rate of 0.91 °C/min. The temperature was kept at 60 °C during the whole process of crystallisation. The stirring was kept constant with 400 rpm in these two experiments. The morphologies of crystals were measured off-line using the optical microscope at the different stage of crystallisation. The electrical impedance parameters (Z', Z" and θ) were measured on-line at 1 MHz to study the effect of polymorphs. A flow chart given by Figure 5.1 summarizes the experimental procedure.

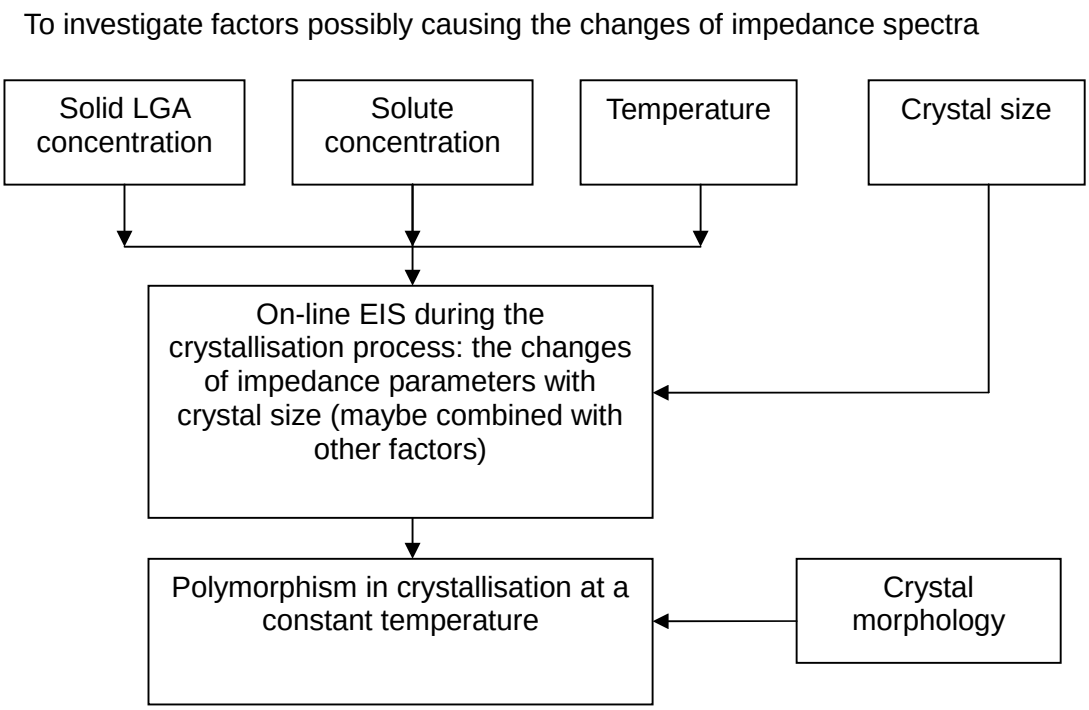

Figure 5.1: Flow chart of the experimental procedure

5.3 Effect of Solid LGA Concentration

The electrical impedance spectra from different concentrations of solid LGA phase in a saturated solution at 20 °C are shown in Figure 5.2. The complex impedance plot reverses the order of the data with respect to frequency so that the low frequency data are at the right of Figure 5.2 (a) and frequency increases towards the left of the plot. Two features can be observed in the complex impedance plot: several small arcs at about 1 Hz – 1000 Hz and larger arcs at higher frequency ranges. The reason for the small arc is probably due to the electrode polarisation (Dudley et al., 2003) effect at the electrode/solution interface. Although the electrode polarisation effect can be decreased significantly by using a four-electrode sensor, it might not be fully eliminated (Stoneman et al., 2007). The big arc is the characteristic of dielectric dispersion in the crystal suspension, which reflects the polarisation of charged crystals under the applied electric field. If the small arc is neglected and the big arc is assumed a regular semicircle, then a parallel RC equivalent circuit can be used as a static model to simulate the EIS results. The analysis is qualitative since the assumption of a semicircle is idealised.

The impedance of parallel RC circuit can be expressed by Equation (4.4), which has been given in the Chapter 4, section 4.3.1:

$$Z = \frac{1}{Y} = \frac{R}{1 + j\omega RC} = \frac{R}{1 + (\omega RC)^2} - j\frac{\omega R^2 C}{1 + (\omega RC)^2} \tag{4.4}$$

where, R is the resistance, C is the capacitance, and ω is the frequency.
The impedance imaginary part is a function of frequency:

$$Z''(\omega) = -\frac{\omega R^2 C}{1 + (\omega RC)^2} \tag{4.6}$$

As analysed in Chapter 4, section 4.3.1, the impedance imaginary part reaches a minimum value at the relaxation frequency, which can be expressed by Equation (4.9):

$$\omega_{relaxation} = \frac{1}{RC} \tag{4.9}$$

The relaxation frequency can be obtained from the peak position in Figure 5.2 (c).

From Figure 5.2 (b), it can be seen that in the high frequency range (300 kHz-20 MHz),

the impedance real parts do not show significant change with increasing the concentration of the solid LGA phase. However, in the low frequency range (1 Hz-100 kHz), the impedance real parts decrease a small amount (less than 20 ohm) with addition of the solid LGA phase. The small change is probably caused by a slight modification of the ionic concentration in the suspensions since the increase of solid LGA concentration might affect the dissociation of L-glutamic acid in aqueous solution.

From Figure 5.2 (c), it can be seen that the relaxation frequencies do not change with increasing the concentration of solid LGA phase. Similarly, the impedance imaginary parts showed no significant change with increasing amounts of the solid LGA phase. Figure 5.2 (d) shows that with increasing concentration of the solid LGA phase, the impedance phase angle maintains almost a constant value. Therefore, it can be concluded that there is no significant effect of solid LGA phase on $\omega_{relaxation}$, values of *Z*" and phase angle (θ) over the frequency range investigated.

Since the impedance imaginary part and phase angle show peaks at a high frequency range (>100 kHz), the impedance parameters (Z', Z" and θ) are further analysed at the fixed frequency (1 MHz) to understand the effect from solid phase concentration. Table 5.1 shows the data of the impedance real part, imaginary part, and phase angle at 1 MHz from crystal suspensions with different solid phase concentrations. The results demonstrate that at 1 MHz, the impedance parameters have no significant change with increasing solid phase concentration.

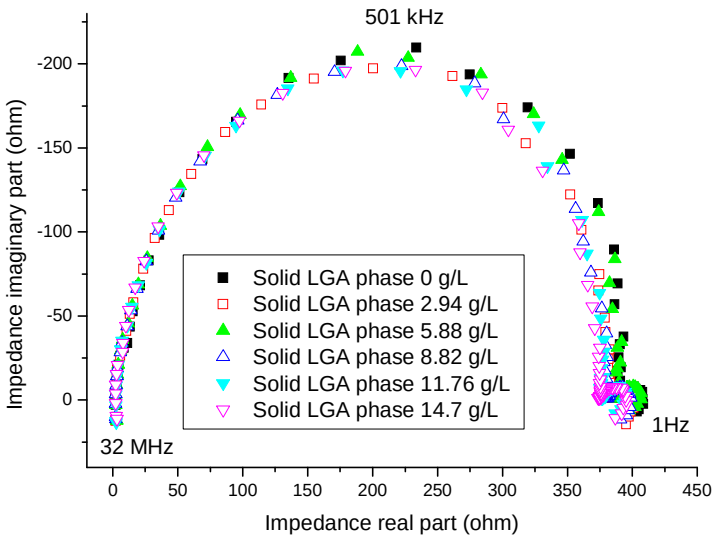

(a) the complex impedance plot

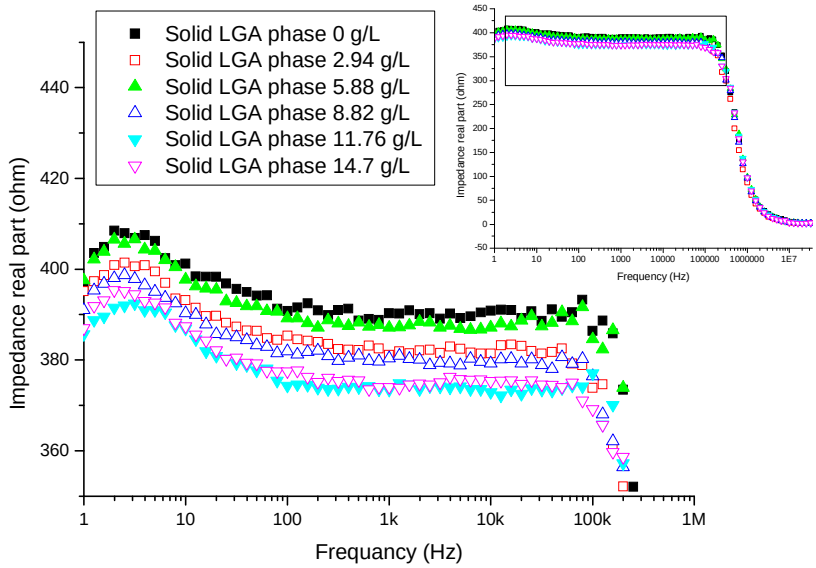

(b) impedance real part vs. frequency plot

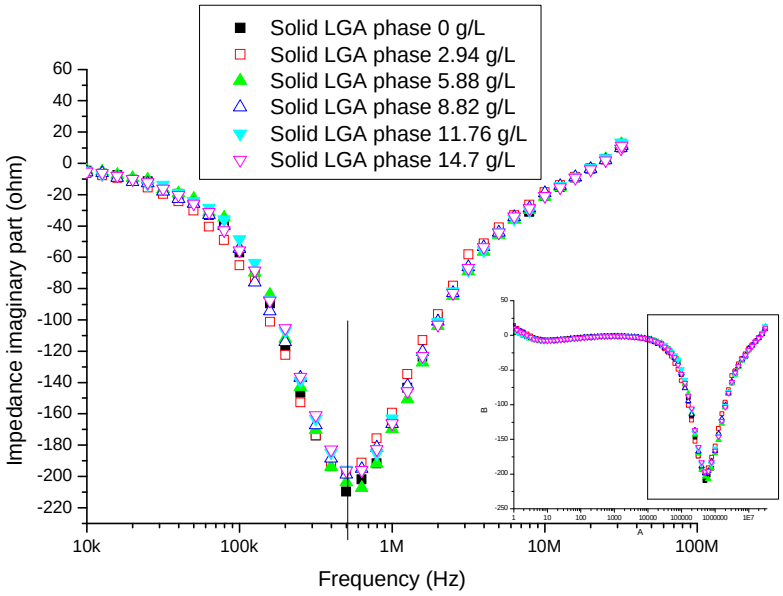

(c) impedance imaginary part vs. frequency plot

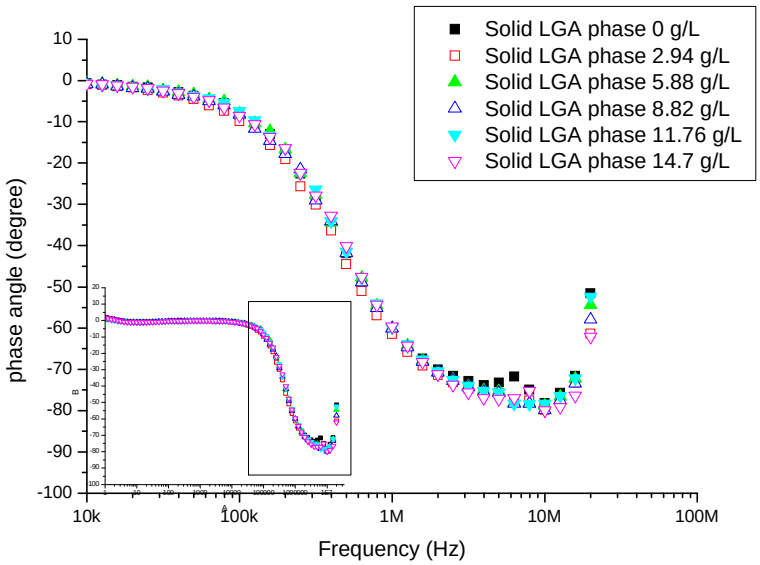

(d) impedance phase angle vs. frequency plot

Figure 5.2: (a) complex impedance plot; (b) impedance real part vs. frequency; (c) impedance imaginary part vs. frequency; (d) impedance phase angle vs. frequency plots in the saturated LGA solutions with different concentration of solid LGA phase

Table 5.1: the impedance data at 1 MHz in crystal suspensions with different solid phase concentration

Crystal concentration (g/L)	**Impedance real part (ohm)**	**Impedance imaginary part (ohm)**	**Phase angle (degree)**
0	95.014	-165.603	-60.155
2.94	96.743	-159.446	-61.453
5.88	97.903	-169.719	-60.021
8.82	96.074	-166.446	-60.006
11.76	96.999	-165.209	-59.582
14.70	97.423	-166.180	-59.619

5.4 Effect of Solute Concentration

The effect of solute concentration is studied with an under-saturated LGA solution at 20 °C. The electrical impedance spectra for different solute concentrations in under-saturated solutions at 20 °C are shown in Figure 5.3. The Cole-Cole plot (Figure 5.3 (a)) is similar to the one in Figure 5.2 (a). From Figure 5.3 (b), it can be seen that at the frequency range from 1Hz-100 kHz, the impedance real parts decrease with increasing LGA solute concentration. Since all of the tested solutions are under-saturated, no crystal particles are present and the effect is due to the change in ionic concentration. Higher ionic concentrations in the solution cause higher conductivity or lower impedance real part. Figure 5.3 (c) shows the solute concentration effect on impedance imaginary part. It can be seen that the relaxation frequencies decrease a small amount with decreasing ionic concentrations. The relaxation might be explained by the kinetic polarisation model, in which a hydration shell of water molecules forms around a solute ion, and the water molecules tend to reorient in order to face the opposite charge of ion in the centre (Wei et al., 1992). In addition, at the low frequency range (<100 kHz), the values of the impedance imaginary part, Z", manifest no significant changes with decreasing solute concentration. However, at the higher frequency range (>100 kHz), the absolute values of Z" increase with decreasing ionic concentration. Figure 5.3 (d) shows that with increasing solute concentration, the absolute values of phase angle do not change significantly.

In a way similar to the case presented in section 5.3, the impedance parameters (Z', Z", and θ) are further analysed at a fixed frequency (1 MHz). Table 5.2 shows the data of the impedance real part, imaginary part, and phase angle at 1MHz in solutions with different solute concentrations. The results show that the impedance imaginary part and phase angle decrease with decreasing solute concentration. However, with decreasing solute concentration, the impedance real part increases firstly and then decreases showing a maximum value at a solute concentration of 4 g/L.

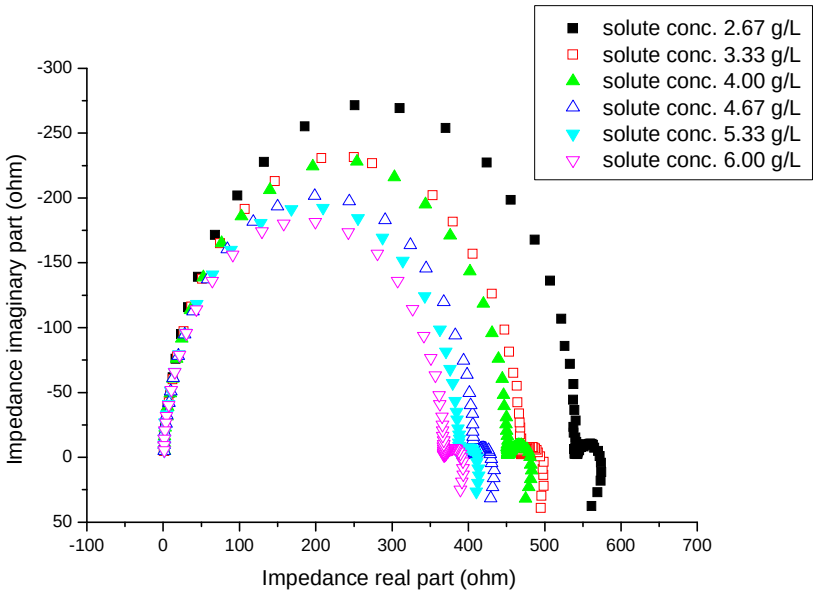

(a) the complex impedance plot

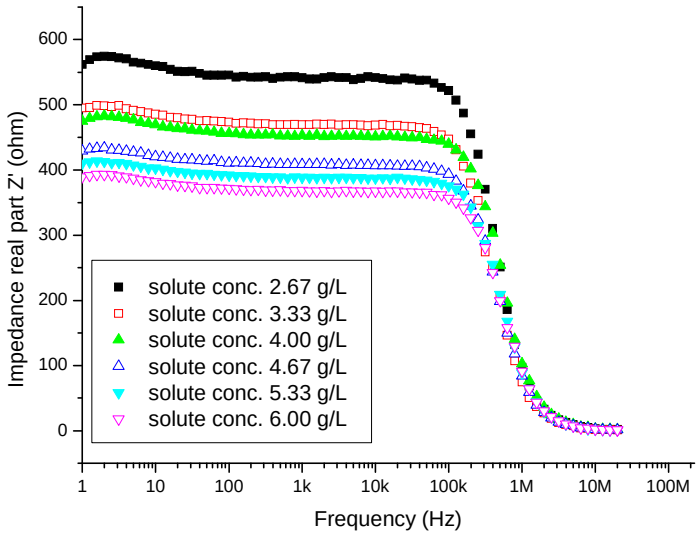

(b) impedance real part vs. frequency plot

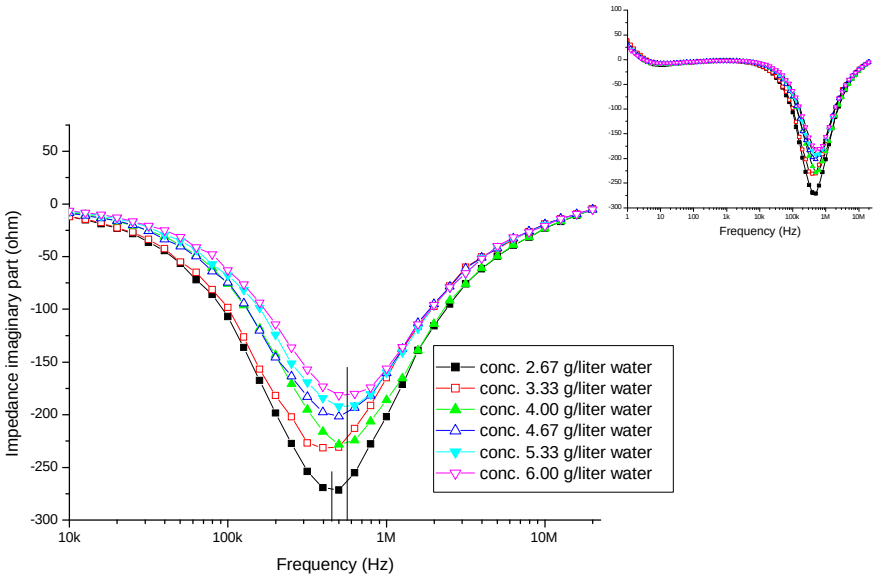

(c) impedance imaginary part vs. frequency plot

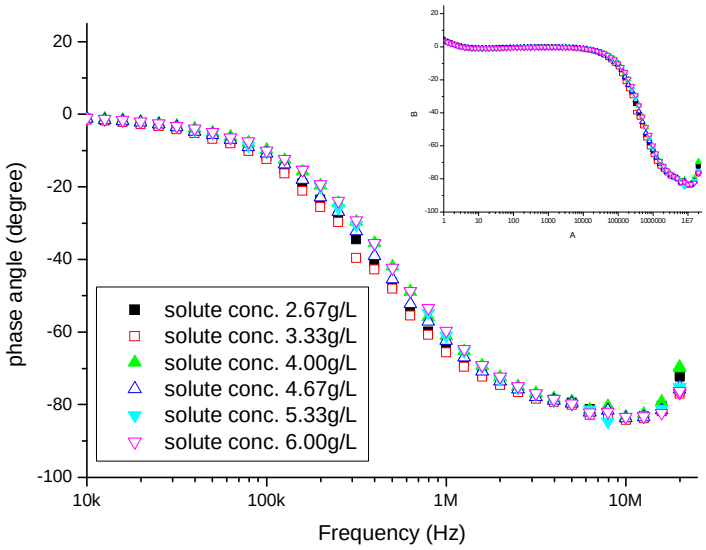

(d) impedance phase angle vs. frequency plot

Figure 5.3: (a) complex impedance plot; (b) impedance real part vs. frequency; (c) impedance imaginary part vs. frequency; (d) impedance phase angle vs. frequency plots in the unsaturated LGA solutions with different LGA solute concentration

Table 5.2 the impedance data at 1 MHz in unsaturated LGA solutions with different solute concentration

LGA Solute concentration (g/L)	Impedance real part (ohm)	Impedance imaginary part (ohm)	Phase angle (degree)
2.67	97.324	-201.846	-64.258
3.33	74.949	-165.039	-65.576
4.00	102.796	-185.841	-61.051
4.67	84.135	-160.458	-62.330
5.33	88.854	-160.013	-60.957
6.00	91.428	-156.287	-59.672

5.5 Effect of Temperature

The temperature effect on the relaxation frequency was studied in aqueous LGA solutions under the conditions of crystallisation and non-crystallisation. The results are shown in Figure 5.4. In the temperature interval from 50.0 °C to 25.6 °C, the relaxation frequency decreases a large amount when the nucleation and growth are occurring in the solution compared with the case where there is no nucleation and growth. It has been demonstrated that the change of the relaxation frequency is essentially independent to the solid phase concentration; therefore the decrease of $\omega_{relaxation}$ may be mainly attributable to the change of crystal sizes and partially attributable to the change of ionic concentration that occurs in the LGA crystallisation process.

The temperature effect on the impedance real part and imaginary part was studied and the results are presented in Figure 5.5 (the change of Z' and Z" during LGA (21.9 g/litre) crystallisation process) and Figure 5.6 (the change of Z' and Z" without crystallisation (5.0 g/litre LGA solution)). Comparing these two figures, it can be seen that the impedance imaginary part decreases with temperature with an approximately linear relationship in the non-crystallising LGA solution. However, in the crystallising LGA solution, the impedance imaginary part does not show a linear relationship with temperature. The impedance imaginary part decreases more rapidly at temperatures below the start-point of the nucleation. The change of slope in Z" is probably due to two effects, the decreasing solute concentration and the increasing crystal size because the solid concentration effect on Z" is very small and the temperature gradients are almost

the same in the two cases. In both Figures 5.5 and 5.6, the impedance real parts (Z') increase with decreasing temperature, but the variation of Z' is much smaller than the variation of Z".

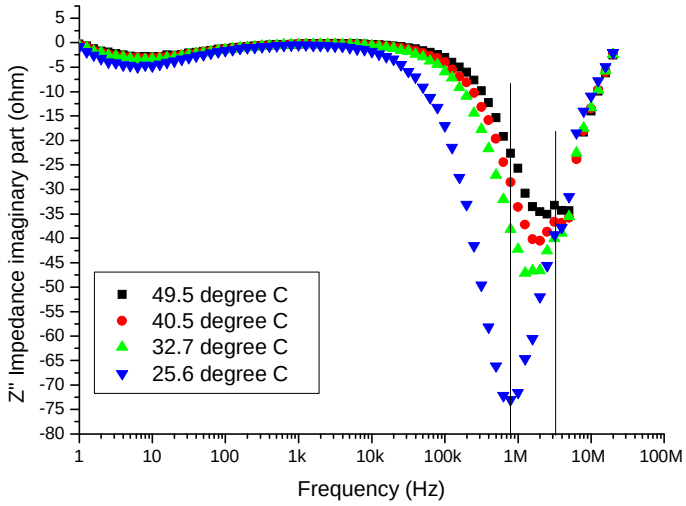

(a) during crystallisation process

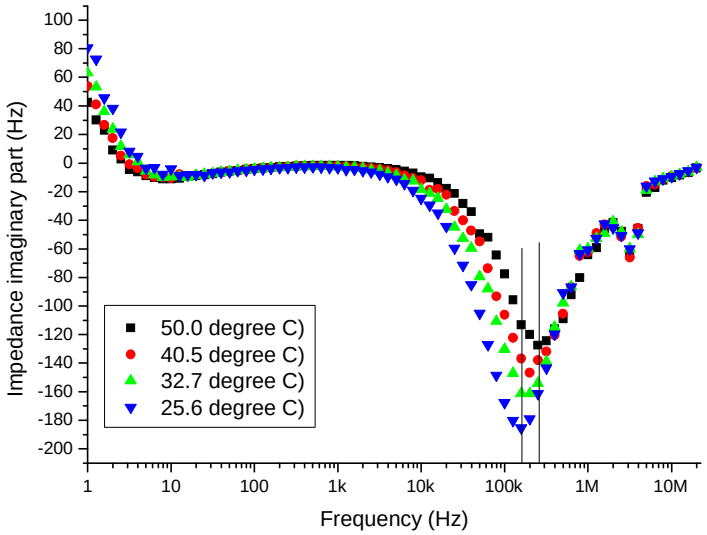

(b) without crystallisation process

Figure 5.4: impedance imaginary part vs. frequency plot of LGA solution (a) during the crystallisation process; (b) without the crystallisation process at 50.0 °C, 40.5 °C, 32.7 °C, and 25.6 °C

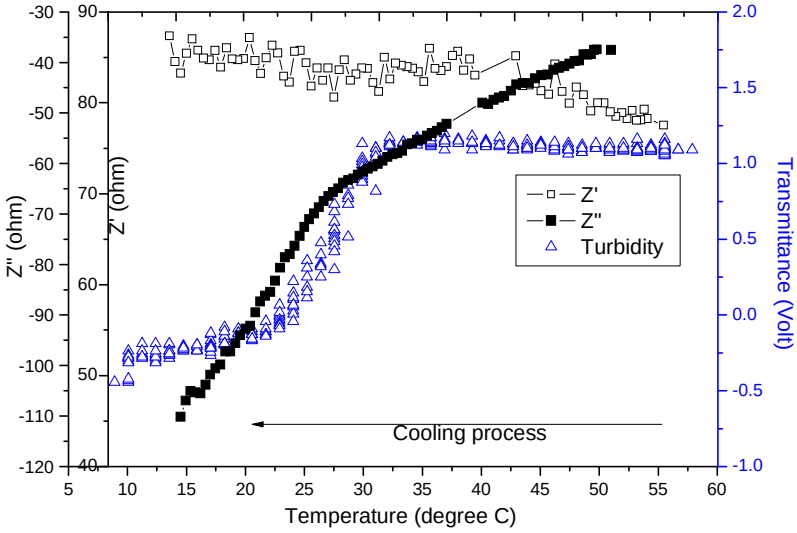

Figure 5.5: Change of impedance (Z' and Z") at frequency 1259 kHz and turbidity with temperature during LGA crystallisation

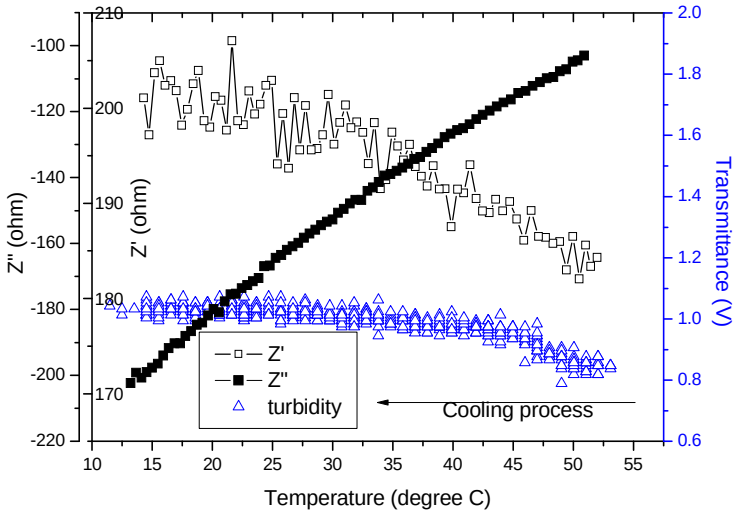

Figure 5.6: Change of impedance (Z' and Z") at frequency 631 KHz and turbidity with temperature without the crystallisation process

5.6 On-line EIS during Crystallisation Processes

5.6.1 Electrical Impedance Spectra

Figure 5.7 shows the temperature and turbidity profiles associated with the LGA crystallisation during a cooling process. It can be determined from Figure 5.7 that the nucleation started at about 30 °C and the crystallisation was almost completed at 10 °C. The cooling rate from 50 °C to 10 °C can be calculated using the temperature profile by linear fitting of the temperature values from a time of 1500 seconds to 5000 seconds. The fitting result is shown in Figure 5.8, and the calculated cooling rate is 0.68 °C/min.

The crystal morphology was observed during the crystallisation process using the off-line optical microscope measurements. From the microscopic pictures (Figures 5.9 and 5.10), it can be seen that only the α-form exists during the whole crystallisation process. At the late stage of crystallisation, aggregation occurs, it can be observed that several prismatic shape crystals bind together and form a large particle with an irregular shape.

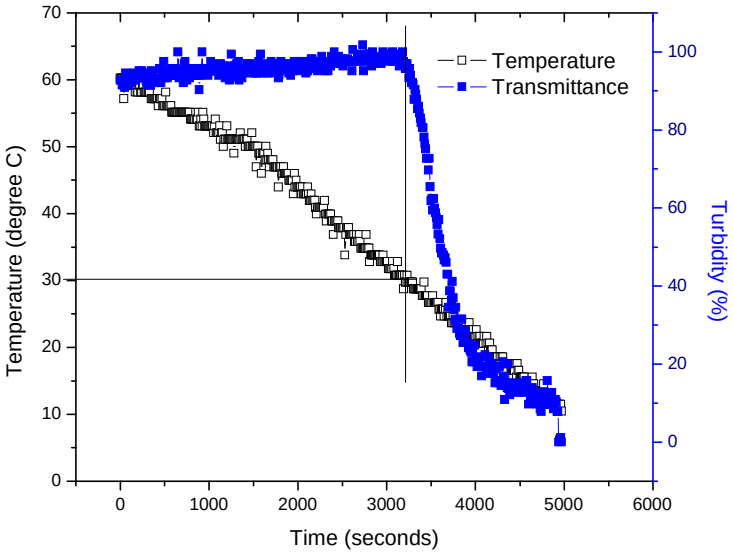

Figure 5.7: Temperature and turbidity profiles

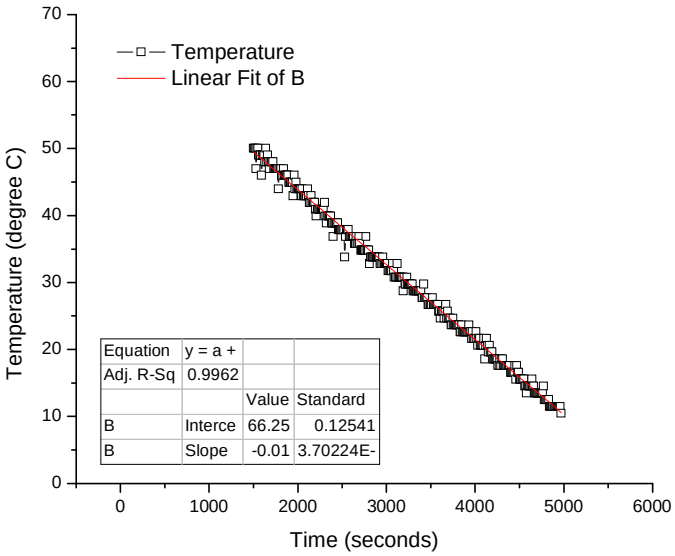

Figure 5.8: Linear fitting result for temperature profile

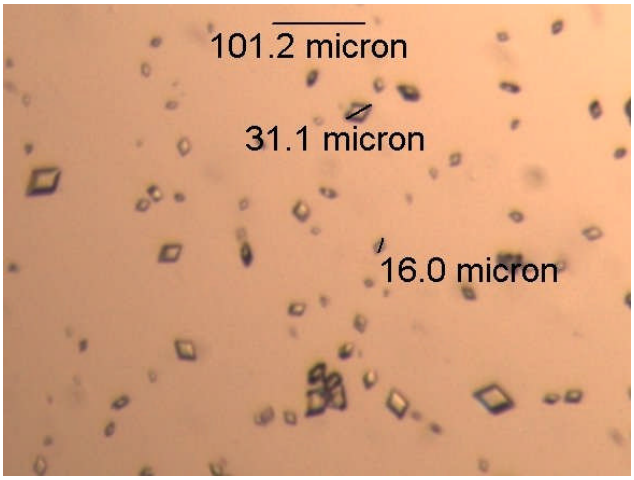

Figure 5.9: Crystal morphology at the early stage of crystallisation

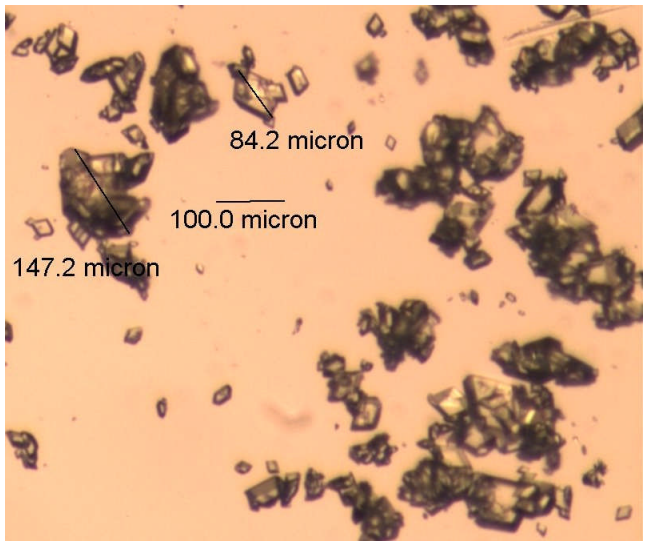

Figure 5.10: Crystal morphology at the late stage of crystallisation (around 10 °C)

The electrical impedance spectra of an LGA solution (21.9 g/L) during the cooling process were recorded on-line. Figure 5.11 shows the electrical impedance spectra of the LGA solutions at 50.7 °C, 40.0 °C, 29.5 °C and 19.5 °C, respectively. The temperatures recorded are the temperatures at the start-point of the EIS scan. The measurement of electrical impedance spectra from 1 Hz to 20 MHz takes around 2.5 minutes, and the temperature of the LGA solutions change during the elapsed time. However, since it is difficult to obtain the average temperature during a spectrum measurement, the temperature at the start-point is used to indicate the solution temperature associated with a particular spectrum.

Figure 5.11 (a) shows a typical complex impedance plot which is similar to Figure 5.2 (a). It is apparent that with decreasing temperature the impedance real part (Z') increases and the impedance imaginary part (Z") decreases. In the temperature interval from 29.5 °C to 19.5 °C (the range over which crystallisation occurred), the changes in Z' and Z" become more significant. In Figure 5.11 (b), it can be seen that the increase in the real part of impedance with decreasing temperature becomes larger when nucleation and growth are occurring in the temperature interval from 29.5 °C to 19.5 °C. In this temperature range, the nucleation and growth of crystals occurs very quickly, therefore, the increasing solid phase concentration and decreasing ionic concentration occur spontaneously. As discussed in sections 5.3 and 5.4, impedance real parts are related to the solid phase concentration and solute LGA concentration. In addition, it has been demonstrated in section 4.3.1 that the impedance real parts increase with increasing particle size at a plateau range of frequencies (f <100 kHz).

Thus, the significant increase of impedance real parts during the crystallisation process (29.5 °C -19.5 °C) might be caused by three factors, including the solid phase concentration, solute LGA concentration and the crystal size.

From Figure 5.11 (c), it can be seen that the relaxation frequency ($\omega_{relaxation}$) decreases with decreasing temperature. However, in the temperature interval from 29.5°C to 19.5°C (the range over which crystallisation occurred); the decrease in relaxation frequency becomes much more significant than the one in the temperature intervals from 50.7°C to 40.0°C and from 40.0°C to 29.5°C, respectively. Since the effect of solid phase concentration is very small and therefore can be ignored, the significant decrease of relaxation frequency during crystallisation might be caused by the combination of effects from crystal size and ionic concentration. From the results shown in section 5.4, the changes of ionic concentration show a relatively large effect on the values of the impedance imaginary part but a small effect on the relaxation frequencies. The dependence of $\omega_{relaxation}$ on the crystal size is similar to the case in silica suspensions, which can be explained in terms of the polarisation of the counter ions in the diffuse double layer (DDL) associated with the crystalline particles.

As illustrated in Figure 5.11 (d), the absolute values of phase angle increases with decreasing temperature. The phase angle is related to the electrical polarisation of the double layer around the crystals. As discussed in Chapter 4, section 4.4.2, the relative change of phase angle is a function of particle size. However, in a crystallisation process, the temperature, solid phase concentration, and solute concentration all change with time, therefore, the quantitative analysis using the theoretical model shown in section 4.4.2 is unrealistic. Based on the analysis in sections 5.3 and 5.4, the change of phase angle is mainly caused by the changes of temperature and crystal size.

In order to establish the variation in relaxation frequencies during nucleation and growth, the relaxation frequencies were measured and recorded throughout the temperature interval from 17.5 to 52.0°C. Figure 5.12 shows how the relaxation frequencies change with temperature and the corresponding changes in turbidity. It can be seen that the relaxation frequency does not change significantly at the higher temperatures (41°C - 52°C) i.e. above the onset temperature for crystallisation. However, it can be noticed that the decrease in the relaxation frequency becomes more rapid below 41°C. As shown in Figure 5.8, the temperature gradient is almost constant between temperature ranges of 50-10 °C. Thus, the rapid change in $\omega_{relaxation}$ from

41 °C is linked to crystal nucleation and growth in solution. Because the turbidity sensor shows the starting-point of crystallisation is about 30 °C, it is proposed that the EIS measurement may have higher sensitivity for the detection of the starting-point of nucleation than a turbidimetric approach. It is possible, since there is a time lag in detection of the start of nucleation due to the sensitivity of the optical turbidity probe while the crystals grow to a detectable size (De Anda et al., 2005). Since the solid phase concentration makes no significant contribution to the decrease in $\omega_{relaxation}$ and the temperature gradient is constant, the change in $\omega_{relaxation}$ may reflect an increase in crystal size if the small effect from ionic concentration could be excluded. In Figure 5.12, the relaxation frequency does not change significantly at the higher temperatures (41–52 °C), but decreases rapidly below 41 °C. An almost constant rate of decrease in the relaxation frequency of about - 41.7 kHz/°C was observed in the temperature range from 41 °C to 17 °C, which is evidence of the relaxation frequency being related to the crystal size.

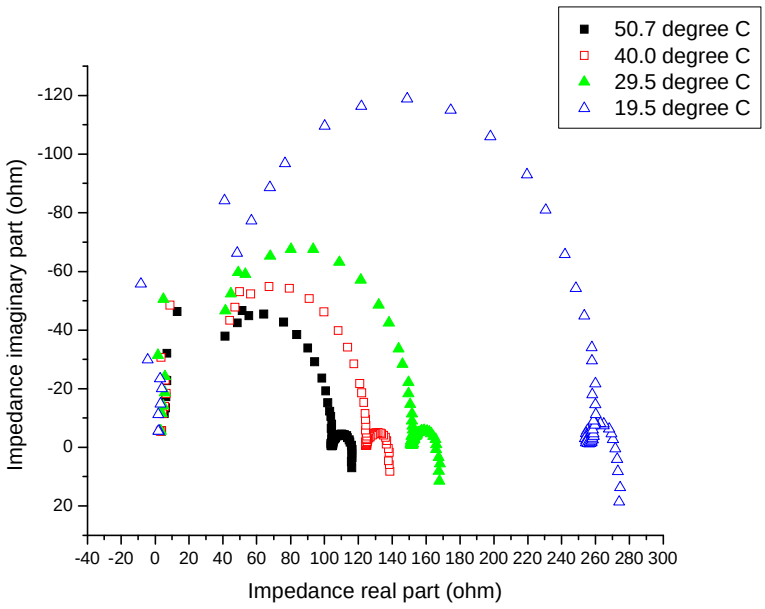

(a) the complex impedance plot

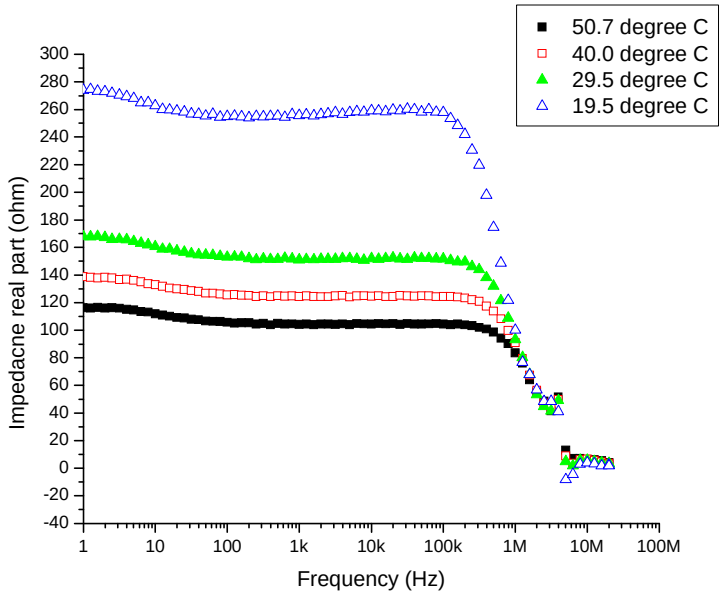

(b) impedance real part vs. frequency plot

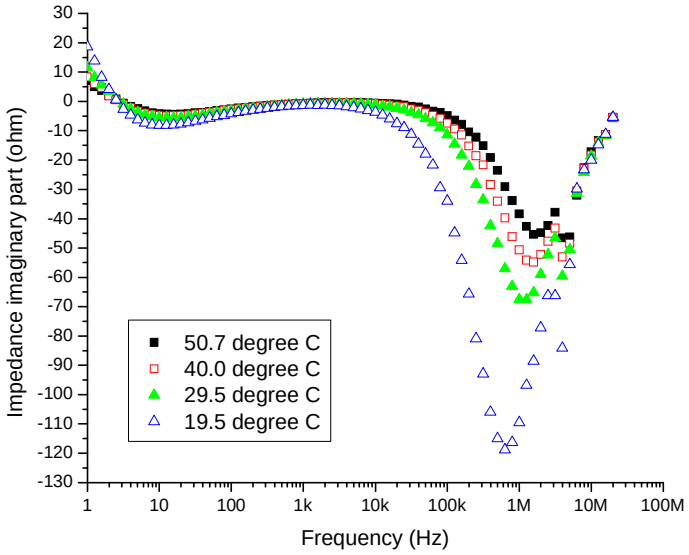

(c) impedance imaginary part vs. frequency plot

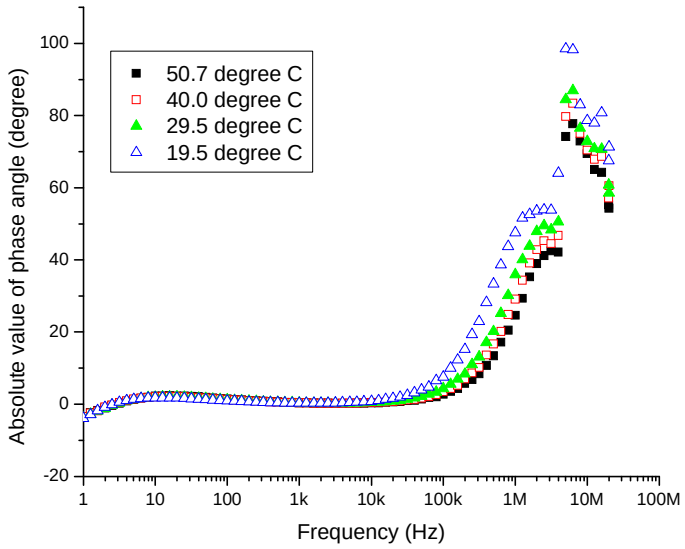

(d) impedance phase angle vs. frequency plot

Figure 5.11: (a) complex impedance plot; (b) impedance real part vs. frequency; (c) impedance imaginary part vs. frequency; (d) impedance phase angle vs. frequency plots of LGA solution during crystallisation process at 50.7 °C, 40.0 °C, 29.5 °C, and 19.5 °C

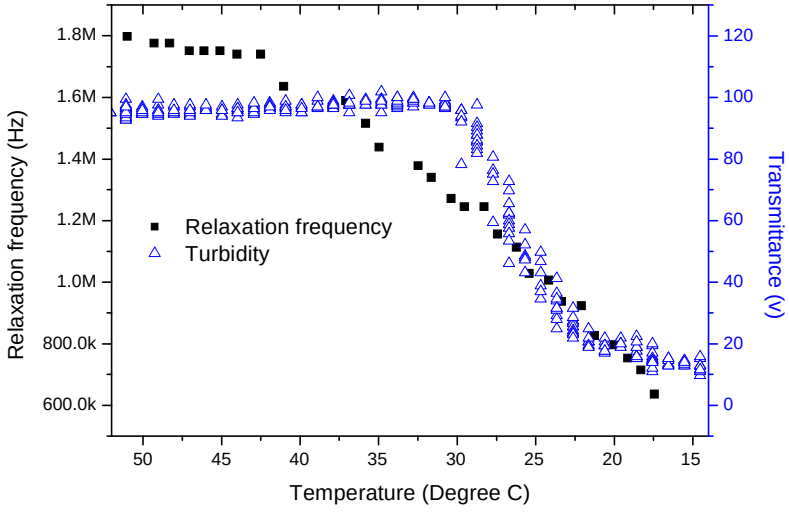

Figure 5.12: Relaxation frequencies change with temperature during LGA crystallisation processes

5.6.2 Electrical Impedance Parameters Changing with Time

In order to decrease the time consumed by measuring the electrical impedance spectra with a wide range of frequencies, an impedance measurement using a fixed frequency was used to study the changes of impedance parameters (real part, imaginary part and phase angle) with time in the crystallisation process. In this section, the electrical impedance parameters measured at 1MHz during a crystallisation process are analysed.

The temperature and turbidity profiles in the crystallisation process are shown in Figure 5.13. The cooling rate can be calculated by linear fitting of the temperature profile from 0-7500 seconds. The fitting result is shown in Figure 5.14, and the calculated cooling rate is 0.40 °C/min. From the turbidity profile, it can be seen that the starting-point of crystallisation is at about 33 °C. The crystal morphology was observed from the microscopic pictures (Figures 5.15 and 5.16). It can be seen that only the α form exists during the whole crystallisation process. At the late stage of crystallisation, aggregation occurs similar with the case shown in section 5.6.1.

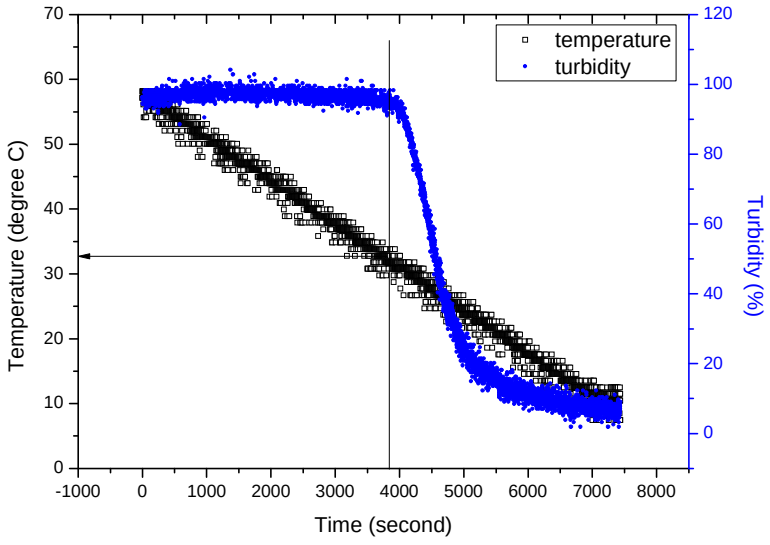

Figure 5.13: Temperature and turbidity profiles during crystallisation with a medium cooling rate

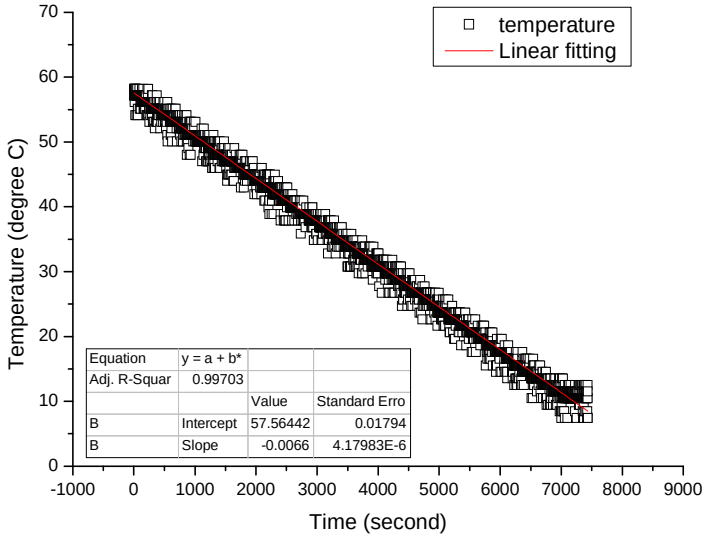

Figure 5.14: Linear fitting result for a temperature profile with a medium cooling rate

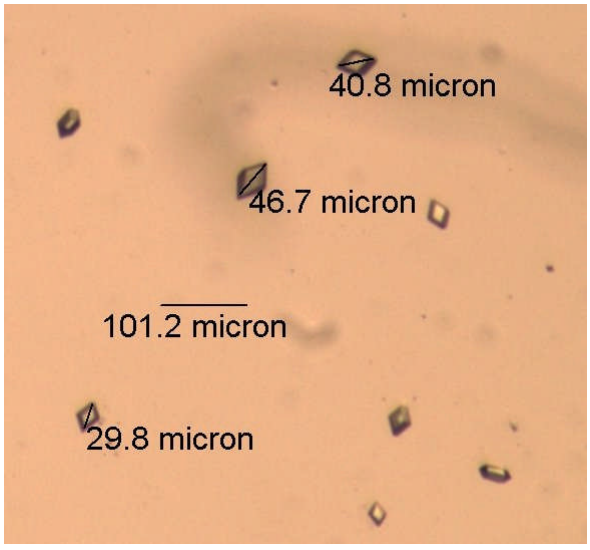

Figure 5.15: crystal morphology at the early stage of crystallisation with a cooling rate of 0.40 °C/min

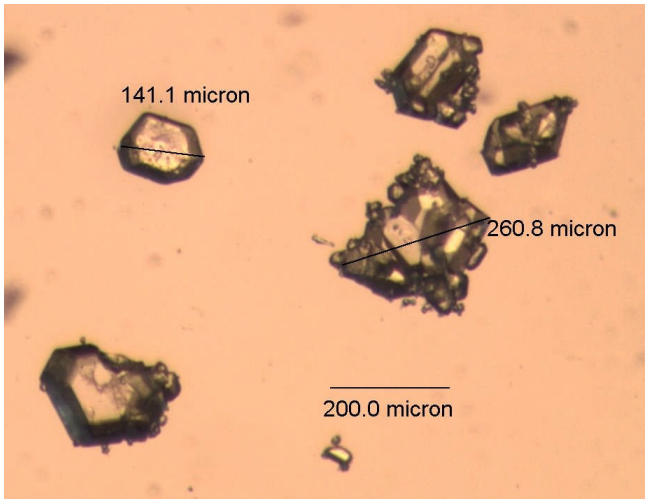

Figure 5.16: crystal morphology at the late stage of crystallisation with a cooling rate of 0.40 °C/min

Figure 5.17 shows the profiles of turbidity and FBRM chord length distributions during the crystallisation with a cooling rate of 0.40 °C/min. It can be seen that both turbidity and FBRM measurements give the same starting-point of crystallisation. At the early stage of crystallisation, the particle counts increases with time. At the late stage of crystallisation, the particle counts of 1-5 μm,10-23 μm and 100-251 μm remain almost constant, but the particle counts of 29-86 μm kept increasing. The chord length distributions at different stages of crystallisation (at 3800, 4500, 5500, 3000, 7435 seconds) are measured by FBRM and the results are shown in Figure 5.18. It can be seen from Figure 5.18 that from 3800 to 5500 seconds, the primary crystal size increases significantly. After 5500 seconds, the crystal size distribution shows no significant change although the number percentage still increases.

Figure 5.19 shows the change of impedance real part (Z'), imaginary part (Z") and phase angle (θ) at the frequency of 1MHz during the crystallisation with a cooling rate of 0.40 °C/min. From Figure 5.19, it can be found that the tendencies of Z" and θ are very similar, i.e. decrease slowly with decreasing temperature before nucleation, but the rate of decrease becomes faster after crystallisation starts. The impedance real part (Z') increases with decreasing temperature before nucleation, but the rate of increase becomes faster at the middle stage of the crystallisation (4500-5500 seconds). Z' reaches its greatest value at around 5500 seconds and decreases at the late stage of crystallisaton (5500-7435 seconds).

Here, the crystallisation is analysed in three stages: (1) the early stage (3800-4500

seconds); (2) the middle stage (4500-5500 seconds); (3) the late stage (5500-7435 seconds). The changing rates of Z', Z" and θ at the different stages are calculated using the linear fitting method and the results are shown in Table 5.3. EIS results in Figure 5.19 can be understood in conjunction with the chord length distribution analyses in Figure 5.18 and may be interpreted as follows:

- In stage (1), both particle sizes and particle counts increase with time. The nucleation and growth occurs in the early stage of crystallisation, similar to the phenomenon described in the literature (Mougin et al., 2003). EIS results in Table 5.3 show that the absolute values of the changing rates in Z', Z" and θ increase after nucleation occurs. The change in the rate of decrease of Z" and θ could be due to the decrease of solute concentration and increase of particle size, since the increase of solid concentration has almost no effect on impedance parameters (Z', Z" and θ) and the temperature gradient is constant.

- In stage (2), both particle sizes and particle counts increase continuously with time. The chord length distribution at 4500 and 5500 seconds show that the number of counts at channel of 29-86 μm is comparatively more than the other channels, which means growth of crystals is dominant at this stage accompanied by low nucleation. EIS results in Table 5.3 show that the absolute values of the changing rates in Z" and θ are significantly greater (roughly increase 2 times) compared with stage (1). This observation can probably be interpreted as due to the fast rate of decrease of solute concentration and increasing of particle size at this stage. In this stage, the rate of change in Z' becomes smaller compared with stage (1) and Z' reaches a maximum value at the end of this stage. It is believed that the main reason for this result is the decrease of solute concentration since the temperature gradient remains constant during this stage.

- In stage (3), only the number counts at channel of 29-86 μm continuously increased with time, which means that the crystal might grow continuously by consuming the small crystals (< 29 μm). The EIS results show that Z" and θ continuously decrease with time but the absolute values of changing rate in Z" and θ become smaller than those in stage (2). The impedance real part starts to decrease at this stage, which might be explained by the decrease of solute concentration. From the discussion in sections 5.3 and 5.4, the change of solid concentration shows no significant effect on impedance real part at high frequency (1 MHz). However, with decreasing solute concentration, the impedance real part

increases first and then decreases. In addition, from the discussion in Chapter 4, the particle size effect on impedance real part is insignificant at high frequency (such as 1 MHz). Therefore, the changing of Z' in the crystallisation process is mainly related to the decrease of solute concentration.

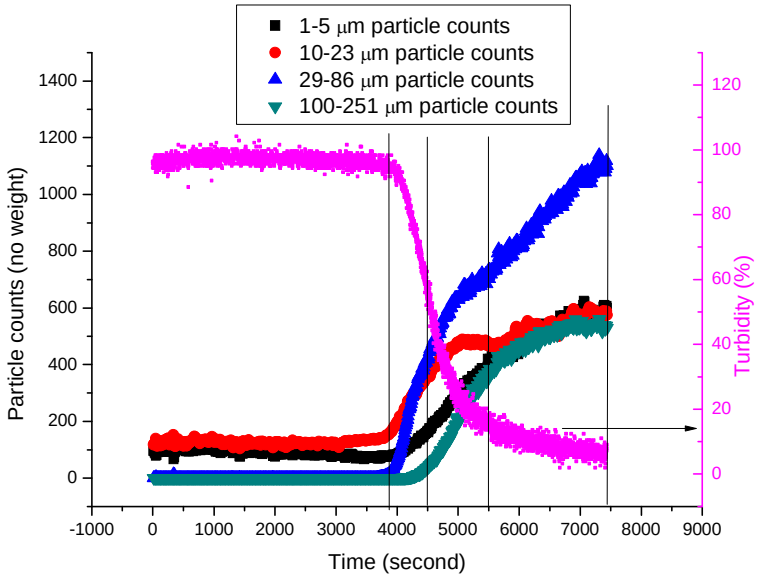

Figure 5.17: Profiles of turbidity and the FBRM chord length distribution during LGA crystallisation with cooling rate of 0.40 °C/min

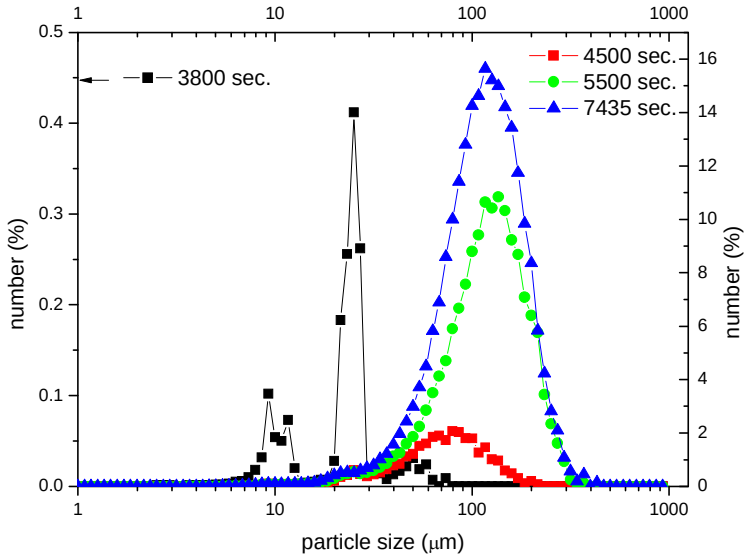

Figure 5.18: Chord length distributions at different stages of crystallisation (FBRM measurement) with a cooling rate of 0.40 °C/min

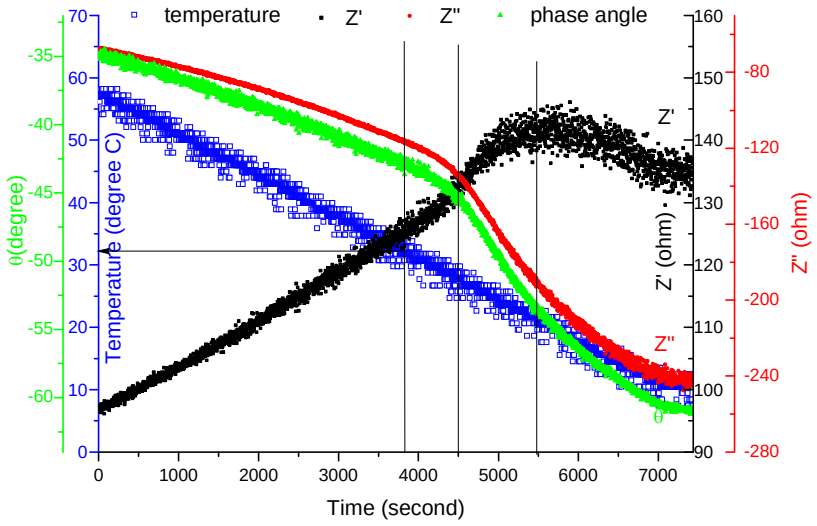

Figure 5.19: Change of impedance real part (Z'), imaginary part (Z"), and phase angle (θ) at frequency 1 MHz with time during LGA crystallisation with a cooling rate of 0.40 °C/min

Table 5.3: The changing rates of impedance parameters at the different stages in crystallisation process

Changing rates of impedance parameters	**dZ'/dt (ohm/second)**	**dZ"/dt (ohm/second)**	**dθ/dt (degree/second)**
Before nucleation (0-3800 seconds)	0.01827	-0.03113	-0.0051
Stage (1) (3800-4500 seconds)	0.02693	-0.07177	-0.0102
Stage (2) (4500-5500 seconds)	0.01707	-0.14185	-0.02043
Stage (3) (5500-7435 seconds)	-0.01079	-0.06279	-0.00925

5.7 Polymorphism in Crystallisation Processes

Polymorphism occurs in crystallisation processes when a molecule is able to pack in different ways and give rise to two or more crystal structures. Since the crystal morphology often represents a critically important property not only to the end-use functional properties, but also to downstream processing and handling of the product, there has been a growing interest in monitoring and controlling the crystal polymorphs during crystallisation processes, particularly in the pharmaceutical and fine chemical industries. The use of electrical impedance spectroscopy for studying crystal polymorphs on-line is novel. In this section, the crystallisation processes existing a single α form of L-glutamic acid and polymorphic transformation between the α form and β form are studied and compared using on-line EIS measurement. In order to eliminate the temperature effect, it was designed to carry out the crystallisation process at a constant temperature. In the experiments, the LGA solution was cooled down to a certain temperature (for example 30 °C) and holding constant temperature through the process. During the cooling phase, no nucleation could occur; hence the crystallisation process that follows after an induction time can be considered to be isothermal. The relationship between the polymorphic transformation and the impedance parameters (Z', Z" and θ) is discussed.

5.7.1 Crystallisation with a Single α Form

Figure 5.20 shows the temperature and turbidity profiles during crystallisation at a constant temperature of 30 °C. The cooling rate from 65 °C to 30 °C is 0.97 °C/min. From the changing of turbidity profile, it can be seen that crystallisation started at 30 ˚C after an induction time (about 6 minutes). The crystal morphology at the early stage and late stage was observed from the microscopic pictures shown in Figures 5.21 and 5.22. It can be seen that only α form exists during the whole crystallisation process.

The changes of impedance real part (Z'), imaginary part (Z") and phase angle (θ) at a frequency of 1MHz during the crystallisation at 30 °C are shown in figure 5.23. It can be seen that during the cooling stage (0-2000 seconds), crystallisation does not occur and thus, the changes in impedance real part, imaginary part and phase angle are only caused by the temperature changing. After 2500 seconds, the nucleation starts at a constant temperature (30 °C). During this stage (2500-6600 seconds), the changes of impedance parameters are temperature independent. Similar to the analysis in section

5.6.2, the changes of Z', Z" and θ with time can be separated into three stages. At the early stage (2600-3000 seconds), the rates of change are relatively small shown by the flat curves. During the medium stage (3000-5000 seconds), the rates of change become larger than those at the early stage. At the late stage (5000-6600 seconds), the rate of change decrease again. The relationship between the changes of impedance parameters and the crystal size with other factors has been discussed in section 5.6.2. In this section, the focus is on the crystal morphology; therefore, the results obtained in the crystallisation process with a single form (α) will be compared with the results obtained in a polymorphic transformation process in the next section.

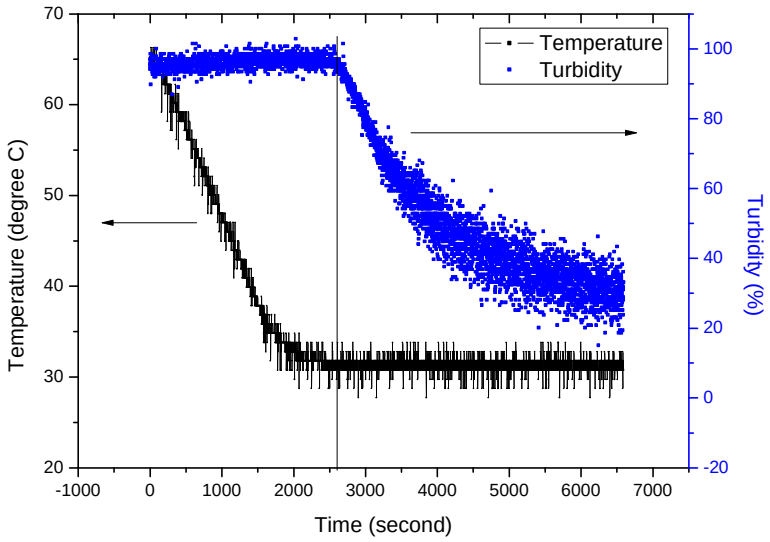

Figure 5.20: Temperature and turbidity profiles for crystallisation at a constant temperature of 30 °C

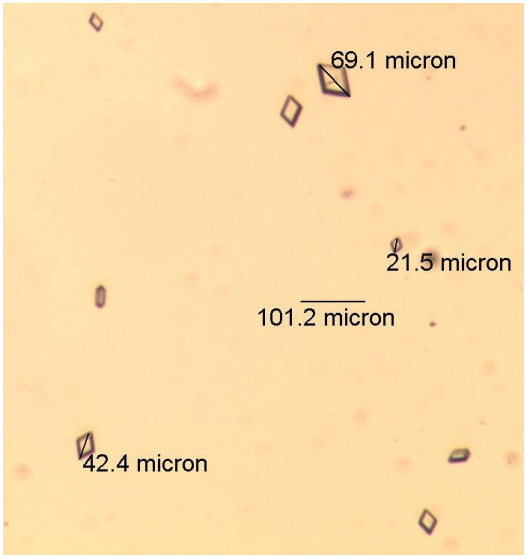

Figure 5.21: crystal morphology at the early stage of crystallisation at a constant temperature of 30 °C

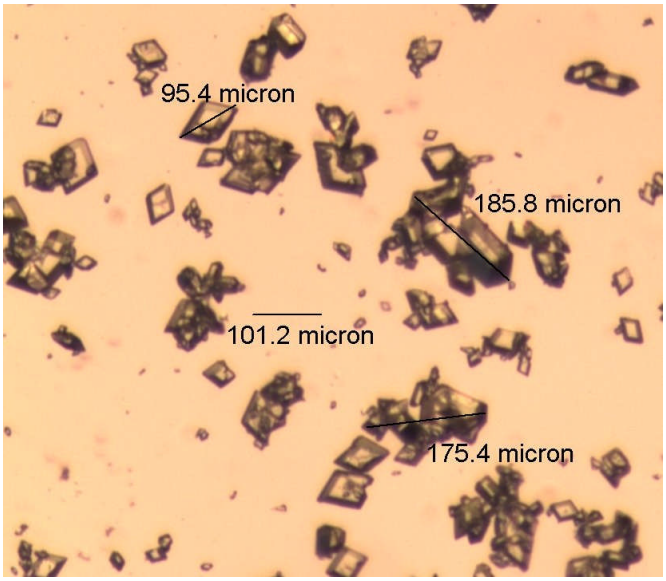

Figure 5.22: crystal morphology at the late stage of crystallisation at a constant temperature of 30 °C

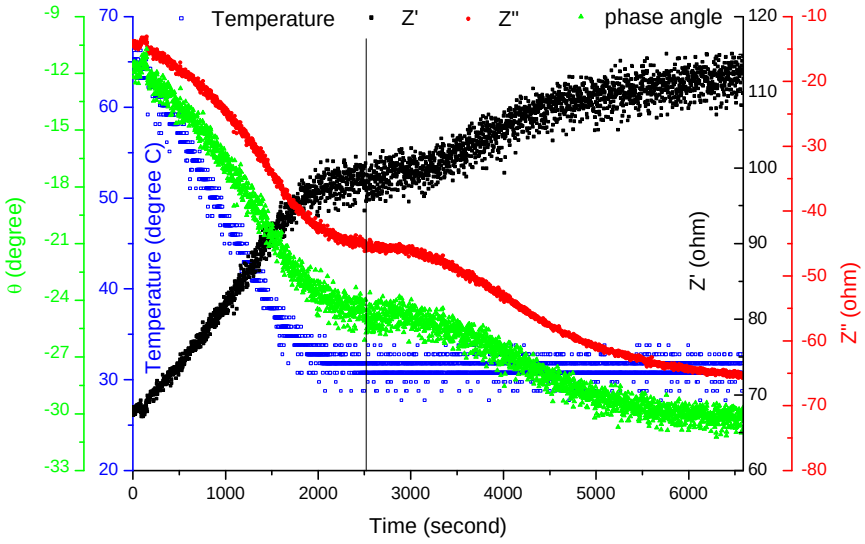

Figure 5.23: Change of impedance real part (Z'), imaginary part (Z"), and phase angle (θ) at frequency 1 MHz with time during LGA crystallisation at a constant temperature of 30 °C

5.7.2 Polymorphic Transformation

Figure 5.24 shows the temperature and turbidity profiles for the crystallisation at a constant temperature of 60 °C. The cooling rate from 80 °C to 60 °C is 0.91 °C/min. From the turbidity profile, it can be seen that the crystallisation started at 60 ˚C after a very short induction time. The crystal shape was observed off-line by the optical microscope and the microscopic pictures at different stages of crystallisation are shown in Figure 5.25. From Figure 5.25, the polymorphic transformation process between the α form and β form can be observed directly. It can be seen that at the beginning of crystallisation (1600 seconds), both the α form and β form exist but the α form is dominant. With increasing time, the amount of β form increases. After 4000 seconds, the α form decreases significantly, and the β form becomes dominant. Then the crystals of β form continuously grow with the dissolution of α form. Finally, at the time of 7000 seconds, the crystals of α form can no longer be observed.

The changes of the impedance real part (Z'), imaginary part (Z") and phase angle (θ) at 1MHz during the crystallisation at 60 °C are shown in figure 5.26. It can be seen that during the period from 1600 seconds to 4000 seconds, the impedance real part shows an approximate plateau. Similarly, the impedance imaginary part and phase angle show an approximate plateau at the early stage of crystallisation (1600-3300 seconds).

In order to compare the crystallisation process involving a polymorphic transformation and the one only exhibiting a single α form, the changes of impedance parameters are compared in the two different cases, respectively. The results are shown in Figure 5.27-5.29. In these figures, the starting-point of the nucleation is set to be 0 in the time scale for the two different cases. Since the temperature of crystallisation is different in the two cases, it has no meaning to compare the absolute values of the impedance parameters due to the effect of the temperature. The reason that different temperatures were used in the two cases is mainly due to the difficulties in obtaining the single α form and polymorphic transformation process at the same temperature in our experiments. Therefore, the effect of crystal polymorphs is studied by comparing the changing rates of impedance parameters in the two cases.

From Figure 5.27, it can be seen that the rate of change in the impedance real part is much smaller during the polymorphic transformation process than the crystallisation process with a single α form. After the β form becomes dominant in the solution (at the 2400 seconds in Figure 5.27), the increasing rate of impedance real part becomes larger with the growth of β form crystals. Similarly, from Figures 5.28 and 5.29, it can be seen that the rates of change in the impedance imaginary part and phase angle are much smaller during the polymorphic transformation process than those with a single α form. The decreasing rates of Z'' and θ become larger after the β form becomes dominant in the solution. Therefore, it might be supposed that the small rate of change of impedance parameters is a feature of polymorphic transformation. This phenomenon might be related to the solute concentration which remain almost constant during a polymorphic transformation process (Scholl et al., 2006). Although the transformation of α form to β form can be monitored on-line by the changing of electrical impedance parameters, it is still difficult to determine the crystal morphology at a certain time from the current EIS results. A potential solution by a model-based separation is proposed in the future work.

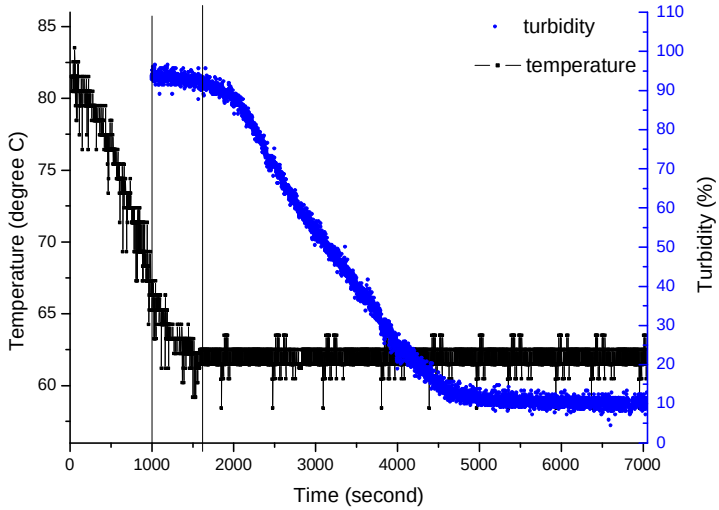

.

Figure 5.24: Temperature and turbidity profiles for crystallisation at constant temperature of 60 °C

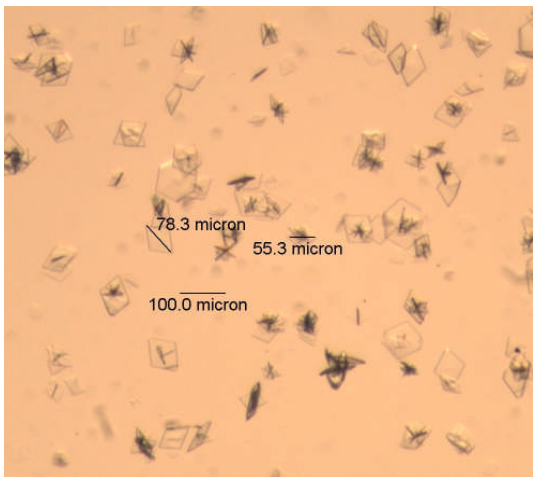

(a) at 1600 seconds

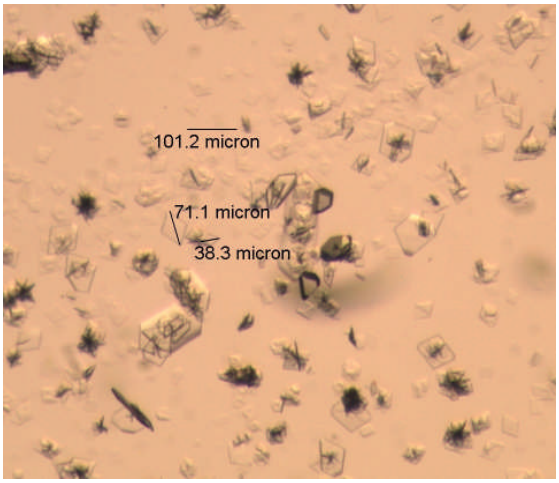

(b) at 2460 seconds

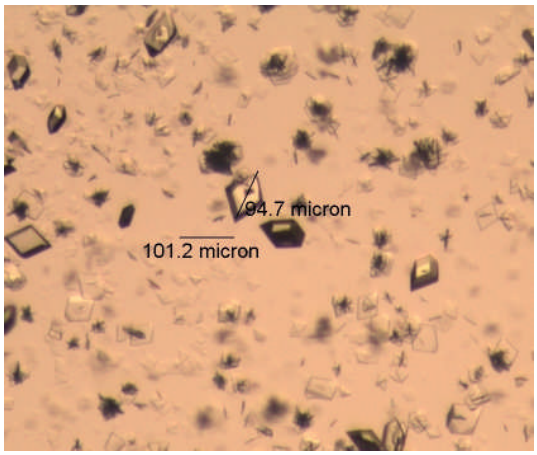

(c) at 3300 seconds

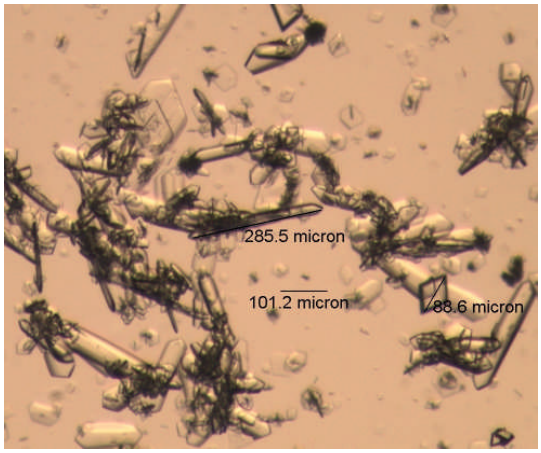

(d) at 4000 seconds

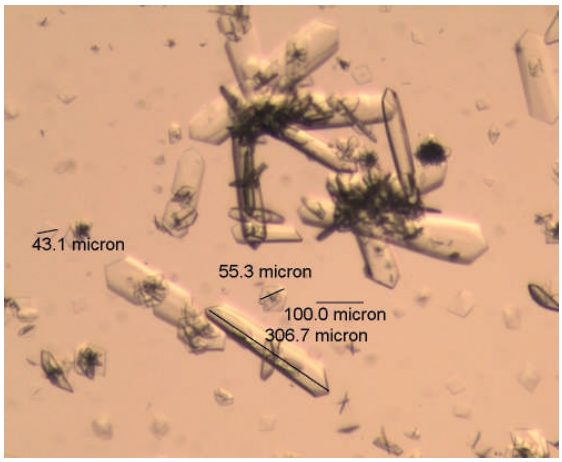

(e) at 4500 seconds

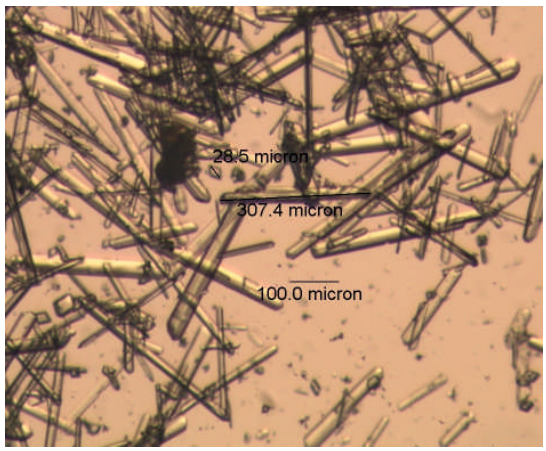

(f) at 5400 seconds

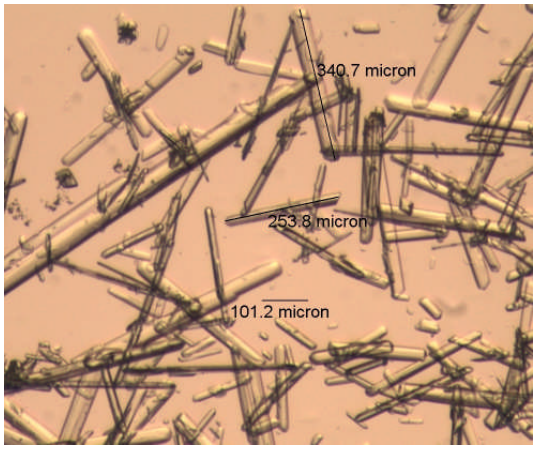

(f) at 6300 seconds

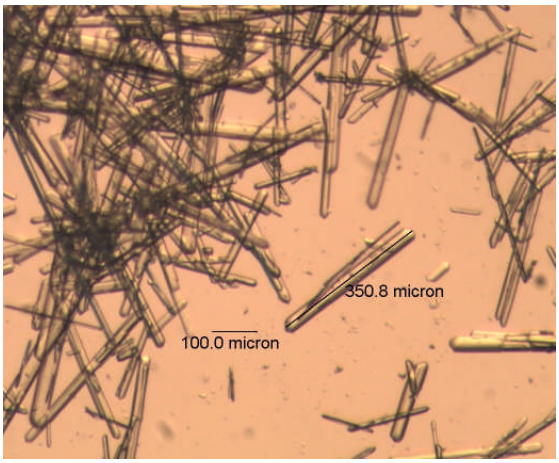

(g) at 7000 seconds

Figure 5.25: crystal morphology at different stage of polymorphic transformation

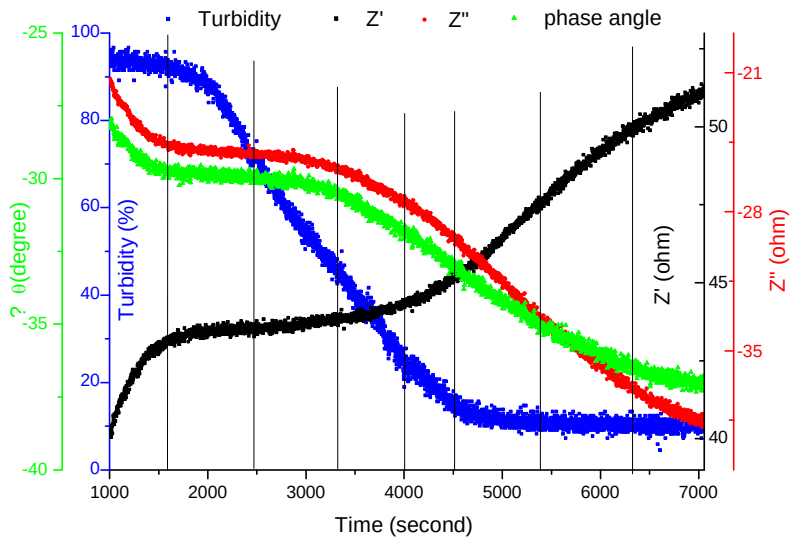

Figure 5.26: Change of impedance real part (Z'), imaginary part (Z") and phase angle (θ) at frequency 1 MHz with time during LGA crystallisation at 60 °C

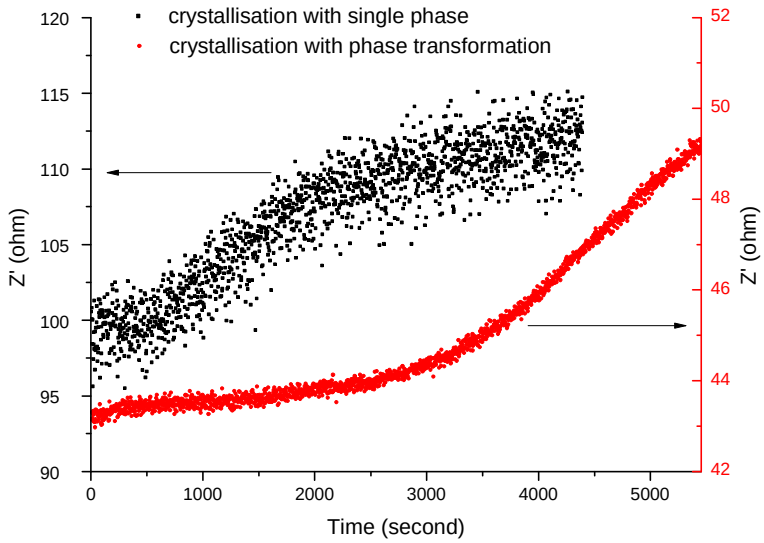

Figure 5.27: Change of impedance real part (Z') at frequency 1 MHz with time in the crystallisation existing single α form and polymorphic transformation

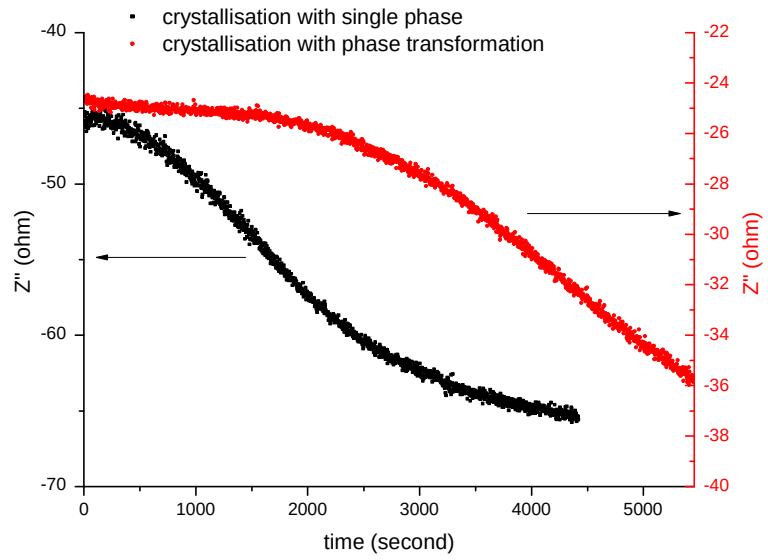

Figure 5.28: Change of impedance imaginary part (Z") at frequency 1 MHz with time in the crystallisation existing single α form and polymorphic transformation

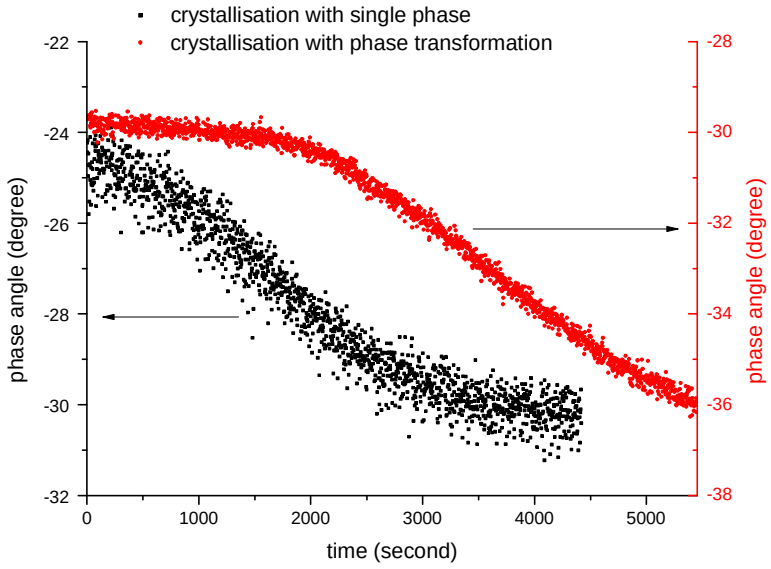

Figure 5.29: Change of phase angle (θ) at frequency 1 MHz with time in the crystallisation existing single α form and polymorphic transformation

5.8 Summary

In summary, the on-line electrical impedance spectra during L-glutamic acid crystallisation processes are studied in this chapter. The effects of solid concentration, solute concentration, and temperature were studied first. The solid concentration has no significant effect on all of the impedance parameters (Z', Z", θ and $\omega_{relaxation}$) at high frequency (1 MHz). However, the solute concentration has a significant effect on Z' Z" and θ at 1 MHz. The relaxation frequency is influenced by three factors at the same time during the crystallisation process, including solute concentration, temperature and crystal size. If crystallisation can be carried out under a constant temperature or a constant temperature gradient, the effect of temperature can be neglected. The effects from the solute concentration and crystal size are two factors changing simultaneously which are very difficult to separate using EIS experiments. The study of EIS during the crystallisation processes shows that the relaxation frequency decreases significantly after the start-point of crystallisation due to the combination of effects from crystal size and ionic concentration. In addition, the changing of relaxation frequencies with temperature and the corresponding changes in turbidity are studied. A dramatic shift in relaxation frequency can be observed when the temperature is lower than 41 °C, which is higher than the start-point of nucleation shown by the turbidity measurement. Therefore, it is proposed that the relaxation frequency extends the observable range of starting-point of nucleation beyond that accessible by turbidity measurement.

The results in the study of polymorphism during the crystallisation process show that the polymorphic transformation can be monitored on-line using the changing rates of impedance parameters. Slow rates of change in the impedance parameters (Z', Z" and θ) can be observed during the transformation of α form to β form. This phenomenon is supposed to be a feature of polymorphic transformation process because in the crystallisation with single α form, the rates of change in impedance parameters are much larger than those in the polymorphic transformation process. However, due to the specific crystallisation conditions and dynamic changes in the LGA crystallisation process, it is not possible to determine the crystal morphology at a certain time from the impedance parameters.

Chapter 6
Electrical Impedance Tomography Spectroscopy

Summary: Electrical impedance tomography based on EIS measurement conducted using different materials, including non-conductive plastic bar, banana, and silica suspensions are reported in this chapter. The responses of electric polarisation of colloidal particles on tomographic images and the observation of particle size effect from tomographic images are studied and discussed.

6.1 Introduction

The electrical impedance tomography (EIT) technique shares the same basic measurement principle with the electrical impedance spectroscopy. Both of them use the four electrodes system to provide an exciting current to two electrodes and measure the voltage difference between the other two electrodes. Electrical impedance spectroscopy cannot provide an “image” of the sample but can give impedance parameters over a wide range of frequencies. Electrical impedance tomography utilizes a set of electrodes (could be 8, 16, 32, or 64) to measure the impedance of samples from different electrodes pairs and then obtain the images by data acquisition and reconstruction process. The current form of EIT technique may provide images at several fixed frequencies (Brown, 2003); however, electrical impedance tomography based on EIS measurement or namely, electrical impedance tomography spectroscopy (EITS) can produce imaging over a wide range of frequencies, using this principle (Yerworth et al., 2003).

In this chapter, the experimental results on tomographic imaging based on EIS measurement using a sensor of 8 electrodes are reported. The measurement strategy, effect of common mode voltage, EIT results on different materials, including non-conductive polymer bar, banana and silica suspensions are discussed and analysed.

6.2 Methodology

The methodology of electrical impedance tomography based on spectroscopy measurement has been described in Chapter 3, section 3.6. EIS measurement can directly give the data of the impedance real part, imaginary part, phase angle and magnitude of the impedance across the measurement electrodes. EIS measurements corresponding to frequency spectra from DC to 20 MHz were acquired from a sensor of eight electrodes fitted with a vessel (refer to previous chapter) using the Solartron 1260 impedance analyzer. The data (for example, impedance real part) at a specific sampling frequency can be sorted out from spectra responding data and arranged in tabular form as shown in Table 6.1. Then, images were reconstructed based on these data using the back projection algorithm embedded in P2000 software (ITS, System 2000 version 7.0 user's manual).

Table 6.1: The data of impedance real part for tap water at a sampled frequency (80 kHz)

	Voltage measurement pairs						
Current injection pairs	Impedance real part (ohm)	02-03	03-04	04-05	05-06	06-07	07-08
	08-01	80.9492	44.8483	39.8293	44.7582	79.6553	
	01-02		80.1088	44.7399	39.8187	44.5037	79.5785
	02-03			80.4046	44.8568	39.5477	44.5118
	03-04				79.2120	44.0059	39.2464
	04-05					78.3294	43.9771
	05-06						78.5740

The sensitivity theorem has been widely used for image reconstruction in conventional electrical impedance tomography, particularly the single-step method based on the sensitivity coefficient back projection (SBP) method (Wang, 2002). The SBP method uses a normalized transpose matrix of the sensitivity matrix as a weighting matrix and the SBP algorithm can be expressed by (Wang, 2002):

$$[\frac{\Delta\sigma_i}{\sigma_0}] = [\overline{s}]^T [\frac{\Delta V_i}{V_0}] \quad (6.1)$$

where, i is the pixel number, σ_0 and $\Delta\sigma_i$ are the reference conductivity and

conductivity change at pixel *i*, V_0 and ΔV_i refer to the reference voltage and the voltage change at pixel *i*, $[\overline{s}]$ is the sensitivity matrix.

In Equation (6.1), V_0 and ΔV_i are the values measured by the instrumentation. The matrix, $[\frac{\Delta\sigma_j}{\sigma_0}]$, can be calculated using Equation (6.1). The conductivity at every pixel can be calculated by:

$$\sigma_i = (1+\frac{\Delta\sigma_i}{\sigma_0})\sigma_0 \tag{6.2}$$

where, σ_0 is the measured conductivity for homogeneous distribution at the time of taking reference.

For the measurement of EITS, the impedance real part, imaginary part, phase angle and magnitude at a specific frequency can be obtained from the impedance spectra. The tomographic images of the impedance real part, imaginary part, phase angle and magnitude can be reconstructed with the same algorithm used in the conventional EIT.

In this chapter, three experiments using different materials are discussed. The first experiment studied the images of non-conductive plastic bar (the handle of screwdriver) in tap water at low (1000 Hz) and high (1 MHz) frequencies. The conductivity of tap water is 346 μs/cm. The second experiment studied the images of banana in tap water at low and high frequencies. The third experiment studied the images of silica suspensions in water. In this part, images of one silica suspension in water were studied first, followed by the two silica suspensions of different particle size. In order to eliminate the possible effects of ionic conductivity on the impedance imaginary part and phase angle, care was taken in the preparation of the disperse phase and reference. The details of preparation are shown as follows:

(1) one silica suspension in water:

Disperse phase: an original silica suspension (220 nm, 23.5 wt%) with a conductivity of 68.4 μs/cm. The conductivity of suspension in this case is same with the conductivity of silica suspension in the case which has been shown and discussed in section 4.6, Figure 4.24.

Reference: water including a sample chamber filled with the same water. The conductivity of the water was adjusted to 69.3 μs/cm using KCl solution (2 mol/l).

(2) two silica suspensions in water:

Disperse phase: two silica suspensions were adjusted to the same concentration, 19.5

wt%. One suspension comprised 35 nm particles and the conductivity was adjusted to 204.4 µs/cm using KCl solution (1 mol/l). Another suspension comprised 220 nm particles and the conductivity was adjusted to 205.8 µs/cm using KCl solution (1 mol/l).

Reference: water including two chambers filled with the same water. The conductivity of the water was adjusted to 204 µs/cm using KCl solution (2 mol/l).

6.3 EITS Measurement using an 8-electrode Sensor

6.3.1 Common Mode Voltage Rejection Ratio (CMMR)

Since the measurement principle of EIT is based on the relative changing of the boundary voltages, a reference must be taken at the beginning of the measurement. Tap water is commonly used as the reference in laboratory research, therefore a series of electrical impedance spectra of tap water were measured using an 8-electrode sensor. Figure 6.1 shows the electrical impedance spectra (1 Hz-32 MHz) of tap water measured at different electrode pairs (electrode pairs 1 and 2 are fixed for current exciting). It can be seen that the electrical impedance spectra measured at different electrode pairs show significant inconsistencies at their phase angles. This result is unexpected since the phase angles of impedance spectra obtained from different electrode pairs were expected to be similar to the phantom of tap water without disperse phase (particle) inside.

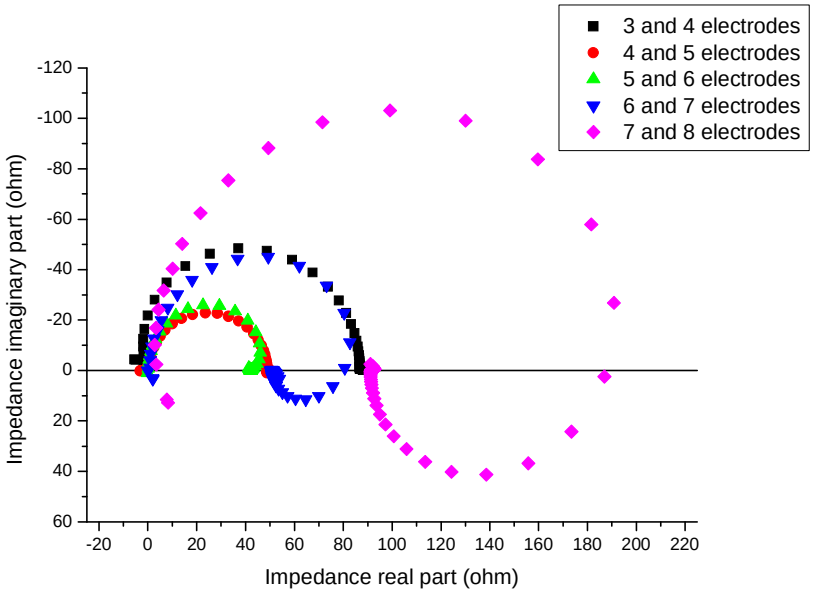

Figure 6.1: Electrical impedance spectra of tap water measured at different electrode pairs (electrode pairs 1 and 2 are used for current exciting over 1Hz-32MHz

The possible reasons for the results shown in Figure 6.1 could come from the electrode-electrolyte effects (surface property, shape, size et al.) or the common mode voltages along with differential voltage measurements, which may cause the most problematic imaging error with EIT reconstruction. In order to find out what caused the main effect, a mock sensor using eight resistors, which were connected in a ring, was carried out. Although the circuit including eight resistors cannot present the real situation of the phantom with 8-electrodes, it may provide an approximate analysis with a simple measurement and calculation. Eight resistors with individual resistance of 1000 ohm were connected in a ring (shown in Figure 6.2). The exciting current (20 mA) through the impedance analyzer is then applied to resistor 1. Electrical impedance spectra (1Hz-32MHz) are measured at resistors 3, 4, 5, 6, and 7, respectively, and shown in Figure 6.3.

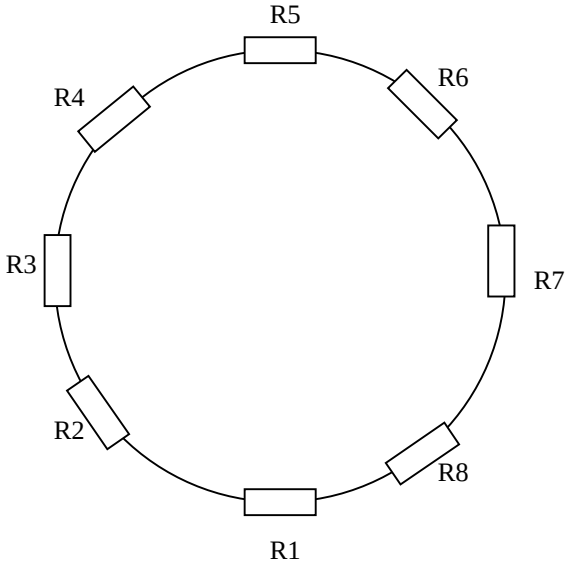

Figure 6.2: The schematic of eight resistors connected in a ring

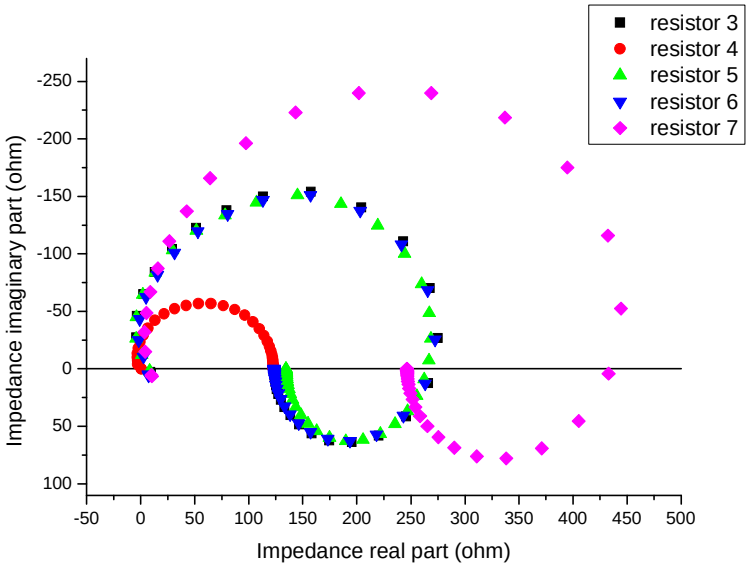

Figure 6.3: Electrical impedance spectra measured on resistors 3, 4, 5, 6 and 7, respectively (1Hz-32MHz)

If the exciting current is applied to resistor 1 and the voltage drop is measured at resistor 3, the measurement circuit will be shown in Figure 6.4. Since R1 to R8 have the same resistance (1000 ohm), the current (I_1) passing through R1 and the current (I_2) passing through R2 – R8 have the relationship:

$$I_1 = 7I_2 \tag{6.3}$$

$$I_1 + I_2 = 7I_2 + I_2 = 0.02\text{A} \tag{6.4}$$

$$I_2 = 0.0025\text{A} \tag{6.5}$$

Therefore, the voltage measured at R3 can be calculated by:

$$V_{R3} = I_2 \times R3 = 0.0025 \times 1000 = 2.5\text{V} \tag{6.6}$$

At low frequency (for example, 1 Hz), the impedance real part measured at R3 can be calculated by:

$$Z' = \frac{V_{R3}}{A_{\text{exciting}}} = \frac{2.5}{0.02} = 125\Omega \tag{6.7}$$

This result is very close to the experimental data. Under ideal conditions, the

impedance real part measured on the other resistors (R4, R5, R6, R7) should be the same as R3. However, the experimental results shown in Figure 6.3 present different values of Z' on different resistors. Since there is no effect from electrode-electrolyte interfaces, it is believed that the measurement errors in Figure 6.3 arise from the common mode voltage effect on the spectroscopy analyser. The impedance spectra measured from the different resistors show similar measurement errors to the one obtained from the phantom with 8 electrodes (Figure 6.1). Therefore, the main reason for the inconsistent impedance on different electrode pairs should be caused by the limits of the common mode voltage rejection ratio (CMMR) of the impedance spectroscopy analyser.

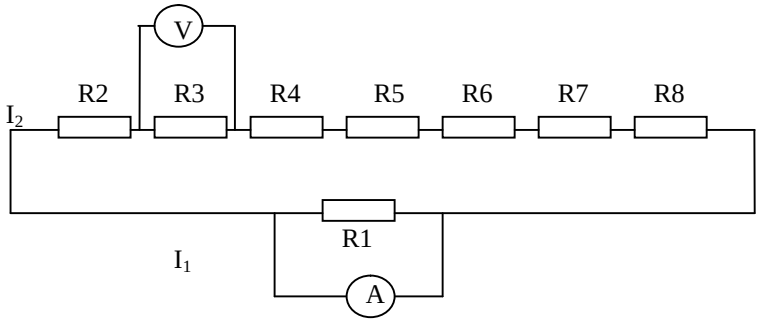

Figure 6.4 Electrical circuit of impedance measurement in the 8 resistors system

6.3.2 Method for Reducing Common Mode Voltage Effect

A method is proposed for reducing the common mode voltage effect. The method is based on the reciprocal theorem for a two ports, four terminals system and called the reciprocal measurement method (RMM). The details of the strategy are described as follows:

In this method, the measurement strategy of EIS using an 8-electrode sensor is different from the traditional EIT measurement. In traditional EIT measurement, the exciting current is applied to electrodes 1 and 2 as shown in Figure 3.18. Voltages are measured sequentially (clockwise) on other adjacent electrode pairs (from electrode 3 to 8). For an 8-electrodes sensor, the total number of measurements is five, including the measurements between electrodes 3 and 4, electrodes 4 and 5, electrodes 5 and 6, electrodes 6 and 7, electrodes 7 and 8, respectively. In order to reduce the common mode voltage effect, the voltage measurement is firstly carried out on the adjacent

electrode pairs 3 and 4, 4 and 5, 5 and 6, in a clockwise direction. Then voltage is measured on the adjacent electrode pairs 7 and 8, 6 and 7, in the counter-clockwise direction. It is easy to achieve the reciprocal measurement since in our experiment, electrical impedance spectra on the different electrode pairs are measured manually. EIS results of tap water obtained by this method are shown in Figure 6.5. It can be found that the impedance spectra on electrode pairs 4 and 5, 5 and 6, 6 and 7 are almost consistent, but they are significantly different from those measured on electrode pairs 3 and 4, 7 and 8. It is proved that the common mode voltage effect can be reduced to a certain extent by the RMM, but cannot be removed completely.

Figure 6.6 compares two reconstructed impedance real part images of non-conductive polymer bar in tap water obtained at 79.4 kHz by the traditional method and the RMM. The exact same material and devices were used in the measurement and the second phase (non-conductive plastic bar) was fixed at exactly the same position (centre of the phantom). It can be verified by Figure 6.6 that tomographic imaging can be obtained successfully from EITS measurement and the data reconstruction process. In addition, it can be found that the position of the second phase is different in two images. In the image measured using the RMM, the second phase locates at the centre of phantom, but in the image measured using the traditional method, the second phase moves to the edge. The possible reason is due to the common mode voltage effect as investigated, which was significantly reduced by using the reciprocal measurement method.

In order to prove the influence of the RMM, an experiment using a commercial ERT system (ITS P2000 system) was carried out to measure a tomographic image of non-conductive plastic bar in tap water and the result is shown in Figure 6.7. In the experiment using the commercial ERT system, the operating frequency and exciting voltage are 76.8 kHz and 15 mA, respectively, which are all similar to those used in the EITS measurement (79.4 kHz and 20 mA). In addition, the image obtained using a commercial ERT system is impedance real part image. Therefore, Figures 6.6 and 6.7 are comparable. It can be observed easily that the image obtained from the commercial ERT system is similar to the one measured by the RMM. Therefore, the effect of RMM on reducing common mode voltage can be proved. In the following section, the images are all obtained using the RMM if no further illustration is given.

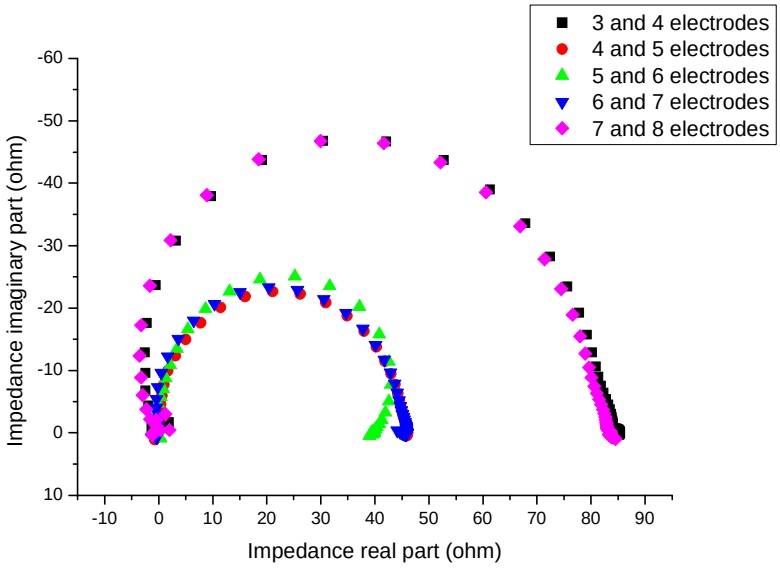

Figure 6.5: Electrical impedance spectra of tap water measured at different electrode pairs (electrode pair 1 and 2 is fixed for current exciting) using the RMM

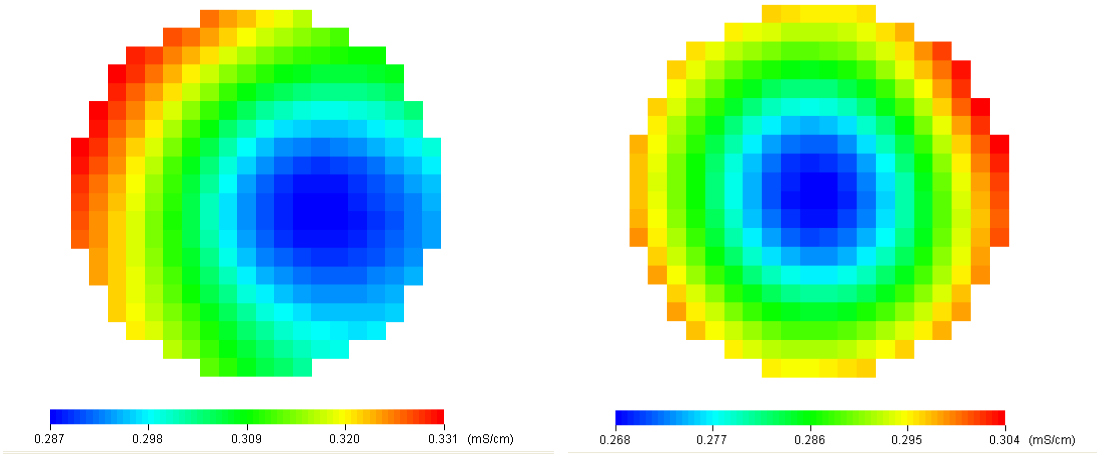

(a) (b)

Figure 6.6: Reconstructed impedance real part images of non-conductive plastic bar in tap water obtained at 79.4 kHz by (a) traditional method; (b) RMM

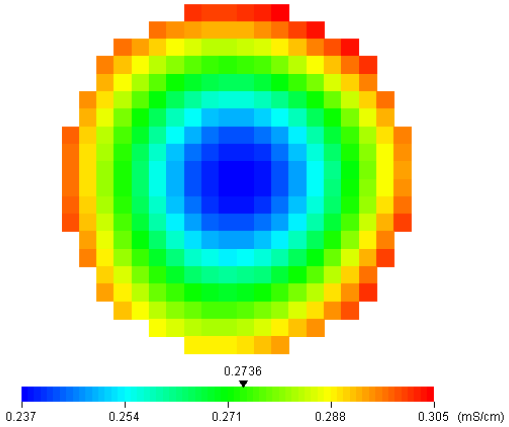

Figure 6.7: Tomographic image of non-conductive plastic bar in tap water obtained at 76.8 kHz using P2000 ERT system

6.3.3 Images at Low and High Frequency

In this section, images based on EIS measurements at low (1000 Hz) and high frequency (1 MHz) are reported and discussed. The disperse phase was a non-conductive plastic bar and the continuous phase is tap water, which is also called the reference. As it is known, the highest frequency, at which the commercial ERT system (ITS P2000 system) can work, is 76.8 kHz. However, EIS measurement can be carried out from 1 Hz to 32 MHz. Thus, it becomes possible to obtain images at frequencies higher than 76.8 kHz using the EIS-based tomography imaging technique. In addition, EIS measurement could provide the values of the impedance real part, imaginary part, phase angle and magnitude. Therefore, it is easy to obtain the relative changes based on these values and obtain images of the real part, imaginary part, phase angle and magnitude, respectively. Figures 6.8 and 6.9 show the reconstructed images of a non-conductive plastic bar (disperse phase) in tap water (continuous phase) obtained at 1000 Hz and 1 MHz, respectively. It can be seen that at both 1000 Hz and 1 MHz, the impedance real part image and magnitude image of the disperse phase can be observed clearly. The blue colour shows that the conductivity of the disperse phase is lower than the continuous phase. The major difference shown in Figures 6.8 (b) and 6.9 (b) is that the impedance imaginary part image of the disperse phase can only be observed at high frequency (1 MHz). A possible reason is that the relative change of the imaginary part at high frequency becomes large, which has been shown by the electrical impedance spectra in Figure 6.10. It can be seen from Figure 6.10 that the relative change of the impedance imaginary part between disperse phase (non-conductive plastic bar with relative dielectric constant ≈ 1.6-2.0) and mixture phase (tap

water plus non-conductive plastic bar) is very small at low frequency (for example, 1000 Hz), but is large at high frequency (for example, 1 MHz). The large relative change at 1 MHz presents an imaginary part image for the disperse phase in tap water. In Figure 6.9 (c), a red strip area is reconstructed in the phase angle image, which relates to the change of phase angle at high frequencies although the shape does not reflect the shape of the object. It is assumed this may be caused by the effect introduced by either the common voltage or the reciprocal measurement method (RMM).

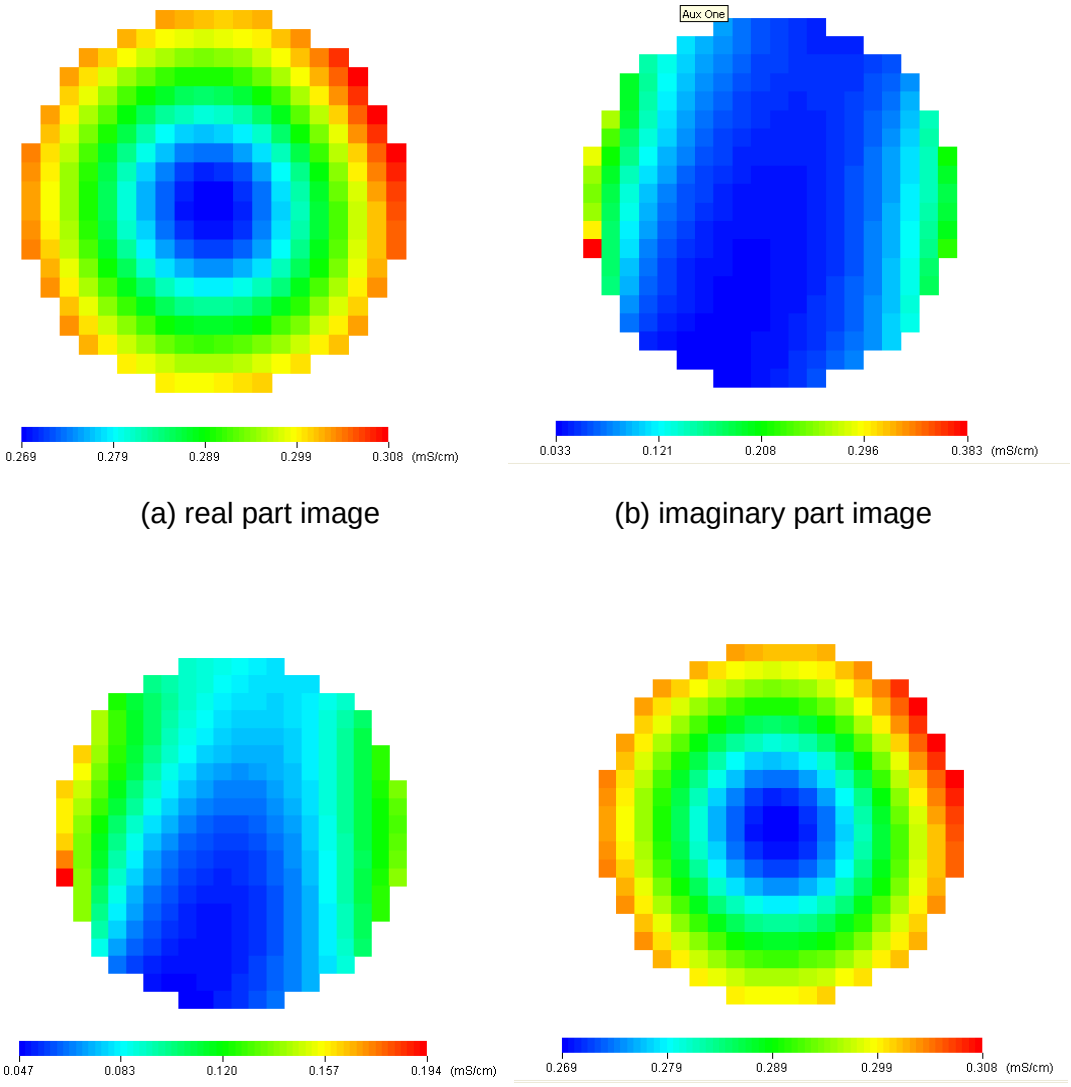

(a) real part image

(b) imaginary part image

(c) phase angle (tan (θ)) image

(d) magnitude part image

Figure 6.8: Reconstructed images of non-conductive plastic bar in tap water obtained at 1000 Hz (a) real part image, (b) imaginary part image, (c) phase angle (tan (θ)) image, and (d) magnitude part image

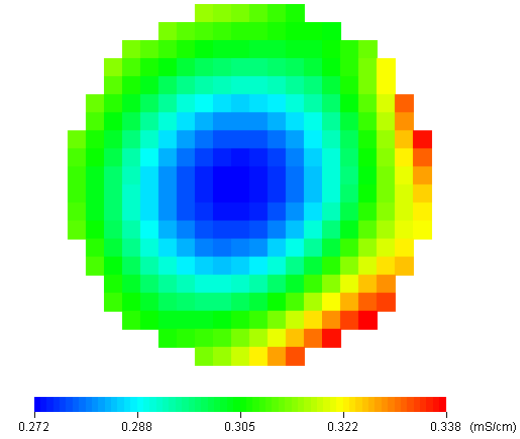

(a) real part image

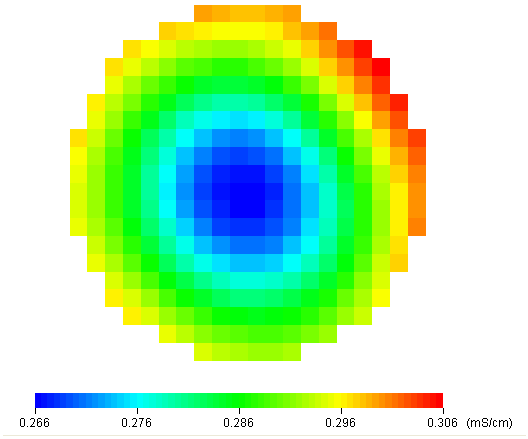

(b) imaginary part image

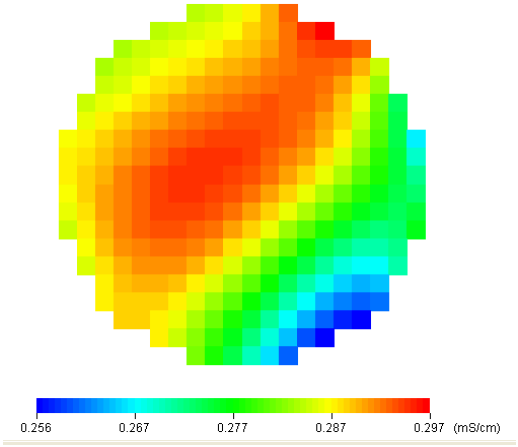

(c) phase angle (tan(θ)) image

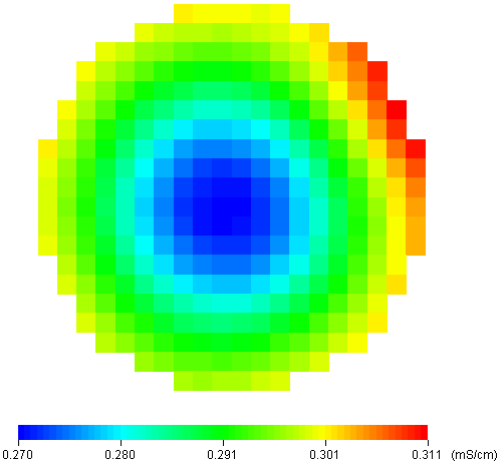

(d) magnitude part image

Figure 6.9: Reconstructed images of non-conductive plastic bar in tap water obtained at 1 MHz (a) real part image, (b) imaginary part image, (c) phase angle (tan (θ)) image, and (d) magnitude part image

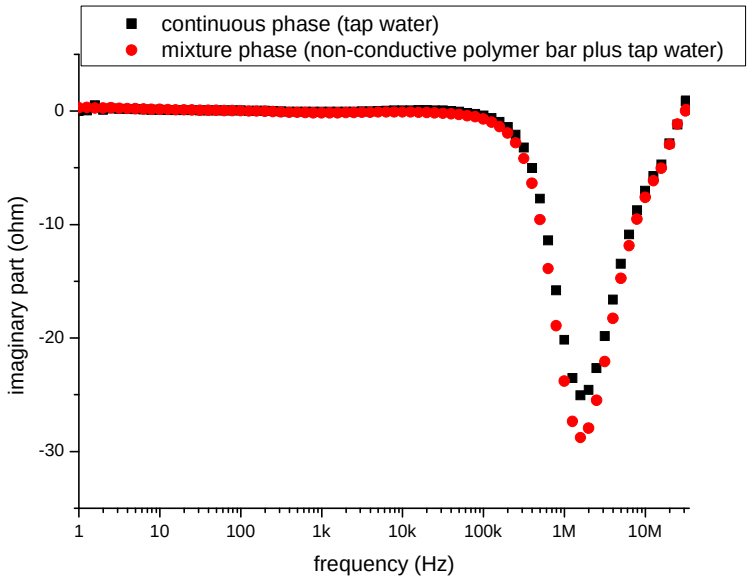

Figure 6.10 electrical impedance spectra of continuous phase (tap water) and mixing phase, measured at electrode pair of 5 and 6 (exciting current was applied to electrode pair of 1 and 2)

6.3.4 Images of Banana in Tap Water

In this section, images of a banana in tap water based on EITS measurements at low (1000 Hz) and high frequencies (79.4 kHz) are reported and discussed. Figures 6.11 and 6.12 show the reconstructed images of the banana in tap water obtained at 1000 Hz and 79.4 kHz, respectively. It can be found that at both 1000 Hz and 79.4 kHz, the impedance real part image and magnitude image of banana can be observed clearly. The blue colour shows low conductivity and the red colour shows high conductivity. Here, an interesting phenomenon is observed for the real part images. The conductivity of the banana at 1000 Hz is lower than the conductivity of tap water; however, at 79.4 kHz it is higher than that of tap water. This phenomenon is probably due to the intrinsic properties of the natural banana skin or caused by the EIS-based tomographic image measurement method. In order to find out the reason another experiment, in which the real part image of the banana in tap water was measured at 1200 Hz and 76.8 kHz using P2000 ERT system, was carried out and the results are shown in Figure 6.13. By comparing Figure 6.13 with Figures 6.11 (a) and 6.12 (a), it can be seen that the phenomenon exists, whichever method is used. Therefore, the change on conductivity is caused by the intrinsic property of a banana skin. As a biological material, banana has a higher dielectric constant (≈ 68) (Sipahioglu and Barringer, 2003) than non-

conductive plastic (for example, polycarbonate plastic ≈ 1.6-2.0). The impedance real part can be shown by the Equation below:

$$Z' = \frac{R}{1+(\omega RC)^2} \tag{6.8}$$

At low frequency (ω→ 0), $Z' \approx R$. The impedance real part is mainly determined by the resistance of materials. However, at high frequency (ω→ ∞), Z' is related to capacitance C as well. A higher dielectric constant causes a significant capacitance and therefore a small Z'. The results shown in Figures 6.11 and 6.12 can be explained by the above discussion qualitatively.

At high frequency (Figure 6.12), banana shows phase angle and imaginary part images, which do not occur at low frequency. In this section, all of the phase angle images are obtained from the values of tan(θ). As discussed in Chapter 4, section 4.3.2, tan(θ) is related to the electrical polarisation density, $\vec{P}_e$ by equations:

$$\tan\theta = -\frac{\omega C}{G} = -\frac{k\omega\varepsilon_0(1+\chi_e)}{k\sigma} = -\frac{\omega\varepsilon_0}{\sigma} - \frac{\omega\varepsilon_0\chi_e}{\sigma} \tag{4.23}$$

$$\vec{P}_e = \varepsilon_0\chi_e\vec{E} \tag{4.14}$$

Under an external alternating electrical field, banana showed an electric polarisation on the walls of the cell, which is similar to the electric double layer around a colloidal particle. The electric polarisation can be presented by both the imaginary part and phase angle, tan(θ). Therefore, the images in Figure 6.12 (b) and (c) reflect the electric polarisation of the banana at relatively high frequency (79.4 kHz).

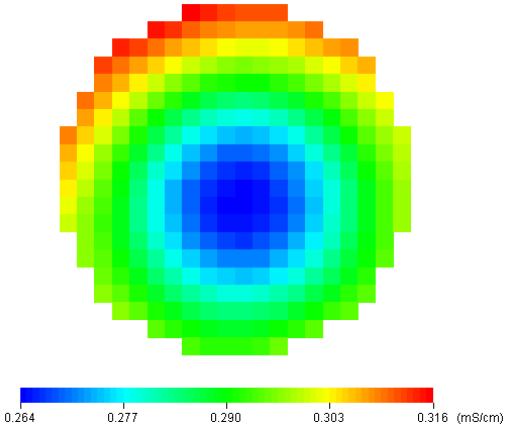

(a) real part image

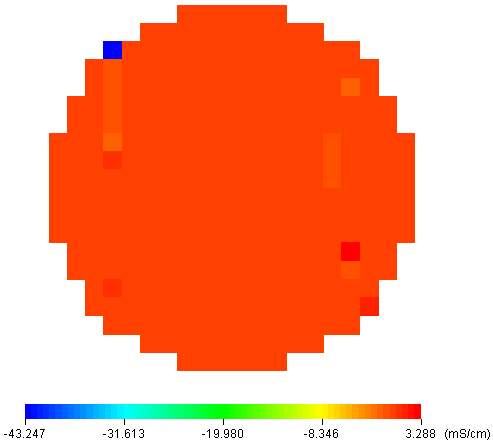

(b) imaginary part image

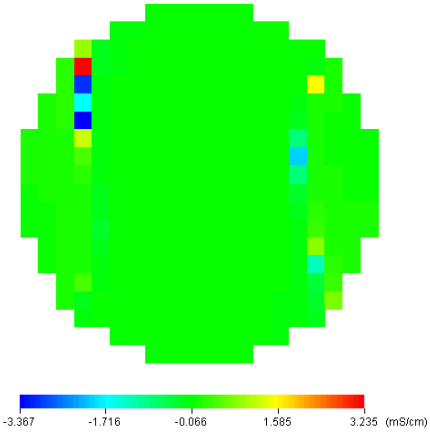

(c) phase angle (tan(θ)) image

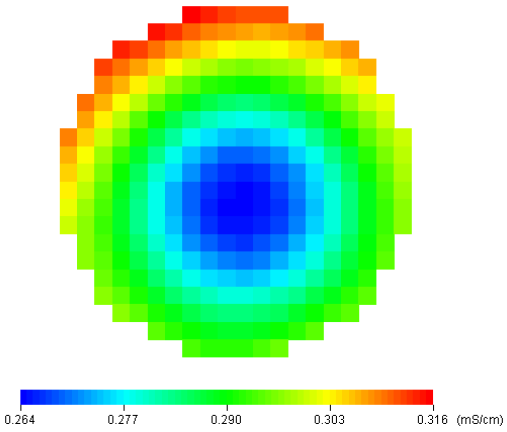

(d) magnitude part image

Figure 6.11: Reconstructed images of the banana in tap water obtained at 1000 Hz (a) real part image, (b) imaginary part image, (c) phase angle (tan (θ)) image, and (d) magnitude part image

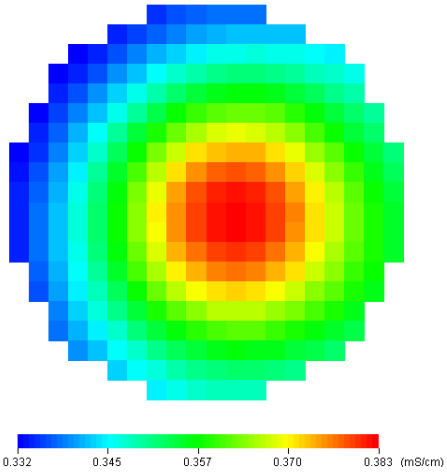

(a) real part image

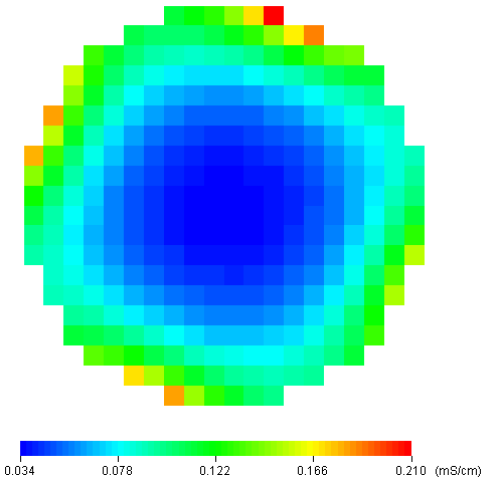

(b) imaginary part image

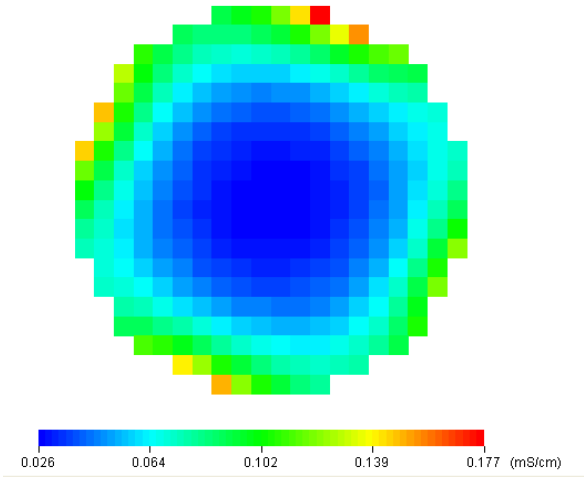

(c) phase angle (tan (θ)) image

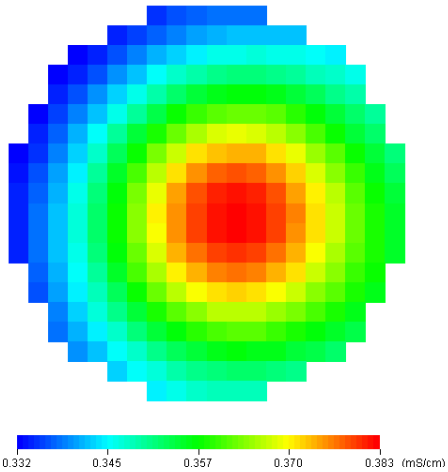

(d) magnitude part image

Figure 6.12: Reconstructed images of banana in tap water obtained at 79.4 kHz (a) real part image, (b) imaginary part image, (c) phase angle (tan (θ)) image, and (d) magnitude part image

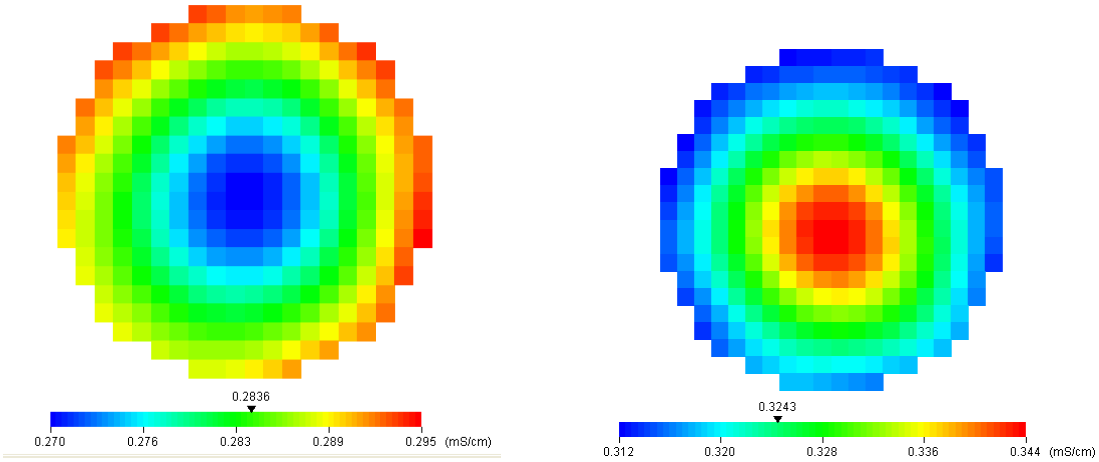

(a) at 1200 Hz (b) at 76.8 kHz

Figure 6.13: Tomographic image of banana in tap water obtained at (a) 1200 Hz and (b) 76.8 kHz using the P2000 ERT system

6.3.5 Images of Silica Suspensions

In this section, images of silica suspensions in water based on EIS measurement are reported and discussed. The methodology and materials have been described in detail in section 6.2. The results are shown in Figures 6.14, 6.15 and 6.16. Firstly, the images of silica suspension (220 nm, 23.5 wt%) in water are discussed. Figures 6.14 and 6.15 show the reconstructed images of silica suspension (220 nm, 23.5 wt%) in water obtained at 1000 Hz and 79.4 kHz, respectively. From Figure 6.14, no significant effect of colloidal suspension can be observed in all of the images at low frequency. From Figure 6.15 (b) and (c), the effect of silica suspension can be observed clearly in the imaginary part and phase angle images with a yellow or green coloured strip existing in the middle of the phantom. No obvious effect of silica suspension can be observed in the images of impedance real part and magnitude (Figure 6.15 (a) and (d)).

Similar to the discussion in the case of banana in section 6.3.4, the imaginary part image and phase angle image represent the electric polarisation of double layers on the surface of colloidal particles. Since the conductivity of the silica suspension is adjusted to the same value as the conductivity of water, no contribution from conductivity is involved in the images of the imaginary part and phase angle. The only contribution is from the electric polarisation of colloidal particles. As discussed in Chapter 4, section 4.3.2, the electric polarisation of colloidal particles relates to the

particle size. Therefore, in the secondary part of the experiments, the images of two silica suspensions of different particle size are studied.

Figure 6.16 shows the reconstructed images of two silica suspensions (220 nm and 35 nm) with the same concentration and conductivity of water obtained at 316 kHz. Because the conductivities of two silica suspensions are adjusted to the same value as the conductivity of water, the relative changes of impedance parameters are very small. In order to get images of good quality, the frequency of 316 kHz was chosen to get large relative changes. From Figure 6.16 (b) and (c), the effect of silica suspensions can be observed by a yellow or green colour strip existing in the middle of the phantom. However, the difference due to the particle size cannot be observed. The possible reasons are complicated. One of the possible reasons is that the relative changes caused by different particle size are so small that they cannot be distinguished in the reconstructed pictures. Another possible reason is the common mode voltage effect, which cannot be fully eliminated in the hardware and operation and therefore cause systemic error in the tomographic measurements.

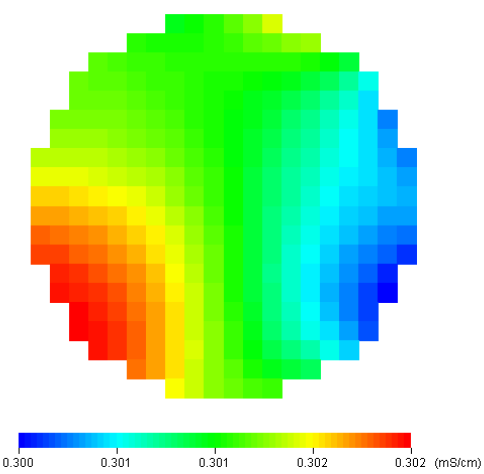

(a) real part image

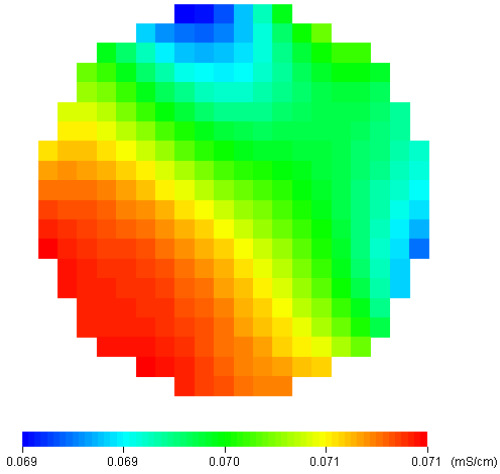

(b) imaginary part image

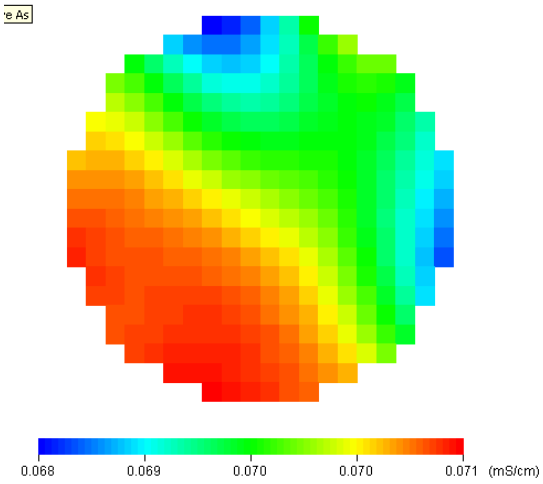

(c) phase angle (tan (θ)) image

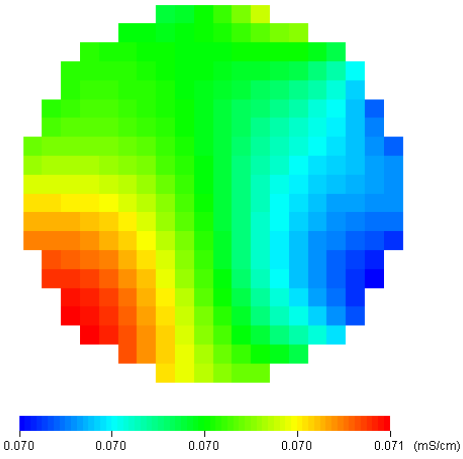

(d) magnitude part image

Figure 6.14: Reconstructed images of silica suspension (220 nm, 23.5 wt%) in water obtained at 1000 Hz (a) real part image, (b) imaginary part image, (c) phase angle (tan (θ)) image, and (d) magnitude part image

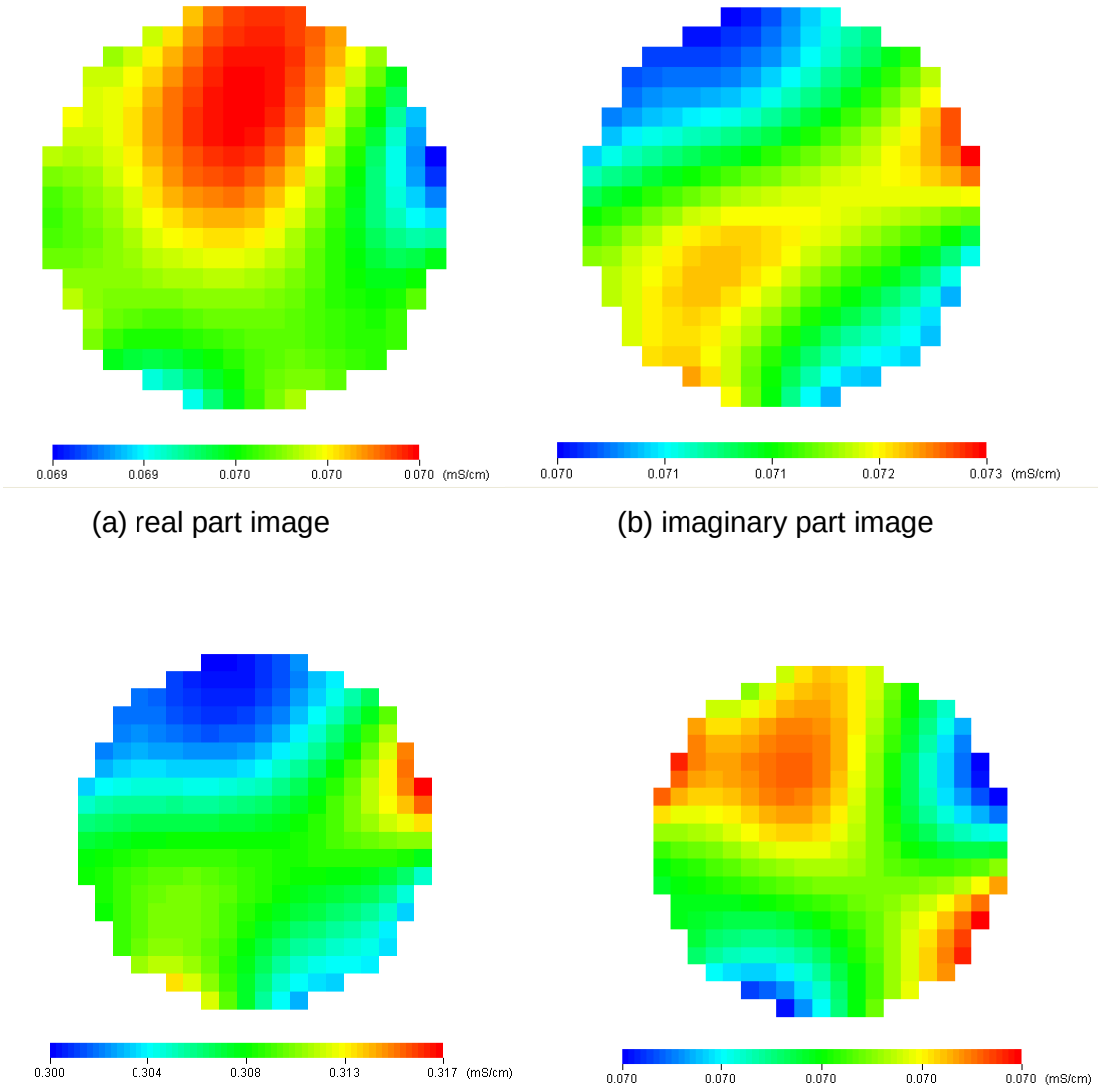

(a) real part image

(b) imaginary part image

(c) phase angle (tan (θ)) image

(d) magnitude part image

Figure 6.15: Reconstructed images of silica suspension (220 nm, 23.5 wt%) in water obtained at 79.4 kHz (a) real part image, (b) imaginary part image, (c) phase angle (tan (θ)) image, and (d) magnitude part image

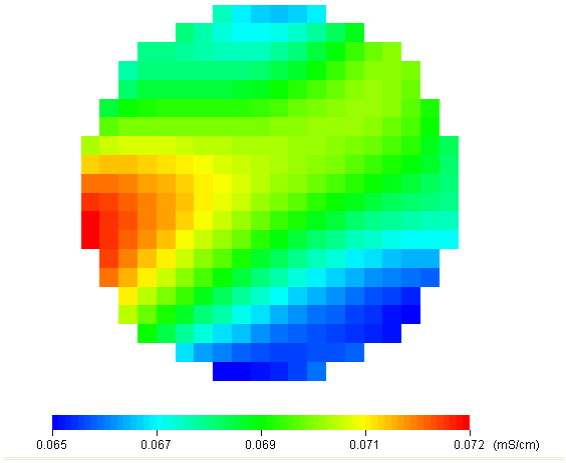

(a) real part image

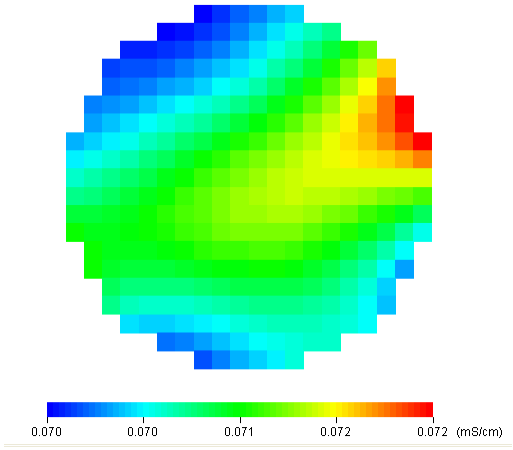

(b) imaginary part image

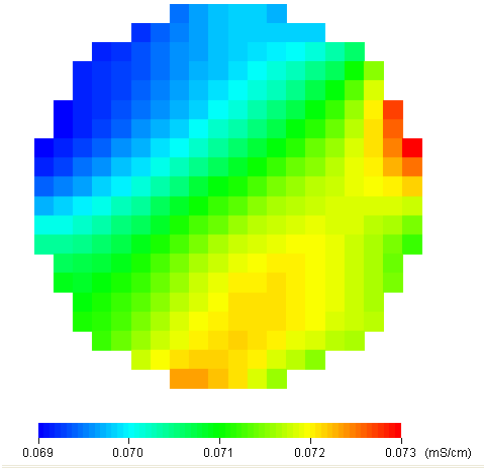

(c) phase angle (tan (θ)) image

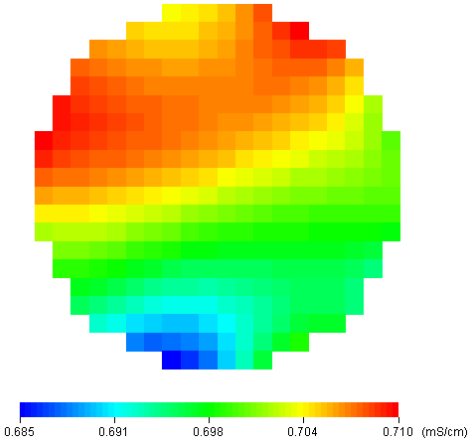

(d) magnitude part image

Figure 6.16: Reconstructed images of two silica suspensions (220 nm and 35 nm, 19.5 wt%) in water obtained at 316 kHz (a) real part image, (b) imaginary part image, (c) phase angle (tan (θ)) image, and (d) magnitude part image

6.4 Summary

The electrical impedance tomography imaging based on EIS measurement has been verified experimentally. The common mode voltage effect exists in the EIS measurement from electrode pairs at different locations. The reciprocal measurement method is proposed to reduce the common mode voltage effect, which works well for the imaging of most impedance parameters except the imaging of phase angle at 1MHz in the experiments. The imaginary part and phase angle images of banana in tap water can be observed clearly, which reflects the electric polarisation of banana at relatively high frequency (79.4 kHz). The feasibility of applying the electrical impedance tomography technique for particle characterisation has been studied by measuring the images of silica suspensions in water. At the frequency of 79.4 kHz, the imaginary part and phase angle images of silica suspension can be observed and show the characterisation of the electrically polarised double layer on the particle surface. However, the particle size effect cannot be observed experimentally from EITS measurement. The phase angle image of particle suspensions with different particle size shows an abnormal strip pattern. The possible reasons for this result could be the common mode voltage effect on the measurement and the limits of the imaging resolution from an 8-electrode EITS sensor. The further work will be discussed in the final chapter of the thesis.

Chapter 7
Conclusions and Future Work

7.1 Conclusion

This PhD thesis describes the study of electrical impedance spectroscopy and tomography on particles in suspensions and during crystallisation processes. The research in this thesis was carried out in three parts, the investigation of EIS responses from the silica suspensions, the application of the method for on-line characterisation of crystallisation processes and the development of the electrical impedance tomography spectroscopy (EITS) method for the verification of EITS with different materials.

Overall new methods for characterising colloidal particles based on electrical impedance spectroscopy have been developed and verified. The EIS testing vessel, and on-line sensor, including a four-electrode impedance cell and a non-destructive inserting device, have been designed and applied in obtaining the electrical impedance spectra in silica suspensions and during crystallisation. The experimental devices for on-line monitoring of crystallisation processes and electrical impedance tomography spectroscopy (EITS) measurement have also been designed and reported in detail.

In the investigation of EIS responses from the silica suspensions, the effects of the particle size, particle concentration and ionic concentration on the electrical impedance parameters, including the impedance real part, imaginary part, phase angle (θ) and relaxation frequency have been studied experimentally. A semi-empirical theoretical model has been established to explain the relationship between the relative changes in tan(θ) and the particle size. A linear proportional relationship between the particle size and the relative changes in tan(θ) has been observed at the particle concentrations of 10.0 wt% and 5.0 wt%. However, this relationship becomes insignificant at particle concentrations of 1.0 wt% and 0.5 wt%. The relaxation frequency as a function of particle size based on the existing theoretical model has been demonstrated by the results of experiments with colloidal silica suspensions. In addition, effects of the particle concentration and ionic concentration on the electrical impedance spectra have been studied. The results indicate that the electrical impedance parameters including the impedance real part, imaginary part, relaxation frequency and phase angle all represent the influences from the particle and ionic concentrations. Therefore, for the samples with different particle concentrations and ionic concentrations, the separation

of particle size effect from other effects is very challenging if it is only dependent on the impedance data. However, the theoretical model based on the parallel RC equivalent circuit provides a method based on the relative changes in tan(θ) to approach the separation of variables utilising the particle volume fraction and conductivity of background solution in the derivation. The model has been successfully used to analyse some experimental results, but it does not work very well for all data. Further development on the theoretical model is necessary.

On-line characterisation of crystallisation processes with electrical impedance spectroscopy method has been demonstrated through a series of experiments. The electrical impedance spectra associated with L-glutamic acid (LGA) nucleation-growth processes is detected on-line as a function of particle size, concentration and ionic concentration. The relaxation frequency decreases significantly after the start-point of crystallisation due to a combination of effects from crystal size and ionic concentration. The decrease in the relaxation frequency becomes more rapid below 41°C, which is above the starting-point of nucleation as shown by turbidity measurement. Therefore, it is proposed that the relaxation frequency extends the observable range of the starting-point of nucleation beyond what is accessible by turbidity measurement. The results in the study of polymorphism during crystallisation processes show that the polymorphic transformation can be monitored on-line by observing the rates of change in impedance parameters. Slow rates of change in the impedance parameters (Z', Z" and θ) can be observed during the transformation of α form to β form. This phenomenon is believed, as a result of this investigation, to be a feature of polymorphic transformation processes because in the crystallisation with single α form, the rates of change in impedance parameters are much larger than those in the polymorphic transformation process. However, due to the specific crystallisation conditions and dynamic changes in the LGA crystallisation process, it is not able to determine the crystal morphology at a certain time from the impedance parameters.

The electrical impedance tomography imaging based on EITS measurement has been verified experimentally. A reciprocal measurement method is proposed to reduce the common mode voltage effect, which works well for the imaging of most impedance parameters, except the imaging of phase angle at 1MHz in the experiments. The feasibility of applying the electrical impedance tomography spectroscopy technique for particle characterisation has been studied by measuring the images of silica suspensions in water. At a frequency of 79.4 kHz, the imaginary part and phase angle images of silica suspension can be observed and show the characterisation of electric

polarised double layer on the particle surface. However, the particle size effect cannot be observed experimentally from the EITS measurement. The possible reasons have been analysed, which may be due to the limitations of the imaging resolution from an 8-electrode EITS sensor and the common mode voltage rejection ratio of the instruments.

7.2 Future work

The future work could involve both experiments and theoretical modelling, as suggested below:

(1) For the verification of the proposed EIS method, it is suggested that other kinds of materials, for example, titanium dioxide and zinc oxide should be tested and then compared with the results from the silica dioxide tests. The comparison across the different materials allows for a better verification of the method.

(2) Further study on the theoretical model should be carried out in order to establish an algorithm for separating these multi-variables and deriving a solo relationship between the particle size and the electrical impedance parameters. An equivalent circuit model of the RC network (R is the resistor and C is the capacitor) could be designed for simulating a 2-dimensional (2D) or 3-dimensional (3D) particle suspensions. The relative change in tan(θ) can be calculated based on this 2D/3D model, although the equivalent circuit involves a more complicated calculation than that of the simple model with two large parallel electrode plates and an assumption of parallel electric field between the two plates. In addition, the further development on the theoretical model could be helpful to resolve the complex problem in crystallisation processes by separating the variables.

(3) The on-line EIS measurement conducted on the crystallisation processes in this study usually took 2-3 minutes to complete the data collection over the whole frequency range (1Hz-32MHz). As is known, accompanying the nucleation and growth of crystals, the crystal size, concentration, and ionic concentration all change with time. The speed of data acquisition does not satisfy the crystallisation process. Therefore, it is suggested to obtain a fast data collection speed for the on-line EIS measurement. It could be approached by a fast spectral sensing method, which uses a linear frequency modulated “chirp” excitation signal, and “wavelet” extraction of spectral data from the detected response. The method can offer

benefits of fast spectral sensing over a wide frequency range within several milli-seconds. Some preliminary studies have been done at the University of Leeds, but the application of this technique in the on-line monitoring of crystallisation processes needs to be studied further.

(4) In the experiments on crystallisation processes, the solid concentration and solute concentration were not measured due to the lack of requisite instrumentation. In the future work, if the instrumentation were available, it is suggested to measure the solid concentration and solute concentration on-line using ATR-FTIR spectroscopy and Raman spectroscopy, respectively. The profiles of solid concentration and solute concentration make the quantitative analysis possible relying on a suitable theoretical model. Besides, the off-line microscope measurement during the phase transformation process can be improved by Raman spectroscopy, which can measure the solid concentrations of the α phase and β phase on-line.

(5) Both of the case studies included in this work are centred upon the proposal of a mathematical model of the electrical properties of the material, and the verification of the model through a systematic experiment process. The verification experiments have been designed to eliminate all process variables during crystallisation processes except each specific measured. In design studies for implementation the aim may be to identify which process variables will have major influence on electrical spectroscopy measurements, and which are less sensitive. To reveal this form of data it would be useful to process the multivariate data using an appropriate statistical technique, for example principal component analysis. This would be expected to reveal which process variables are highly correlated and which are not, forming a useful dataset for application studies.

(6) The instrumentation can be improved to decrease the effect of common mode voltage in the electrical impedance tomography imaging measurement. A transformer or a voltage buffer from an operational amplifier with a high common mode voltage rejection ratio could be designed to isolate the common mode voltage and decrease the effect of common mode voltage.

(7) It is also suggested that the 8-electrode sensor could be updated to a 16-electrode sensor in order to get a good resolution for the imaging of the distribution of dielectric properties of colloids. The current EITS measurement operates manually

using the electrical impedance analyzer, which is really time consuming. In order to get fast and automatic data acquisition, the hardware needs to be improved. The fast spectral sensing method which has been described in point (3), is now under further construction at the University of Leeds, which should be a good choice for applying the proposed method for imaging the spatial and temporal distribution of particle characteristics in process applications.

Reference

Abbas, A., Nobbs, D. and Romagnoli, J. A., "Investigation of on-line optical particle characterization in reaction and cooling crystallization systems. Current state of the art", *Measurement Science and Technology*, vol. 3, 349-356, (2002).

Abbireddy, C. O. R. and Clayton, C. R. I., "A review of modern particle sizing methods", *Proceedings of the Institution of Civil Engineers-Geotechnical Engineering*, vol. 162, 193-201, (2009).

Allen, T., "Particle size measurement", Chapman & Hall, London, (1990).

Allen, T., "A review of sedimentation methods of particle-size analysis", *Particle Size Analysis*, vol. 102, 454-476, (1992).

Allen, T., "Particle size measurement ", vol. 1, (1997).

Arroyo, F. J., Carrique, F., Bellini, T. and Delgado, A. V., "Dielectric dispersion of colloidal suspensions in the presence of stern layer conductance: Particle size effects", *Journal of Colloid and Interface Science*, vol. 210, 194-199, (1999).

Asami, K., "Characterization of heterogeneous systems by dielectric spectroscopy", *Progress in Polymer Science*, vol. 27, 1617-1659, (2002).

Babchin, A. J., Chow, R. S. and Sawatzky, R. P., "Electrokinetic measurements by electroacoustical methods", *Advances in Colloid and Interface Science*, vol. 30, 111-151, (1989).

Ballario, C., Bonincontro, A. and Cametti, C., "Dielectric dispersions of colloidal particles in aqueous suspensions with low ionic-conductivity", *Journal of Colloid and Interface Science*, vol. 54, 415-423, (1976).

Barchini, R. and Saville, D. A., "Dielectric response measurements on concentrated colloidal dispersions", *Journal of Colloid and Interface Science*, vol. 173, 86-91, (1995).

Barrett, P. and Glennon, B., "Characterizing the metastable zone width and solubility curve using lasentec fbrm and pvm", *Chemical Engineering Research and Design*, vol. 80, 799-805, (2002).

Barth, H. G. and Sun, S. T., "Particle-size analysis", *Analytical Chemistry*, vol. 57, R151-R175, (1985).

Bier, M., "Electrophoresis: Theory, methods, and applications", vol. II, Academic press, (1967).

Blum, G., Maier, H., Sauer, F. and Schwan, H. P., "Dielectric-relaxation of colloidal particle suspensions at radio frequencies caused by surface conductance", *Journal of Physical Chemistry*, vol. 99, 780-789, (1995).

Boone, K., Lewis, A. M. and Holder, D. S., "Imaging of cortical spreading depression of eit - implications for localization of elieptic foci", *Physiological Measurement*, vol. 15, A189-A198, (1994).

Bradshaw-Hajek, B. H., Miklavcic, S. J. and White, L. R., "The actual dielectric response function for a colloidal suspension of spherical particles", *Langmuir*, vol. 26,

7875-7884, (2010).

Brar, S. K. and Verma, M., "Measurement of nanoparticles by light-scattering techniques", *Trac-Trends in Analytical Chemistry*, vol. 30, 4-17,

Brown, B. H., "Electrical impedance tomography (eit): A review", *Journal of Medical Engineering & Technology*, vol. 27, 97-108, (2003).

Brown, B. H., Barber, D. C., Morice, A. H. and Leathard, A. D., "Cardiac and respiratory-related electrical-impedance changes in the human thorax", *Ieee Transactions on Biomedical Engineering*, vol. 41, 729-734, (1994).

Brown, B. H. and Seagar, A. D., "The sheffield data collection system", *Clin Phys Physiol Meas*, vol. 8 Suppl A, 91-7, (1987).

Canagaratna, S. G., "Voltage dependence of the charge-transfer resistance", *Journal of Electroanalytical Chemistry*, vol. 108, 371-372, (1980).

Carrique, F., Arroyo, F. J. and Delgado, A. V., "Effect of size polydispersity on the dielectric relaxation of colloidal suspensions: A numerical study in the frequency and time domains", *Journal of Colloid and Interface Science*, vol. 206, 569-576, (1998).

Carrique, F., Arroyo, F. J., Jimenez, M. L. and Delgado, A. V., "Dielectric response of concentrated colloidal suspensions", *Journal of Chemical Physics*, vol. 118, 1945-1956, (2003).

Carrique, F., Quirantes, A. and Delgado, A. V., "Dielectric-relaxation and distribution function of relaxation-times in dilute colloidal suspensions", *Colloids and Surfaces a-Physicochemical and Engineering Aspects*, vol. 97, 141-149, (1995).

Carrique, F., Ruiz-Reina, E., Arroyo, F. J., Jimenez, M. L. and Delgado, A. V., "Dielectric response of a concentrated colloidal suspension in a salt-free medium", *Langmuir*, vol. 24, 11544-11555, (2008).

Carvell, J. P. and Dowd, J. E., "On-line measurements and control of viable cell density in cell culture manufacturing processes using radio-frequency impedance", *Cytotechnology*, vol. 50, 35-48, (2006).

Cheng, Y. S., Barr, E. B., Marshall, I. A. and Mitchell, J. P., "Calibration and performance of an api aerosizer", *Journal of Aerosol Science*, vol. 24, 501-514, (1993).

Cole, K. S. and Cole, R. H., "Dispersion and absorption in dielectrics i. Alternating current characteristics", *Journal of Chemical Physics*, vol. 9, 341-351, (1941).

Cook, R. D., Saulnier, G. J., Gisser, D. G., Goble, J. C., Newell, J. C. and Isaacson, D., "Act3 - a high-speed, high-precision electrical-impedance tomograph", *Ieee Transactions on Biomedical Engineering*, vol. 41, 713-722, (1994).

Cosgrove, T., "Colloid science: Principles, methods and applications", Blackwell publication, Oxford, (2005).

De Anda, J. C., Wang, X. Z., Lai, X., Roberts, K. J., Jennings, K. H., Wilkinson, M. J., Watson, D. and Roberts, D., "Real-time product morphology monitoring in crystallization using imaging technique", *Aiche Journal*, vol. 51, 1406-1414, (2005).

Debye, P., "A method for the determination of the mass of electrolytic ions", *Journal of Chemical Physics*, vol. 1, 13-16, (1933).

Delacey, E. H. B. and White, L. R., "Dielectric response and conductivity of dilute suspensions of colloidal particles", *Journal of the Chemical Society-Faraday Transactions Ii*, vol. 77, 2007-2039, (1981).

Delgado, A., Gonzalezcaballero, F. and Bruque, J. M., "On the zeta-potential and surface-charge density of montmorillonite in aqueous-electrolyte solutions", *Journal of Colloid and Interface Science*, vol. 113, 203-211, (1986).

Delgado, A. V., Arroyo, F. J., Gonzalez-Caballero, F., Shilov, V. N. and Borkovskaya, Y. B., "The effect of the concentration of dispersed particles on the mechanisms of low-frequency dielectric dispersion (lfdd) in colloidal suspensions", *Colloids and Surfaces a-Physicochemical and Engineering Aspects*, vol. 140, 139-149, (1998).

Delgado, A. V., Gonzalez-Caballero, F., Hunter, R. J., Koopal, L. K. and Lyklema, J., "Measurement and interpretation of electrokinetic phenomena", *Journal of Colloid and Interface Science*, vol. 309, 194-224, (2007).

Dharmayat, S., Hammond, R. B., Lai, X. J., Ma, C. Y., Purba, E., Roberts, K. J., Chen, Z. P., Martin, E., Morris, J. and Bytheway, R., "An examination of the kinetics of the solution-mediated polymorphic phase transformation between alpha- and beta-forms of l-glutamic acid as determined using online powder x-ray diffraction", *Crystal Growth & Design*, vol. 8, 2205-2216, (2008).

Dickin, F. and Wang, M., "Electrical resistance tomography for process applications", *Measurement Science & Technology*, vol. 7, 247-260, (1996).

Doi, A., "Comment on warburg impedance and related phenomena", *Solid State Ionics*, vol. 40-1, 262-265, (1990).

Dowding, P. J., Goodwin, J. W. and Vincent, B., "Factors governing emulsion droplet and solid particle size measurements performed using the focused beam reflectance technique", *Colloids and Surfaces A: Physicochemical and Engineering Aspects*, vol. 192, 5-13, (2001).

Dudley, L. M., Bialkowski, S., Or, D. and Junkermeier, C., "Low frequency impedance behavior of montmorillonite suspensions: Polarization mechanisms in the low frequency domain", *Soil Science Society of America Journal*, vol. 67, 518-526, (2003).

Dukhin, A. S. and Goetz, P. J., "Ultrasound for characterizing colloids: Particle sizing, zeta potential, rheology", Elsevier Science B.V., (2002).

Dukhin, S. S. and Shilov, V. N., "Kinetic aspects of electrochemistry of disperse systems .2. Induced dipole-moment and the nonequilibrium double-layer of a colloid particle", *Advances in Colloid and Interface Science*, vol. 13, 153-195, (1980).

Ehara, K., Mulholland, G. W. and Hagwood, R. C., "Determination of arbitrary moments of aerosol size distributions from measurements with a differential mobility analyzer", *Aerosol Science and Technology*, vol. 32, 434-452, (2000).

Eshel, G., Levy, G. J., Mingelgrin, U. and Singer, M. J., "Critical evaluation of the use of laser diffraction for particle-size distribution analysis", *Soil Science Society of America Journal*, vol. 68, 736-743, (2004).

Feldman, Y., Polygalov, E., Ermolina, I., Polevaya, Y. and Tsentsiper, B., "Electrode polarization correction in time domain dielectric spectroscopy", *Measurement Science & Technology*, vol. 12, 1355-1364, (2001).

Ferrari, E. S. and Davey, R. J., "Solution-mediated transformation of alpha to beta l-glutamic acid: Rate enhancement due to secondary nucleation", *Crystal Growth & Design*, vol. 4, 1061-1068, (2004).

Fixman, M., "Thin double-layer approximation for electrophoresis and dielectric response", *Journal of Chemical Physics*, vol. 78, 1483-1491, (1983).

Garti, N. and Zour, H., "The effect of surfactants on the crystallization and polymorphic transformation of glutamic acid", *Journal of Crystal Growth*, vol. 172, 486-498, (1997).

Gerhardt, R., "Impedance and dielectric-spectroscopy revisited - distinguishing localized relaxation from long-range conductivity", *Journal of Physics and Chemistry of Solids*, vol. 55, 1491-1506, (1994).

Gersing, E. and Osypka, M., "Eit using magnitude and phase in an extended frequency-range", *Physiological Measurement*, vol. 15, A21-A28, (1994).

Glickman, Y. A., Filo, O., Nachaliel, U., Lenington, S., Amin-Spector, S. and Ginor, R., "Novel eis postprocessing algorithm for breast cancer diagnosis", *Ieee Transactions on Medical Imaging*, vol. 21, 710-712, (2002).

Grosse, C. and Delgado, A. V., "Dielectric dispersion in aqueous colloidal systems", *Current Opinion in Colloid & Interface Science*, vol. 15, 145-159, (2010).

Grosse, C. and Foster, K. R., "Permittivity of a suspension of charged spherical-particles in electrolyte solution", *Journal of Physical Chemistry*, vol. 91, 3073-3076, (1987).

Grosse, C. and Tirado, M., "Improved calibration of impedance analyzers for measurements on highly conductive liquids", *Ieee Transactions on Instrumentation and Measurement*, vol. 50, 1329-1333, (2001).

Gun'ko, V. M., Zarko, V. I., Leboda, R. and Chibowski, E., "Aqueous suspension of fumed oxides: Particle size distribution and zeta potential", *Advances in Colloid and Interface Science*, vol. 91, 1-112, (2001).

Hammond, R. B., Lai, X. J., Roberts, K. J., Thomas, A. and White, G., "Application of in-process x-ray powder diffraction for the identification of polymorphic forms during batch crystallization reactions", *Crystal Growth & Design*, vol. 4, 943-948, (2004).

Harris, N. D., Suggett, A. J., Barber, D. C. and Brown, B. H., "Applications of applied potential tomography (apt) in respiratory medicine", *Clinical physics and physiological measurement : an official journal of the Hospital Physicists' Association, Deutsche Gesellschaft fur Medizinische Physik and the European Federation of Organisations for Medical Physics*, vol. 8 Suppl A, 155-65, (1987).

Hauttmann, S. and Muller, J., "In-situ biomass characterisation by impedance spectroscopy using a full-bridge circuit", *Bioprocess and Biosystems Engineering*, vol. 24, 137-141, (2001).

He, C. Y., Liu, B. G., Li, M. and Gao, C. X., "Alternating current impedance

spectroscopy measurement under high pressure", *Review of Scientific Instruments*, vol. 82, 4, (2011).

He, K. J. and Zhao, K. S., "Dielectric analysis of a nanoscale particle in an aqueous solution of low electrolyte concentration", *Langmuir*, vol. 21, 11878-11887, (2005).

Henry, D. C., "The cataphoresis of suspended particles part i - the equation of cataphoresis", *Proceedings of the Royal Society of London Series a-Containing Papers of a Mathematical and Physical Character*, vol. 133, 106-129, (1931).

Hinch, E. J., Sherwood, J. D., Chew, W. C. and Sen, P. N., "Dielectric response of a dilute suspension of spheres with thin double-layers in an asymmetric electrolyte", *Journal of the Chemical Society-Faraday Transactions Ii*, vol. 80, 535-551, (1984).

Hodge, I. M., Ingram, M. D. and West, A. R., "Impedance and modulus spectroscopy of polycrystalline solid electrolytes", *Journal of Electroanalytical Chemistry*, vol. 74, 125-143, (1976).

Holden, P. J., Wang, M., Mann, R., Dickin, F. J. and Edwards, R. B., "Imaging stirred-vessel macromixing using electrical resistance tomography", *Aiche Journal*, vol. 44, 780-790, (1998).

Holder, D. S., "Electrical-impedance tomography with cortical or scalp electrodes during global cerebral-ischemia in the anesthetized rat", *Clinical Physics and Physiological Measurement*, vol. 13, 87-98, (1992).

Holder, D. S., "Electrical impedance tomography: Methods, history and applications", *Institute of physics publishing Bristol and philadelphia*, vol., (2005).

Hunter, R. J., "Zeta potential in colloid science", Academic press, London, (1981).

Hunter, R. J., "Foundations of colloid science", Oxford University Press, (2001).

Jacques, S. D. M., Pile, K. and Barnes, P., "An in-situ synchrotron x-ray diffraction tomography study of crystallization and preferred crystal orientation in a stirred reactor", *Crystal Growth & Design*, vol. 5, 395-397, (2005).

Jimenez, M. L., Arroyo, F. J., Carrique, F. and Delgado, A. V., "Surface conductivity of colloidal particles: Experimental assessment of its contributions", *Journal of Colloid and Interface Science*, vol. 316, 836-843, (2007).

Kijlstra, J., Vanleeuwen, H. P. and Lyklema, J., "Low-frequency dielectric-relaxation of hematite and silica sols", *Langmuir*, vol. 9, 1625-1633, (1993).

Kim, B. S., Isaacson, D., Xia, H. J., Kao, T. J., Newell, J. C. and Saulnier, G. J., "A method for analyzing electrical impedance spectroscopy data from breast cancer patients", *Physiological Measurement*, vol. 28, S237-S246, (2007).

Kitamura, M., "Polymorphism in the crystallization of l-glutamic acid", *Journal of Crystal Growth*, vol. 96, 541-546, (1989).

Kitamura, M., "Controlling factor of polymorphism in crystallization process", *Journal of Crystal Growth*, vol. 237, 2205-2214, (2002).

Klang, V., Matsko, N. B., Valenta, C. and Hofer, F., "Electron microscopy of

nanoemulsions: An essential tool for characterisation and stability assessment", *Micron*, vol. 43, 85-103, (2012).

Lim, K. H. and Franses, E. I., "Electrical-properties of aqueous dispersions of polymer microspheres", *Journal of Colloid and Interface Science*, vol. 110, 201-213, (1986).

Liu, J. Y., "Scanning transmission electron microscopy and its application to the study of nanoparticles and nanoparticle systems", *Journal of Electron Microscopy*, vol. 54, 251-278, (2005).

Lyklema, J., Springer, M. M., Shilov, V. N. and Dukhin, S. S., "The relaxation of the double-layer around colloidal particles and the low-frequency dielectric-dispersion .3. Application of theory to experiments", *Journal of Electroanalytical Chemistry*, vol. 198, 19-26, (1986).

Ma, Z. H., Merkus, H. G., de Smet, J., Heffels, C. and Scarlett, B., "New developments in particle characterization by laser diffraction: Size and shape", *Powder Technology*, vol. 111, 66-78, (2000).

Ma.T, "Feasibility study of using spectroscopic imaging for measuring particle size distribution", PhD thesis, University of Leeds, (2007).

Macdonald, J. R., "Impedance spectroscopy, emphasizing solid materials and systems", A Wiley-Interscience publication, (1987).

Mangelsdorf, C. S. and White, L. R., "Electrophoretic mobility of a spherical colloidal particle in an oscillating electric-field", *Journal of the Chemical Society-Faraday Transactions*, vol. 88, 3567-3581, (1992).

Mangelsdorf, C. S. and White, L. R., "Dielectric response of a dilute suspension of spherical colloidal particles to an oscillating electric field", *Journal of the Chemical Society-Faraday Transactions*, vol. 93, 3145-3154, (1997).

Marshall, I. A., Mitchell, J. P. and Griffiths, W. D., "The behaviour of regular-shaped non-spherical particles in a tsi aerodynamic particle sizer", *Journal of Aerosol Science*, vol. 22, 73-89, (1991).

Marzantowicz, M., Dygas, J. R., Krok, F., Lasinska, A., Florjanczyk, Z. and Zygadlo-Monikowska, E., "In situ microscope and impedance study of polymer electrolytes", *Electrochimica Acta*, vol. 51, 1713-1727, (2006).

Mazzeo, B. A. and Flewitt, A. J., "Two- and four-electrode, wide-bandwidth, dielectric spectrometer for conductive liquids: Theory, limitations, and experiment", *Journal of Applied Physics*, vol. 102, 6, (2007).

McEwan, A., Cusick, G. and Holder, D. S., "A review of errors in multi-frequency eit instrumentation", *Physiological Measurement*, vol. 28, S197-S215, (2007).

McKenzie, L. C., Haben, P. M., Kevan, S. D. and Hutchison, J. E., "Determining nanoparticle size in real time by small-angle x-ray scattering in a microscale flow system", *Journal of Physical Chemistry C*, vol. 114, 22055-22063, (2010).

McLachlan, D. S. and Sauti, G., "The ac and dc conductivity of nanocomposites", *Journal of Nanomaterials*, vol., 9, (2007).

Metherall, P., Barber, D. C., Smallwood, R. H. and Brown, B. H., "Three-dimensional electrical impedance tomography", *Nature*, vol. 380, 509-512, (1996).

Metin, C. O., Lake, L. W., Miranda, C. R. and Nguyen, Q. P., "Stability of aqueous silica nanoparticle dispersions", *Journal of Nanoparticle Research*, vol. 13, 839-850, (2011).

Mougin, P., Thomas, A., Wilkinson, D., White, G., Roberts, K. J., Herrmann, N., Jack, R. and Tweedie, R., "On-line monitoring of a crystallization process", *Aiche Journal*, vol. 49, 373-378, (2003).

Mougin, P., Wilkinson, D. and Roberts, K. J., "In situ measurement of particle size during the crystallization of l-glutamic acid under two polymorphic forms: Influence of crystal habit on ultrasonic attenuation measurements", *Crystal Growth & Design*, vol. 2, 227-234, (2002).

Muller, J. W., "Crystallisation", *Oxford: Elsevier Butterworth-Heinemann*, vol. Fourth edition, (2004).

Murphy, D. and Rolfe, P., "Aspects of instrumentation design for impedance imaging", *Clinical physics and physiological measurement : an official journal of the Hospital Physicists' Association, Deutsche Gesellschaft fur Medizinische Physik and the European Federation of Organisations for Medical Physics*, vol. 9 Suppl A, 5-14, (1988).

Myerson, A. S., "Handbook of industrial crystallization", *Butterworth-Heinemann*, vol., (2001).

Nathierdufour, N., Bougeard, L., Devaux, M. F., Bertrand, D. and Demonredon, F. L., "Comparison of sieving and laser diffraction for the particle-size measurements of raw-materials used in foodstuff", *Powder Technology*, vol. 76, 191-200, (1993).

Neuberger, A., "Dissociation constants and structures of glutamic acid and its esters", *Biochemical Journal*, vol. 30, 2085-2094, (1936).

Novak, S., Drazic, G. and Macek, S., "A study of ceramic-suspension solidification using complex-impedance spectroscopy", *Journal of the European Ceramic Society*, vol. 21, 2081-2084, (2001).

O'Brien, R. W., "The response of a colloidal suspension to an alternating electric-field", *Advances in Colloid and Interface Science*, vol. 16, 281-320, (1982).

O'Brien, R. W., "The high-frequency dielectric-dispersion of a colloid", *Journal of Colloid and Interface Science*, vol. 113, 81-93, (1986).

O'Brien, R. W., "Electro-acoustic effects in a dilute suspension of spherical-particles", *Journal of Fluid Mechanics*, vol. 190, 71-86, (1988).

O'Brien, R. W., Cannon, D. W. and Rowlands, W. N., "Electroacoustic determination of particle-size and zeta-potential", *Journal of Colloid and Interface Science*, vol. 173, 406-418, (1995).

O'Brien, R. W., Midmore, B. R., Lamb, A. and Hunter, R. J., "Electroacoustic studies of moderately concentrated colloidal suspensions", *Faraday Discussions*, vol. 90, 301-312, (1990).

O'Brien, R. W. and White, L. R., "Electrophoretic mobility of a spherical colloidal

particle", *Journal of the Chemical Society-Faraday Transactions Ii*, vol. 74, 1607-1626, (1978).

O'Konski, C. T., "Electric properties of macromolecules 5. Theory of ionic polarization in polyelectrolytes", *Journal of Physical Chemistry*, vol. 64, 605-619, (1960).

Ono, T., Kramer, H. J. M., ter Horst, J. H. and Jansens, P. J., "Process modeling of the polymorphic transformation of l-glutamic acid", *Crystal Growth & Design*, vol. 4, 1161-1167, (2004).

Peters, T. M., Chein, H. M., Lundgren, D. A. and Keady, P. B., "Comparison and combination of aerosol-size distributions measured with a low-pressure impactor, differential mobility particle sizer, electrical aerosol analyzer, and aerodynamic particle sizer", *Aerosol Science and Technology*, vol. 19, 396-405, (1993).

Porter, D. A. and Easterling, K. E., "Phase transformations in metals and alloys", CRC Press, (1992).

Provder, T., "Challenges in particle size distribution measurement past, present and for the 21st century", *Progress in Organic Coatings*, vol. 32, 143-153, (1997).

Rosell, J. and Riu, P., "Common-mode feedback in electrical-impedance tomography", *Clinical Physics and Physiological Measurement*, vol. 13, 11-14, (1992).

Rosen, L. A. and Saville, D. A., "Dielectric-spectroscopy of colloidal dispersions - comparisons between experiment and theory", *Langmuir*, vol. 7, 36-42, (1991).

Saka, E. E. and Guler, C., "The effects of electrolyte concentration, ion species and ph on the zeta potential and electrokinetic charge density of montmorillonite", *Clay Minerals*, vol. 41, 853-861, (2006).

Sauer, B. B., Stock, R. S., Lim, K. H. and Ray, W. H., "Polymer latex particle-size measurement through high-speed dielectric-spectroscopy", *Journal of Applied Polymer Science*, vol. 39, 2419-2441, (1990).

Saville, D. A., "Dielectric behavior of colloidal dispersions", *Colloids and Surfaces a-Physicochemical and Engineering Aspects*, vol. 92, 29-40, (1994).

Sawatzky, R. P. and Babchin, A. J., "Hydrodynamics of electrophoretic motion in an alternating electric-field", *Journal of Fluid Mechanics*, vol. 246, 321-334, (1993).

Schlaberg, H. I., Jia, J., Qiu, C., Wang, M. and Li, H., "Development and application of the fast impedance camera-a high performance dual-plan electrical impedance tomography system", *5 th International Symposium on Porcess Tomography in Poland, Zakopane*, vol., (2008).

Scholl, J., Bonalumi, D., Vicum, L., Mazzotti, M. and Muller, M., "In situ monitoring and modeling of the solvent-mediated polymorphic transformation of l-glutamic acid", *Crystal Growth & Design*, vol. 6, 881-891, (2006).

Schurr, J. M., "On theory of dielectric dispersion of spherical colloidal particles in electrolyte solution", *Journal of Physical Chemistry*, vol. 68, 2407-&, (1964).

Schwan, H. P., Schwarz, G., Maczuk, J. and Pauly, H., "On low-frequency dielectric dispersion of colloidal particles in electrolyte solution", *Journal of Physical Chemistry*,

vol. 66, 2626-&, (1962).

Schwarz, G., "A theory of low-frequency dielectric dispersion of colloidal particles in electrolyte solution", *Journal of Physical Chemistry*, vol. 66, 2636-&, (1962).

Seagar, A. D., Barber, D. C. and Brown, B. H., "Theoretical limits to sensitivity and resolution in impedance imaging", *Clin Phys Physiol Meas*, vol. 8 Suppl A, 13-31, (1987).

Sher, L. D. and Schwan, H. P., "Microelectrophoresis with alternating electric fields", *Science*, vol. 148, 229-&, (1965).

Shukla, A., Prakash, A. and Rohani, S., "Online measurement of particle size distribution during crystallization using ultrasonic spectroscopy", *Chemical Engineering Science*, vol. 65, 3072-3079, (2010).

Sihvola, A., "Dielectric polarization and particle shape effects", *Journal of Nanomaterials*, vol., 9, (2007).

Sipahioglu, O. and Barringer, S. A., "Dielectric properties of vegetables and fruits as a function of temperature, ash, and moisture content", *Journal of Food Science*, vol. 68, 234-239, (2003).

Stoneman, M. R., Kosempa, M., Gregory, W. D., Gregory, C. W., Marx, J. J., Mikkelson, W., Tjoe, J. and Raicu, V., "Correction of electrode polarization contributions to the dielectric properties of normal and cancerous breast tissues at audio/radiofrequencies", *Physics in Medicine and Biology*, vol. 52, 6589-6604, (2007).

Szczepanik, Z. and Rucki, Z., "Field analysis and electrical models of multi-electrode impedance sensors", *Sensors and Actuators A: Physical*, vol. 133, 13-22, (2007).

Threlfall, T. L., "Analysis of organic polymorphs - a review", *Analyst*, vol. 120, 2435-2460, (1995).

Wall, S., "The history of electrokinetic phenomena", *Current Opinion in Colloid & Interface Science*, vol. 15, 119-124, (2010).

Wang, M., "Inverse solutions for electrical impedance tomography based on conjugate gradients methods", *Measurement Science & Technology*, vol. 13, 101-117, (2002).

Wang, M., "Electrode models in electrical impedance tomography", *Journal of Zhejiang University Science*, vol. 6A, 1386-1393, (2005).

Wang, M., Dickin, F. J. and Beck, M. S., "Improved electrical-impedance tomography data-collection system and measurement protocols", Computational Mechanics Publications Ltd, (1993).

Wang, M., Dickin, F. J. and Williams, R. A., "Modeling and analysis of electrically conducting vessels and pipelines in electrical-resistance process tomography", *Iee Proceedings-Science Measurement and Technology*, vol. 142, 313-322, (1995).

Wang, M., Dorward, A., Vlaev, D. and Mann, R., "Measurements of gas-liquid mixing in a stirred vessel using electrical resistance tomography (ert)", *Chemical Engineering Journal*, vol. 77, 93-98, (2000).

Wang, M., Yin, W. and Holliday, N., "A highly adaptive electrical impedance sensing system for flow measurement", *Measurement Science & Technology*, vol. 13, 1884-1889, (2002).

Wei, Y. Z., Chiang, P. and Sridhar, S., "Ion size effects on the dynamic and static dielectric-properties of aqueous alkali solutions", *Journal of Chemical Physics*, vol. 96, 4569-4573, (1992).

Weiss, M., Verheijen, P. J. T., Marijnissen, J. C. M. and Scarlett, B., "On the performance of an on-line time-of-flight mass spectrometer for aerosols", *Journal of Aerosol Science*, vol. 28, 159-171, (1997).

Xu, J. Y., Wang, M., Wu, Y. X., Schlaberg, H. I., Zheng, Z. C. and Williams, R. A., "An experimental study of in-situ phase fraction in jet pump using electrical resistance tomography technique", *Chinese Physics Letters*, vol. 24, 512-515, (2007).

Yerworth, R. J., Bayford, R. H., Brown, B., Milnes, P., Conway, M. and Holder, D. S., "Electrical impedance tomography spectroscopy (eits) for human head imaging", *Physiological Measurement*, vol. 24, 477-489, (2003).

Yorkey, T. J., Webster, J. G. and Tompkins, W. J., "Comparing reconstruction algorithms for electrical-impedance tomography", *Ieee Transactions on Biomedical Engineering*, vol. 34, 843-852, (1987).

Zhao, K. S. and He, K. J., "Dielectric relaxation of suspensions of nanoscale particles surrounded by a thick electric double layer", *Physical Review B*, vol. 74, 10, (2006).

Zoltowski, P., "On the electrical capacitance of interfaces exhibiting constant phase element behaviour", *Journal of Electroanalytical Chemistry*, vol. 443, 149-154, (1998).

Zou, Y. and Guo, Z., "A review of electrical impedance techniques for breast cancer detection", *Medical Engineering & Physics*, vol. 25, 79-90, (2003).

Appendix

List of Publications:

1. **Y. Zhao**, M. Wang and R. B. Hammond, “Characterisation of Nano-particles: Relationship between Particle Size and Electrical Impedance Spectra”, *Journal of Nanoscience and Nanotechnology*, in press, (2012).
2. **Y. Zhao**, M. Wang and R. B. Hammond, “Characterisation of Crystallisation Processes with Electrical Impedance Spectroscopy”, *Nuclear Engineering and Design,* 241, 1938-1944, (2011).
3. **Y. Zhao**, M. Wang and R.B. Hammond, “Electrical Impedance Spectroscopy Study on Colloidal Suspensions for Particle Size Determination”, *PITTCON-2010*, Orlando, US, (2010).
4. M. Nahvi, B. S. Hoyle and **Y. Zhao**, “Experimental Verification Trials for Fast Spectro-tomography Sensing in Process Reactors”, *Proceedings of 6th World Congress on Industrial Process Tomography*, September, Beijing, China, (2010).
5. **Y. Zhao**, M. Wang and R.B. Hammond, “Characterisation of Crystallisation Processes with Electrical Impedance Spectroscopy”, *Proceedings of what where when multi-dimensional advances for industrial process monitoring*, June, Leeds, UK, (2009).
6. **Y. Zhao**, M. Wang and R.B. Hammond, “Electrical Impedance Spectroscopy Study on Charged Particles in Crystallisation Processes”, *PITTCON-2009*, Chicago, 1300-13P, (2009).
7. **Y. Zhao**, “Electrical Impedance Spectroscopy Study on Charged Particles in Suspension/Crystallisation Process”, *Workshop insight of the virtual centre for industrial & process tomography*, Leeds, UK, summer (2008).